

**Best
Available
Copy**

2828

2828

(1)



Science Center
Rockwell International

EVR

Noted

13

AO 2828.2

AD A139280

INTERDISCIPLINARY PROGRAM
FOR
QUANTITATIVE FLAW DEFINITION
SPECIAL REPORT FIRST YEAR EFFORT

Covering Period July 1, 1974 - June 30, 1975

Contract Number F33615-74-C-5180

Prepared For

Advanced Research Projects Agency
Arlington, Virginia

and

Air Force Materials Laboratory
Air Force Systems Command
Wright-Patterson AFB, Ohio

17 SEP 1975

DTIC
ELECT
MAR 22 1984
A

DTIC FILE COPY

This document has been approved
for public release and sale; its
distribution is unlimited.

84 03 20 082



INTERDISCIPLINARY PROGRAM
FOR
QUANTITATIVE FLAW DEFINITION

SPECIAL REPORT FIRST YEAR EFFORT

Covering Period July 1, 1974 - June 30, 1975

Contract Number F33615-74-C-5180

Prepared For

Advanced Research Projects Agency
Arlington, Virginia

and

Air Force Materials Laboratory
Air Force Systems Command
Wright-Patterson AFB, Ohio

A handwritten signature in cursive script, reading "Donald O. Thompson".

Donald O. Thompson
Program Manager
Center for Advanced NDE

Unclassified

SECURITY CLASSIFICATION OF THIS PAGE (When Data Entered)

REPORT DOCUMENTATION PAGE		READ INSTRUCTIONS BEFORE COMPLETING FORM
1. REPORT NUMBER	2. GOVT ACCESSION NO. AD-A179280	3. RECIPIENT'S CATALOG NUMBER
4. TITLE (and Subtitle) Interdisciplinary Program for Quantitative Flaw Definition-Special Report First Year Effort		5. TYPE OF REPORT & PERIOD COVERED Special Report, First Year Effort - July 31, 1974- June 30, 1975
7. AUTHOR(s) Donald O. Thompson, Program Manager		8. CONTRACT OR GRANT NUMBER(s) F33615-74-C-5180
9. PERFORMING ORGANIZATION NAME AND ADDRESS Science Center, Rockwell International 1049 Camino Dos Rios Thousand Oaks, California 91360		10. PROGRAM ELEMENT, PROJECT, TASK AREA & WORK UNIT NUMBERS AO 2828
11. CONTROLLING OFFICE NAME AND ADDRESS		12. REPORT DATE September 17, 1975
14. MONITORING AGENCY NAME & ADDRESS (if different from Controlling Office) Air Force Materials Laboratory Air Force Systems Command Wright-Patterson Air Force Base, Ohio 45433		13. NUMBER OF PAGES 290
16. DISTRIBUTION STATEMENT (of this Report) Approved for Public Release		15. SECURITY CLASS. (of this report) Unclassified
17. DISTRIBUTION STATEMENT (of the abstract entered in Block 20, if different from Report)		15a. DECLASSIFICATION/DOWNGRADING SCHEDULE
18. SUPPLEMENTARY NOTES		
19. KEY WORDS (Continue on reverse side if necessary and identify by block number) non-destructive evaluation; non-destructive testing; quantitative ultrasonics; signal processing; adhesive bonds; composites; residual stress; acoustic emission; exo-electrons		
20. ABSTRACT (Continue on reverse side if necessary and identify by block number)		

DD FORM 1 JAN 73 1473

EDITION OF 1 NOV 65 IS OBSOLETE

Unclassified
SECURITY CLASSIFICATION OF THIS PAGE (When Data Entered)

TABLE OF CONTENTS

Page

PROJECT 1 SUMMARY	1
PROJECT 2 SUMMARY	3
PROJECT 3 SUMMARY	4

INDIVIDUAL REPORTS

PROJECT I - Quantitative Flaw Definition	6
PROJECT II - Bond Strength182
PROJECT III - Failure Prediction251



Accession For	
WHS 0001	<input checked="" type="checkbox"/>
DTIC TAB	<input type="checkbox"/>
Unannounced	<input type="checkbox"/>
Justification	
By	
Distribution/	
Availability Codes	
Dist	Avail and/or Special
A-1	



Science Center
Rockwell International

This document reports on 3 projects:

PROJECT I

FLAW CHARACTERIZATION BY ULTRASONIC TECHNIQUES

p3

Summary

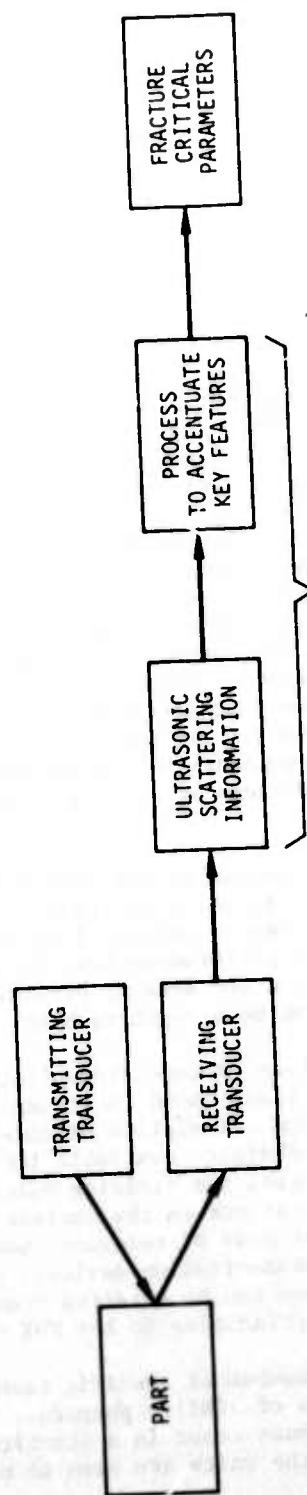
In the initiation of this program four specific objectives were set forth. These were: (1) to pursue advanced research in quantitative techniques for NDE, (2) to establish a focal point for NDE research, (3) to enhance communication between the research community and the NDE user, and (4) to promote the image of NDE. The first objective was accomplished by a series of coordinated technical tasks which will be summarized in the following paragraphs. The remaining three objectives were also reached in a very real, though more intangible, sense. This progress was most clearly exemplified by the success of the ARPA/AFML review of quantitative NDE held at the Science Center on July 15-17, 1975. This meeting was a review of the technical work of the first year of the program, and also included a large number of selected papers in closely related areas. Over 170 participants were present, and the distribution of their affiliations; government agencies - 29%, private industry - 50%, and universities - 21%; illustrates the communication across disciplinary and functional lines that was established. The active discussions and lengthy technical sessions is further evidence of the focussed attention that was brought to bear on the NDE problems and potential solutions at the meeting.

The direct technical part of the program at the Center for Advanced NDE has been divided into 3 projects. Each is directed toward a specific problem area identified by the DOD and Science Center personnel to satisfy two major requirements. First, major DOD systems performance must be limited by the inability to make the required inspection and second, promising technology on new ideas must be available which can be brought to bear.

Project I is addressed to the problem of nondestructively obtaining data for the fracture mechanics analysis of flaws found in structures. Thus, it is desired to determine the size, shape, and orientation of defects as located by existing techniques. A survey of techniques available led to the conclusion that ultrasonics had the greatest potential for yielding quantitative information, particularly when the flaw is not on the surface and the effort has been focussed in this area. A great body of relevant knowledge has been developed in the fields of ultrasonic communication devices, geophysics, and solid state physics; major progress can be expected from a concentrated effort to apply these well established principles to the NDE field.

Project I has been divided into a number of specific technical tasks which can be grouped together into units of similar purpose. Figure 1 is a diagram of the information flow that must occur in a quantitative ultrasonic system for defect characterization and the units are seen to coincide with the individual steps that are required.

QUANTITATIVE FLAW DEFINITION



UNIT I
TRANSDUCERS
Lakin - Piezoelectric
Maxfield - Electromagnetic
Thompson - Electromagnetic

UNIT V
SAMPLE PREPARATION
Paton - Diffusion Bonding

UNIT II
DATA PROCESSING
Kino - Imaging
Yee - Digital Frequency Analysis
Packman - Indicia Analysis
White - SAW Filters

UNIT III
DEFECT CHARACTERIZATION
Krumhansl - Basic Theory
Adler - Scattering Measurements
Tittmann - Scattering Measurements



Science Center
Rockwell International

UNIT VI
SYSTEM INTEGRATION
Kraut - Review of FBH Theory

Fig. 1

Each of the technical tasks produced significant results, and an enumeration of these is impossible in this summary. They may be found in the individual reports which follows. However, a number of important accomplishments achieved by the group should be identified. The key to quantitative defect characterization is the gathering and processing of the information carried by ultrasonic wave scattered from the defect. The most familiar way to do this is through the formation of an image, and significant advances in the necessary technology were achieved in this program. Other complementary schemes applicable in different regimes of wavelength and defect size and based upon the detection and recognition of particular features of the scattered fields, such as their variations with frequency and angle, have also been found to have considerable promise. An important part of the second year's work will be the refinement of these techniques and evaluation of them on a common set of samples.

In order to interpret these scattering measurements, it is necessary to have mathematical models for the scattering. Several models of various complexity have been investigated during the year, and these will be invaluable in unraveling the rich phenomena that are observed experimentally.

As noted previously, a great deal of knowledge is available in other disciplines in which elastic wave phenomena are studied. An important part of the first year's work has been to integrate results from the electrical engineering, solid state physics, and geophysics communities into the NDE effort. One example of this is the development of filters which compensate for the narrow bandwidth of piezoelectric transducers and, hence, improve their depth resolution as well as their utility in ultrasonic spectroscopy.

One of the important areas in NDE is standardization. At the present time, the flat bottom hole is used as a reference for the setup and calibration of instruments. During this year, experiments were performed which substantially increased our understanding of the ultrasonic scattering that takes place during this procedure. In addition, diffusion bonding techniques were developed which allow us to embed different shaped defects within solids. This has enabled us to prepare sets of samples with internal defects of well characterized shape for the study of the various experimental techniques. It also shows promise for producing a new type of calibration standard in the future.

PROJECT II

NONDESTRUCTIVE EVALUATION OF ADHESIVELY BONDED SYSTEMS ; and -> p 4

Summary

A very serious limitation on the utilization of adhesive bonds in aircraft structures is the inability to nondestructively evaluate their strength. This problem also retards the use of fiber reinforced composites where the susceptibility to moisture degradation in the polymer matrix and at the fiber-to-matrix interface leads to decreased design allowables and the less than full utilization of these structurally efficient materials. This project is designed to investigate the fundamental physical properties of weakened adhesive joints and polymer matrix composites in order to determine which measurement techniques or procedures have the greatest promise of accurately reflecting the strength properties of a part.

For adhesive joints between metal sheets, two separate sources of weakness are recognized. These are the cohesive strength of the bulk adhesive itself and the strength of adhesion between the metal and the polymeric adhesive. The former was investigated by examining how the bulk physical properties of the polymer layer influenced the measureable properties of an ultrasonic wave reflected from the two metal-to-adhesive interfaces that bound the adhesive. It was determined that the attenuation in the polymer makes a dramatic change in the frequency dependence of the reflection coefficient of the layer and must be taken into account carefully if measurements of this frequency dependence are used to deduce the elastic properties of an in-situ adhesive layer to determine its physical state and, hence, its strength. The latter strength property (adhesion) was investigated by attempting to observe small changes that occur in ultrasonic signals when they are reflected from the very thin layer of different acoustic properties that occurs at an interface where thin layers of differing chemical composition determine the layer strength. It was found that the signal reflected directly backward from the interface was too strongly modified by other interface effects to exhibit any properties that could be related to the bond strength. Thus future experiments should utilize ultrasonic waves which interact with the interface at an angle or even propagate parallel to the adhesive layer.

For the problem of moisture degradation in polymer matrix composites, measurements of the strength properties of graphite-epoxy test panels were conducted as a function of exposure to boiling water. Two different types of composite materials were used; one in which the fiber-to-matrix interface was susceptible to moisture attack and one which repelled water from the interface. Concurrent with the strength tests, an extensive series of physical property measurements on the panels were also conducted so that the mechanism of degradation could be elucidated and potential techniques for nondestructive evaluation could be defined. As a result, the effects of moisture at the fiber-to-matrix interface could be distinguished from the effects of moisture on the matrix material alone and four potential useful nondestructive evaluation techniques were delineated.

PROJECT III

NONDESTRUCTIVE MEASUREMENT OF STRENGTH RELATED PROPERTIES

Summary

One of the most valuable potentials of quantitative NDE is to perform a nondestructive test on a part to predict its remaining safe life. In principle, this can be done by a quantitative determination of a physical property that is related to that mechanical state of the material which controls the failure process. One such failure related mechanical state is the degree of residual stress present in a part. Another is the acoustic emission signal generated by a part when its load approaches the ultimate failure stress. Both of these are being investigated as part of Project III.

Present methods of measuring residual stress in a nondestructive manner are based on X-ray techniques that are cumbersome and often time consuming. They also only measure those stresses that extend over large distances compared to the metallic grain size. This is satisfactory for those cases where the failure mechanism involves the opening of cracks at the surface such as in stress corrosion cracking and in the latter stages of fatigue failure, but is unsatisfactory for those cases where failure is initiated by plastic flow on a microscopic scale such as during the very early stages of fatigue failure and in the pre-yield microslip that sets up stress concentrations to initiate general yielding. Previous experiments have shown that the non-linear phenomenon of ultrasonic harmonic generation not only reflects microscopic internal stress that controls dislocation motion, but that it is a well defined physical property of a material that can be nondestructively measured conveniently. In order to establish the quantitative relationship between harmonic generation and the state of internal stress, measurements have been made on pure aluminum and its alloys as a function of work hardening, precipitation hardening and fatigue damage. The results show that harmonic generation is indeed a sensitive indicator of the state of internal stress, but that a more systematic study supported by dislocation theory and direct measures of dislocation parameters must be made before a quantitative nondestructive test method can be demonstrated.

For those residual stresses that extend over large distances compared to the grain size, a new, ultrasonic technique was investigated. This method utilizes the efficiency by which electromagnetic induction excites ultrasonic waves to perform a nondestructive measurement of the localized magnetostriction on the surface of a ferromagnetic material. Since this magnetostriction is a very distinctive function of stress, it can be used to measure the level of stress at the site of excitation of the ultrasonic waves. The results obtained in the preliminary experiments were very encouraging and further work to define the limitations of the technique will be undertaken next year.



Science Center
Rockwell International

Acoustic emission has been a most valuable tool not only for locating flaws in large structures when they are subjected to proof loads, but also for indicating the approach of catastrophic failure. Its primary drawback of having no guidelines by which to distinguish extraneous noises from those produced by a flaw has been the focus of our studies which were aimed at establishing a correspondence between the characteristics of an emission signal and the microscopic failure process that produced it. The results obtained thus far show clearly that the emission signals produced by failure in aluminum alloys are generated by the abrupt fracture of second phase particles in the material and that plastic flow of the matrix is very quiet.

PROJECT I

QUANTITATIVE FLAW DEFINITION

UNIT I - Transducers

- Task 1 Piezoelectric Transducers
 K. M. Lakin, University of Southern California
- Task 2 Optimization and Application of Electrodynamic
 Ultrasonic Wave Transducers
 B. W. Maxfield, Cornell University
- Task 3 Superconducting Magnets for Electromagnetic
 Transducers
 R. B. Thompson, Science Center, Rockwell International

UNIT II - Data Processing

- Task 1 Imaging and Processing of Angular Scattering
 G. S. Kino, Stanford University
- Task 2 Analog Data Processing
 R. M. White, University of California-Berkeley
- Task 3 Digital Techniques of Ultrasonic Flaw Characterization
 B. G. W. Yee, General Dynamics

UNIT III - Defect Characterization

- Task 1 Models for the Frequency Dependence of Ultrasonic Scattering
 From Real Flaws
 L. Adler, University of Tennessee
- Task 2 Defect Characterization by Spatial Distribution
 of Ultrasonic Scattered Energy
 P. Packman, Vanderbilt University
- Task 3 Experimental Studies of Ultrasonic Wave Scattering From
 Embedded Objects
 B. R. Tittmann, Science Center, Rockwell International
- Task 4 Theoretical Description of Scattering Phenomena
 J. A. Krumhansl, Cornell University

UNIT IV - System Integration

Task 1 Flaw Characterization Systems
E. A. Kraut, Science Center, Rockwell International

UNIT V - Sample Preparation

Task 1 Sample Preparation
N. E. Paton, Science Center, Rockwell International

PROJECT I, UNIT I, TASK I

PIEZOELECTRIC TRANSDUCERS

K. M. Lakin
University of Southern California

This report covers the nine month period from the start of this task. The three sub-tasks are transducer construction, transducer circuit modeling, and construction of a data acquisition system for use in radiation field pattern analysis. The three parts of this program are intended to interact such that NDE transducers of current interest and commercial manufacture may be rapidly characterized for quantitative NDE applications. In addition, the construction of transducers using single crystal materials is being investigated in order to achieve consistent and identical performance between several transducers. The materials of interest are those available on the open market such as lithium niobate and barium sodium niobate with emphasis placed upon the former. Circuit modeling of the transducer structure is undertaken in order that the transfer function between electrical input (output) and acoustic output (input) can be predicted. For commercial transducers of unknown internal construction, it will be necessary to measure this response.

Since the electrical terminal measurements are only one dimensional in nature, it is necessary to examine the field pattern of the transducer function. In all cases, both magnitude and phase of the transfer function is being examined even though the phase information is not employed by current NDE ultrasonic techniques, except holography.

Transducers

In order to access the parameters associated with transducer design and construction, a single transducer was fabricated using 36° rotated Y-cut LiNbO_3 as the piezoelectric and grey cast iron as the backing medium. The details of this transducer construction were given in the third quarterly report. The piezoelectric disk was bonded to the backing using a conducting epoxy. This bond proved to be quite troublesome in that its finite thickness caused a sizable frequency dependent change in the mechanical load impedance presented to the piezoelectric disk. In order to give a quantitative description of this effect, the radiation resistance was calculated as a function of frequency, as shown in figure 1, using bond thickness as a parameter with an assumed velocity of 3.5 Km/sec. for the bond region. By comparing such plots to the experimental results, figure 2, the nature of the bond region could be determined. This was possible since the magnitude of the radiation resistance is sensitive to the bond impedance and the frequency of maximum radiation resistance is sensitive to the thickness-velocity ratio for the larger bond thickness. From this we determined that the epoxy has an impedance of $11.5 \times 10^6 \text{ kg/sec} \cdot \text{m}^2$ and thickness-velocity ratio of $0.02 \mu\text{sec}$. It was apparent then that the bond thickness used in the experimental device



Science Center
Rockwell International

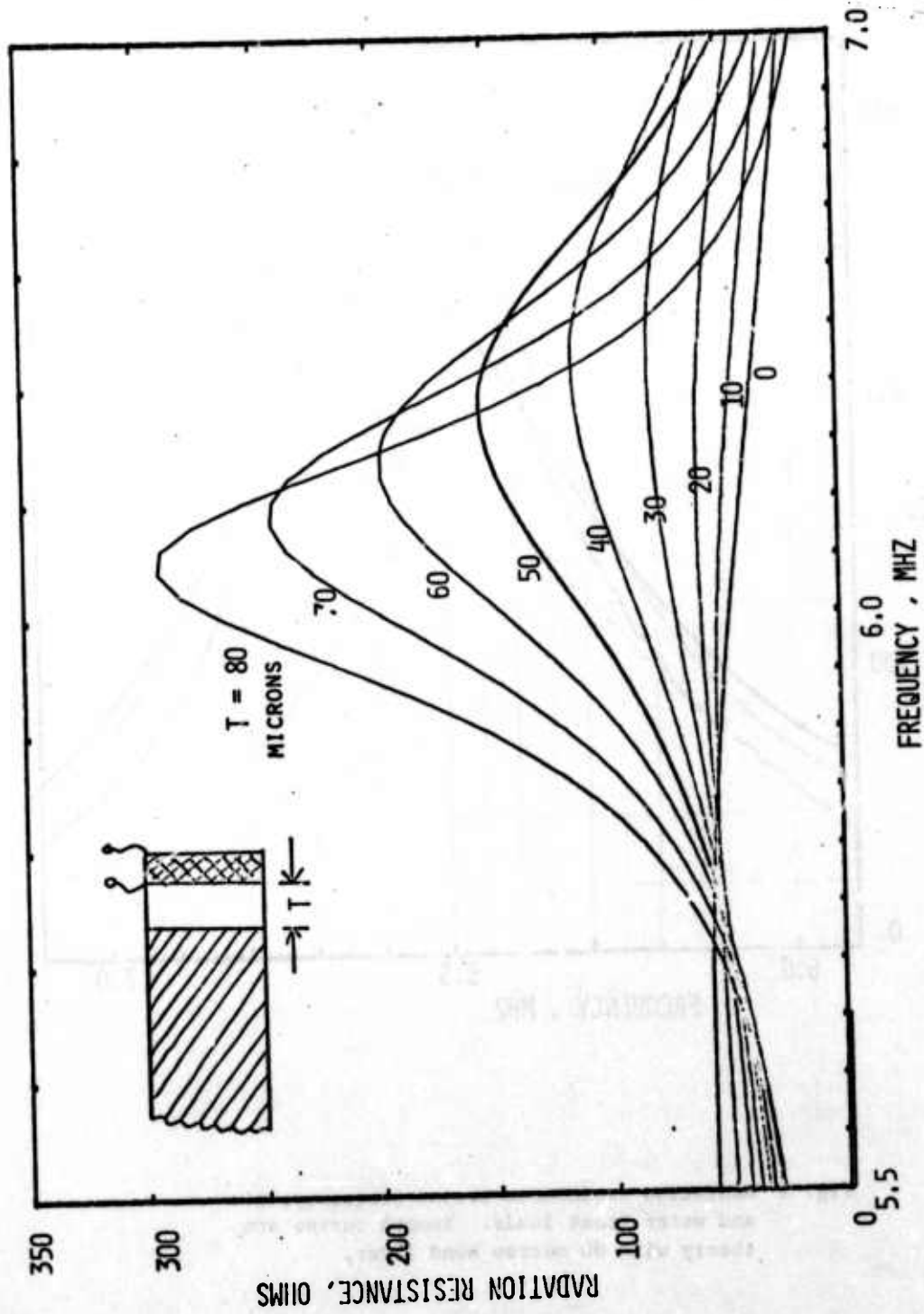


Fig. 1 Calculation of radiation resistance versus frequency, bond thickness is the parameter, T .

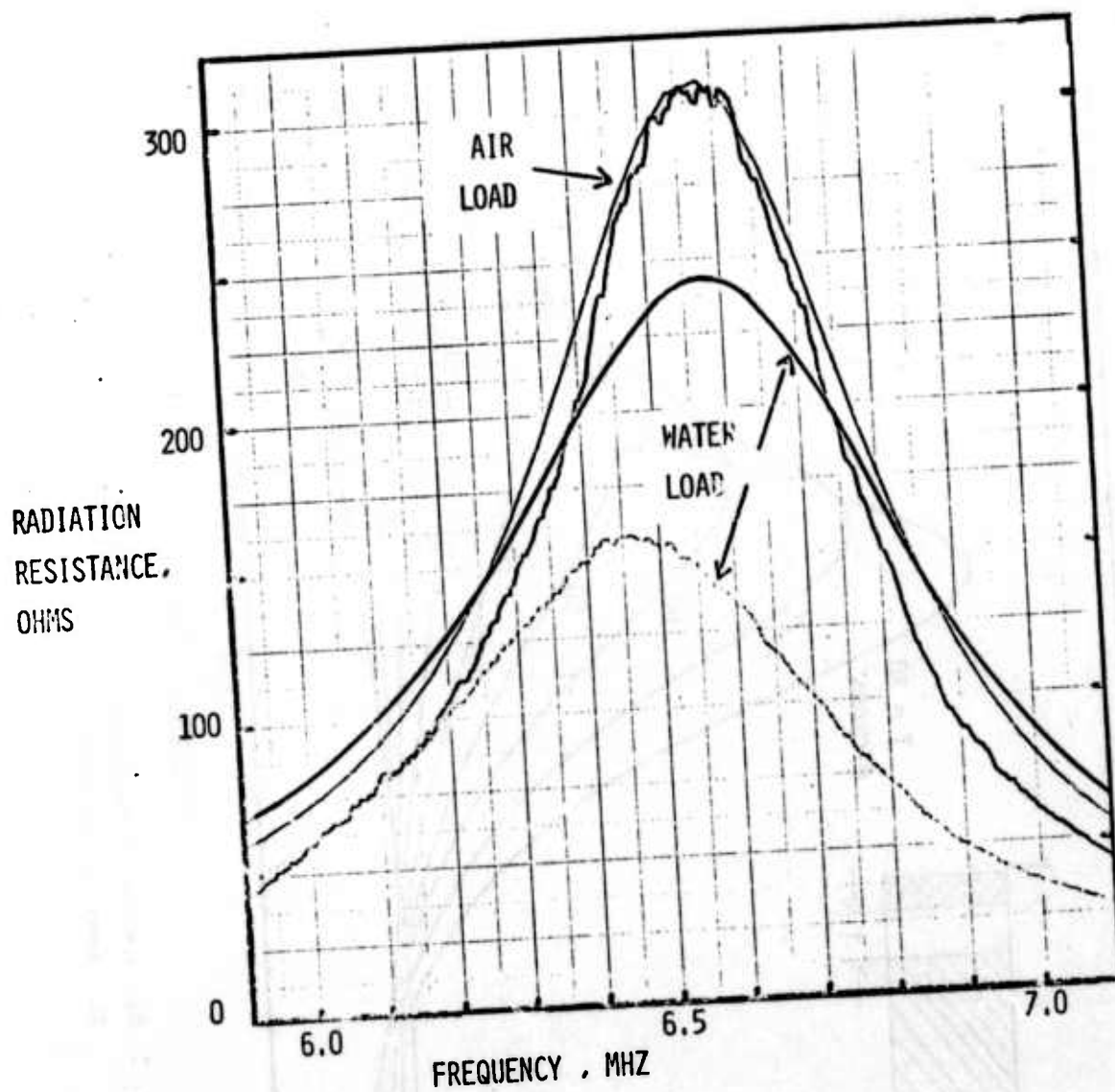


Fig. 2 Radiation resistance versus frequency, air and water front loads. Smooth curves are theory with 80 micron bond layer.

was 80 microns or approximately 4 mils. Although not the intent of this experiment, it appears that such a procedure could be used to give a quick and accurate measurement of the acoustical properties of thin bonds and associated materials not normally available in bulk form. The affect of non-uniform bond thickness was not examined but clearly of importance since it would result in a tilting of the radiated wave fronts.

Experiment and theory did not agree quite as well when the transducer was placed in water. The much lower observed radiation resistance is thought due to stray capacitance since the "hot" electrode of the transducer was exposed to the water. An additional shunt capacitance of 20 pf. is all that is required to transform the series loss to the lower value. At this writing, the capacitance loading effect has not been included in the circuit modeling. In any case, the hot electrode will not be exposed on any further design.

Transducer Modeling

Circuit modeling of transducers employs the Mason [1] equivalent circuit for the piezoelectric disk cast in the form shown in figure 3. This network is most easily described by a set of y-parameters describing a three-port network. In this case the acoustic loads are characterized by admittances rather than impedances as is customary. The ports are labeled 1, 2, 3 where 1 and 2 are acoustic ports and 3 is the electrical port. Using this designation, the y-parameters for the disk are given by:

$$y_{11} = y_{22} = A \left(\frac{1}{2} \csc \phi - B \cot \phi - 1 \right)$$

$$y_{12} = y_{21} = A \left(B \cot \phi - \frac{1}{2} \csc^2 \phi \right)$$

$$y_{13} = y_{23} = y_{32} = y_{31} = A$$

$$y_{33} = - \left(\frac{A}{B} \right) \cot \phi$$

$$y_{22} = y_{11}$$

where

$$A = j2f_o C_o K^2 Z_T$$

$$B = \frac{f_o K^2}{f \pi}$$

$$= \frac{\pi f}{2 f_o}$$

$$f_o = v/2L \text{ disk resonant frequency}$$

$$C_o = \text{clamped capacitance}$$

$$K^2 = \text{electromechanical coupling factor}$$

$$Z_T = \text{disk mechanical impedance}$$

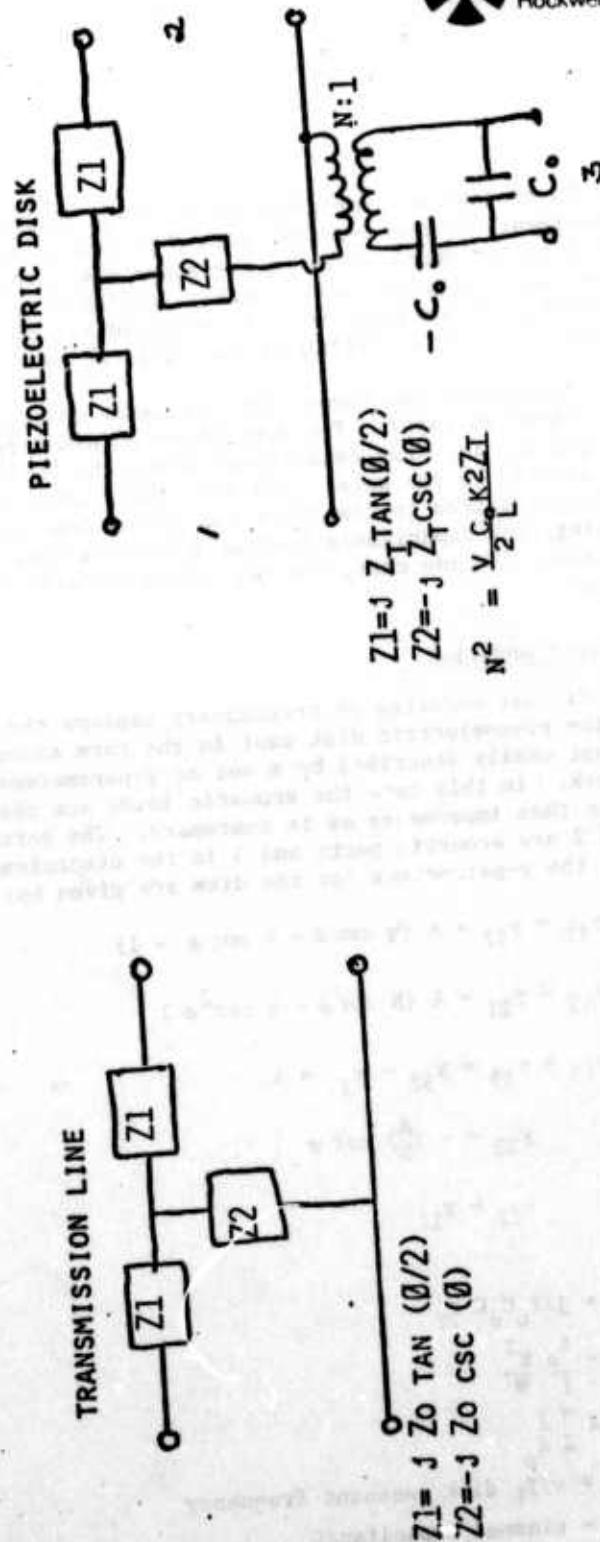
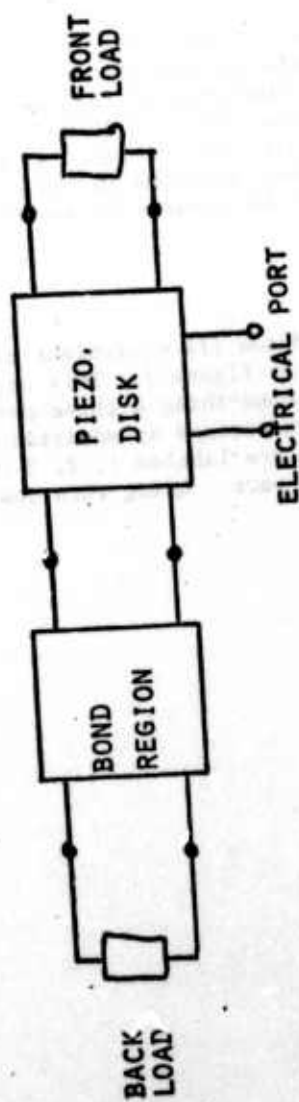


Fig. 3 Parallel field excitation Mason model of piezoelectric disk and transducer model

From these y parameters the electrical terminal admittance is readily found from

$$Y = y_{33} - y_{13}^2 \frac{2(y_{12} - y_{11}) + Y_{T1} + Y_{T2}}{(y_{12} + Y_{T1})(y_{12} + Y_{T2}) - y_{11}^2}$$

where Y_{T1} and Y_{T2} are the acoustic port terminations. The values of Y_{T1} and Y_{T2} are obtained by considering the loading regions. If the loads are single half-spaces then Y_{T1} and Y_{T2} are real and equal to the reciprocal of the respective media impedances. Otherwise the load admittances must be determined by a transmission line analysis.

In calculating the transfer function from the electrical port, 3, to one of the acoustic ports, the other acoustic port is given an equivalent impedance or admittance. This reduces the circuit element to a two-port and is readily described by well-known techniques. The new y parameters for the two-port, composed of ports 1 and 3, are

$$\begin{aligned} y_{11}^1 &= y_{11} - Y_1 \\ y_{12}^1 - y_{21}^1 &= y_{13} - Y_2 \\ y_{22}^1 &= y_{33} - Y_3 \\ Y_1 &= y_{12}^2/D \\ Y_2 &= y_{12} y_{13}/D \\ Y_3 &= y_{13}^2/D \\ \Gamma &= y_{11} + Y_{T2} \end{aligned}$$

where the 3 port has been relabeled the 2' port for convenience.

Now, any two-port scattering parameter [2] may be determined using the primed y parameters. The transfer functions are,

$$S_{12} = S_{21} = \frac{-2y_{12}^1}{(1 + y_{11}^1)(1 + y_{22}^1) - y_{12}^1{}^2}$$

At this time the transfer function has not been included in the computer codes but is in the process of being programmed.

Radiation Field Pattern

The radiation field pattern of an NDE transducer is an important element in the overall quantitative description. Of importance is beam intensity

relative to the assumed axis of the transducer, on axis and off axis diffraction peaks and nulls. The diffusion pattern is wavelength dependent causing an uncertainty in wide band pulse measurements.

The field pattern right at the transducer is of interest because it determines the remote field pattern and also gives some insight into the operation of the transducer. In order to accurately characterize the beam pattern it is necessary to measure the amplitude and phase of the radiation over several side-lobes as well as the main beam. It is also necessary to accumulate this data in matrix form so that the inverse transform may be carried out on the computer.

The experimental set-up for pattern measurements is shown in figure 4. The system is controlled by a PDP-11/10 mini-computer through a laboratory peripheral system (LPS). The actual measurement is performed by a network analyzer or vector voltmeter. A phase lock reference signal is established at the input and compared with the test signal derived from a receiving transducer. The spatial location of the transmitting transducer is determined by a X-Y table having 15" travel along X or Y in increments of 1 mil. The table's stepping motors are driven by the numerical control system which accepts standards ASCII codes from high speed paper tape reader or directly from the LPS. The interface between LPS and ICON-350 was the most difficult part of the setup because of different logic levels employed by the two systems. In addition, a language interpreter was required in the PDP-11 software in order to allow the two systems to converse properly.

Using the setup as shown, the system has demonstrated over 80 dB dynamic range with less than 10 mw. RF into the transmitting transducer. Typical results showing magnitude are shown in figure 5 for the point receiver scan of a 3/4" dia transducer at 5 MHz.

The diffraction pattern data has not yet been correlated with the transducer aperture field pattern although the computer codes to do this have been written and demonstrated on the IBM-370. These codes must now be transferred to the PDP-11 system assuming the core memory is large enough, otherwise the data will be transferred to the IBM-370 or PDP-10.

References

1. A. H. Meitzler and E. K. Sittig "Characterization of piezoelectric transducers used in ultrasonic devices operating above 0.1 GHz" J. Appl. Phys. 40 11, 434], Oct. 1967.
2. Ramo, Whinnery, and Van Duzer Fields and Waves in Communication Electronics Wiley, New York, 1965, p. 603.

RADIATION FIELD PATTERNS EXPERIMENTAL SET-UP

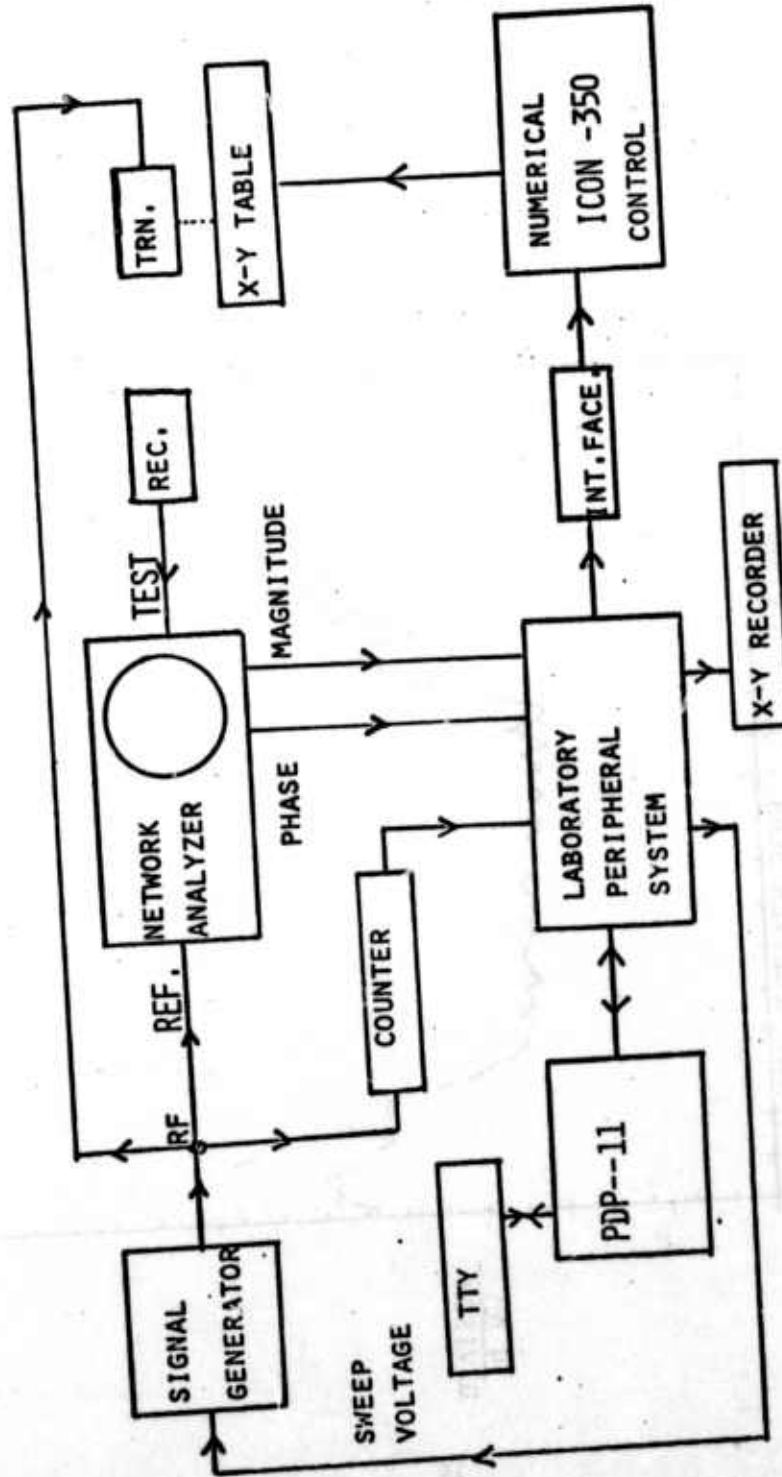


Fig. 4 Experimental set-up for radiation measurements.

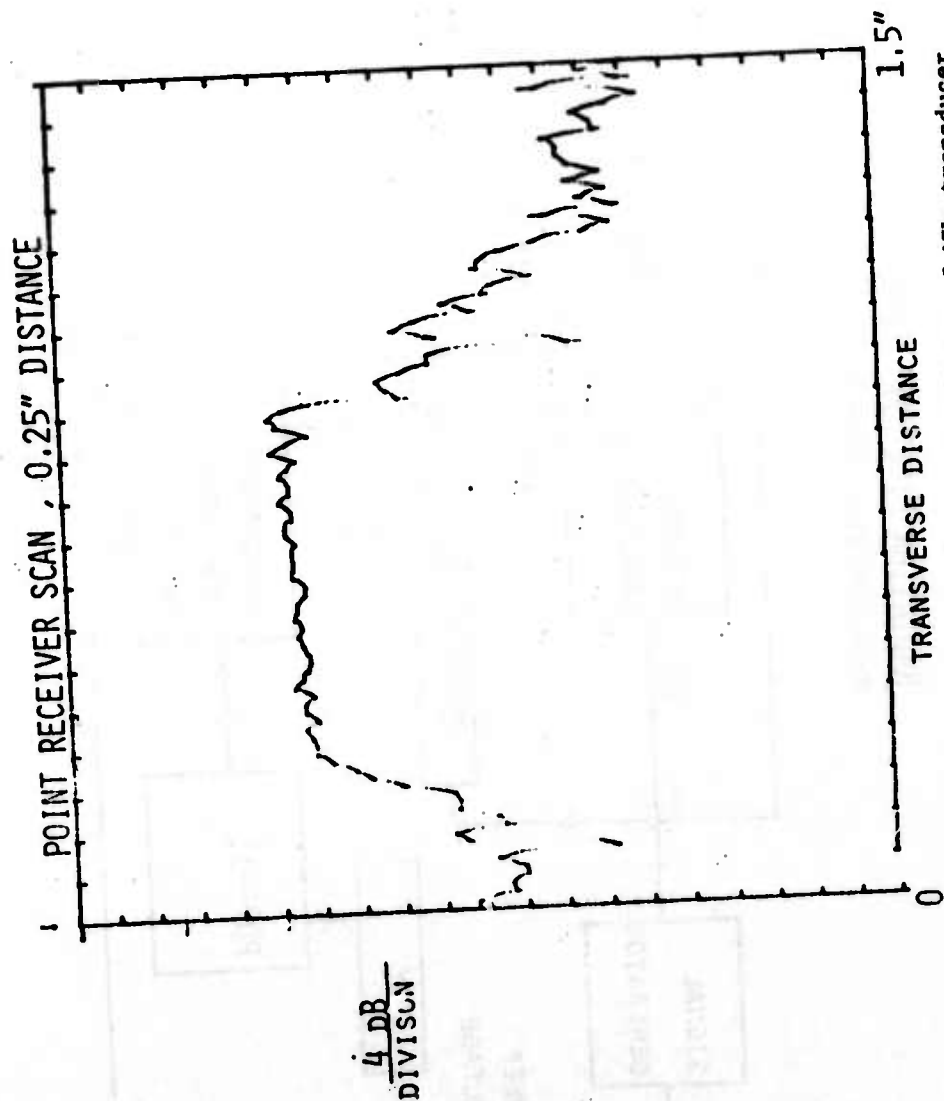


Fig. 5 Point receiver scan of 3/4" dia. 5 MHz transducer



Science Center
Rockwell International

PROJECT I, UNIT I, TASK 2

OPTIMIZATION AND APPLICATION OF ELECTRODYNAMIC ACOUSTIC WAVE TRANSDUCERS

B. W. Maxfield
Cornell University

Introduction

Electromagnetic acoustic wave transducers (EMATS) have an insertion loss that ranges from 20 to 60 db larger than that obtainable in resonant piezoelectric plate transducers. Despite this reduced signal level, large signal-to-noise ratios (S/N) can be realized using EMATS. The advantages of EMATS include their freedom from mechanical contact, ability to generate shear waves normal to the surface, ability to control the shear wave polarization direction and, if desired, broadband response. In order to exploit most successfully the desirable features of EMATS, one should explore ways to reduce the insertion loss (improve efficiency) but, equally important, one must determine, by measurement and calculation, the magnitude and precise origin of a variety of non-ideal EMAT characteristics. These are performance features which in principle could be eliminated but which in practice must be present if the best possible S/N is to be obtained; they include the influence of fringing fields, effects related to the coil-surface separation distance (lift-off effects) and diffraction effects. To date, all of these have received very little attention in the quantitative evaluation of EMATS.

Our approach to this problem is similar to methods that have been employed in the study of piezoelectric transducing elements; we measure the acoustic response (displacement) produced at a given distance from the generator. Instead of using the common water tank methods, however, we have exploited the non-contact feature of EMATS to design a scanning system which measures the displacement field (acoustic mode pattern) of the generator in the material being studied. This method can be applied to piezoelectric, magnetostrictive, EMAT or any other form of displacement generator and, by plating the surface of an insulator with a metal film, it can be used to determine displacement field in insulating as well as conducting materials. Both shear and compressional components of displacement can be measured. Another advantage of our method that is immediately apparent is the ability to measure directly any diffraction effects due to the finite size of defects or voids within the material without the added complication of metal-water reflections. Of course, the same specimen and its defect structure can be investigated over a wide frequency range.

In addition to reliable measurements, it is essential to have quantitative calculations with which to compare. Although the basic principles behind the operation of EMATS are well established, the necessary calculations are far from straightforward. For example, for a quantitative understanding of EMATS, it is necessary to calculate the current distribution in a conducting sheet placed in the vicinity of the generator coil. Calculation of such current distributions is straightforward but results in closed form have only been obtained for one special case, a single loop of radius r_0 placed such that the



plane of the loop is parallel to the conducting surface and a distance h above it. For all other cases of coil geometry, approximate numerical methods must be used to calculate the current distribution. Surprisingly, relatively little work on this topic exists in the literature. Development of adequate numerical methods may well be time consuming. Also, present indications are that substantial computing time will often be necessary.

Although a single loop of wire is neither a useful nor efficient coil geometry, we realized that the solution for the single loop case could be used as an excellent approximation to a practically useful coil geometry, namely a planar spiral coil as shown in Fig. 1a. When a planar spiral coil is wound with small pitch (center-to-center wire spacing $d < 0.1 r$, where r is the winding radius), a series of concentric rings is an excellent approximation to the spiral coil (see Fig. 1b). It is relatively easy to sum the contributions from each loop to obtain the total induced current density for a planar spiral coil. The driving force on the ion lattice results from the Lorentz force between this induced current and the applied static magnetic field, a radially oscillating surface stress is produced. Measurements we have done to date have been restricted to the shear wave produced in this manner.

By applying existing solutions for the induced current distribution and making reasonable approximations to calculate diffraction effects, it should be possible to calculate the acoustic displacement field (acoustic mode pattern) from a spiral coil to better than 5% accuracy for the types of planar spiral coils one would normally choose. Consequently we have chosen the planar spiral coil geometry for an extensive quantitative study of EMATS. This reporting period has seen the successful measurement of the acoustic mode pattern of a planar spiral coil and the initiation of related calculations.

The next section describes the system that we devised for the mode pattern measurements as well as results of a typical measurement. Section III contains a detailed discussion and presentation of our calculations and a comparison with our measurements while section IV presents a brief outline of the next phases of our work.

Experimental Observation

As shown in Fig. 2, we have employed a two-coil method to measure acoustic mode patterns; the receiver coil is scanned to measure the displacement field produced by a fixed generator coil. The receiver is a small, flat rectangular solenoid coil of cross sectional area about 1×2 mm and a surface area 2×2 mm. It consists of 30 turns of 42 SWG wire shielded against radiation from the spiral transmitter coil and spurious electromagnetic pickup (coils of smaller size ($1 \times 1 \times 1$ mm) can be fabricated if necessary). Acoustic mode pattern measurements are made with the semiautomatic scanning device shown in Fig. 7; the horizontal direction is stepped manually while the vertical is a mechanical gear driven scan. The receiver coil must be pressed lightly against the metal surface and since it is very small, the receiver coil-surface distance must be both small and constant. Otherwise large errors can result.



Fig. 1(a): A planar spiral coil and (b): the approximation of a planar spiral coil by a series of connected circular loops.

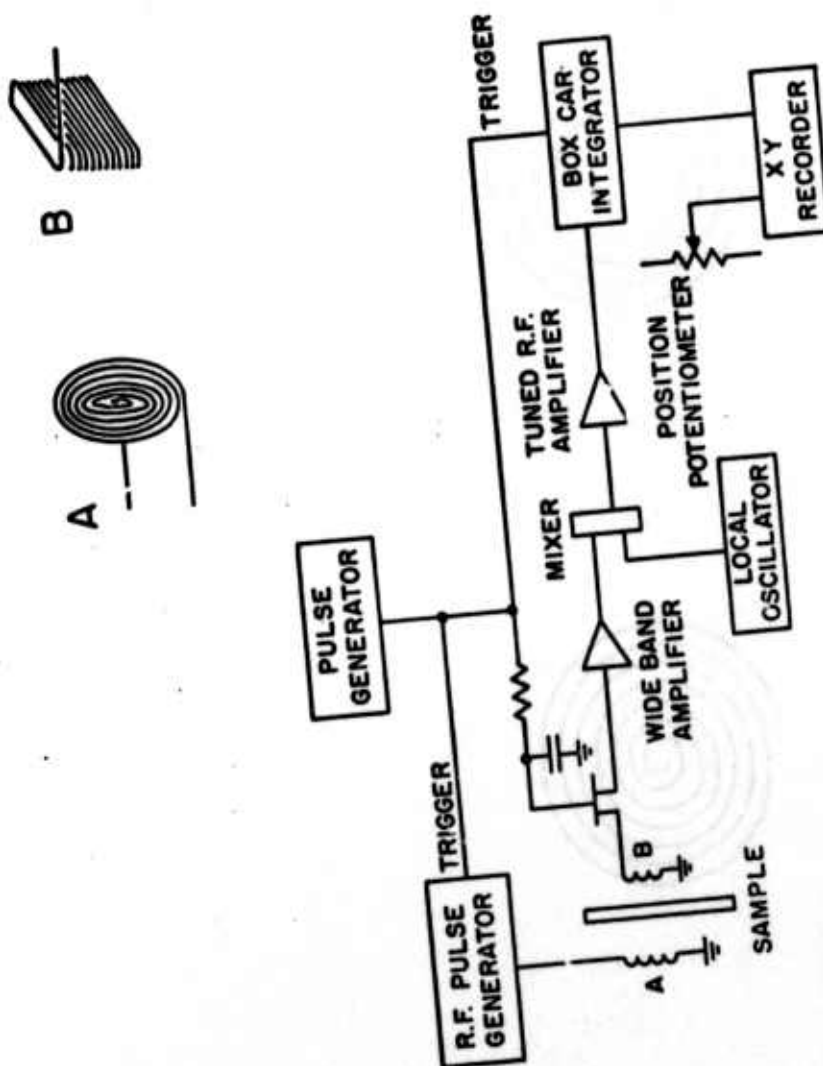


Fig. 2: Pictorial representation (not to scale) of our scanning apparatus.
Receiver coil has a 2 x 2 mm front surface area while the generator coil is 19 mm diameter and made of 38 SWG wire.



A block diagram of the electronics is shown in Fig. 3. This is similar to the conventional system used for piezoelectric transducer. A pulsed oscillator is externally triggered to provide the r.f. current to the generator coil. If necessary, the output from the receiver coil can be blanked off by a FET switch during the drive pulse but, preferably, if the receiver coil is adequately shielded this switch may be omitted. The signal is then amplified, mixed with a local oscillator signal, amplified by a selective amplifier, demodulated and, if necessary, averaged with a box car integrator. In our present experiment, a position measurement, taken from a tracking potentiometer is fed to a chart recorder. The other axis is stepped manually and the chart recorder zero is displaced after each sweep so as to obtain a quasi-3 dimensional representation of the spatial distribution of the acoustic displacement. Figure 4 shows the output resulting from such a series of measurements using a 19 mm diameter, 38 SWG wire generator coil placed 0.25 mm above the surface of an aluminum block 4.9 mm thick.

Certain general characteristics of the mode patterns can be deduced intuitively. The first feature is the two main lobes with a narrow transition region where the displacement goes to zero. This arises because the flat solenoid receiver coil is sensitive primarily to one polarization. Along the line of minimum response, the coil windings are normal to the displacement. One lobe is 180° out of phase with the other since the excitation currents are in opposite directions on either side of center; this of course is not evident in the detected signals.

Theoretical Calculations

Calculation of the acoustic response divides into two separate problems; determining the current distribution induced in the skin depth region of the metal surface, and then calculating the acoustic field resulting from the Lorentz force on these currents. Dodd and Deeds¹ have calculated the induced current distribution for a single circular loop of radius r_0 placed a distance h above the surface; the vector potential within the metal is given by

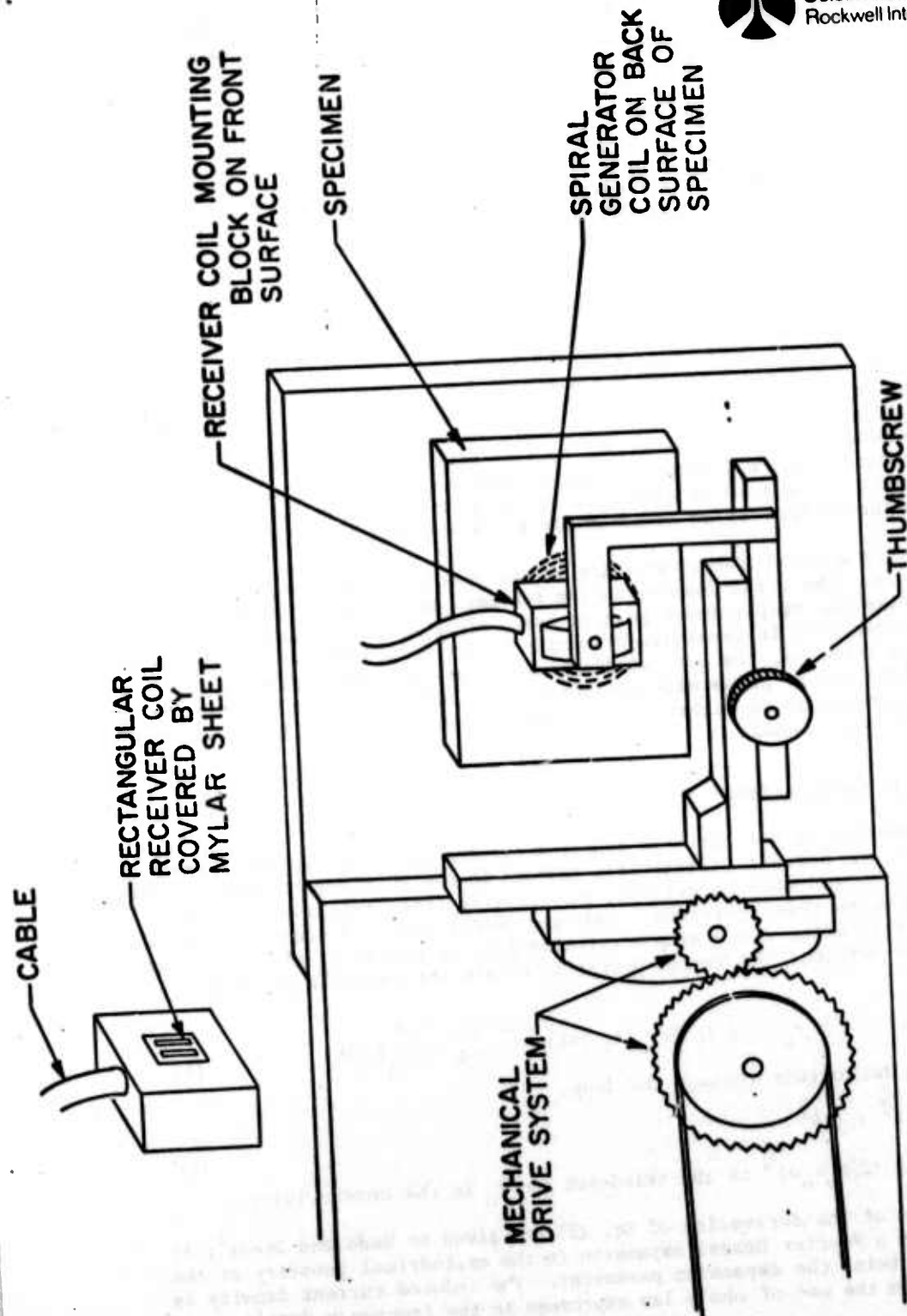
$$A(r, z) = I \mu_0 r_0 \int_0^\infty J_1(kr_0) J_1(kr) e^{-kh} \left\{ \frac{ke^{-k_1 z}}{k + k_1} \right\} dk \quad (1)$$

where I is the current through the loop,

$$k_1^2 = k^2 + j/\delta^2 \quad (2)$$

$j = \sqrt{-1}$, $\delta = (2/\mu_0 \sigma \omega)^{1/2}$ is the skindepth and σ_0 is the conductivity.

Details of the derivation of Eq. (1) are given by Dodd and Deeds¹; it results from a Fourier Bessel expansion in the cylindrical geometry of the coil with k being the expansion parameter. The induced current density is obtained from the use of ohm's law expressed in the frequency domain, namely



Science Center
Rockwell International

Fig. 3: A schematic representation of the apparatus used for our mode pattern measurements. When good shielding of the receiver coil can be achieved, the FET isolation switch is not required.



Science Center
Rockwell International

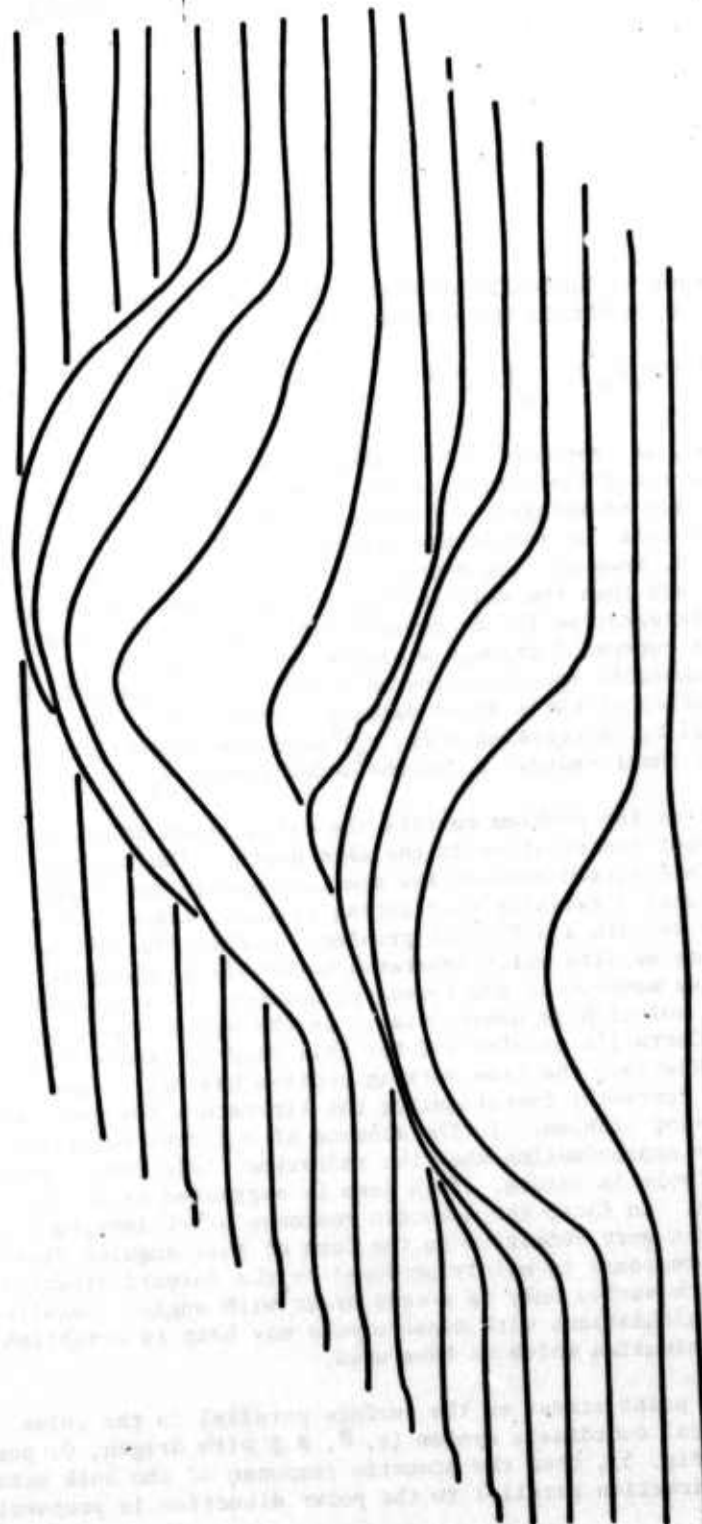


Fig. 4: The acoustic mode pattern of a 19 mm diameter spiral coil as determined using a small rectangular receiver coil as described in the text. Measurements were made at 8.4 MHz with a separation distance, $h = 0.25$ mm.



$$\vec{J} = -j\omega\sigma_0\vec{A} \quad (3)$$

Since the current is basically confined to the skin depth, Eq.(3) may be integrated over z to obtain the current per unit width of the surface,

$$J(r, r_0) = -jI\omega\sigma_0\mu_0 r_0 \int_0^\infty J_1(kr_0)J_1(kr)e^{-kh} \left\{ \frac{k(1 - e^{-k_1\delta})}{k_1(k_1 + k)} \right\} dk \quad (4)$$

For this calculation, we assume $\delta \ll \lambda$, where λ is the acoustic wavelength. In practice, this is not a limitation as all measurements are done in this regime. Equation 4 may be integrated numerically by the Gaussian quadrature method and converges well for reasonable values of h (approximately $h > 0.01 r_0$). For small values of h , however, the expansion parameter k must be taken to rather large values and then the calculations become lengthy and expensive. The result of this integration is the current distribution in the metal surface which results from a current I through a single loop of radius r_0 . Since a spiral coil is a reasonable approximation to a series of concentric loops, the spatial distribution of the induced surface current $J(r)$, for a spiral coil, can be obtained by integrating $J(r, r_0)$ over the appropriate range of r_0 which is from the inner radius, r_a to the outer radius r_b .

The second part of the problem entails the calculation of the acoustic field given the current distribution in the skin depth. The Lorentz force resulting from the interaction between the static magnetic field and the surface current produces a radially oscillating surface stress. This surface stress has presented us with a difficult problem. Within the bulk metal, the normal Navier equation applies which separates naturally to describe longitudinal and transverse waves. At the boundary, however, this equation does not separate and the solution is non-trivial. In the static case, this problem is known as Cerruti's problem and for this case a Green's function solution is known. However, the time varying problem has not to our knowledge been solved. We are currently investigating the literature for more information on this very interesting problem. In the absence of a formal solution, we have proceeded by using an approximation that the radiation field from a point source of shear stress is dipole in nature. This form is suggested by a comparison with electromagnetism. In fact, the acoustic response after integration over the source field is not very sensitive to the form of this angular distribution function because the response is mainly produced by the forward directed part of the wave front which varies only in second order with angle. Detailed comparison of these calculations with measurements may help to establish the validity of the approximation which we have used.

If we consider a point stress on the surface parallel to the polar direction of a spherical coordinate system (r, θ, ϕ) with origin, O , positioned at the point stress (Fig. 5), then the acoustic response of the bulk metal at position r and in a direction parallel to the polar direction is proportional to

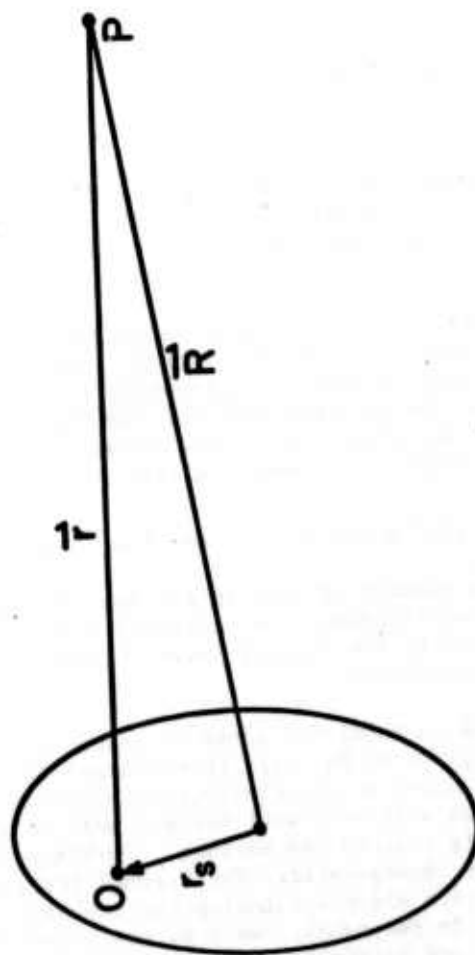


Fig. 5: The coordinate system used for the calculations, Eq. (5). For the response at any point, P, the vector \vec{K} is fixed and the response from all elements of induced current summed.

$$V(r, r_s) \propto \frac{J(r_s) \sin^2 \phi \exp(jqr)}{r} \quad (5)$$

where $J(r_s)$ is the surface current density at a distance r_s from the center of the coil, $q = \omega/v$ is the acoustic wavevector and v the sound velocity. The magnetic field strength is included in the proportionality constant.

As explained in the previous section, we measure the acoustic mode pattern produced by a spiral coil using a small, flat, well shielded rectangular solenoid; this is sensitive primarily to displacements parallel to the windings. Thus, the receiver coil voltage depends upon $\cos \gamma$, where γ is the angle between the directions of the transmitter and receiver coil windings. Hence, the overall response is given by

$$V(\vec{R}) = K \iint J(r_s) \sin^2 \phi \exp(jqr) \cos \gamma e^{-\alpha r} dA \quad (6)$$

where $r = |\vec{r}|$, dA is an element of area in the source plane and α is the ultrasonic attenuation coefficient. For multiple reflections (echoes), r is the distance travelled by the acoustic wave. (The constant K is a calculable constant of proportionality.)

In our calculations, a tabulated array of values of $J(r_s)$ is used to calculate the integral given by Eq. (6); it converges well by the Gaussian technique and the calculation is relatively straightforward for the single spiral coil. This method will work well for any coil of circular geometry placed at a specific height above the surface. Furthermore, non-uniformity in winding may be easily incorporated. The Fresnel integral part takes full account of diffraction effects allowing the acoustic amplitude to be calculated at any point in the metal. We have evaluated the above integrals for specific coil sizes and lift-off parameter, h , so direct comparison with experiment is possible. The results of the amplitude versus lift-off are plotted in Fig. 6; they show the anticipated initial exponential decrease followed by a slower change for large h .

Figure 7 shows the results of a calculation which matched the experimental conditions used for the results shown in Fig. 4.

It is clear that our measurements contain all the general features of the calculations although the diffraction effects are not nearly as sharp as calculated. This could easily result from small non-uniformities in the transmitter coil winding or from slightly non-uniform tracking of the receiver coil; these and other aspects are currently being studied in more detail.

The basic circular shape of the drive coil is apparent; the acoustic mode pattern has a minimum just beyond the drive coil radius. Outside this radius, however, a further subsidiary ring due to diffraction is evident.



Science Center
Rockwell International

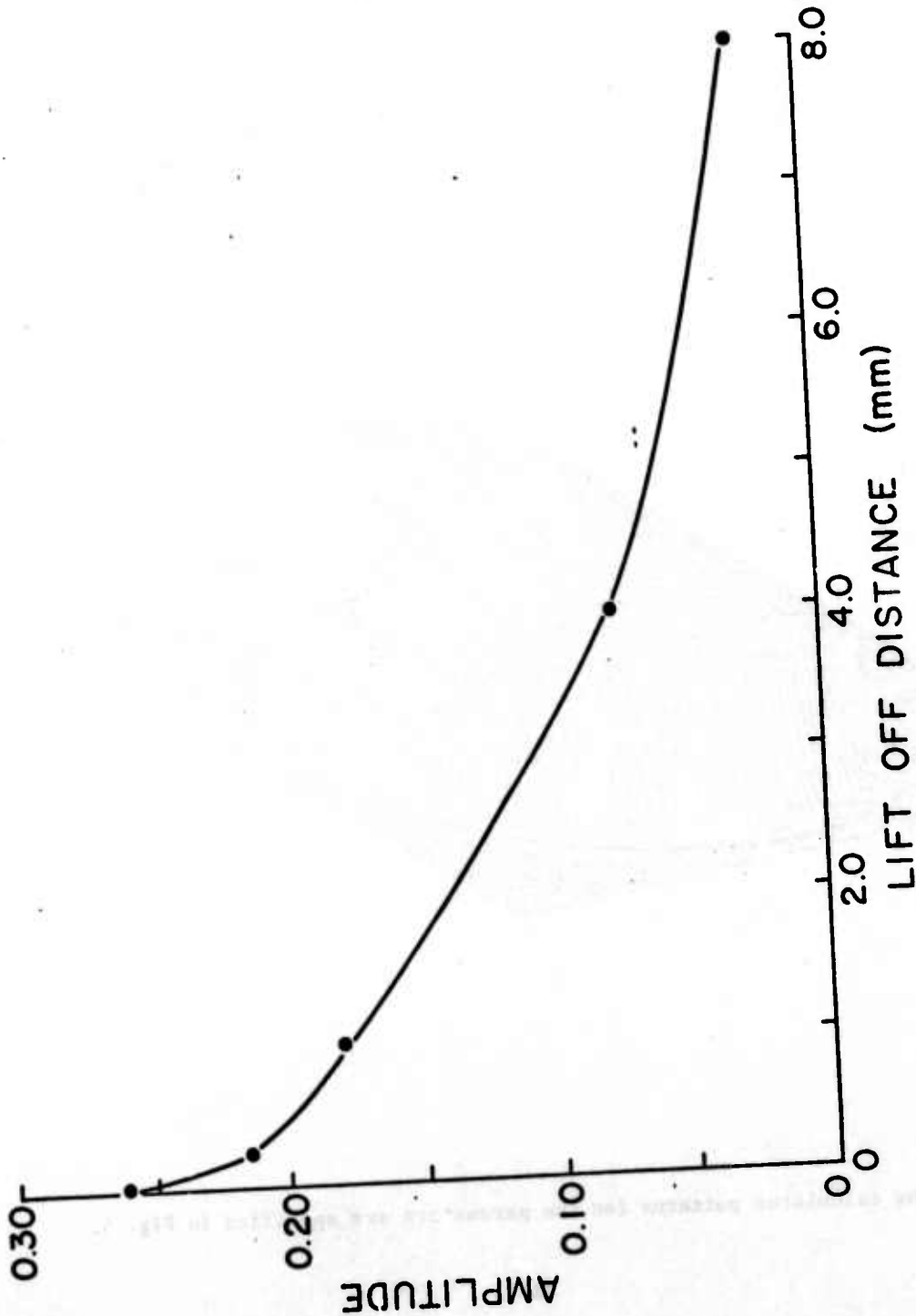


Fig. 6 Dependence of the receiver coil signal (acoustic amplitude) on the distance between the coil & surface. This behavior is representative of most of the central region of the generator coil. Near the center and outer edge, diffraction effects can complicate this behavior.

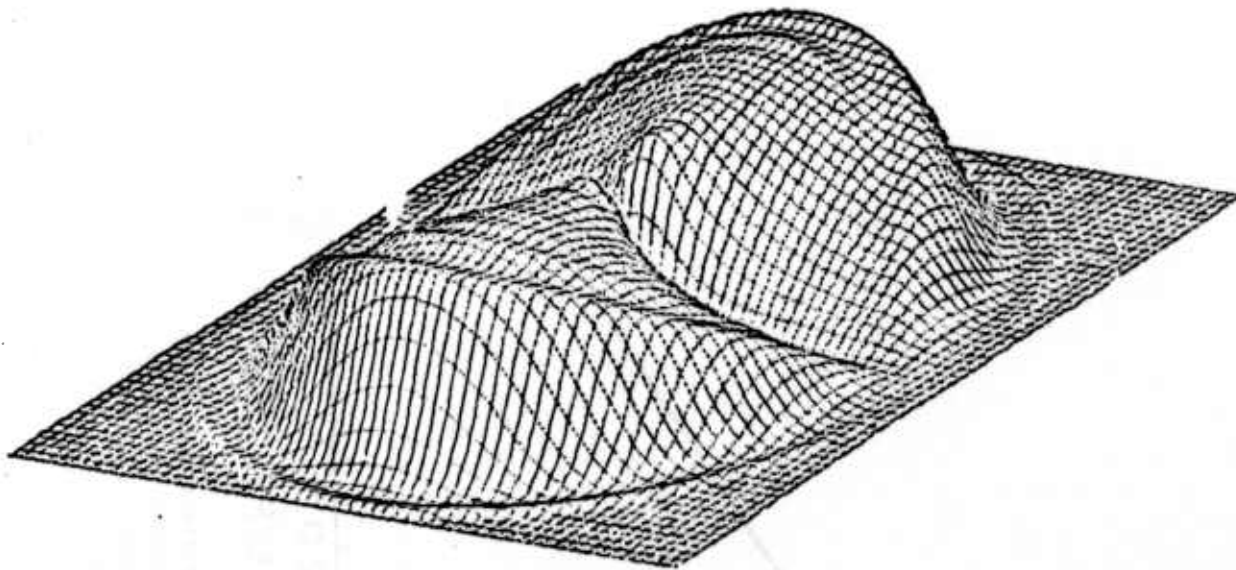


Fig. 7: The calculated patterns for the parameters are specified in Fig. 4.

In this particular case, diffraction effects are not very striking because the receiver is near the source (an early echo) and the frequency is quite large (8 MHz) meaning a small wavelength (about 1 mm). The actual pulse length of 1.2 μ sec was incorporated into the Fresnel integral.

A much better picture of the complete mode pattern generated by a single-spiral coil is obtained by measuring the response for two orthogonal scans and then determining the magnitude of the response at each point. For our present apparatus, both data taking and reconstruction to determine the magnitude are slow. Consequently, this phase of our work has been delayed until some equipment changes can be implemented. However, one can calculate the magnitude of the response and this has been done in Fig. 8. These calculations are identical to those in Fig. 7 except that the $\cos \gamma$ factor, which accounts for the receiver coil polarization sensitivity, is equal to unity.

A more quantitative comparison with experiment is given in Fig. 9 where the experimental and theoretical curves are sections (vertical) through the mode patterns in Figs. 4 and 7 respectively. We have encountered some minor problems in the absolute calibration of our coil system for the coil geometry used in the scanning measurements. Because of this, the experimental and theoretical curves are normalized at one point. The only significant differences are that the right hand side is about 20% too large and slightly more rounded than calculated. This difference in amplitude could be accounted for if this side of the transmitter coil were only 0.1 mm closer to the metal surface and the observed rounding would result if only a few outer turns were situated slightly more than the mean distance from the surface. Receiver coil tracking problems could also account for these differences.

Current and Future Developments

It is evident that great care must be exercised in coil construction if a small coil-surface separation distance (lift-off) is used. We are now making more rigid coils and improving the apparatus to use better tracking and larger tracking forces on the receiver coil. Small, uniform lift-off can probably be accomplished by careful coil construction combined with a thin mylar tracking surface on the receiver coil. Although larger lift-off gives reduced sensitivity (a loss of about 50% for 1 mm lift-off of a 19 mm diameter coil), small changes in lift-off also produce some smaller changes in response. More detailed studies on the influence of lift-off are underway.

The spiral coil is merely the simplest geometry suitable for study, however, our technique will allow us to measure the acoustic mode patterns for many geometries. In particular, sections of coils can be masked off with copper sheet, leaving only particular areas exposed. Such a masked geometry can produce a great efficiency in generating or detecting acoustic

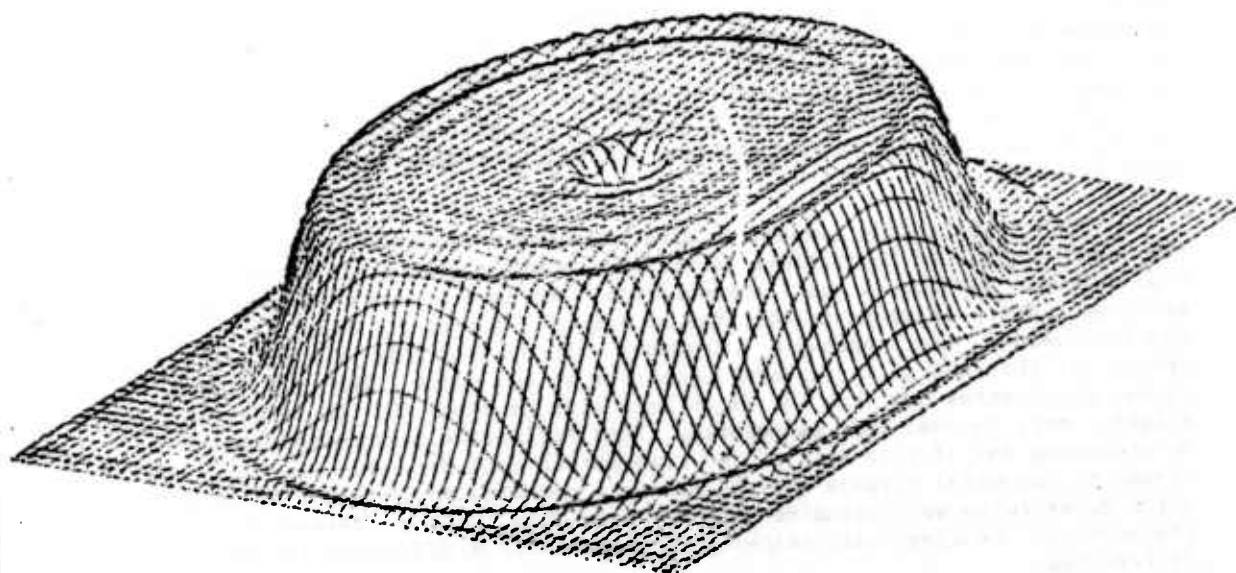


Fig. 8: A completely reconstructed acoustic mode pattern for conditions specified in Fig. 4. This is a calculated response but the measured response is quite similar (see Fig. 9).



Science Center
Rockwell International

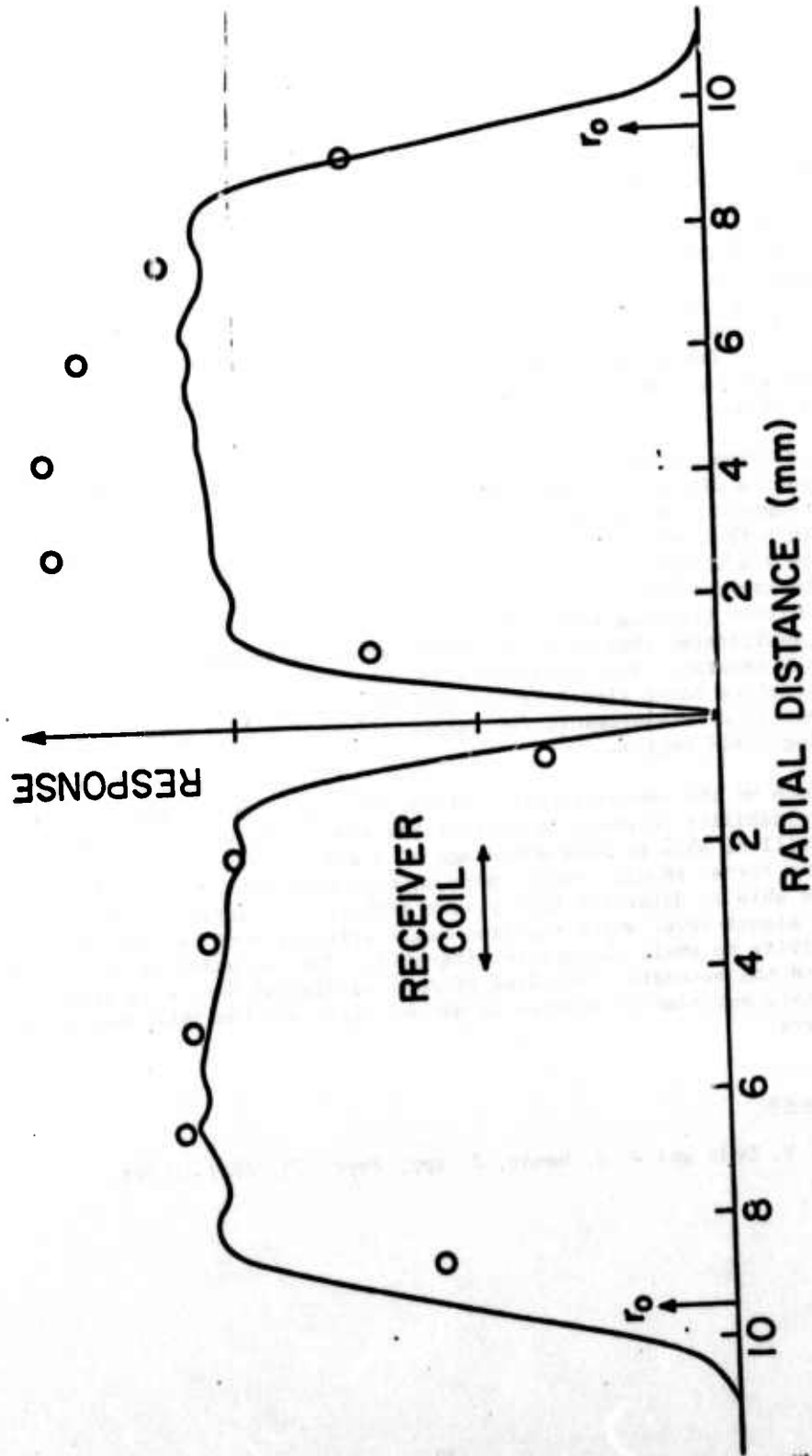


Fig. 9: Quantitative comparison between the measured (open circles) and calculated response for the spiral coil described in Fig. 4.



waves of one particular polarization. However, the effects of the mask on the fringing fields have not been studied in depth. We plan to determine the efficiency (transfer impedance) and mode patterns of many transducers, including bonded piezoelectric elements. The investigation of surface waves and ferromagnetic materials is also planned if time permits. For driving coils with circular symmetry, there is no substantial problem to calculating the theoretical response; however once this symmetry is lost, as in the rectangular solenoid, the problem will not lend itself to the analysis of Dodd and Deeds and a more general method has to be used. We are at present giving consideration to doing similar calculations for non-cylindrical coils.

In order to improve the speed and ease of taking data, we plan to construct a digitally controlled scanning device for use with a small on-line computer. Unlike our present system, this device will be able to scan in both X and Y directions just like an XY recorder. Mechanical control will be via stepping motors with the computer controlling the measurements and storing results on magnetic discs. This new apparatus will also have a more uniform tracking force (between the receiver coil and metal surface). It is anticipated that by paying more careful attention to shielding of both the generator and receiver coils, the FET switch can be eliminated and therefore lower signal levels can be studied. This, in turn, makes it possible to do measurements for larger lift-off and to work farther into the fringing field region.

Much of the non-uniformity evident in Figs. 4 and 9 was attributable to our inability to properly control the small lift-off. The new apparatus, which will be able to take advantage of a greater lift-off and more uniform scanning force, should produce more uniform mode patterns. In addition, we will be able to determine the optimum lift-off for various coil systems (large signal level which requires small lift-off must be compromised with sensitivity to small changes in lift-off). The increased speed in taking data and the automatic recording of data in digital form will greatly facilitate our planned studies on masked coils and the influence of surface roughness.

References

1. C. V. Dodd and W. E. Deeds, J. App. Phys. 39, 2829 (1968).



Science Center
Rockwell International

PROJECT I, UNIT I, TASK 3

SUPERCONDUCTING MAGNETS FOR ELECTROMAGNETIC TRANSDUCERS

R. B. Thompson
Science Center, Rockwell International

Introduction

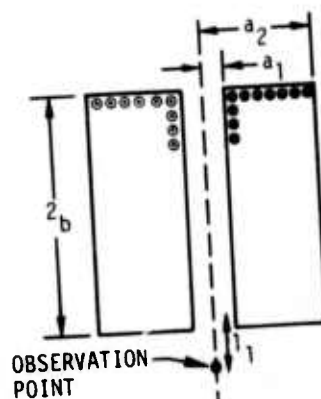
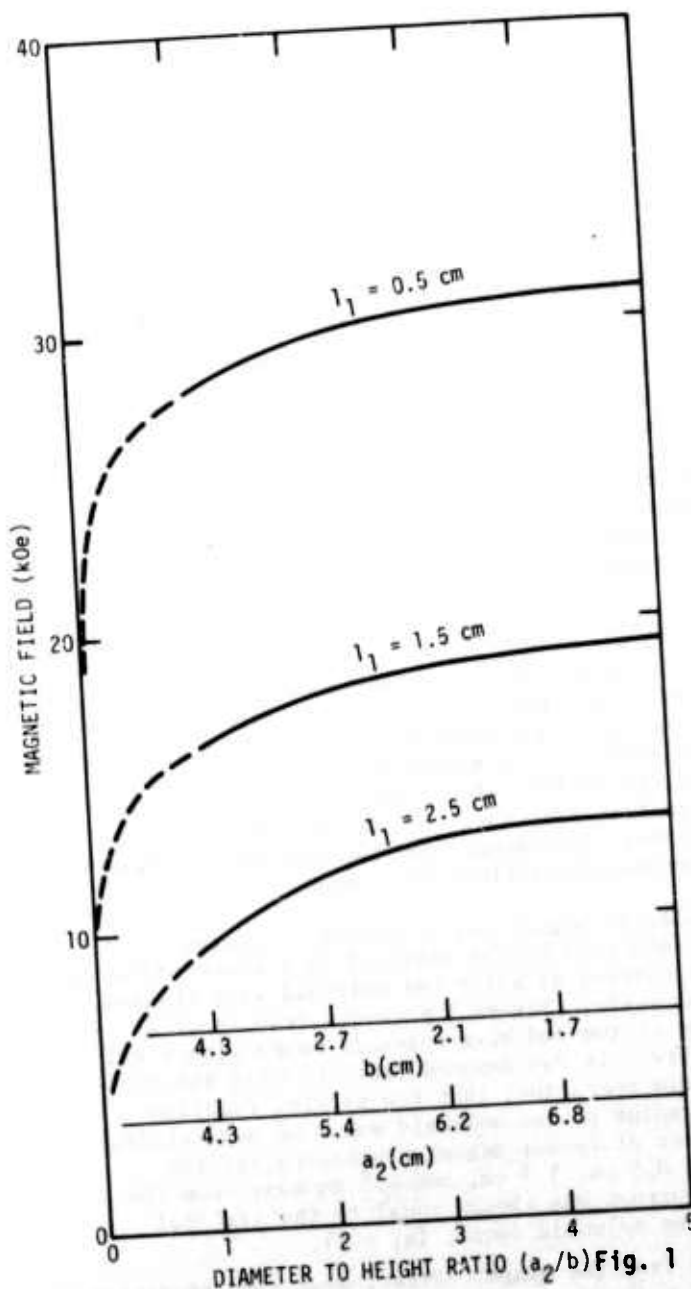
The objective of this task is to investigate the feasibility of using superconducting magnets to increase the efficiency of lightweight, electromagnetic transducer units. Since the efficiency of electromagnetic transducers in converting electrical to mechanical energy is proportional to the square of the static magnetic field strength, the utilization of superconducting magnet technology to produce large fields at modest power levels appears quite attractive if it is compatible with a lightweight transducer unit. The investigation was limited to a two-week preliminary study and consisted of: (1) A simple calculation of the performance that could be expected from an idealized magnet, and (2) consultation with commercial vendors to determine the practical difficulties in constructing the magnet. The results are summarized below.

Design Calculation

It was found that considerable literature^{1,2} is available on designing an optimized superconducting solenoid to produce large, homogeneous fields at the bore center. However, such a solenoid is not necessarily optimized for electromagnetic generation. In this application, the magnet must be placed against the metal part and it is the field at the surface of the metal which should be maximized. This is, of course, smaller than the field at the magnet center, and it also has a different functional dependence upon the geometric parameters of the magnet. Hence, the new design calculations are needed.

The field at the end of a solenoid magnet may be readily computed if the current is known. The ultimate field that can be obtained in a superconducting magnet is limited by the critical current at which the solenoid wire changes from the superconducting to normal state. Figure 1 presents results of a numerical calculation of the field at the end of a solenoid wound with 8 mil diameter, niobium, 48% titanium wire. It was assumed that the wire should weigh 2 kgm (4.4 lbs.) for hand-held operation, that the packing fraction would be 50%, and that the inner radius of the solenoid would be negligible. The maximum axial field is shown for different magnet dimensions (of the specified mass) at axial positions 0.5 cm, 1.5 cm, and 2.5 cm away from the solenoid end. In each case, the current was chosen equal to the critical value³ for the inner windings at the solenoid center ($a_1 = 0$).

Two major points were learned from the graph. First, best results appear to be obtained for large values of a_2/b ; i.e., for somewhat flattened, pancake-shaped solenoids. This occurs because for this shape the field at the observation point is closer in value to that at the center of the coil



$$M = 2 \times 10^3 \text{ gm}$$

$$\bar{\rho} = 4 \text{ gm/cm}^3$$

$$a_1/b \approx 0$$

NIOBIUM, 48% TITANIUM WIRE

Fig. 1 Magnetic Field of Superconducting Solenoid.

The field at various axial positions is shown for a magnet of constant mass as a function of the diameter to height ratio.

Hence, higher external fields can be attained before the critical internal field is reached at which the wire is no longer superconducting. Secondly, the field falls off rapidly with axial distance. It is believed that a realistic distance from metal part to solenoid end is about 1.5 cm (including 1 cm for dewar wall). Fields on the order of 20 kOe can then be expected. This is at least 4 times that which could be expected with a hand-held permanent magnet. The resulting decrease in insertion loss of 24 db for a pulse echo measurement would certainly be a significant improvement.

Commercial Vendor Response

Based on these calculations, a set of desired magnet specifications were prepared as shown in Table I, and illustrated in Fig. 2. These were sent to three commercial vendors on April 22, 1975, with a cover letter asking: (1) whether such a magnet would be feasible at the present time, (2) if so, how much it would cost, and (3) if not, which specifications would have to be relaxed in order to obtain a high magnetic field in a hand-held unit. No responses were received by July 1, so the vendors were contacted by telephone. In each case, they were familiar with the request and clearly had been thinking about it. However, they had apparently not felt it wise to formally respond in writing without knowing more about the problem and about the economic resources that were available for its solution. The responses are summarized below. The vendors are not identified in respect of the informal nature of the verbal communication.

Evaluation of the availability of the proposed system varied considerably. The size requirement clearly indicated a continuous transfer system. It was also clear that 10 kOe fields could be reached, but certainly not unanimous that 40 kOe could be attained. A primary area of difference in response was the value of inner field judged to be acceptable in a hand-held unit subjected to various vibrations and mechanical shocks. The lower the inner field, the less likely that fluctuations would drop the magnet from the superconducting state. It appears that in the most optimistic evaluation, something on the order of \$40K of developmental funds might be needed to obtain a high field, hand-held magnet delivery in excess of 20 kOe. However, it should be noted that much of this is design and development costs, and that subsequent units would be substantially (perhaps an order of magnitude) cheaper.

Conclusions

The variability in response probably accurately reflects the state of change in this emerging technology. It is recommended that contact be maintained with the vendors during the electromagnetic transducer task of this project. Transducers should be constructed and evaluated using permanent magnets. However, in application studies the improved performance possible with superconducting magnets should be kept firmly in mind, and the cost effectiveness continuously weighed. The time does not seem right to launch on a superconducting magnet construction exactly now, but it may not be far away.

TABLE 1
DESIRED SPECIFICATIONS
FOR
SUPERCONDUCTING MAGNET

PURPOSE: HAND-HELD OPERATION FOR ELECTROMAGNETIC GENERATION OF ULTRASOUND
(SEE SKETCH)

MAXIMUM DIMENSIONS:

H = 20 cm (7.9 IN.)

D = 10 cm (3.9 IN.)

MAXIMUM WEIGHT:

M = 3 kgm (6.6 LBS.)

FIELD STRENGTH 0.5 cm FROM DEWAR BOTTOM

H = 40 ko_e

POWER SUPPLY:

AT DISCRETION OF VENDOR

CRYOGENIC SYSTEM:

AT DISCRETION OF VENDOR

PLEASE SPECIFY FIELD UNIFORMITY OVER 1.5 cm DIAMETER DISC COAXIAL
WITH DEWAR AND 0.5 cm FROM BOTTOM.

ELECTROMAGNETIC TRANSDUCER SYST' 4
USING SUPERCONDUCTING MAGNET

Science Center
Rockwell International

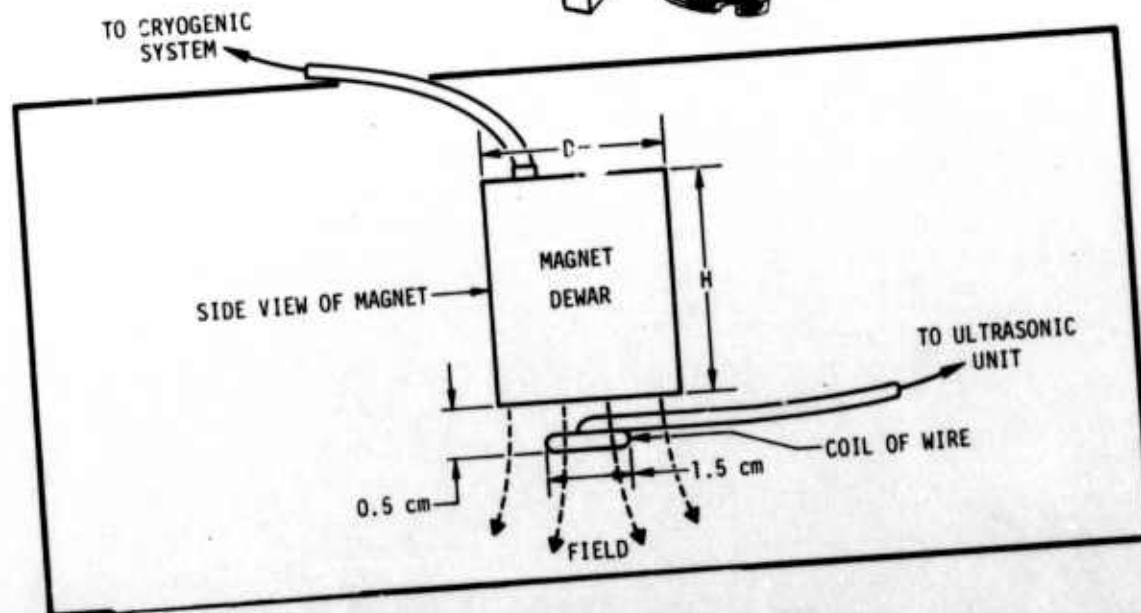
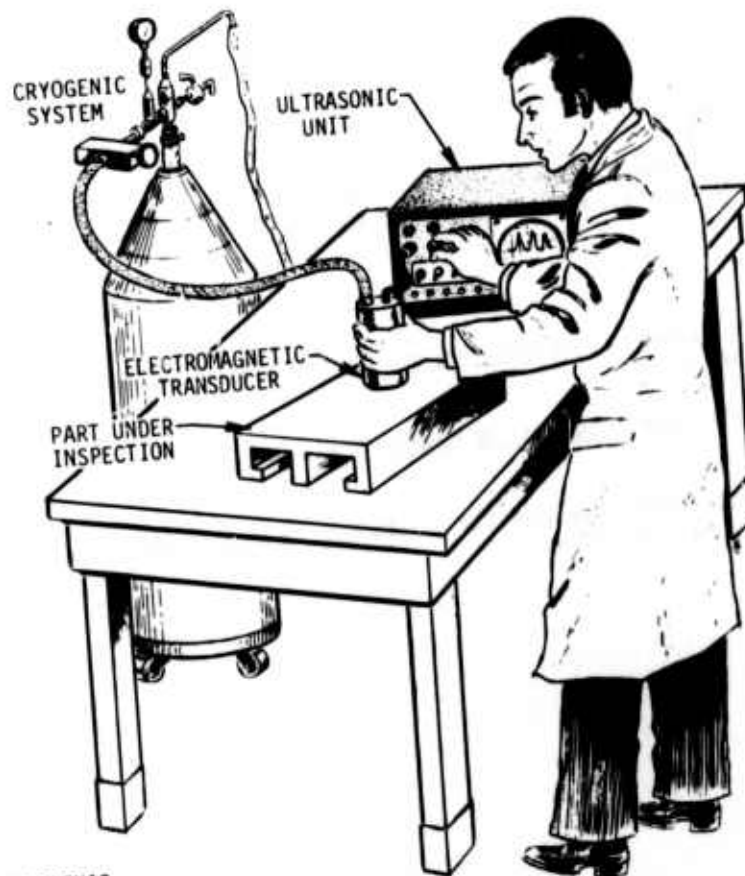


Fig. 2

Acknowledgement

The author would like to acknowledge many stimulating conversations with Dr. B. W. Maxfield of Cornell University.

References

1. D. B. Montgomery, Solenoid Magnet Design (Wiley Interscience, New York, 1969).
2. M. Brechna, Superconducting Magnet Systems (Springer-Verlag, New York, 1973).
3. As specified for Supercon VSF Conductor, Norton Company Supercon Division, Natick, Mass.

PROJECT I, UNIT II, TASK 1

IMAGING AND PROCESSING OF ANGULAR SCATTERING

G. S. Kino, H. J. Shaw, D. Winslow, W. Leung,
J. Havlice, T. Waugh and J. Fraser
Stanford University

Summary

The application of an 83 element electronically focused and scanned transmission system to the imaging of 9" x 3" boron fiber reinforced epoxy laminate samples is described. Good images have been obtained at much higher speeds than with a purely mechanically scanned system. A new type of focused B scan system is also described. Using 2.5 MHz acoustic waves, this has yielded a 2mm definition both normal and parallel to the array, at a distance of 15 cm.

New Techniques For Acoustic Non-Destructive Testing

It has been our aim during the last year to apply electronically focused and scanned acoustic imaging systems to NDT applications. In addition to demonstrating the advantages of using multiple element focused imaging devices rather than a single unfocused transducer, we have shown that the use of electronic focusing can speed up the rate at which information is taken. This makes it feasible to scan large structures in minutes rather than hours, as is the case when only mechanical scanning is used.

Two types of devices have been applied to this work. The first is a C scan transmission device with 83 receiver elements equally spaced along a line 4 inches long, which is used to focus and scan on a line (the x direction) parallel to the array. Scanning in the y direction is carried out by moving the object up and down mechanically. The second type of system is for B scan in which 30 transducers in a line are used as transmitters and an interleaved set of 30 transducers as receivers. This system gives a reflection image of a cross section of an object in a plane passing through the array, i.e., in the x-z plane, with good definition (2mm) in both the x and z directions.

Both of these imaging devices employ an acoustic surface wave delay line with one tap per piezoelectric transducer to obtain the necessary time and phase references for imaging. In the receiver mode, the signal from an individual transducer is mixed with a signal from a corresponding tap on the acoustic surface wave delay line. This yields an output which is the product of the signal from the transducer and the signal from the delay line; the detected output is used to modulate the intensity of the beam on a cathode ray tube. Each transducer can be interrogated in turn by an rf pulse, with



a carrier frequency typically of 50 MHz, sent along the SAW delay line. Thus, one line of the image is scanned in a time corresponding to the time delay from one end to the other of the delay line. At this time is typically of the order of 50 μ sec, the line times correspond to typical TV line scan time.

Because the outputs from the mixers contain both phases and amplitude information, it is possible to synthesize the electronic equivalent of a lens. Put another way, if we consider the system as a receiver, a point source, in the paraxial approximation of optics, gives rise to a signal with a square law variation of phase along the array. If a signal could be inserted in the delay line with the same square law variation in phase, one sideband of the product signal would have the square law variation of phase removed and the signals from all the elements could be added, i.e., we would have constructed a matched filter, matched to the point source. In our case, this is done by sending a linear FM chirp along the delay line. Such a signal has a square law variation of phase with time, hence, with distance along the delay line. A chirp inserted along the delay line is thus, equivalent to a moving electronically focussed lens; the focal length of the lens is adjusted by varying the chirp rate, and the lens automatically scans along a line as the chirp signal passes along the delay line.

We have used an 83 element receiver array of this kind to image debonded regions in a boron fiber reinforced epoxy laminate laid down on a titanium sheet, a material used in the B-1 aircraft by North American Rockwell and supplied to us by them. As we have described in previous progress reports, we illuminate the plate with a strip source, mechanically scan the plate in one direction, and electronically scan and focus in the other, thus obtaining a two-dimensional transmission image. As may be seen from the photographs, we obtain good information on the position of flaws (debonded regions). The present system used in the aircraft industry is mechanically scanned in both directions; ours is electronically scanned in one direction and mechanically scanned in the other. Thus, we can carry out a scan of this 9" x 3" sample in approximately a second, an increase in scan rate of the order of 80 over that taken with purely mechanical scanning. A purely mechanical scan of a large aircraft part could take several hours; an increase in scan rate by a factor 80-100 would reduce this to minutes.

We worked first with a thin laminated panel 1/8" thick and took transmission pictures of this panel which had a number of imperfections in the bonding, as illustrated in the accompanying schematic supplied to us by Caustin. These pictures (Fig. 1) were obtained by using the 83 element electronic scanning and focusing receiver working at 6.4 MHz. At this frequency, the attenuation of the samples is large and the sensitivity of the receiver, which was designed to work at a lower frequency, was very poor. Later we were able to obtain pictures of this sample at lower frequencies. After numerous trials, we found several frequency windows for good acoustic wave transmission through this sample. These frequencies

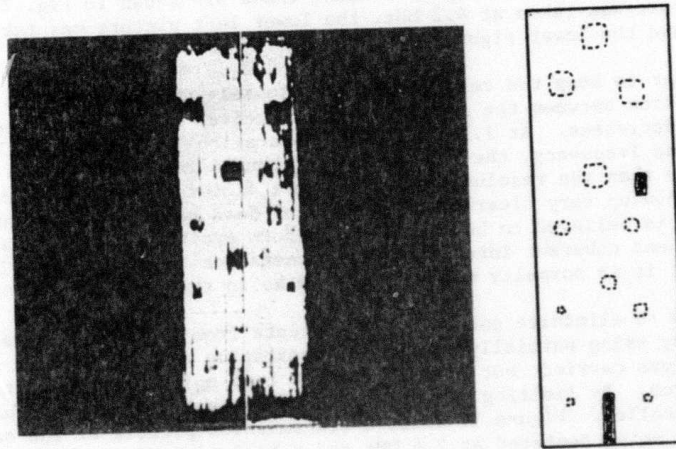


FIG. 1. Composite transmission picture of the thin laminated panel taken at 6.4 MHz.

are 6.4, 4.2, 2.6, and 1.15 MHz. The lowest frequency window is at 1.15 MHz, which corresponds to the fundamental resonant frequency of the titanium plate (calculated as 1.13 MHz), which is bonded to the boron fibers.

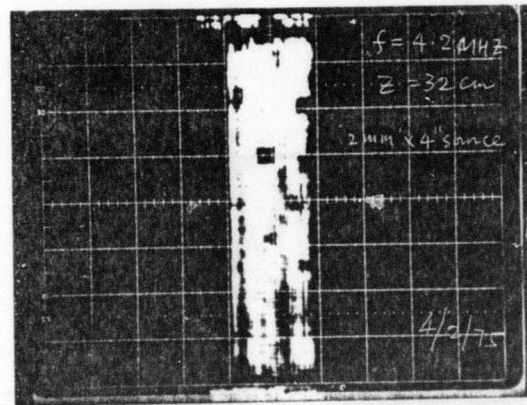
Several acoustic transmission pictures of the complete sample were taken, each in one pass of the mechanical scan; these are shown in Fig. II. The upper picture was taken at 4.2 MHz, the lower left picture was taken at 2.6 MHz, and the lower right was taken at 1.15 MHz.

In order to keep the resolution approximately the same in each picture, the separation between the sample and the receiver has to be reduced as the frequency decreases. At 1.15 MHz, this separation is 20 cm. At this distance and frequency, the resolution is about 5 mm, which is two to three times worse than the resolution in the other pictures. However, the imperfections show up very clearly. The vertical dark band in the picture taken at 2.6 MHz is believed to be due to nonuniform excitation of the transmitting transducer and coherent interference phenomena due to using a single frequency source, but it is normally not as profound as in this case.

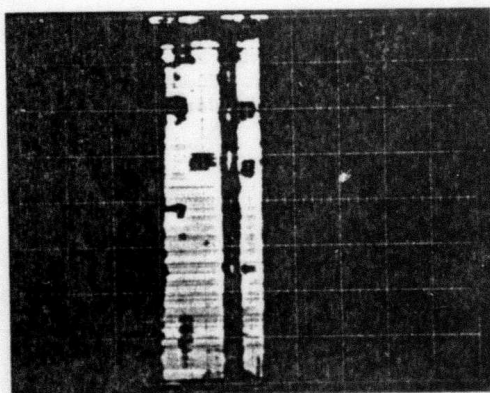
One way to eliminate coherent interference from different parts of the source is by using partially incoherent excitation of the source. An experiment was carried out by using narrow band noise as the excitation to the source. By limiting the bandwidth of the noise, the coherence time can be controlled. Figure IV shows a transmission picture of the same sample with noise centered at 2.6 MHz and a bandwidth of 500 KHz as excitation to the source. This corresponds to a coherence time of approximately $2\mu s$. By comparing Fig. III with Fig. II, it can be seen that the dark interference band has disappeared. However, the resolution and sensitivity decrease, because the signal bandwidth is too large and the focusing ability of the receiver decreases. Further experimentation is underway. We are trying to limit the FM noise bandwidth to about 20 KHz so that the acoustic waves radiated within one line scan time ($50\mu s$) is essentially coherent, but is incoherent between different scans which are separated by approximately $500\mu s$.

When we go to thicker samples, the S/N ratio decreases because the scattering and absorption increase. Hence, it is vital to increase the output power of the transmitter. To further increase the output acoustic power, a large (1" x 4") transducer was made and an acoustic lens was used to focus it into a narrow 4" long line source. Different lenses were tried and it was found that a compound lens made of polystyrene and RTV 602 had the least spherical aberration. However, detailed experiments are yet to be carried out with this system.

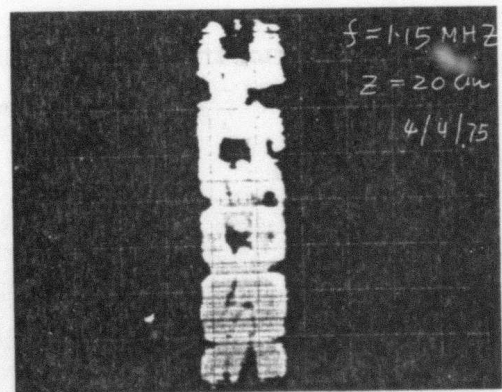
With higher acoustic output power from the source, a thicker sample 0.4" thick (sample No. 907), provided by the Science Center of North American Rockwell was tried. The dimensions and positions of these defects are shown in Fig. IV and Fig. V, respectively. Since this sample is much thicker than the last one, the vertical resolution is worse because the separation between the line source and the sample is larger and the sample



(a) $f = 4.2 \text{ MHz}$



(b) $f = 2.6 \text{ MHz}$



(c) $f = 1.15 \text{ MHz}$

FIG. II. Pictures of the thin laminated panel taken at different frequencies. Note that these pictures are obtained by one single vertical scan.

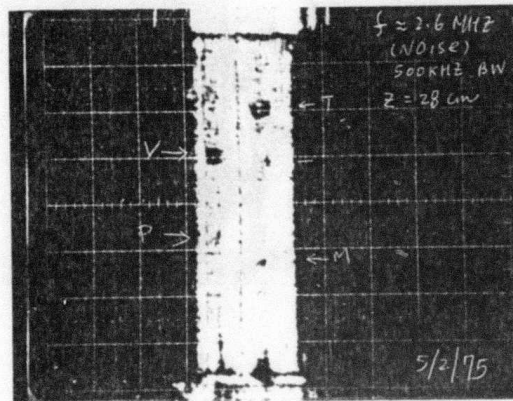


FIG. III. Picture taken with noise centered at 2.6 MHz and a bandwidth of 500 kHz as source excitation. Comparing with the lower left picture in Fig. II, the dark band has disappeared.

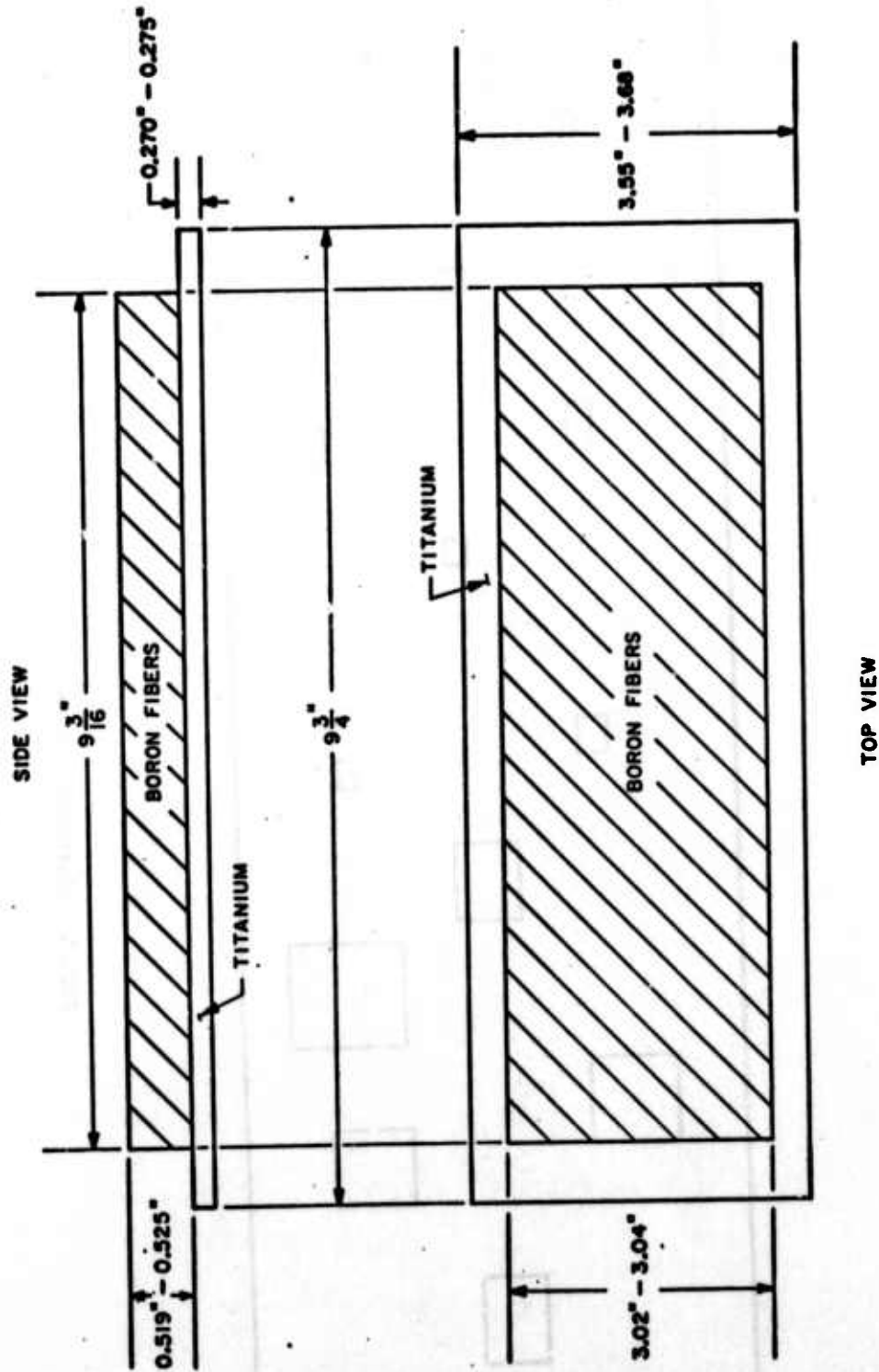


FIG. IV. Dimensions of Sample #907.



Science Center
Rockwell International

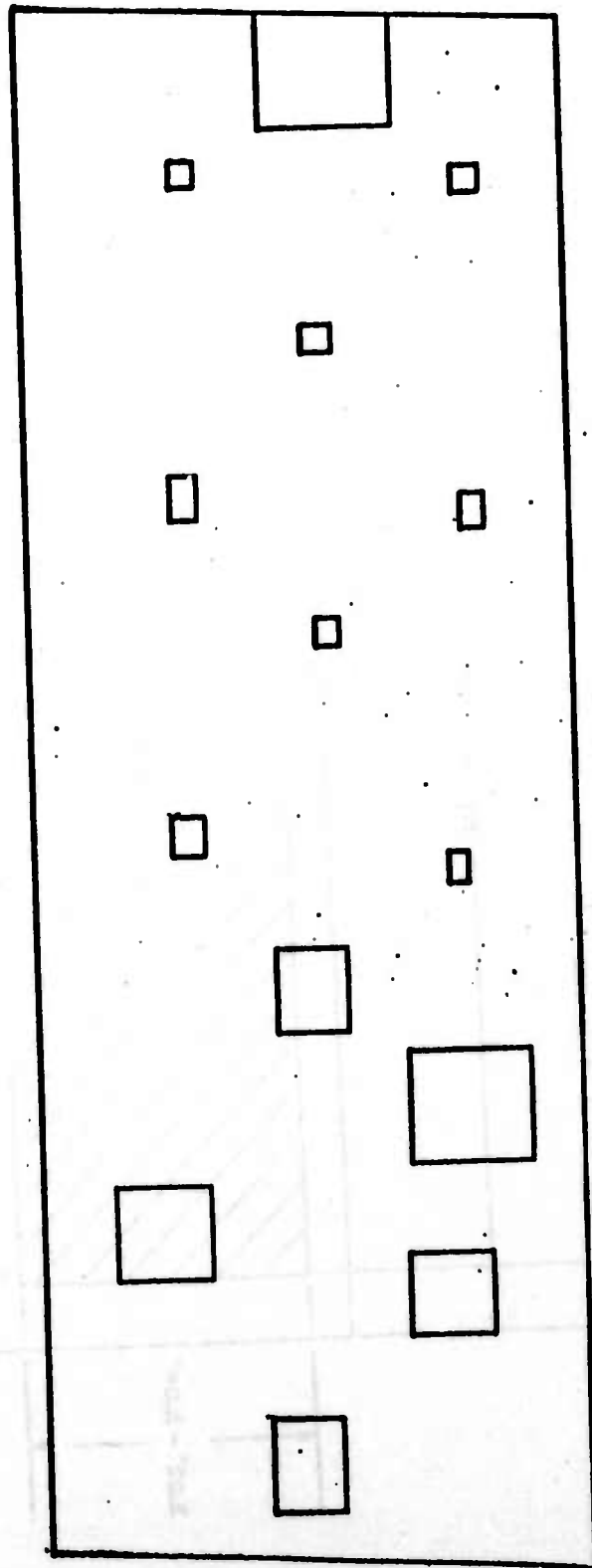


FIG. V. Positions of the defects in Sample #907.

is now in the far field zone of the source in the vertical dimension. Fig. VI shows the actual situation. It is also more difficult to obtain acoustic transmission pictures of these samples in a single sweep. Composite pictures made of two and three pictures corresponding to different parts of the sample were made and are shown in Fig. VII and Fig. VIII, respectively. These pictures were taken at 2.7 MHz. The dark areas in the photos bear a one-one correspondence with all known defects, plus a few indicated defects not supposed to be present. It is also noticed that the frequency used (2.7 MHz) is very close to the 6th harmonic of the fundamental resonance of the titanium plate.

We have also started to take transmission pictures of an even thicker sample (1.25" to 1.4" thick), with defects at different depths, and have obtained images of some of the holes present. As the work progresses, we intend to use a focused transmitter, and examine other structures with this technique such as aircraft honeycomb structures.

We have experimentally demonstrated a new type of imaging system which, we believe, should be by far the most useful for NDT work. This is like a focused sonar system. Here the array is used both as a focused scanned transmitter and as a focused scanned receiver to scan out a two dimensional image of a cross section in the x-z plane perpendicular to the array, with good definition (2mm) in both azimuth and range (x and z). Such a device should, in NDT applications, be the best type for imaging cracks and flaws in, for example, thick metal samples, ceramics, and graphite nose cone materials.

The device operates first as a transmitter, like a moving lens which produces a scanned focused acoustic beam that scans along a line parallel to the array, then operates as a receiver which scans along and is focused on the same line. If the time delay between the receiver chirp and the transmitter chirp is chosen correctly, a signal scattered from a reflecting object on this line will be the product of the definitions of the receiver and transmitter lenses, and hence, about one half of either used alone. At the same time, because of the requirement of correct time delay between transmitter and receiver, only signals from reflecting objects on this line will be received, the range definition typically being approximately equal to the transverse definition. The whole process is repeated by changing the chirp rates (the focal lengths of the lenses) to focus on the next line, and the time delay between receiver and transmitter chirps to correspond to the correct change. Thus, we scan out a raster in the x - z plane line by line and produce a TV image of this raster.

A photograph of an aluminum part in which a series of steps is milled is shown in Fig. IX. The corresponding acoustic reflection image taken in a water tank at a distance of approximately 15 cm with a 2.5 MHz wave is also shown. It will be seen that the step faces 8mm apart and 5mm long, facing the array, are well reproduced and their lengths are very well defined. This system has only been operating for a short while, but we have ascertained

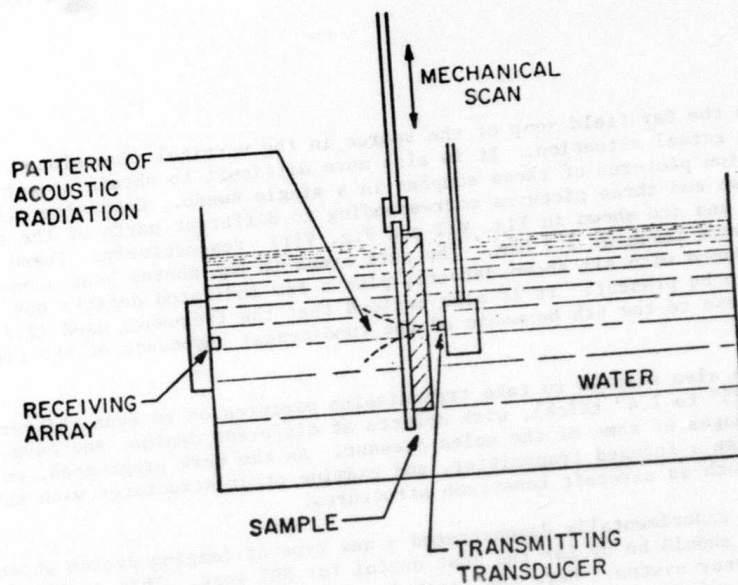


FIG. VI. The experimental arrangement of the setup shows the beam-spread in the vertical dimension.

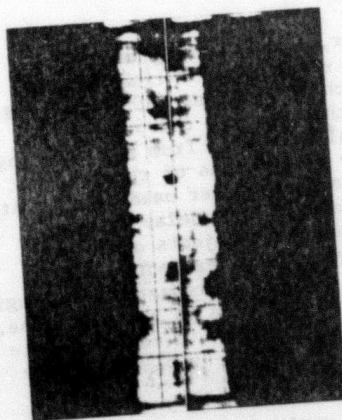


FIG. VII. Sample #907. Picture made with 2 separate scans, taken at 2.7 MHz.

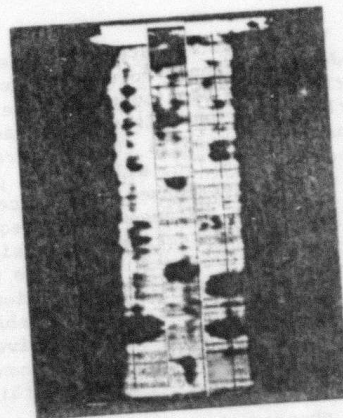


FIG. VIII. Sample #907. Picture made with 3 separate scans, taken at 2.7 MHz.

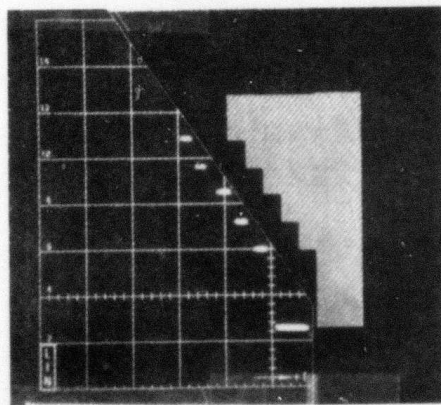


FIG. IX-- Optical photo of an aluminum part and an acoustic reflection image of the same part taken at 2.5MHz in real-time at 30 frame/sec. The present field is approximately 4 cm parallel to the array and 20 cm normal to the array.

that the definition in both the parallel and perpendicular directions to the transducer array are approximately 2mm, at a distance of 15 cm, i.e., half that of the receiver or transmitter alone. The field of view in the direction normal to the array is from 6-26 cm and the present field of view in the direction parallel to the array is approximately 7 cm.

PROJECT I, UNIT II, TASK 2

ANALOG DATA PROCESSING

R. M. White and G. L. Kerber
University of California-Berkeley

Introduction

This portion of the overall program was aimed at analog signal processing applicable to quantitative flaw definition. More specifically, the use of analog signal processing devices such as filters, convolvers, and the like, using surface acoustic waves, was the subject of this investigation. The major emphasis during this report period has been placed on realizing and testing an inverse filter employing surface elastic waves, for the purpose of removing the influence of the frequency response of the NDE ultrasonic transducer. It is planned to complete this work in the next annual period and to give emphasis in that period to analog devices for waveform recognition; some preliminary computer experiments and simulated testing has already begun on that topic.

Inverse Filtering and NDE

In the conventional NDE setup, an ultrasonic transducer coupled to the test object directly or through a water bath is shock excited, producing ultrasonic waves which pass into the test object, reflect or transmit from flaws to either the same or a different transducer, and finally produce electrical signals which are displayed on an oscilloscope or chart recorder. To the extent that the NDE transducer has a finite bandwidth of operation, the ultrasonic signals from the flaw will be distorted; for example, a planar or point flaw will produce a waveform whose duration is a number of cycles of the ultrasonic frequency, rather than being very narrowly defined in the time domain.

This flaw waveform can be processed digitally, as shown by Seydel and Frederick⁽¹⁾, to remove the distortion introduced by the NDE transducers. As sketched in Fig. 1, one wishes to remove the influences of the transducer and medium to leave only the impulse response of the flaw (represented by $g(t)$ in Fig. 1). This can be done by finding the filter function which would be the inverse to the impulse response of the transducers and medium combined. One then constructs the filter having that inverse impulse response, and then passes all future signals obtained from flaws through that inverse filter. In the Seydel-Frederick work this filtering was done in a digital computer; we have made surface acoustic wave (SAW) filters to accomplish the same result.

(1) J. A. Seydel, "Computerized Enhancement of Ultrasonic Non-Destructive Testing Data," Ph.D. Dissertation, University of Michigan, Ann Arbor, 1973.

IMPULSE RESPONSE FREQUENCY RESPONSE

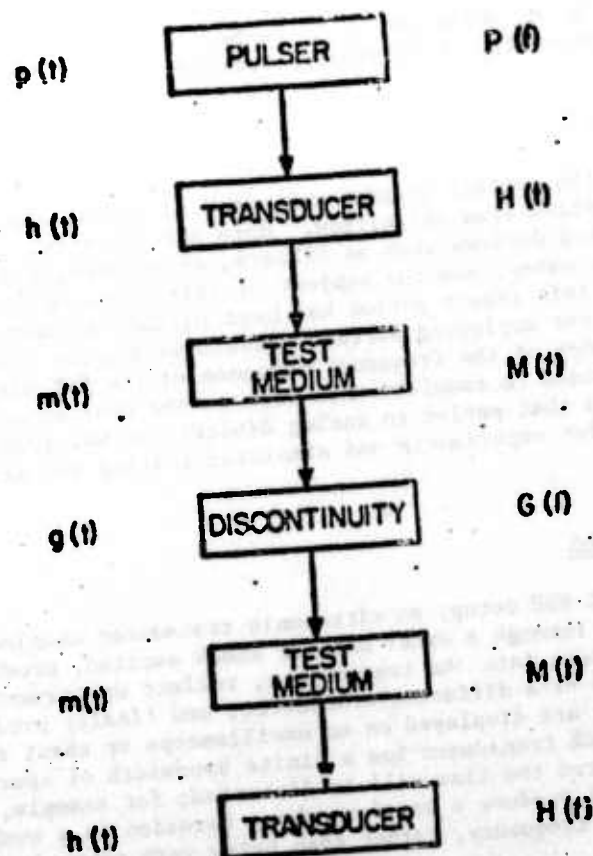


Figure 1. Block diagram of NDE system showing impulse and frequency responses of pulser, input transducer, test medium, and discontinuity (flaw). Figure from Seydel dissertation. The output is the impulse response of the entire system, $y(t)$, where

$$y(t) = p(t) * h(t) * m(t) * h(t) * g(t) = S(t) * g(t).$$

One seeks the inverse

$$S^{-1}(t)$$

for filtering so that one can obtain the characteristic $g(t)$ from $y(t)$. In the above equations the asterisk denotes convolution, i.e.,

$$a(t) * b(t) = \int_{-\infty}^{\infty} a(t') b(t - t') dt'$$

A pictorial sketch of the arrangement appears in Fig. 2, where a test object is shown as a layered solid having layers with differing acoustic impedances (specific acoustic impedance is product of mass density with wave velocity). When the return signal from the NDE transducer passes through the SAW filter designed for that transducer, the distortion introduced by the transducers and medium is removed; and, hopefully, the displayed return will appear as sketched; the near delta functions displayed would correspond to wave incidence on the planes where there is a discontinuity of acoustic impedance.

Filter Design

In order to test the idea we set up a simulated NDE arrangement in which a commercial piezoelectric ceramic transducer (Vernitron, 5 MHz PZT disk, 0.5 inches diameter) was attached (soldered) to a metal (aluminum alloy) cylinder (sketched in Figure 2). Layered structures were made by coupling with oil to additional plates of aluminum or glass (microscope slides). The input NDE transducer was excited (with a pulse from an HP 214A Pulse Generator) while it was connected to an oscilloscope: the waveform corresponding to reflection of the input ultrasonic signal from the flat end of the test object was then photographed (Polaroid 105 positive-negative film) and used to characterize the NDE transducer. The photograph in a digital scanner system employing an IBM 1800 computer, originally used here for picture-processing. A fast-Fourier-transform (FFT) program (run on the CDC 6400 computer) produced the spectrum of the NDE transducer and the solid medium coupled to it. The spectrum was then inverted and an inverse FFT program was run to produce the impulse response of the desired inverse filter. This impulse response served as the starting point in the design of the SAW inverse filter.

In order to realize a practical SAW filter, two additional steps were taken: (1) the impulse response was truncated (shortened in duration) to reduce the complexity of the SAW filter; and (2) the response was weighted so as to prevent undue emphasis of noise at the edges of the operating band of the NDE transducer. The truncation was tested on the digital computer to determine just how much truncation would be possible before the output signal from the filter would be distorted; it was found possible to reduce the impulse response waveform to about thirty percent of its original duration before unacceptable distortion occurred. The weighting used as a Hanning function carried out in the frequency domain; this function tapers off smoothly to zero at the extreme ends of the frequency response of the inverse filter.

The SAW filter transducers are designed to have the truncated and weighted impulse response as determined above. In our test devices built to date, the input SAW transducer has been a wideband, two finger interdigital pair, and the output transducer had the impulse response of the inverse filter; later designs will have a multi-pair input transducer to reduce insertion loss. The output transducer is designed by arranging the

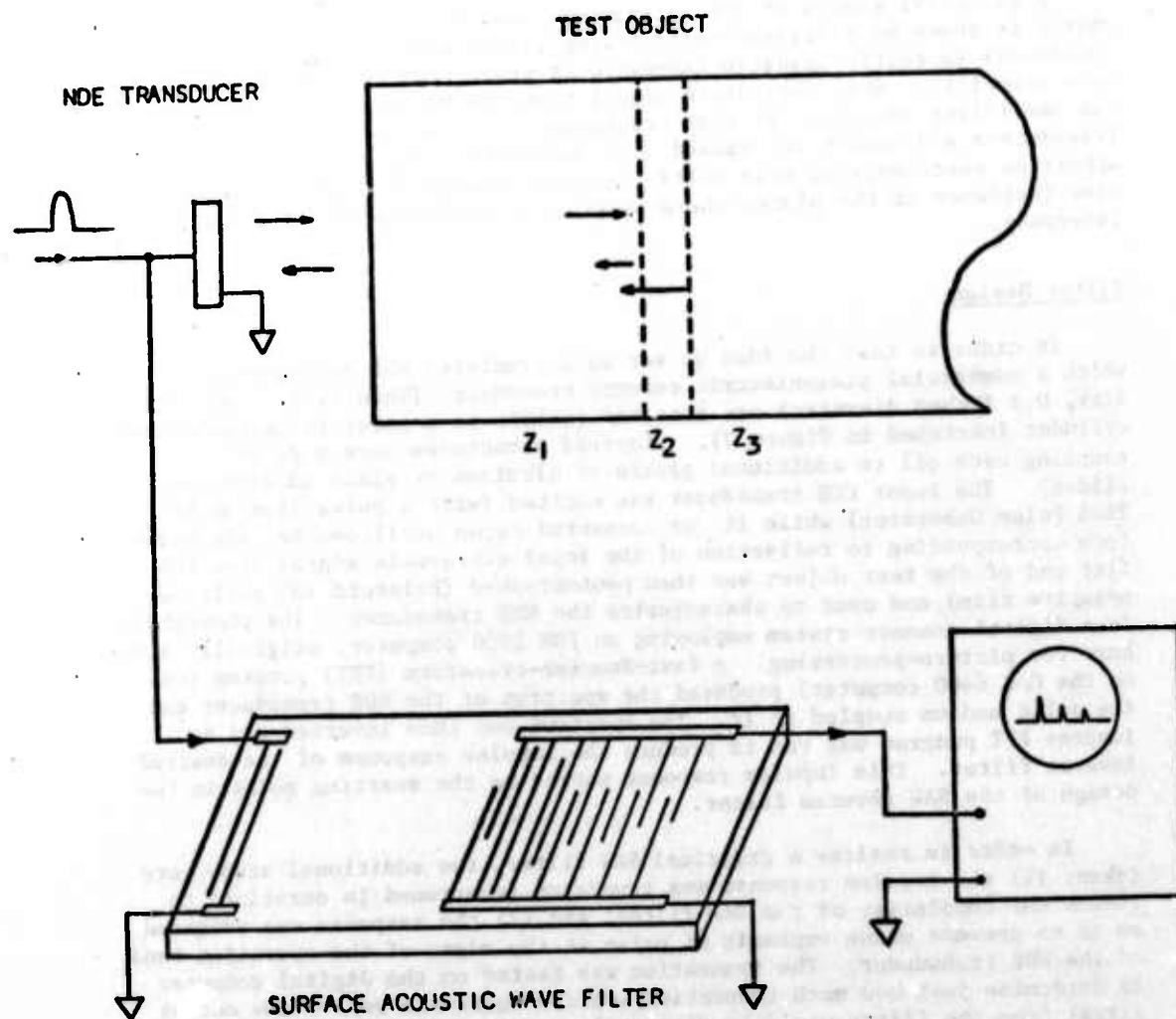


Figure 2. Schematic drawing of simulated NDE setup and SAW inverse filter.



placement of fingers and their overlap to correspond geometrically to the impulse response desired; in one of the filters built and tested, there were only 20 finger pairs in the output transducer.

Test Results

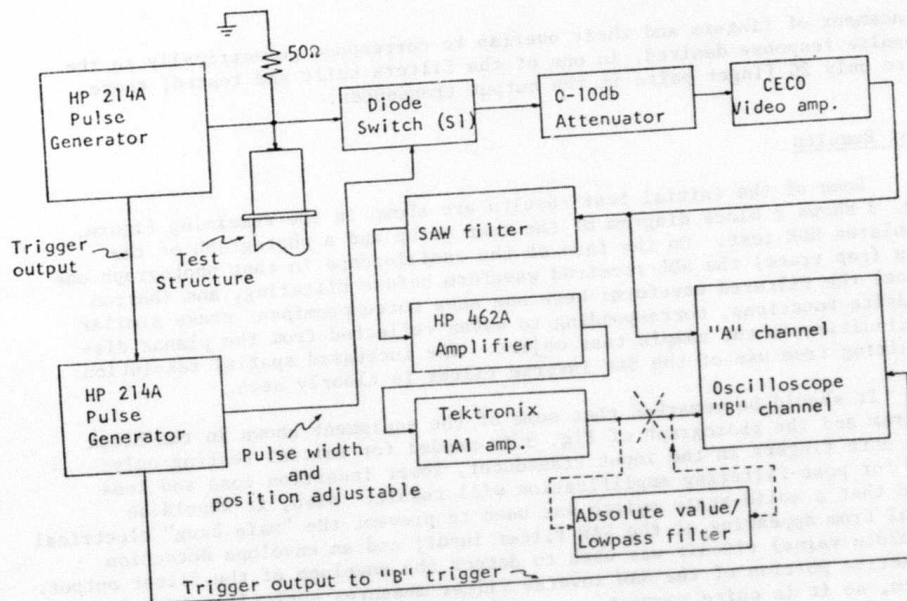
Some of the initial test results are shown in the remaining figure. Fig. 3 shows a block diagram of the test setup and a photograph of the simulated NDE test. On the face of the oscilloscope in that photograph one sees (top trace) the NDE received waveform before filtering, and (bottom trace) the filtered waveform: here one sees three prominent peaks similar to delta functions, corresponding to waves reflected from the planar discontinuities in the sample test object. The increased spatial resolution resulting from use of the SAW inverse filter is clearly seen.

It should be remarked that some of the equipment shown in the block diagram and the photograph of Fig. 3 is needed for initial testing only; with more fingers in the input transducer, lower insertion loss and less need for post-filtering amplification will result. Also, it should be noted that a solid-state switch was used to prevent the "main bang" electrical signal from appearing at the SAW filter input; and an envelope detection (absolute value) circuit was used to detect the envelope of the filter output. The active portion of the SAW inverse filter measures approximately 1.3cm by 3.8 cm, so it is quite compact.

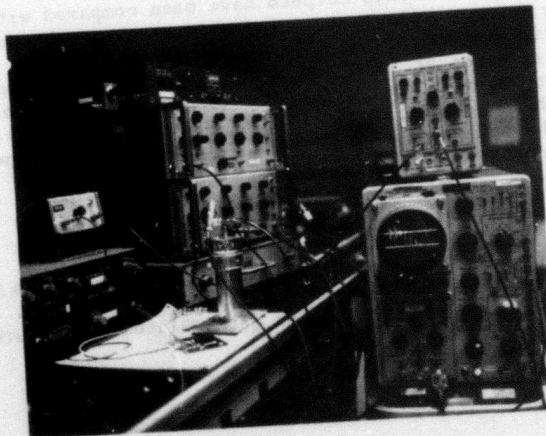
The experimentally obtained outputs have been compared with the waveforms obtained by computer simulation, and good agreement has been found. Also, in an experiment where a SAW inverse filter designed for another NDE transducer (also resonant at 5MHz) was used with this NDE transducer and test object, improvement in the spatial resolution was also observed, but to a lesser degree than when the correct filter was employed. Details of these experimental checks and the design process will be given in papers for publication now in preparation.

Summary

A surface acoustic wave inverse filter design process has been carried out and tested with simulated NDE transducers and test objects. This analog filter yields improved spatial resolution of simulated NDE return in real time processing.



(a)



(b)

Figure 3. Pulse-echo NDE system. (a) Block diagram. (b) Photograph of system.

PROJECT I, UNIT II, TASK 3

DIGITAL TECHNIQUES FOR ULTRASONIC
FLAW CHARACTERIZATION

B. G. W. Yee, J. C. Couchman and J. R. Bell
General Dynamics

Objective

The objective of this task is for General Dynamics' Fort Worth Division to support RISC in their Interdisciplinary Program for Quantitative Flaw Definition by investigating the application of digital computers to collect, process and display data from ultrasonic waves scattering from defects embedded in solids. This objective will be achieved by a series of tasks which will be performed over a three year program. The first year's tasks were:

1. prepare analytical software and hardware for data collection and signal processing.
2. collect and catalog time and frequency domain signatures of spheroids and flat bottom holes,
3. identify measurable quantities for characterizing internal defects, and
4. look for empirical correlations and agreement with theory.

The scope of this year's effort has been limited to the analysis of specimens supplied by RISC (described in Appendix A-1). This will provide data on simple-standardized-specimens for optimum usefulness in cross-correlations with other support task data.

Data Collection

The signal processing systems shown in Figure 1 can scan a specimen by computer control, keep the transducer aimed normal to a specimen, and record all signals detected in any gated interval between the top surface and back surface echo. Gated signal intensities relative to any pre-selected reference standard can be digitized and stored in the computer for later output as a C-scan, isometric display or tabulation. RF waveforms can be digitized as 1024 distinct points and Fourier transformed or otherwise analytically studied.

A flow chart diagram that describes the equipment, data collection, and display capabilities used in Task 1.II.3 is shown in Figure 2. A 15 MHz broad band Panametrics transducer is pulsed by a 5052 PR pulser receiver and the pulse echo received from a test specimen is displayed on

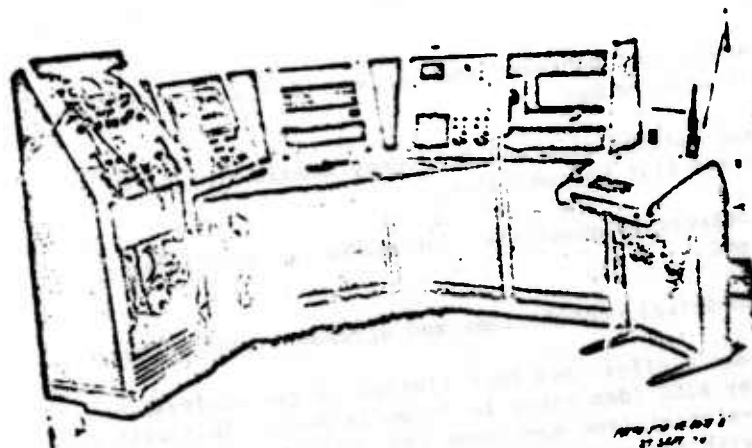
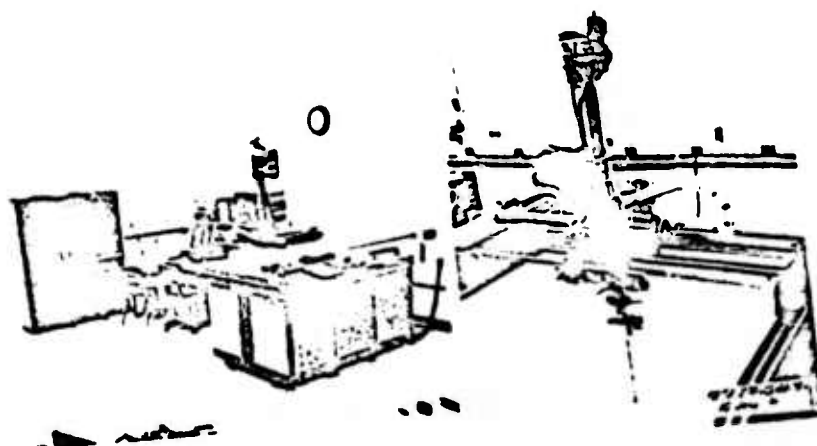


Figure 1 The PDP 11/45 Scanner Signal Processing System (Top)
Showing the Scanner Mechanism (Top-Right) and the
HP-2100 System (Bottom)

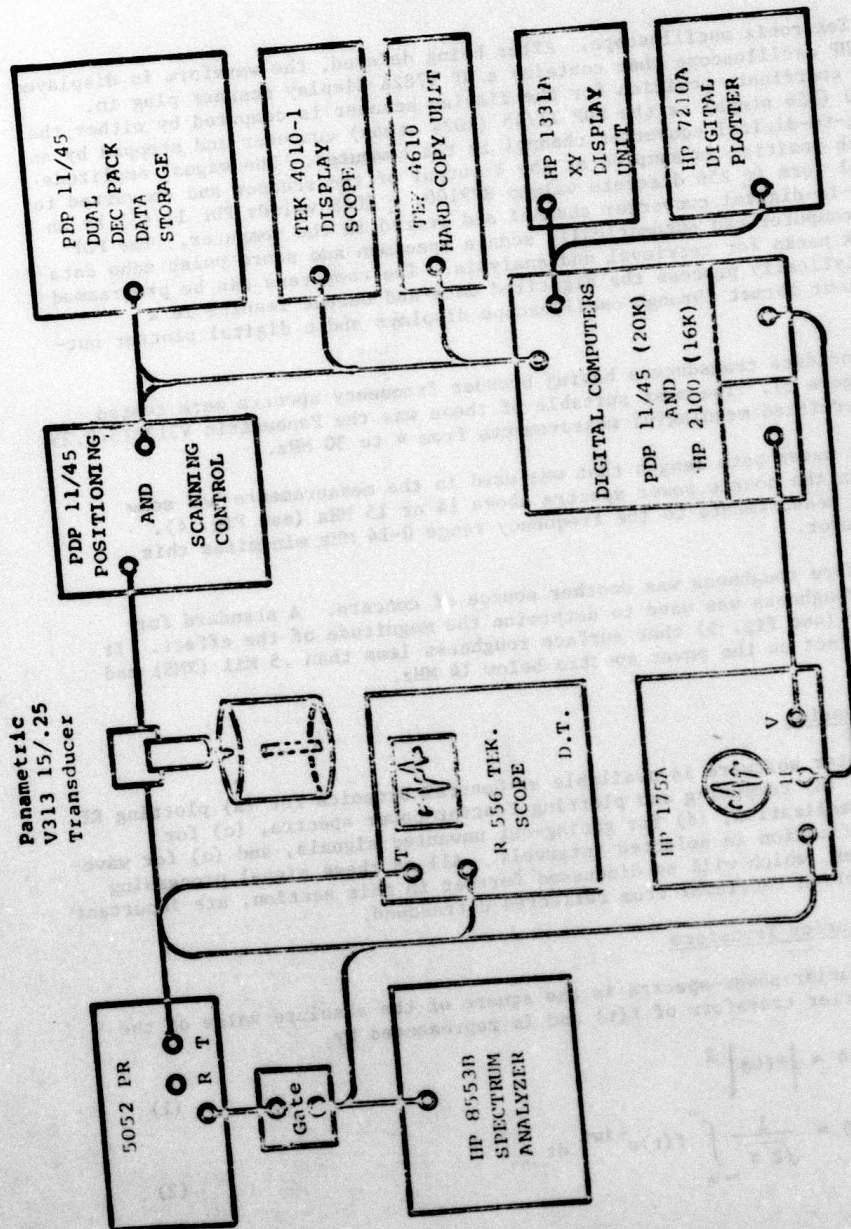


Figure 2 Digital Data Collection and Display Equipment

on a Tektronix oscilloscope. After being delayed, the waveform is displayed on a HP oscilloscope that contains a HP 1782A display scanner plug in. The X coordinate position for the display scanner is computed by either the HP2100 (256 steps) or the PDP 11/45 (1024 steps) computer and stepped by an analog-to-digital converter channel in the computer. The signal amplitude at each position is sampled at the Y output of the scanner and converted to digital form (+ 256 discrete values HP2100, + 2048 values PDP 11/45) by an analog-to-digital converter channel and stored in the computer. The PDP 11/45 computer can automatically scan a specimen and store pulse echo data on disk packs for retrieval and analysis. The computers can be programmed to analytically process the digitized data and output results in a convenient format through oscilloscope displays and a digital plotter output.

Candidate transducers having broader frequency spectra were tested (see Figure 3). The most suitable of these was the Panametric V313(15/0.25) which permitted meaningful measurements from 4 to 30 MHz.

The water path length that was used in the measurements had some effect on the source power spectra above 14 or 15 MHz (see Fig. 4). Limiting measurements to the frequency range 0-14 MHz minimizes this error factor.

Surface roughness was another source of concern. A standard for surface roughness was used to determine the magnitude of the effect. It was found (see Fig. 5) that surface roughness less than .5 Mil (RMS) had little effect on the power spectra below 14 MHz.

Data Processing

Computer software is available at General Dynamics for (a) plotting RF waveforms, (b) computing and plotting Fourier power spectra, (c) for source normalization, (d) for gating-out unwanted signals, and (e) for waveform amplification in selected intervals. All of these signal processing capabilities, which will be discussed further in this section, are important for information retrieval from reflected ultrasound.

a. Fourier Transform

The Fourier-power-spectra is the square of the absolute value of the complex Fourier transform of $f(t)$ and is represented by

$$P(\omega) = |F(\omega)|^2 \quad (1)$$

$$\text{where } F(\omega) = \frac{1}{\sqrt{2\pi}} \int_{-\infty}^{\infty} f(t)e^{-i\omega t} dt \quad (2)$$

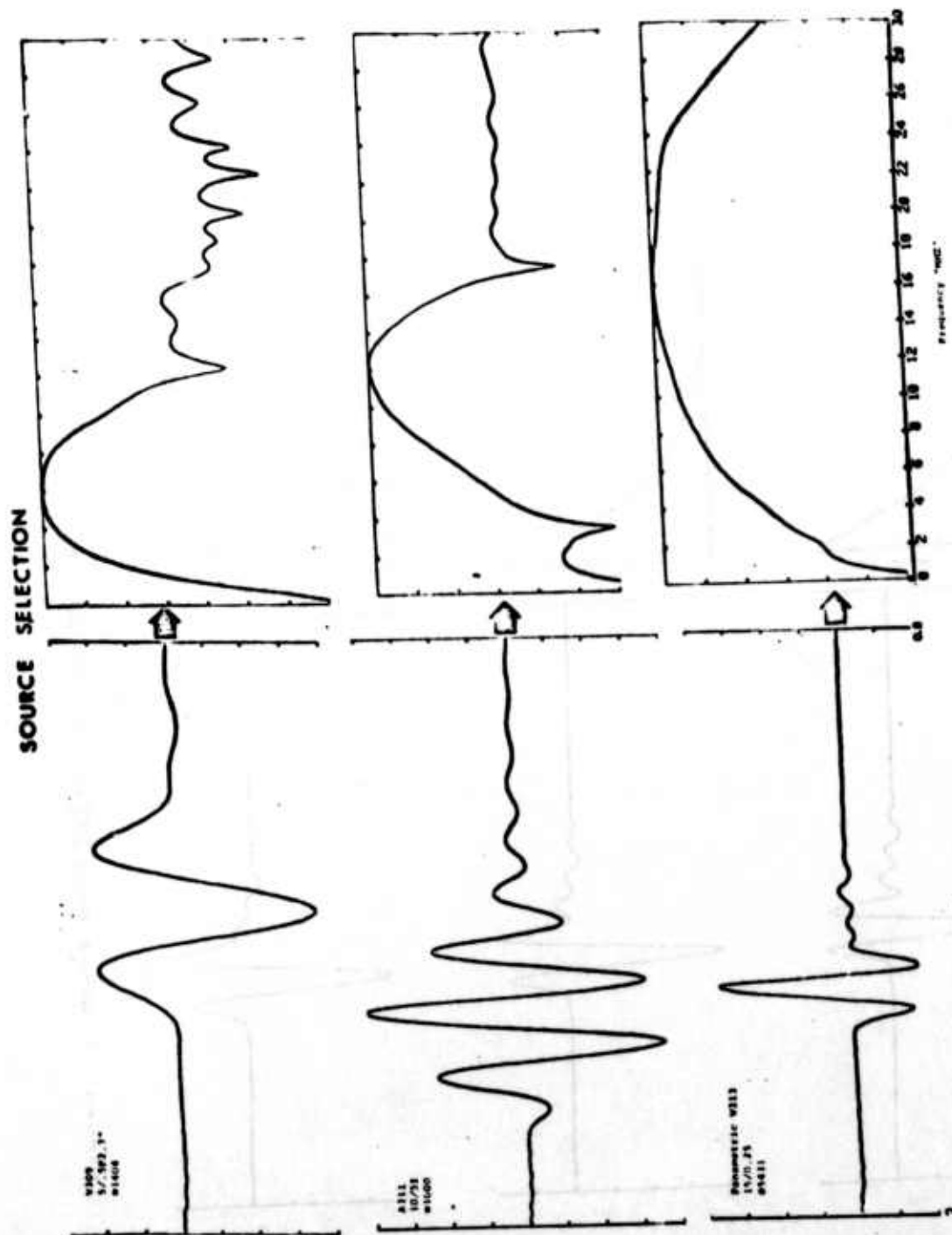


Figure 3 RF Waveforms and Fourier Power Spectra of Candidate Source



Science Center
Rockwell International

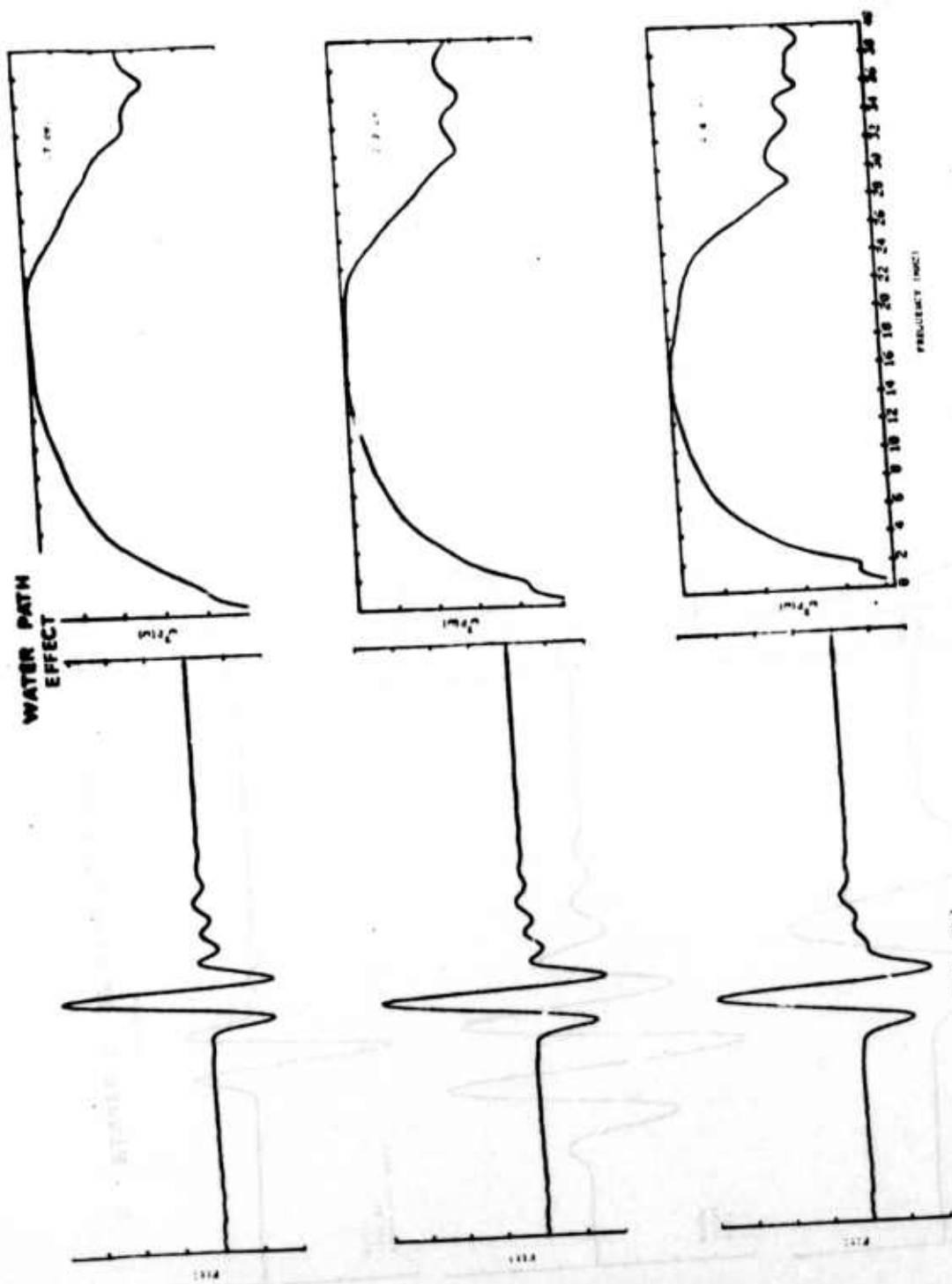


Figure 4 Water Path Effect on the Band Width of Pulsed Ultrasound

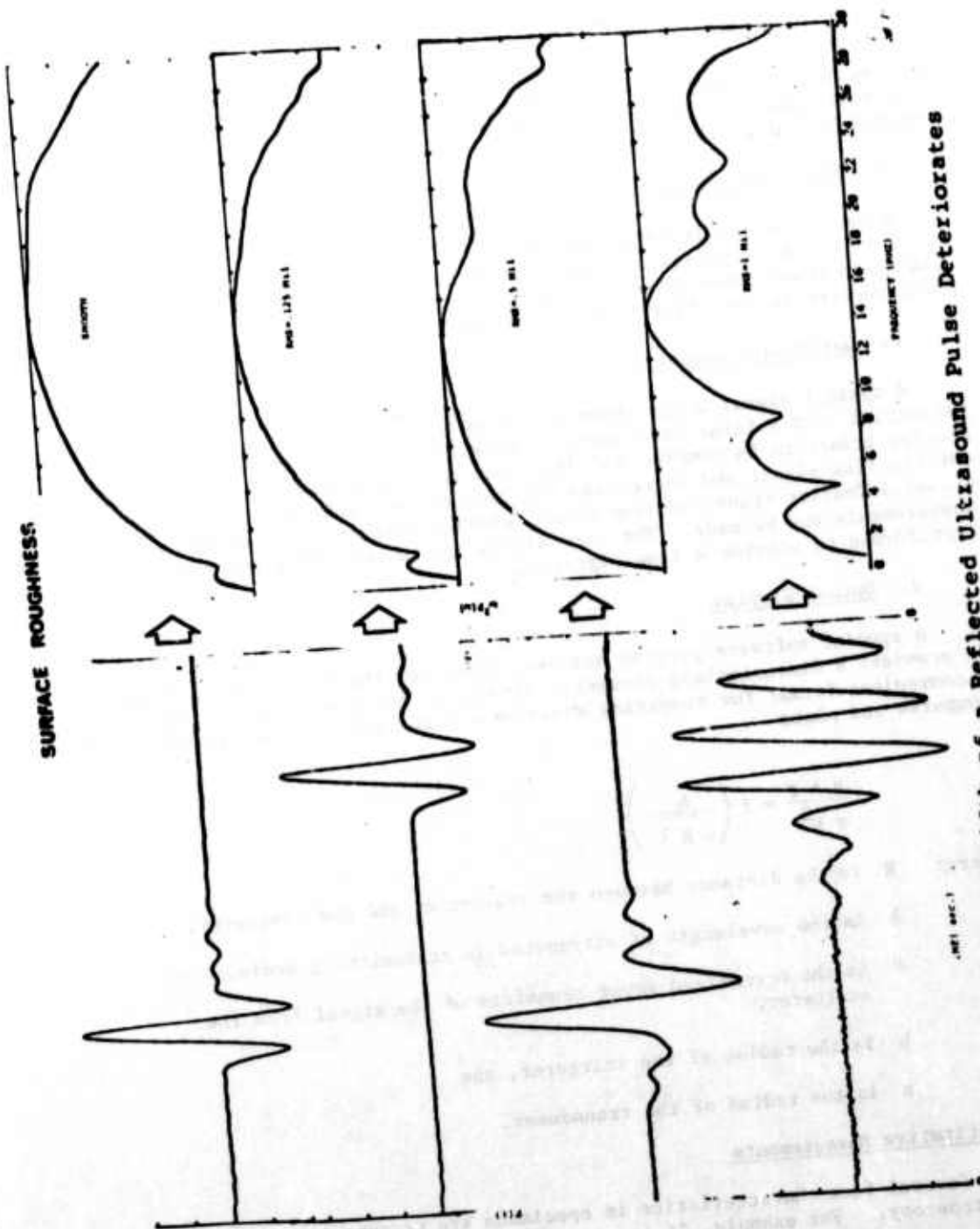


Figure 5 The Band Width of a Reflected Ultrasound Pulse Deteriorates as the Surface Roughness Increases

The function $f(t)$ is fitted by an analytical expression that can be substituted into equation (2) for integration in closed form. $F(\omega)$ and $P(\omega)$ are computed by a digital computer.

b. Source Normalization

A power spectra is normalized by dividing it by the power spectra of the source. The benefits of source normalization is best illustrated by the flaw depth measurement shown in Figure 6. The resulting normalized Fourier power spectra is very flat from 4 to 22 MHz.

c. Gated Gain Capability

A typical signal which shows a top surface reflection, a flaw reflection, and a faint back surface reflection is shown in Fig. 7. The Fourier transform is complex and difficult to quantitatively analyze. Gating out the flaw signal and increasing the gain of the back surface echo produces a useful Fourier transform from which material velocity or specimen thickness measurements may be made. The flaw signal can be amplified and Fourier transformed to provide a flaw signature.

d. Output Display

A special software program has been added for the RISC support task. It provides a dimensionless parameter display of the power spectra that is a convenient format for comparing experiment with theory. The program simply computes and plots

$$\frac{R \lambda P}{\pi b^2} = f \left(\frac{a}{\sqrt{R \lambda}} \right)$$

where: R is the distance between the transducer and the scatterer,

λ is the wavelength of ultrasound in transmitting media,

P is the normalized power transform of the signal from the scatterer,

b is the radius of the scatterer, and

a is the radius of the transducer.

Quantitative Measurements

Several flaw characteristics in specimens are measurable by ultrasonic spectroscopy. For example, it is possible to measure:

- (1) the velocity of sound in a specimen,



Science Center
Rockwell International

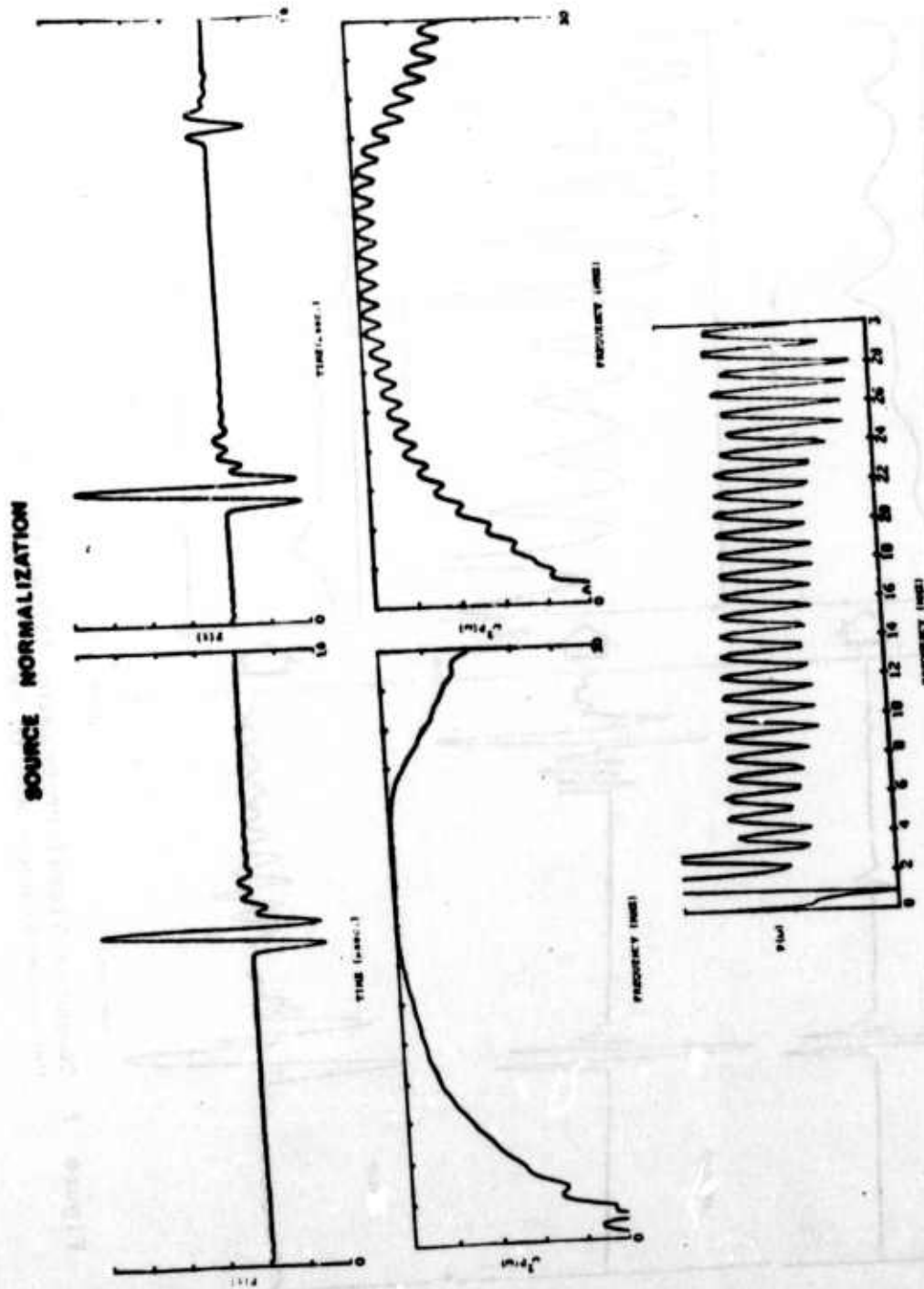


Figure 6 Source Normalization Produces a Flat Power Spectra Between 4 and 22 MHz

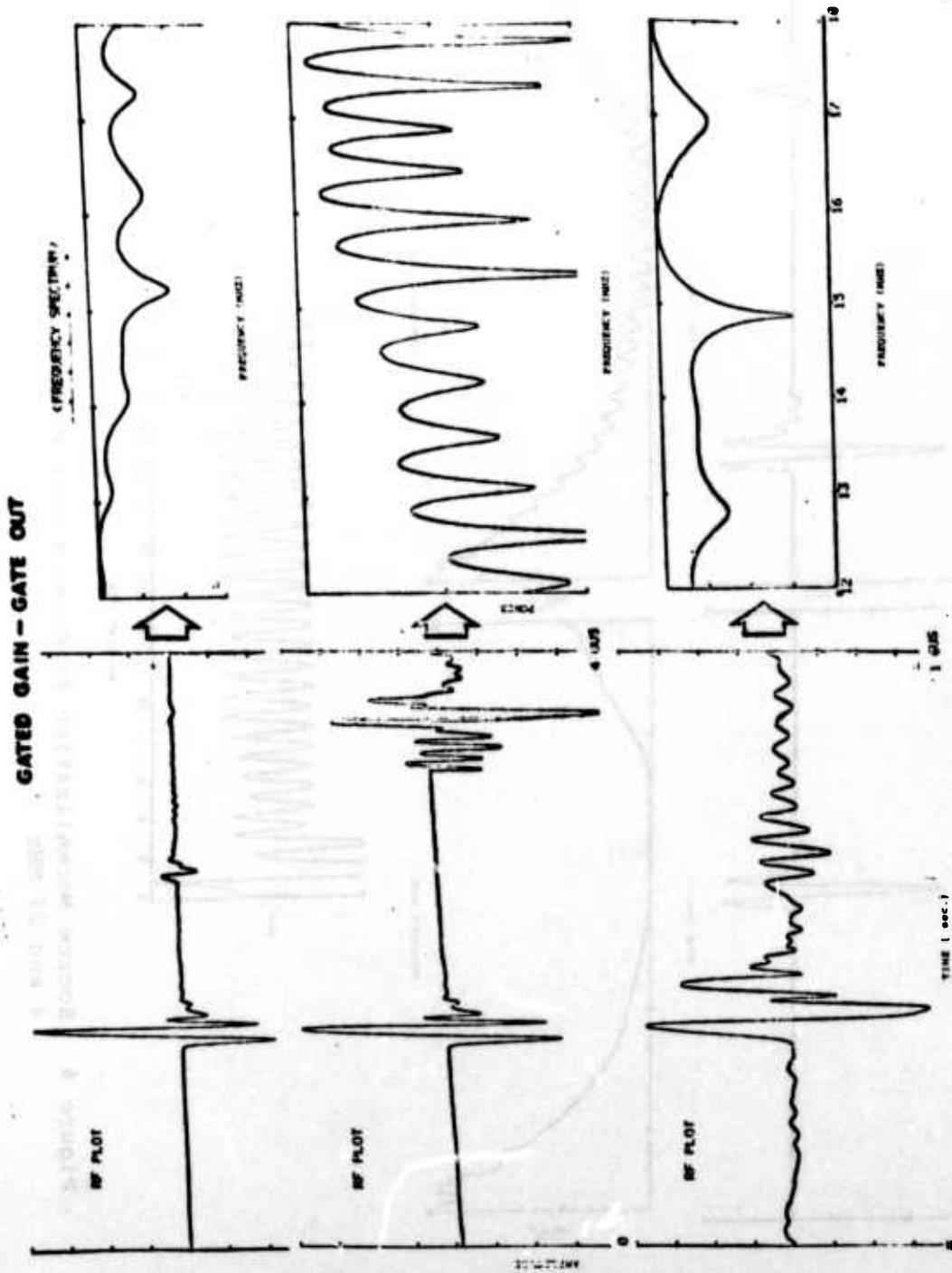


Figure 7 Computer Signal Processing Allows the Operator to Gate-Out unwanted signals and to Amplify Other Signals

- (2) the depth of a flaw in a specimen, and
- (3) the diameter of a simply shaped inclusion*

a. Velocity Measurements

Four one-inch long blank specimens were provided by RISC for velocity measurements. They were representative samples of 1100 aluminum, 2024 aluminum, commercial purity titanium, and Ti-6Al-4V titanium alloy. Specimen thicknesses were measured as one-inch (within one percent). The velocity measurements are shown in Figs. 8 and 9 for aluminum and titanium specimens respectively. The velocity of sound can be computed from the spacing between interference resonance dips from the equation.

$$v = 2t \Delta F$$

where

t is the specimen thickness and

ΔF is the frequency spacing.

The travel time can also be used to measure the velocity of sound but is subject to errors introduced by phase changes in the reflected signal. The velocities measured in this study are tabulated in Table 1.

* Air filled voids do not transmit sound to provide back surface echoes needed for dimension measurements.

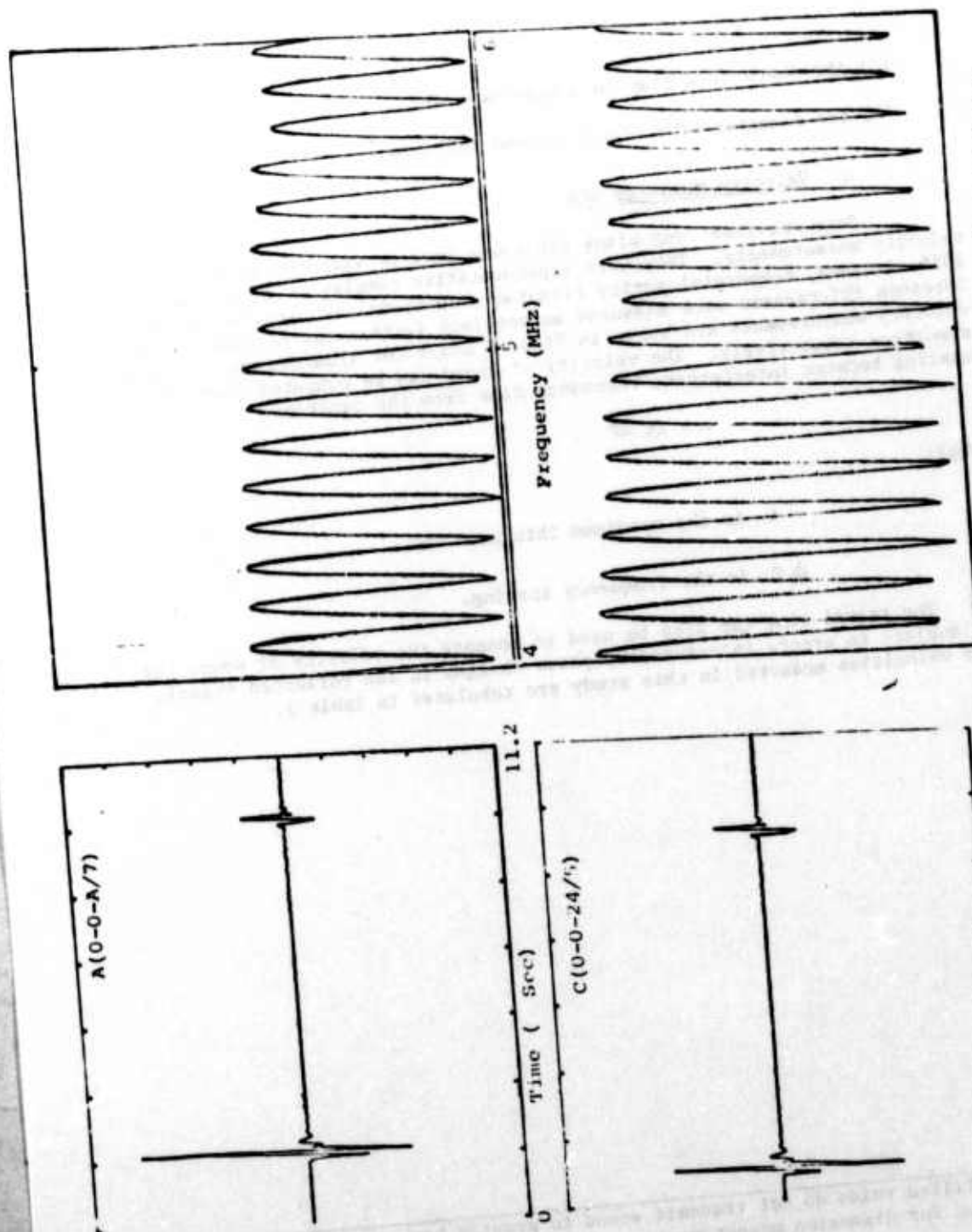


Figure 8 Ultrasonic Spectroscopy Measurement of Sound Velocity in Aluminum

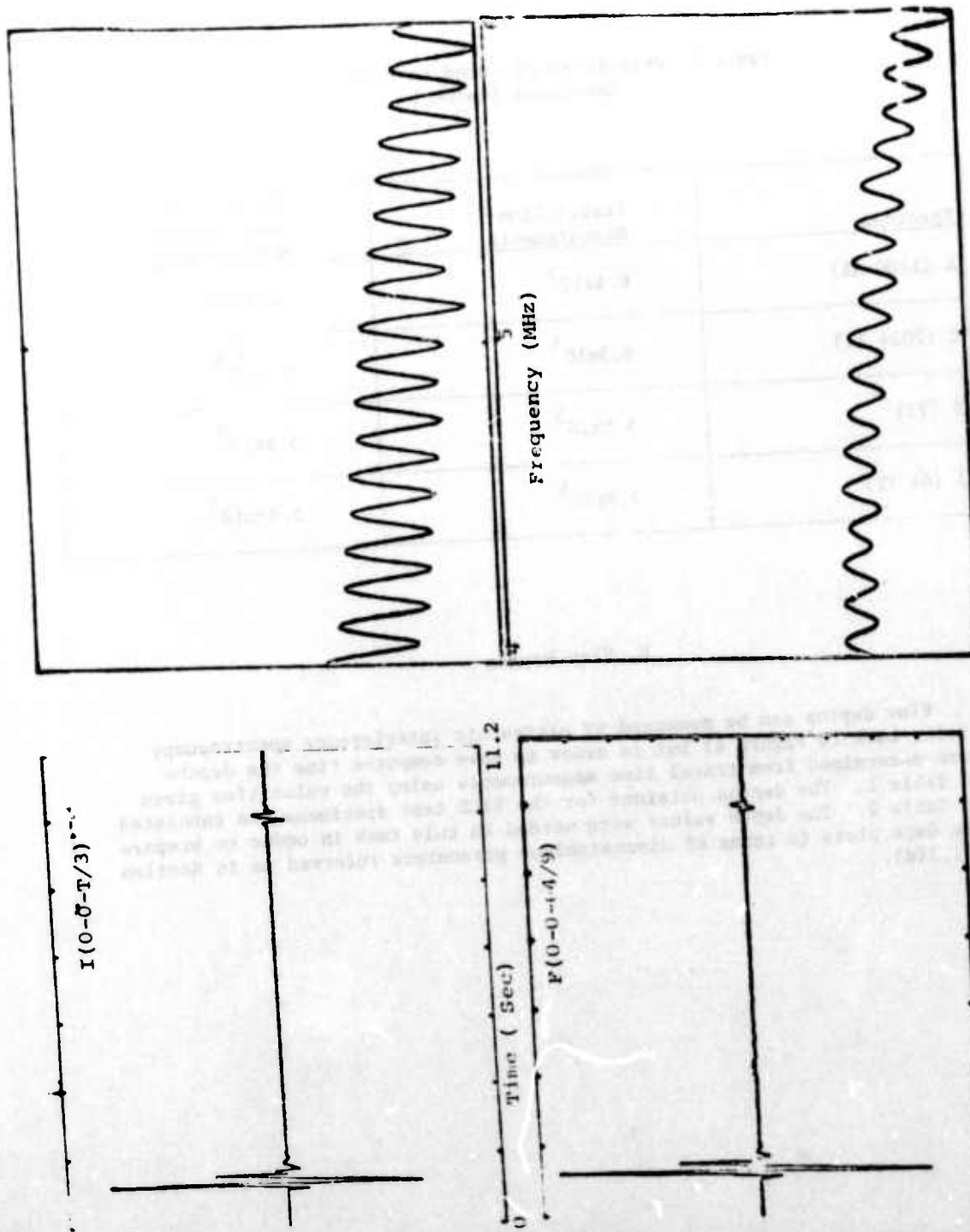


Figure 9 Ultrasonic Spectroscopy Measurement of Sound Velocity in Titanium

Table 1 Velocities of Sound in RISC
Specimens (cm/sec)

Specimen	Travel Time Measurements	Interference Spectroscopy Measurements
A (1100 Al)	6.4×10^5	6.34×10^5
C (2024 Al)	6.3×10^5	6.2×10^5
F (Ti)	5.9×10^5	5.9×10^5
I (64 Ti)	5.9×10^5	5.83×10^5

b. Flaw Depths

Flaw depths can be measured by ultrasonic interference spectroscopy (refer back to Figure 6) but in order to save computer time the depths were determined from travel time measurements using the velocities given in Table 1. The depths obtained for the RICS test specimens are tabulated in Table 2. The depth values were needed in this task in order to prepare the data plots in terms of dimensionless parameters referred to in Section III.2(d).



Science Center
Rockwell International

Table 2 Co-Axial Flaw Depths in
RISC Specimens

Specimens	Depth	Spheroid Specimens	Depth
B(1-8-A/21)	.99"	N(B-2-4-64/35)	1.09"
D(1-8-24/19)	.99"	O(B-2-8-64/36)	1.09"
E(1-8-24/24)	.99"	P(B-2-12-64/37)	1.08"
G(1-8-64/15)	.99"	Q(B-3-2-64/38)	1.09"
H(1-1-64/9)	.99"	R(B-3-4-64/39)	1.09"
J(1-8-T/17)	.99"	S(B-4-4-64/40)	1.09"
M(1-4-64/32)	.99"	T(B-4-8-64/41)	1.09"

Depths reported by RISC were 1" and 1.125" for the FBH and the spheroidal void specimens respectively. The 10 Mil inconsistency for FBH specimens may simply be a consistent error factor introduced by unaccounted for phase changes in the reflected echo. The 3 percent low readings for the spheroid specimens are more difficult to explain. Perhaps some metal compression resulted during the diffusion bonding fabrication.

C. Flaw Dimensions

The air filled voids in the RISC specimens do not transmit sound and therefore do not provide the back surface echoes needed for dimension or acoustic impedance measurements.



Empirical Observations

The amplitude and power spectral signatures of the test specimens are very complex. The figures reproduced in this section typify the data. It may be seen in Figures 10, 11, 12, and 13 that although well defined trends are not readily apparent, significantly reproducible differences can be observed. The RF waveforms for the spherical voids have the most structure (Figures 10 and 11), the RF waveforms from the cylindrical voids tend to ring more, and the RF waveforms from the FBH's are more source-like in appearance with the signal-to-noise ratio tending to increase with flat-bottom-hole diameter.

These ultrasonic echo signatures contain information about the nature of the scatterer. It will, however, require the computation of correlation coefficients or perhaps some sophisticated application of pattern recognition methods to identify the sizes of the flat bottom holes and spheroids contained in the test specimens.

Perhaps the best starting point for next year's work will be with specimens M, Q, R, N, and S (see Appendix A-1) which contain voids having the same cross-sectional area when viewed co-axially but vary in front surface curvature from flat (M) to highly curved (S). Broad classifications such as spheroidal-prolate, spheroidal, spheroidal-oblate, and flat might be reasonable as a starting point.

The ultrasonic signatures of specimens M, Q, R, N, and S are shown in Figures 14 and 15. The latter figure contains power spectra in terms of dimensionless parameters.* As before the amount of noise in the RF signatures increases with the curvature of the surface. The power spectral waveforms certainly differ. The prospect for classification as prolate, spherical, oblate, and flat look promising.

*Notice that the dimensionless parameter plots contain broken-vertical lines - these identify the beginning and end of the region where source energy was highest-data before the first line and after the last line may contain noise.

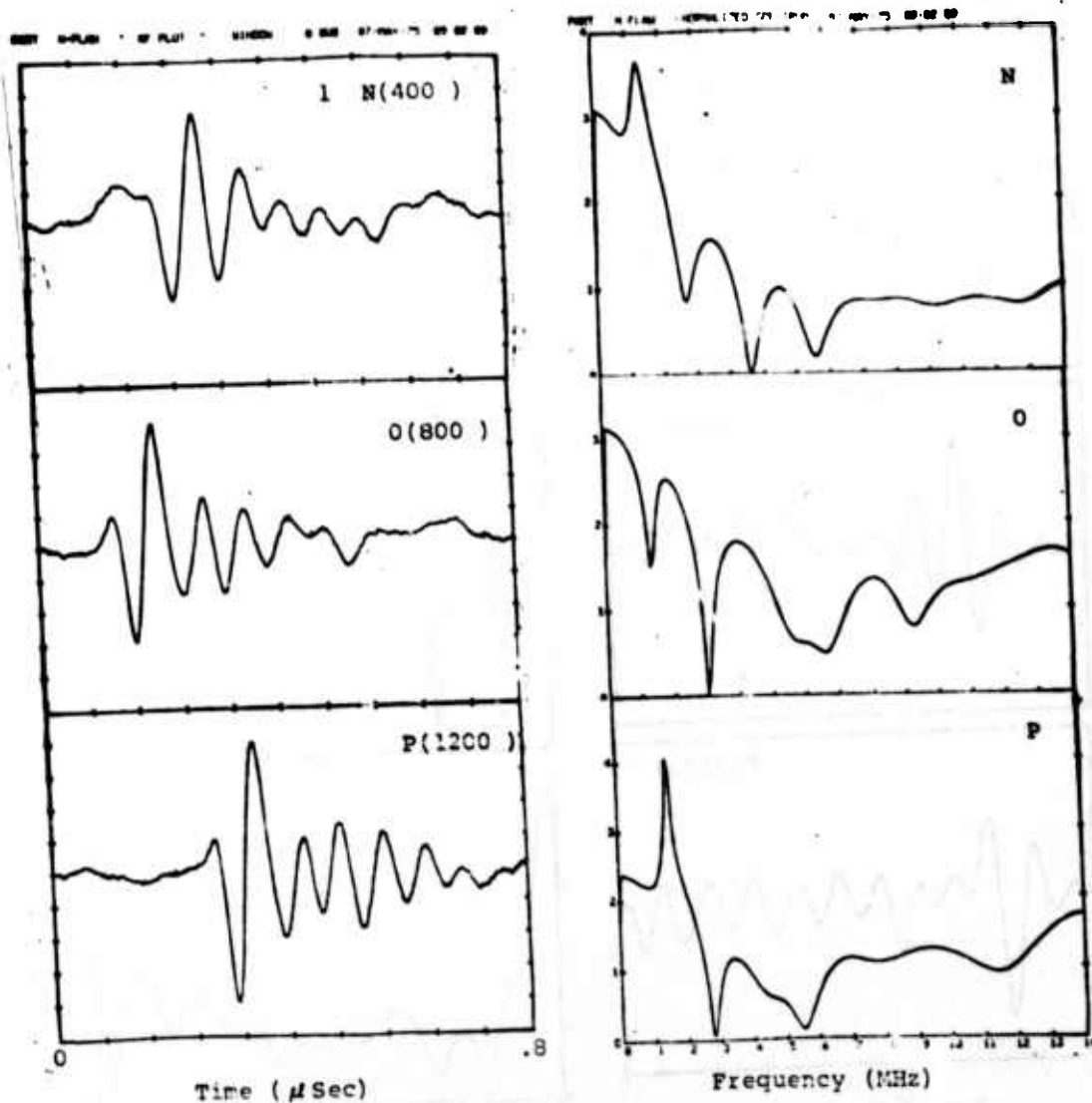


Figure 10 Co-Axial Pulse Echoes and Power Spectra from Spherical Voids

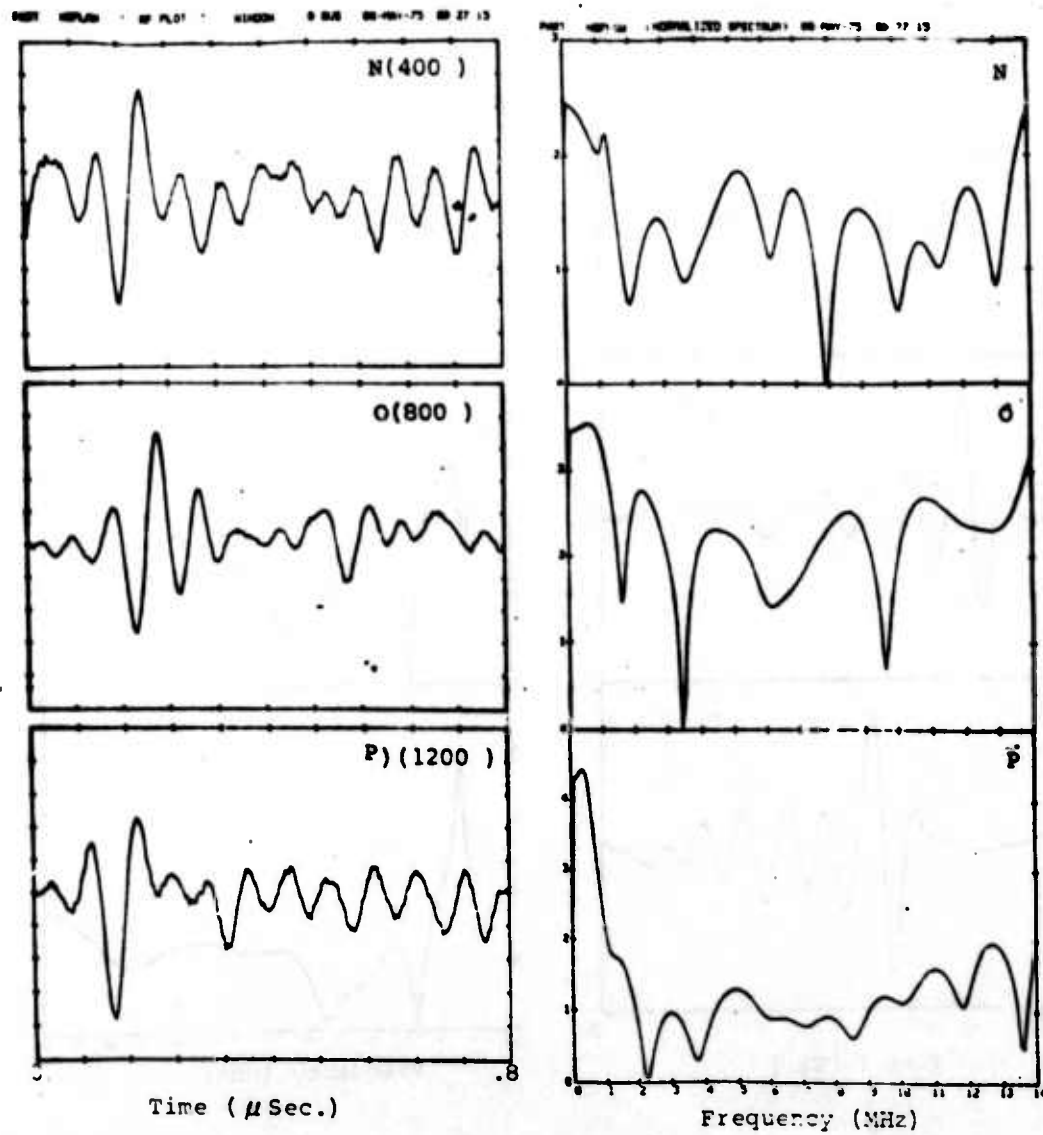


Figure 11 Side View Pulse Echoes and Power Spectra
from Spherical Voids

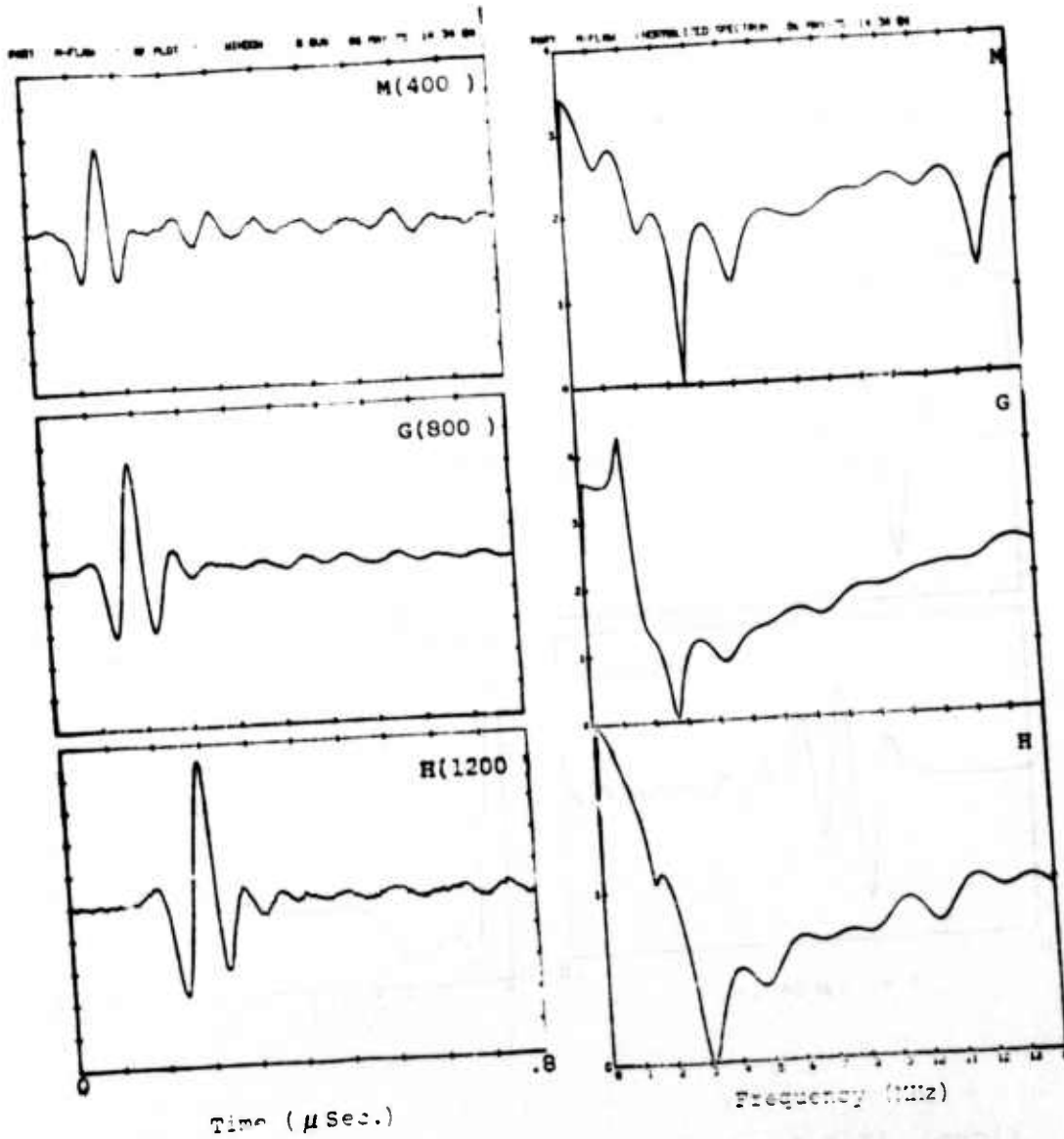


Figure 12 Co-Axial Pulse Echoes and Power Spectra
from Flat Bottom Holes

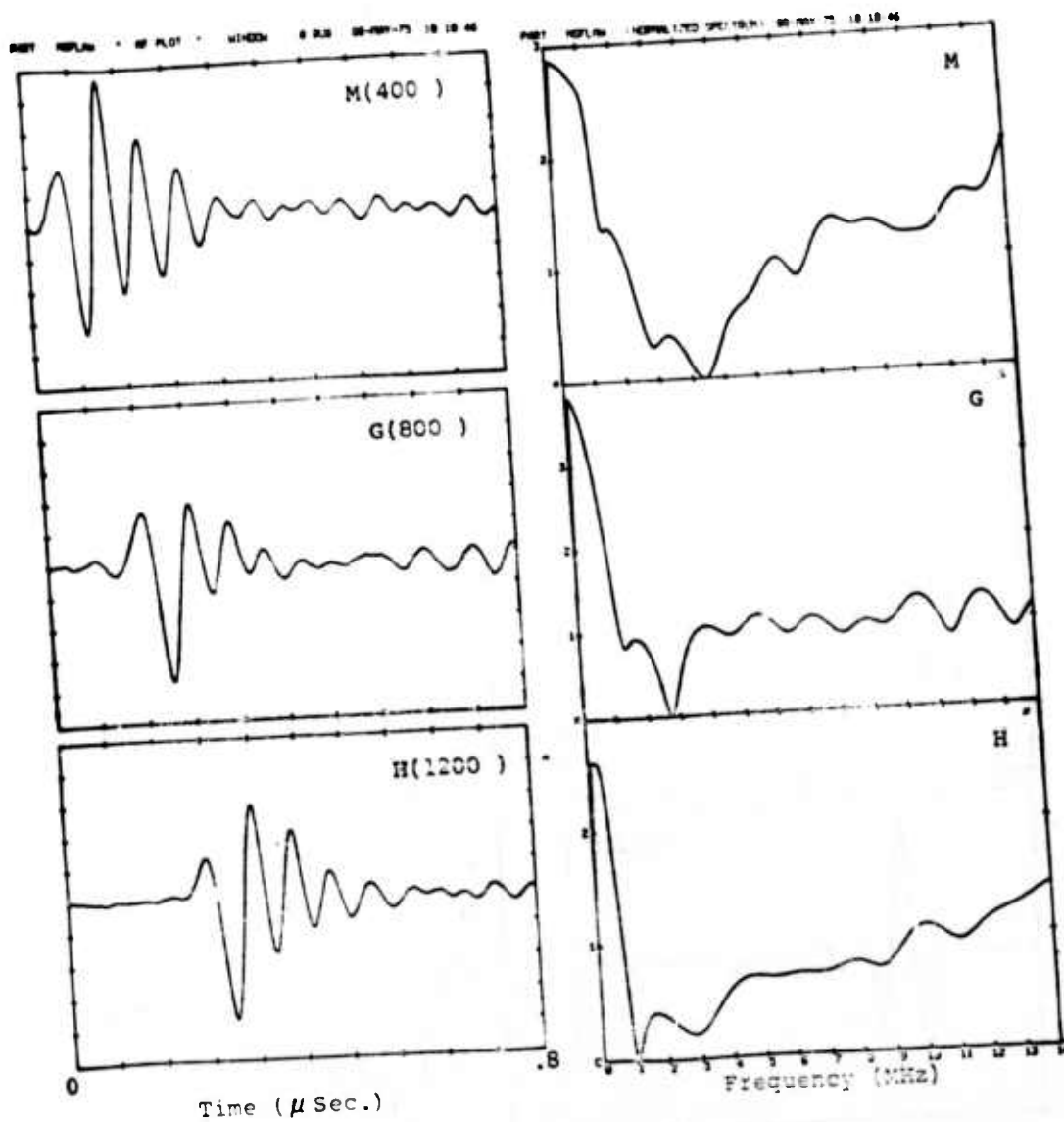


Figure 13 Side View Pulse Echoes and Power Spectra from Cylindrical Voids (Side View of FBH)

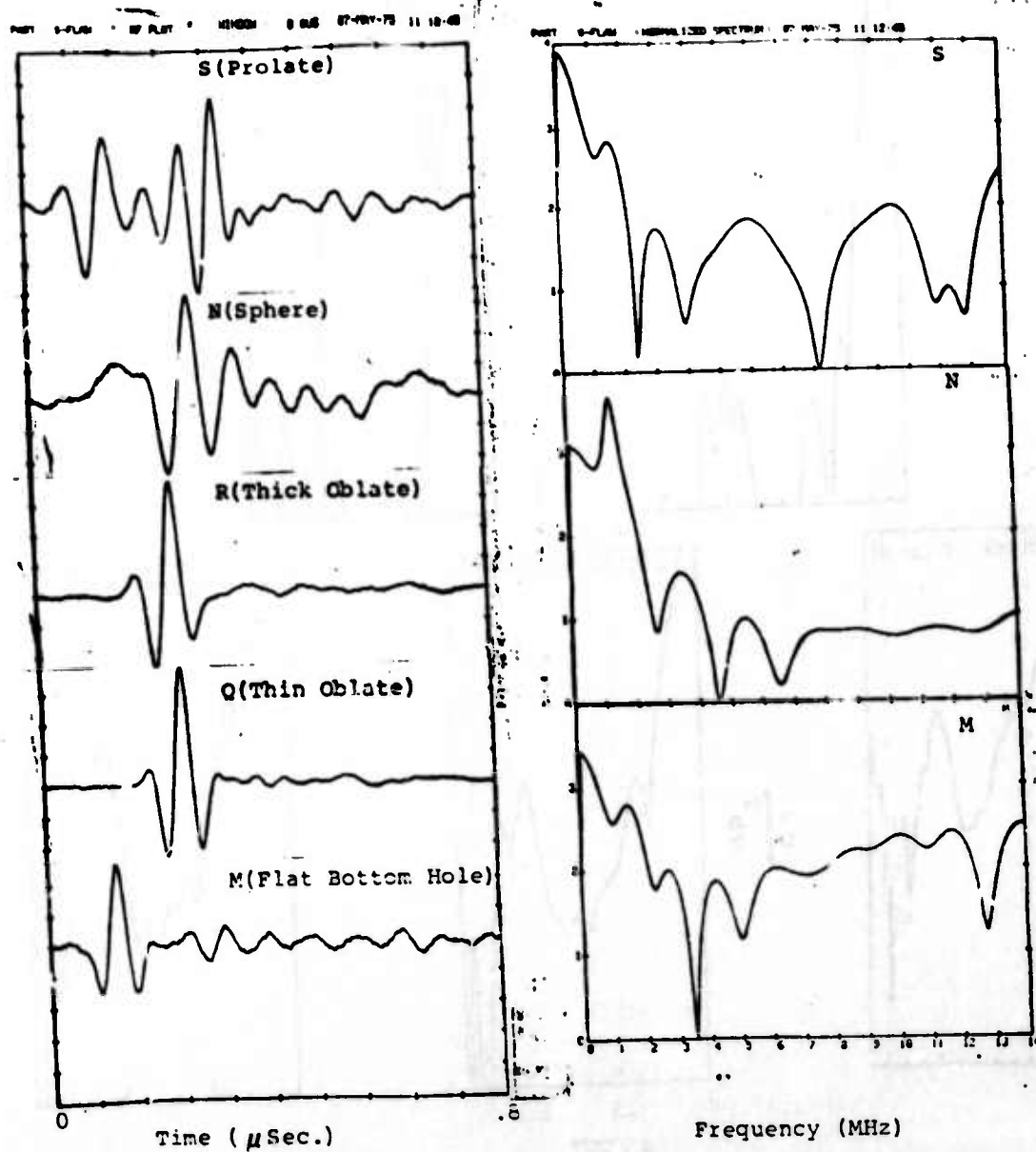


Figure 14 Co-Axial Pulse Echo and Power Spectra from Varying Flaw Shapes that have the same Co-Axial Areas

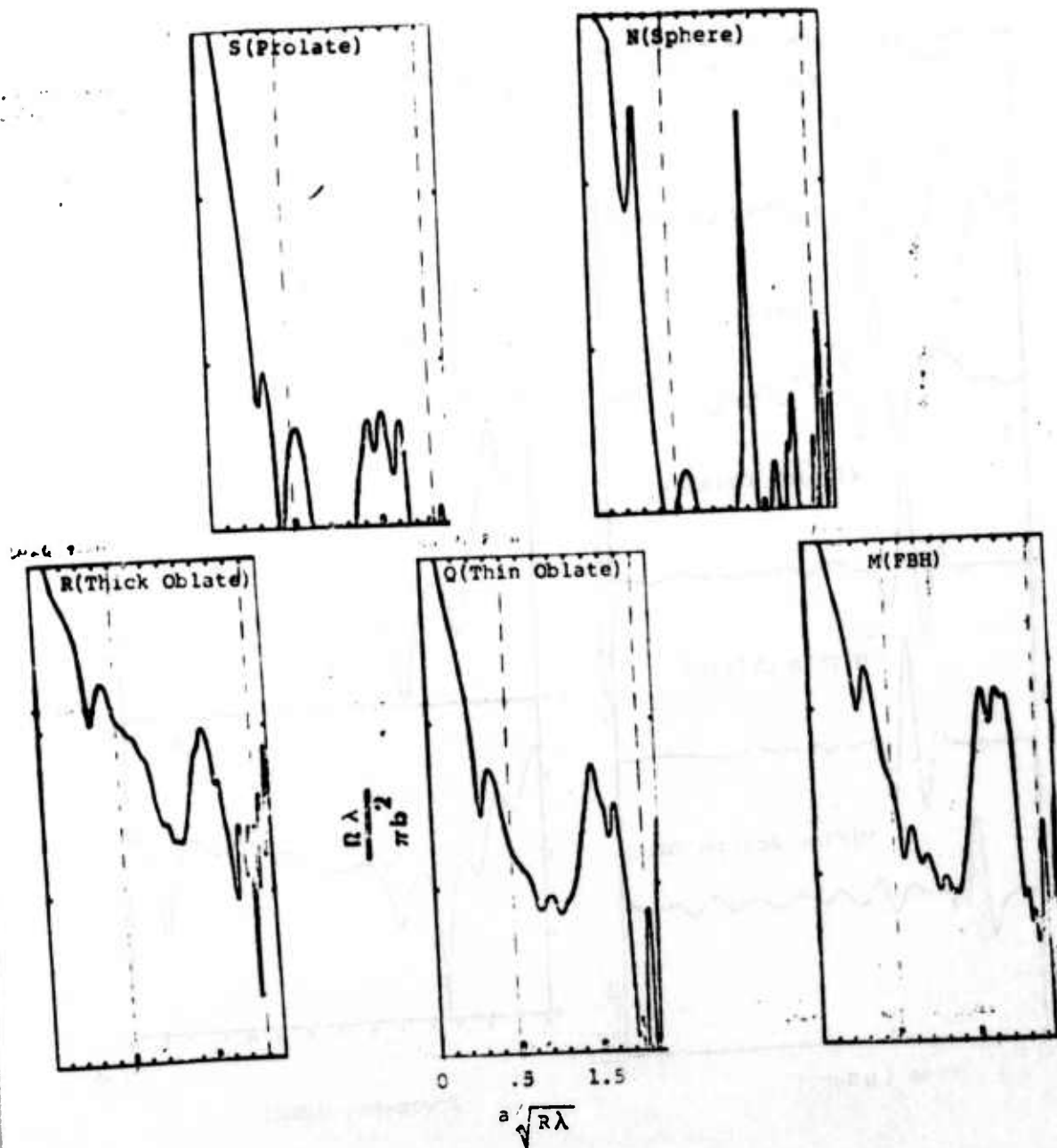


Figure 15 Co-Axial Fourier Power Spectra of Varying Flaw Shapes that have the same Co-Axial Area (Dimensionless Parameter Plots)



Science Center
Rockwell International

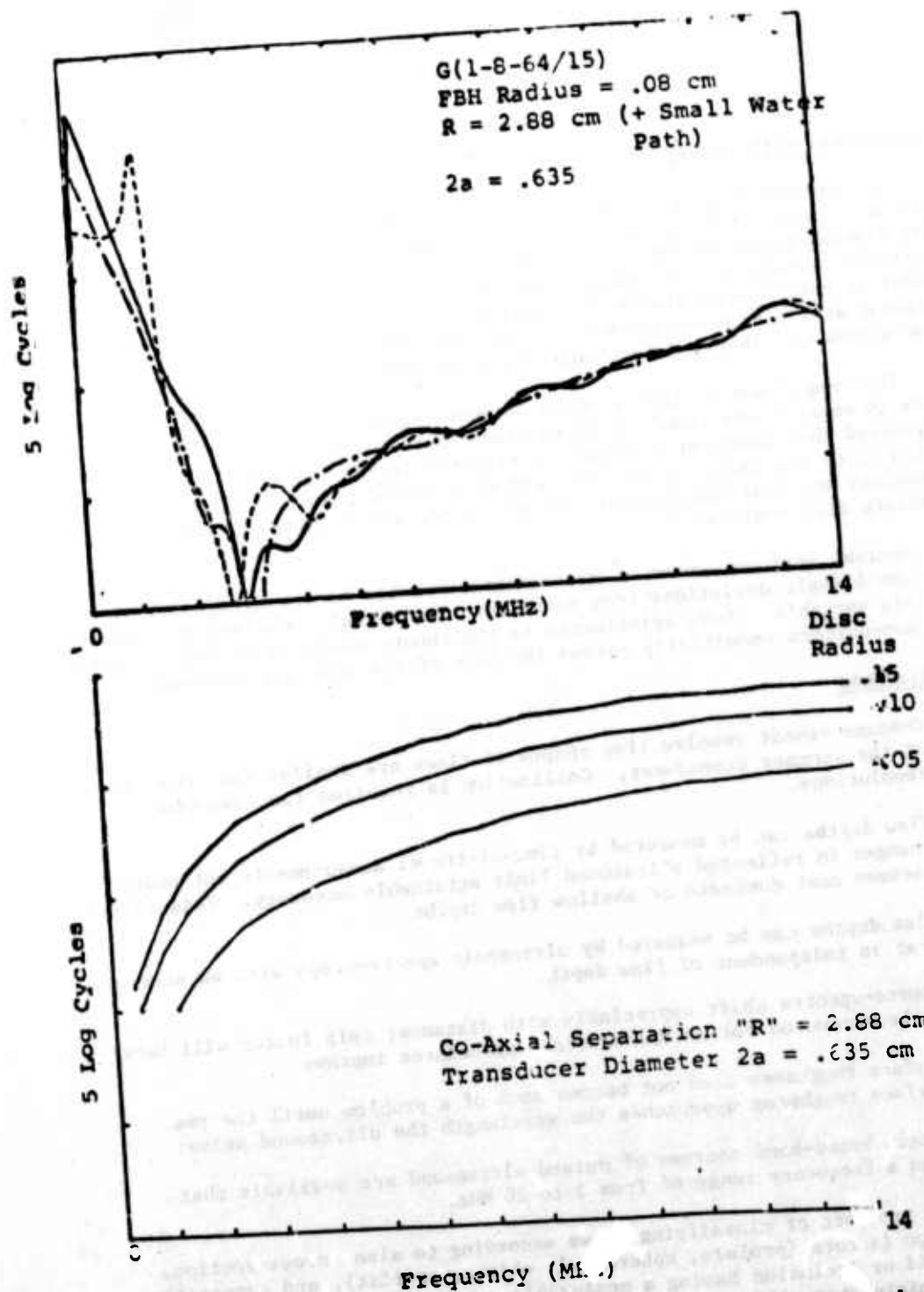


Figure 16 Power Spectra of 800 Diameter FBH taken for Comparison to the Ermolou Predictions as Presented by Tittmann



Comparison with Theory

An unknown water path is inherent in the FBH data shown in Figure 16. The water path is less than one cm and selected for broad band response. The dimensionless parameter data (Figs. 17 and 18), however, were collected with the transducer in contact with the flat surface of the specimen in order to better approximate the theoretical model. A thin water gap was present at the transducer-specimen interface and the presence of this lamination was observed to change the power spectra when pressure was applied.

The comparison to theory would be more rigorous if measurements were made in water where coupling laminations would not be present. It is suggested that computer software be prepared during the next year's work which plots the ratio of the theoretical/measured power as a function of frequency and that measurements be made under water using rod ends to simulate disk scatterers.

Another serious source of experimental trouble is the difficulty of avoiding small angle deviations from normalcy. The signals received are sensitive to this variable. Some adjustments to the theory needs to be made to account for non-uniform sensitivity across the face of the receiver transducer.

Conclusions

1. C-scans cannot resolve flaw shapes if flaws are smaller than the face of the scanner transducer. Collimation is required for improving resolutions.
2. Flaw depths can be measured by time-of-travel measurements but phase changes in reflected ultrasound limit attainable accuracy. This effect becomes most dominate at shallow flaw depths.
3. Flaw depths can be measured by ultrasonic spectroscopy with an accuracy that is independent of flaw depth.
4. Source-spectra shift appreciably with distance; this factor will have to be accounted for as spectroscopy procedures improve.
5. Surface roughness does not become much of a problem until the rms surface roughness approaches the wavelength the ultrasound pulse.
6. Single broad-band sources of pulsed ultrasound are available that span a frequency range of from 3 to 20 MHz.
7. The prospect of classifying flaws according to size, cross-section, shape factors (prolate, spheroidal, oblate, or flat), and composition (void or inclusion having a measurable acoustic impedance) looks promising but will require pattern recognition techniques.



Science Center
Rockwell International

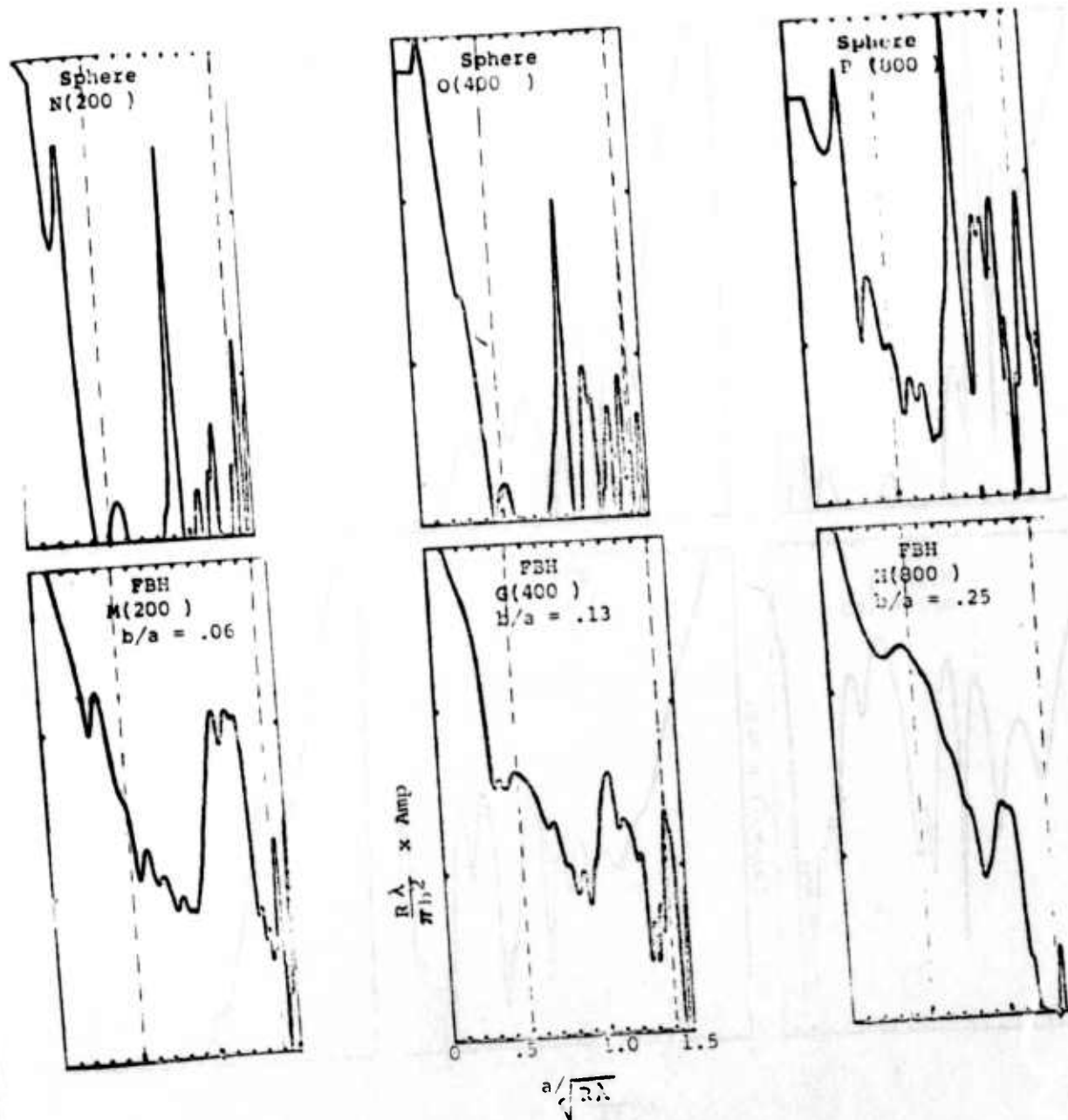


Figure 17 Co-Axial Power Spectra of Spheres and
FBH's in Titanium in Dimensionless
Parameter Representation
($\frac{1}{8}$ " Diameter Transducer)

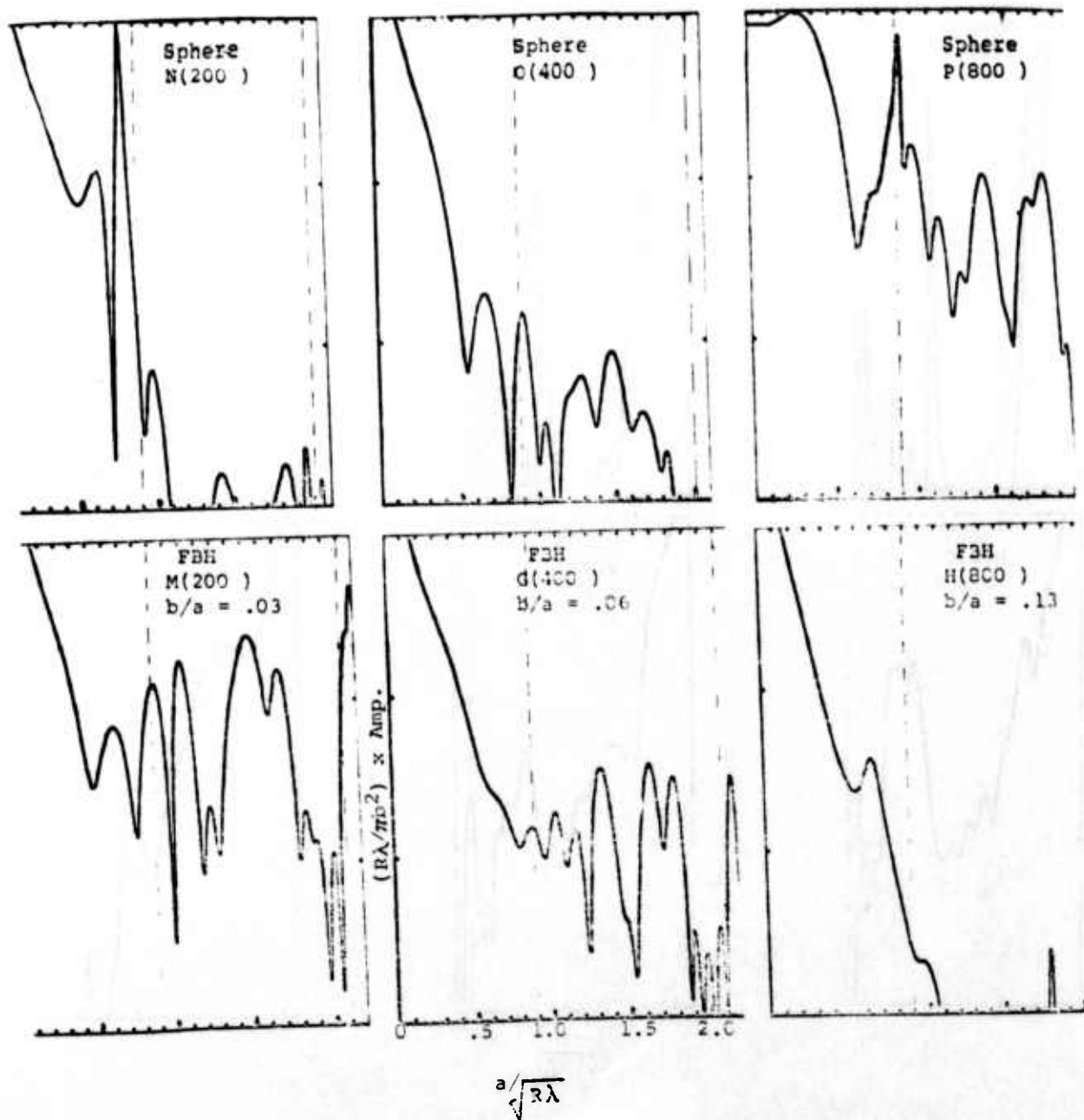


Figure 18 Co-Axial Power Spectra of Spheres and FBH's in Titanium in Dimensionless Parameter Representation ($\frac{1}{2}$ " Diameter Transducer)

8. The use of simple theoretical models to predict realistic experimental results must be done only after careful examination of the effects of all pertinent experimental parameters that are not accounted for in the theory.
9. A very extensive catalog of ultrasonic signatures of spheroids and flat bottom holes have been prepared from this task. These should be understood in terms of reproducibility and significance before more complex flaw structures are added to this program. Metal inclusions having identical geometries but having acoustic impedances that are different than the host material are recommended.
10. Data presented in this report may be better understood after void specimens are opened and tested for surface texture and shape.



Science Center
Rockwell International

APPENDIX A-1 TEST SPECIMENS

Eighteen test specimens were provided by RISC for use by contractors for experimental testing. Specimens were right cylindrical having blanks, flat bottom holes, and spheroidal cavities coaxially located at about 1 inch from the front surface. All coding and reporting on derived data relating to test specimens is presented in this appendix.



Table A.1 Properties of Test Specimens

*See Code	Host Matl.	# Flaws	Geo.	Flaw Type	Vel.	Reptd.	Meas.
A(0-0-A/7)*	Al	0	-	Blank	6.34(5)		
B(1-8-A/21)	Al	1	FBH	Void		1.00	.99
C(0-0-24/5)	Al	0	-	Blank	6.24(5)		
D(1-8-24/19)	Al	1	FBH	Void		1.00	.99
E(1-8-24/24)	Al	1	FBH	Void		1.00	.99
F(0-0-64/9)	Ti	0	-	Blank	5.91(5)		
G(1-8-64/15)	Ti	1	FBH	Void		1.00	.99
H(1-12-64/9)	Ti	1	FBH	Void		1.00	.99
I(0-0-T/3)	Ti	0	-	Blank	5.83(5)		
J(1-8-T/17)	Ti	1	FBH	Void		1.00	.99
M(1-4-64/32)	Ti	1	FBH	Void		1.00	.99
N(B-2-4-64/35)	Ti	1	Sphere	"		1.125	1.09
O(B-2-8-64/36)	Ti	1	Sphere	"		1.125	1.09
P(B-2-12-64/37)	Ti	1	"	"		1.125	1.08
Q(B-3-2/64/38)	Ti	1	Oblate Sphere	"		1.125	1.09
R(B-3-4-64/39)	Ti	1	"	"		1.125	1.09
S(B-4-4-64/40)	"	1	Prolate Sphere	"		1.125	1.09
T(B-4-8-64/41)	"	1	"	"		1.125	1.09

PROJECT I, UNIT III, TASK 1
MODELS FOR THE FREQUENCY DEPENDENCE
OF ULTRASONIC SCATTERING FROM REAL FLAWS

L. Adler
University of Tennessee

Introduction

The overall objective of this investigation is to study models for frequency and angular dependence of scattered ultrasonic waves from "flaws". We have introduced a new theoretical model which was based on a scalar theory—a geometrical theory of diffraction. It can be used for two-dimensional flaws of any shape. The model was adapted for the "flat bottomed hole." An expression for the amplitudes of the scattered energy was derived for non-normal incidence. This expression relates the frequency and amplitude of the scattered sound beam to the size and orientation of the hole. This expression is experimentally verified. An approximate model was also introduced and used to determine size of irregular shaped simulated flaws. Initial experiments were also carried out to use shear wave scattering from notches in aluminum and to study mode conversion.

Diffraction Theory

In order to correlate the parameters of the ultrasonic wave, such as amplitude and frequency distribution, to the parameters of the flaw size, shape and angular orientation, we used diffraction theory. We have adopted a geometrical theory of diffraction—introduced by Keller¹ for electromagnetic waves—to the scattering of sound from "flaws". This theory has several advantages² over the traditionally used Kirchhoff approximation, especially for the study of off-axis scattered energy distribution.

In the geometrical theory of diffraction the concept of the diffracted ray is introduced. A diffracted ray is produced every time a ray interacts with an edge. The diffracted ray may interact again with the edge, thus doubly and multiply diffracted rays may be considered. Now each ray has a value (amplitude and phase) at any point. Therefore, the total diffracted field at any point is the sum of the fields of all rays through that point. The general expression for the diffracted field for an arbitrarily shaped aperture is given by equation (1).

$$U(p) = - \int A(k) \frac{e^{i[k(\psi + s)] + i \frac{\pi}{4}}}{2(2\pi k)^{\frac{1}{2}} \sin \beta} \left[\sec \frac{1}{2}(\theta - \alpha) \pm \csc \frac{1}{2}(\theta + \alpha) \right] \times \left[s \left(1 + \frac{s(\cos \delta - a \beta \sin \beta)}{a \sin^2 \beta} \right)^{\frac{1}{2}} \right] \quad (1)$$



The + or - sign is used whether $U = 0$ or $\frac{\partial U}{\partial n} = 0$ at the surface. $A(k)$ is the amplitude distribution of the incident pulse, ψ is the phase of the incident pulse, s is the distance from the origin to the edge of the aperture, k is the wave number, α is the angle of the incident ray, θ is the angle of the scattered ray, β is the angle between the incident ray and the tangent to the edge, a is the radius of curvature of the aperture, and $\dot{\beta}$ is the derivative of the angle β with respect to the arc length. A schematic diagram of the general problem is shown on Figure 1, where one of the incident and diffracted rays are illustrated together with the other parameters. Equation (1) is a general expression and is valid for two-dimensional flaws. The parameters characterizing a particular geometry are β , $\dot{\beta}$ and a . This theory is a scalar theory.

Flat Bottomed Holes

The end of the flat bottomed circular hole is one of the most used standards in N.D.E. Hence, we have placed special emphasis on the study of the diffraction of sound by circular flaws.

Let us take a circular aperture with radius a . To treat this problem it is sufficient to consider only two diffracted rays in the orientation of equation (1). Taking four rays into account has not given any additional information. The schematic diagram of the problem is shown on Figure 2. Substituting the parameters into equation (1), we obtain

$$\begin{aligned}
 u = & -A(k) \frac{\exp(ik(\psi_0 + r))}{r} \frac{a}{8\pi k} \left[\exp(i(-k a \sin \phi + \pi/4)) \left(\frac{-1}{\sin \phi + \theta} + \frac{1}{\cos \phi - \theta} \right) \cdot \right. \\
 & \cdot \left. \left[\frac{r - a \sin \phi}{r} \left(\frac{a}{r} - \frac{r - a \sin \phi}{r} (-\sin \theta - \sin \phi) \right) \right]^{-1/2} \right] \\
 & + \left[\exp(i(k a (\sin \phi + 2 \sin \theta) + \pi/4)) \left(\frac{1}{\sin \phi + \theta} + \frac{1}{\cos \phi - \theta} \right) \cdot \right. \\
 & \cdot \left. \left[\frac{r + a \sin \phi}{r} \left(\frac{a}{r} - \frac{r + a \sin \phi}{r} (-\sin \theta + \sin \phi) \right) \right]^{-1/2} \right]
 \end{aligned} \quad (2)$$

ORNL-DWG 75-3645

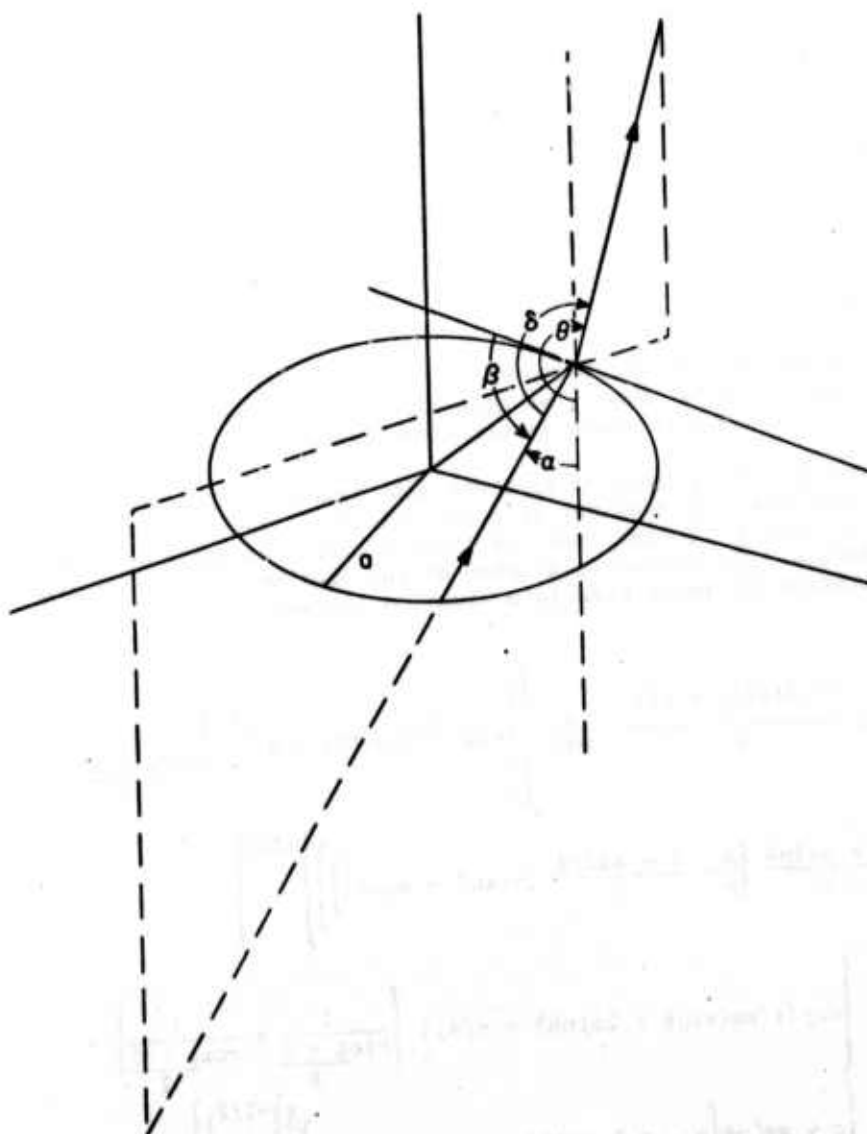


Figure 1. Schematic diagram of "ray diffraction" from aperture.

ORNL-DWG 75-3642

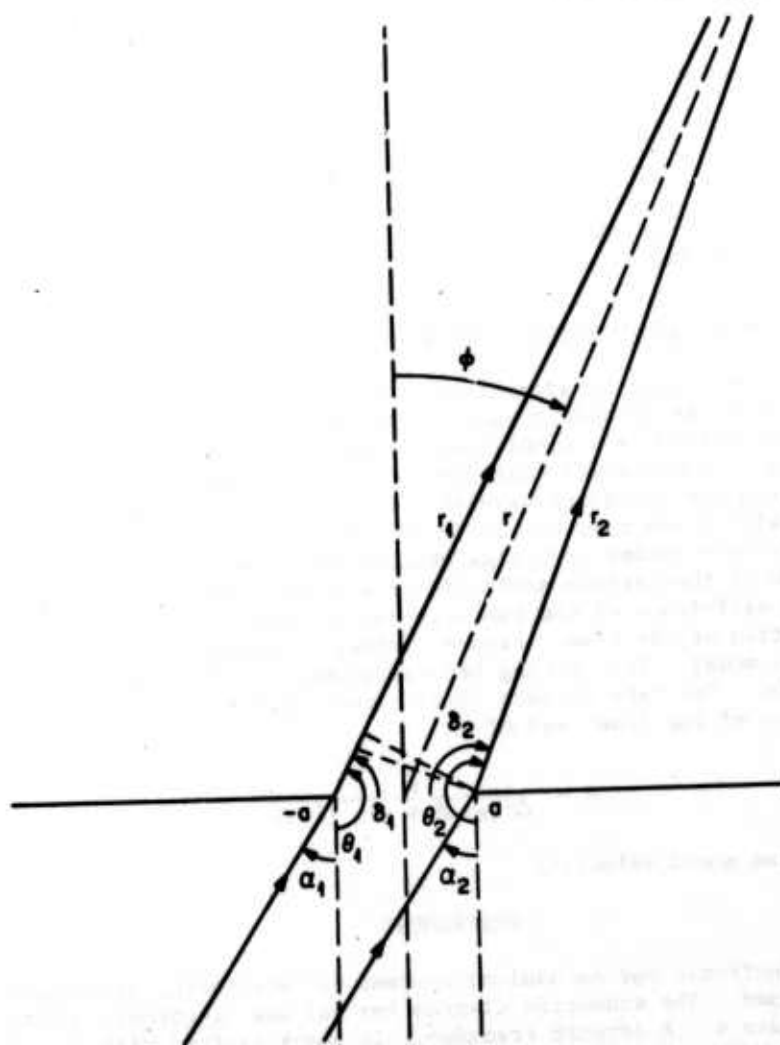


Figure 2. Schematic diagram of "ray diffraction" from flat bottomed hole.

Here $\beta_1 = \beta_2 = \frac{\pi}{2}$ $\dot{\beta} = \frac{-\sin\theta}{a}$ $\theta_1 \sim \pi + \theta$

$r_1 = r - a \sin\theta$ $r_2 = r + \sin\theta$ $\theta_2 \sim \pi - \theta$

Equation (2) reduces to a much simpler form for normal incidence.

$$U(P) = - \int \frac{A(k)}{2\pi r \sin\theta} \left(\frac{4\pi [1 - \cos\theta \cos(2k a \sin\theta)]^{1/2}}{k a \sin\theta} \right) \quad (3)$$

Equation (2) is programmed for Fortran and calculated with the parameters used in the experiment.

Approximate Model (Interference Model)

We have also used an approximate theory to correlate the frequency distribution of the scattered wave to the size and orientation of the "flaw." This model³ is a simplified version of the geometrical theory of diffraction, if one assumes that the two extreme edges of the reflector or flaw will send out secondary wavelets or rays. There are no field values associated with these rays but it is assumed that at any point they will form interference maxima or minima whether they are in or out of phase. The position of the maximum amplitude at a given frequency is then related to the path difference of the two rays and in turn to a given diameter and orientation of the flaw. Figure 3 shows a schematic diagram of the interference model. The spacing between consecutive frequency maxima is denoted by Δf . The interference model gives a simple relation between d , the dimension of the flaw, and Δf as

$$d = \frac{v}{\Delta f (\sin\theta + \sin(\theta + \alpha))} \quad (4)$$

where v is the sound velocity.

EXPERIMENT

Both electronic and mechanical systems for scattering experiments have been redesigned. The schematic diagram for our new electronic system is shown on Figure 4. A ceramic transducer is shock excited with a commercial Immerscope, thus producing a broadband pulse (see Figure 5 for the spectrum of the transmitter). This broadband pulse hits the target, the scattered sound received by a receiver transducer which is identical to the transmitter. The signal is amplified, gated out and displayed on the spectrum analyzer. The new feature of the apparatus is the stepless gate which allows us to obtain a more stable signal to be frequency analyzed. The displays on the two oscilloscopes (before and after the stepless gate) assures one that the gate will not distort the signal. The mechanical system which consists of the transducers clamped into the goniometer system and the turntable with the two different samples used is shown on Figure 6. Throughout

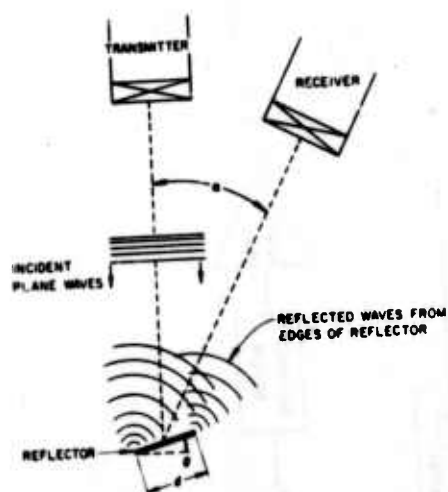


Figure 3. Interference model.

ORNL-DWG 75-3818

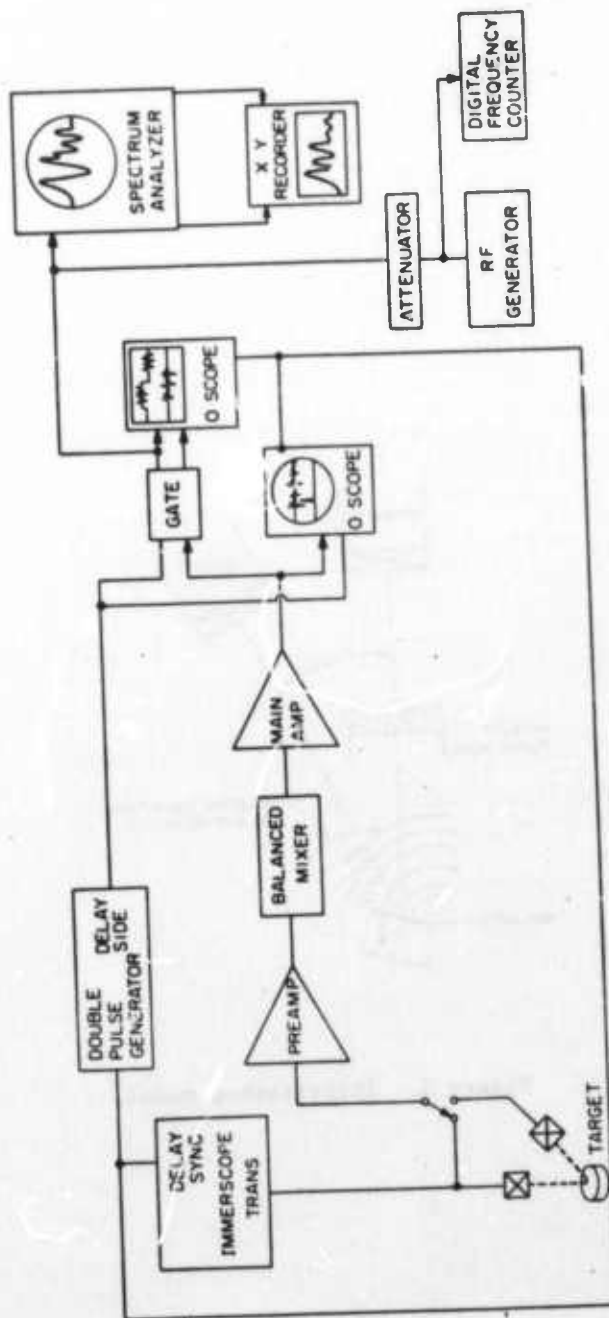


Figure 4. Schematic diagram of the apparatus.



Science Center
Rockwell International

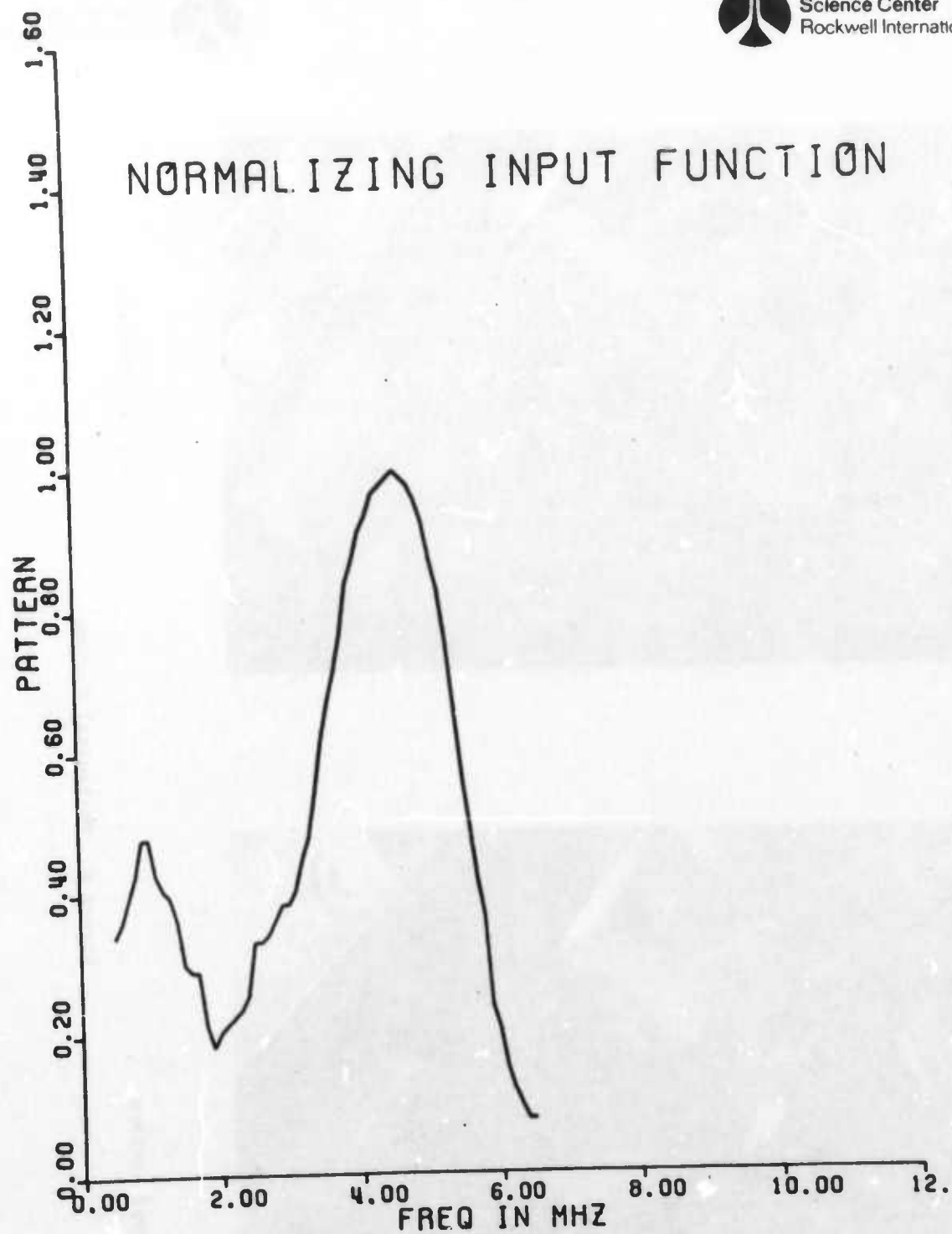
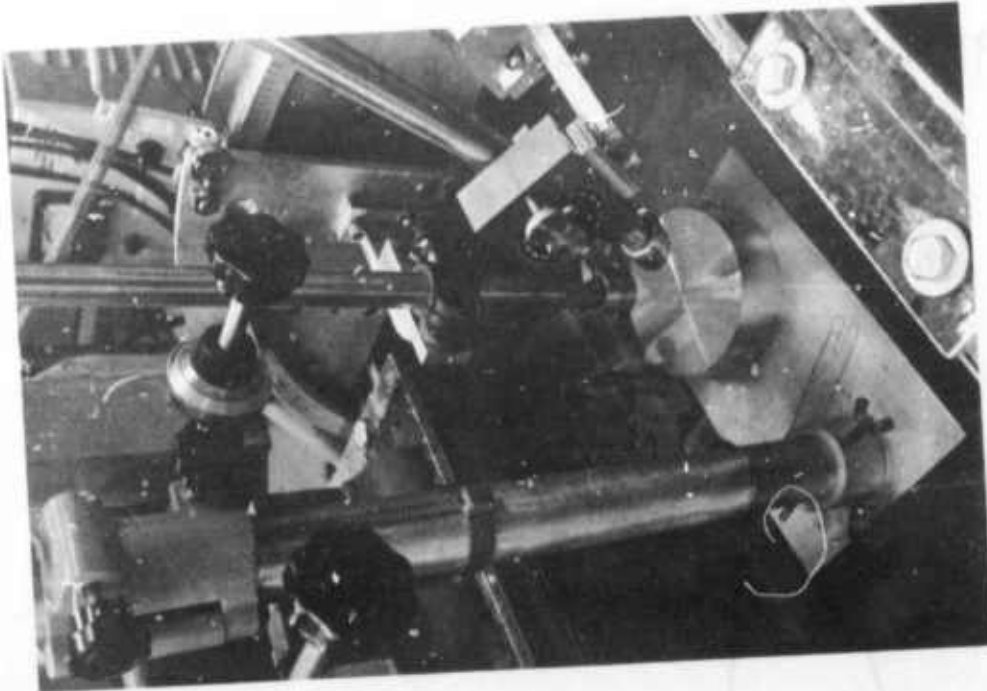


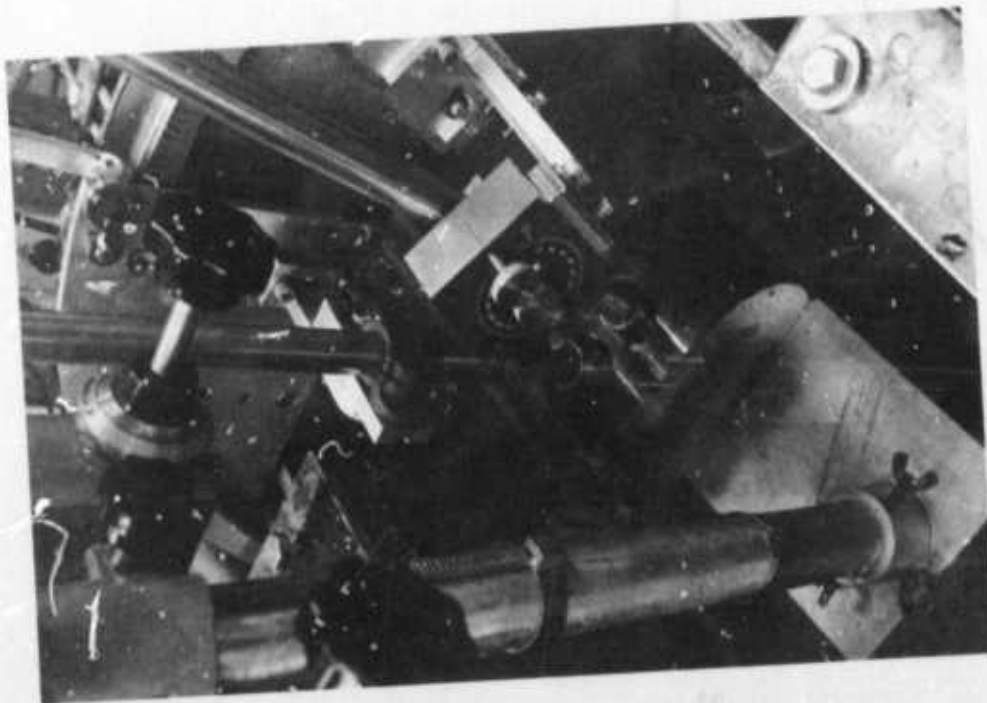
Fig. 5 Amplitude distribution of the incident wave vs. frequency.



Science Center
Rockwell International



(b) flat surface



(a) curved surface

Figure 6. Mechanical system.



the experiment the relative amplitudes were measured. The amplitude values were read off directly from the display of the spectrum analyzer.

COMPARISON OF THEORY AND EXPERIMENT

Brass Circular Rods

We have used ends of circular brass rods as reflectors in water to simulate flat bottomed holes. The diameters of the "flaws" were .125 inch (.3 cm) and .25 (~.6 cm). The frequency ranged from 1 to 5 MHz. Both incident and scattered angles were varied up to 40° . Figure 7 shows good agreement between experiment and theory for a 1/8 inch disk of 3 MHz for the scattered energy as the function of scattered angle. The agreement is also excellent for the same reflector as a function of frequency when the scattered angle is 15° (Figure 8). The agreement between experiment and theory is also very good for a .245 circular reflector, as shown on Figure 9.

Flat Bottomed Holes in Aluminum Samples

Two different types of samples were used to study scattering from flat bottomed holes: (1) a flat circular disk with a 1/8 inch hole in it, prepared by Rockwell Science Center, and (2) curved cylindrical surface with 1/8, 1/4, and 1/2 inch flat bottomed holes. Both these samples are shown together on Figure 6. (Surface conditions may affect the data).

The frequency distribution of the scattered energy for the 250 mill flat bottomed hole in the curved sample is shown on Figure 10. The angle of incidence was 0 and the diffracted angle is 25° . The agreement is excellent. Figure 11 also shows excellent agreement for a 500 mill flat bottomed hole when the off axis angle is 12° .

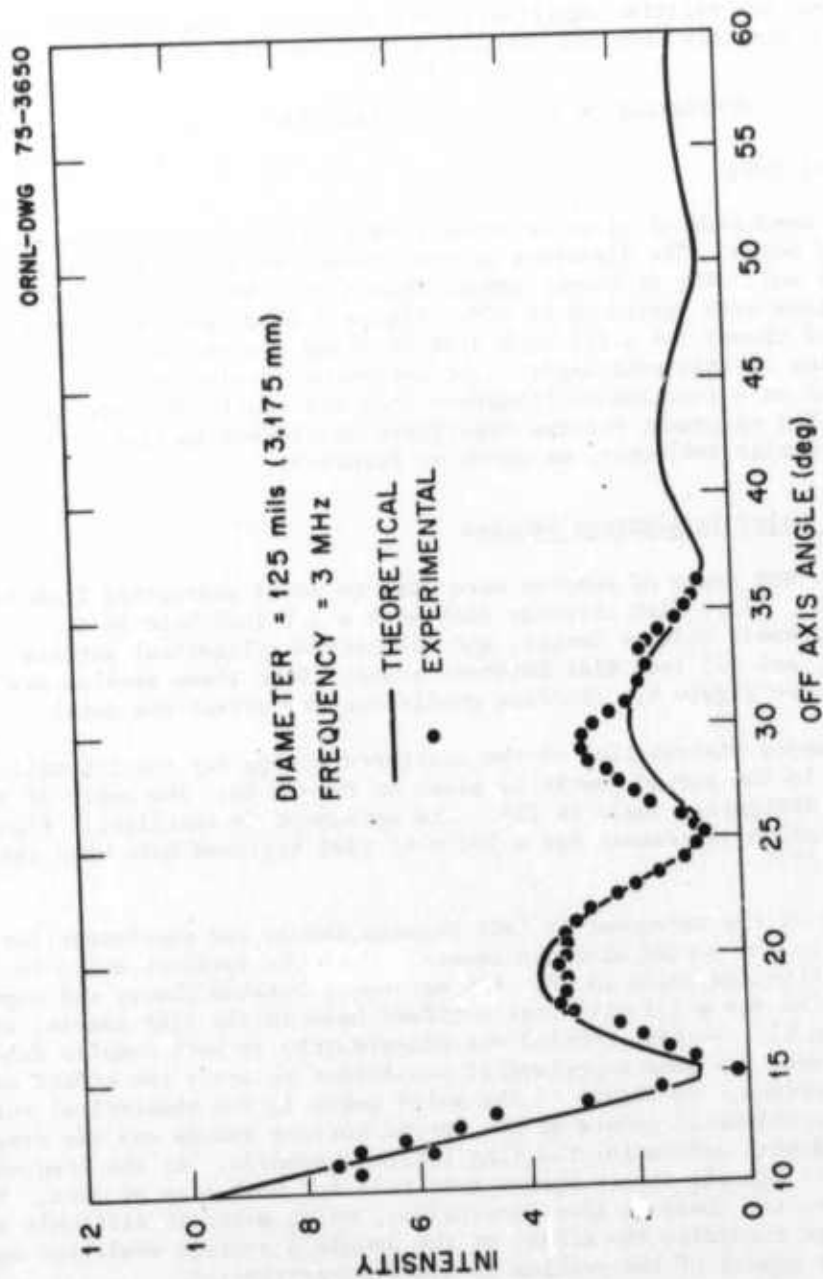
On Figure 12 the agreement is fair between theory and experiment for a 500 mill hole in the curved aluminum sample. Here the incident angle is 18° and the diffracted angle is 4° . The agreement between theory and experiment is good also for a 125 mill flat bottomed hole in the flat sample, as shown on Figure 13. We have carried out measurements in both samples (shown on Figure 6) under the same experimental conditions to study the effect of the sample's surface. On Figure 14 the solid curve is the theoretical curve, the dots are experimental points in the curved surface sample and the crosses are the experimental points for the flat bottomed samples. At the frequency region above 2.5 MHz the theory agrees very well for both sets of data. For the lower frequencies there is some uncertainty, which makes it difficult to draw conclusions regarding the effect of the sample's surface condition on the data. This aspect of the problem is under investigation.

Three-Dimensional Plots

We have programmed equation (2) to obtain three-dimensional plots to study some of the fine structures. Typical plots are amplitude-frequency-

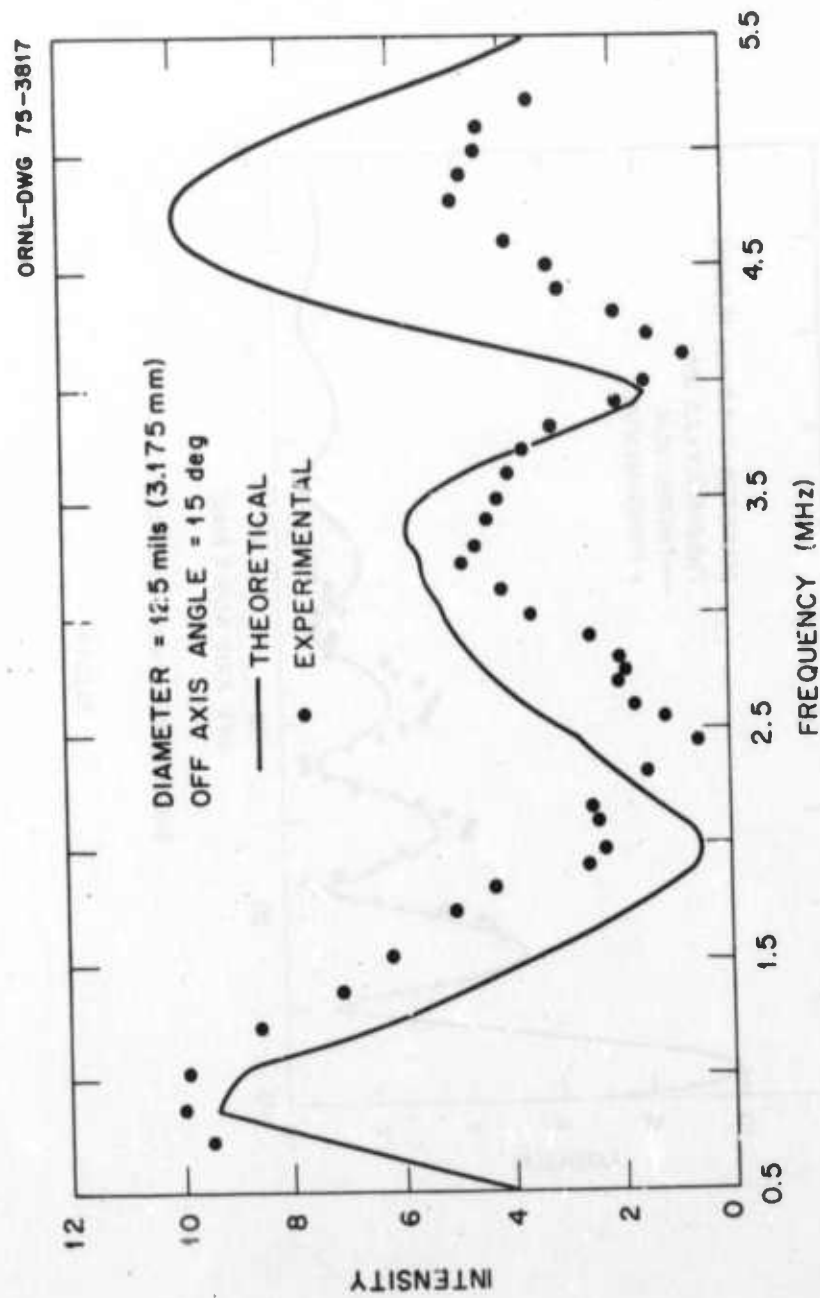


Science Center
Rockwell International



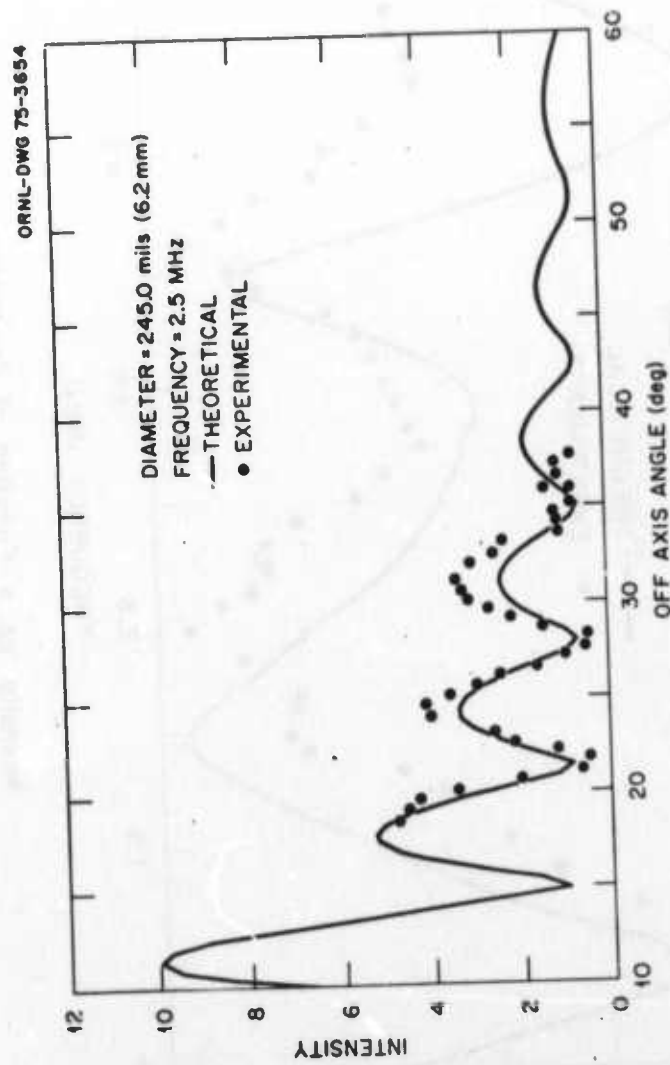
Intensity as a Function of Angle.

Figure 7



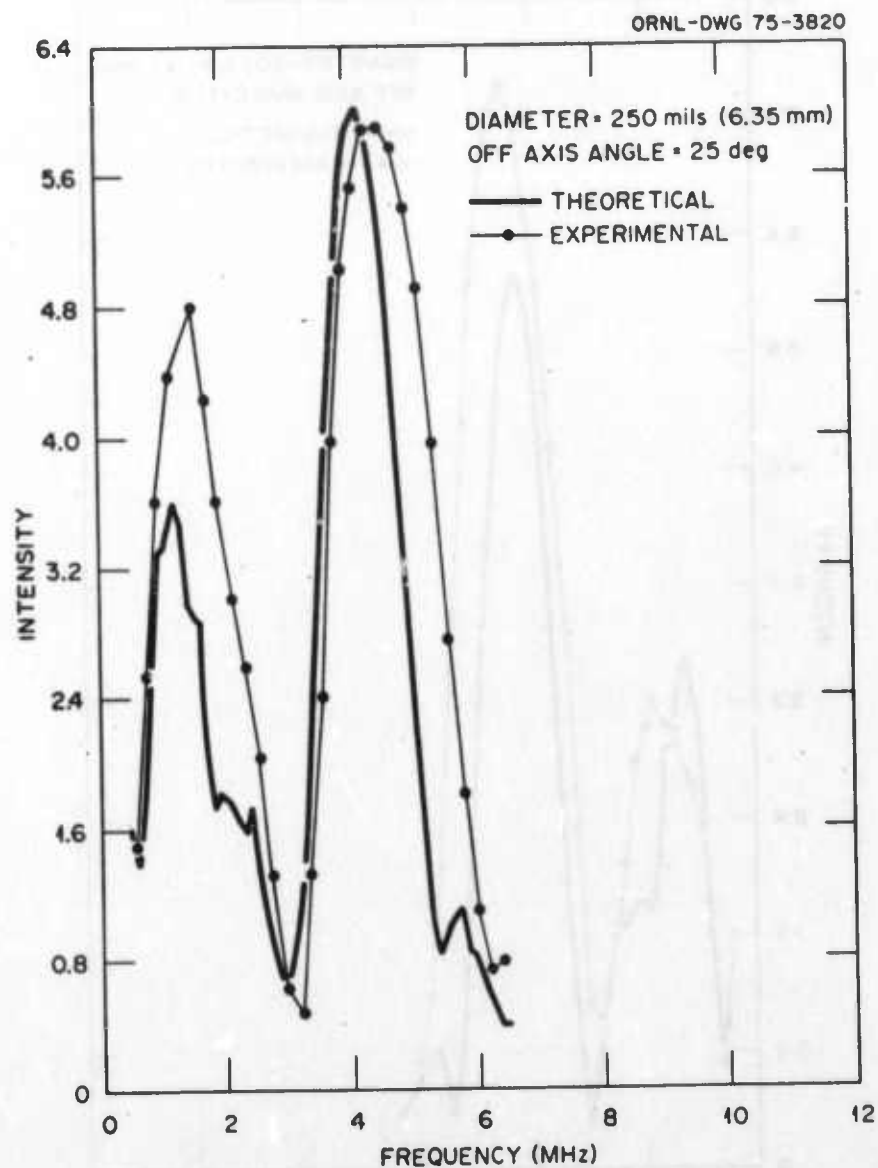
Intensity as a Function of Frequency.

Figure 8



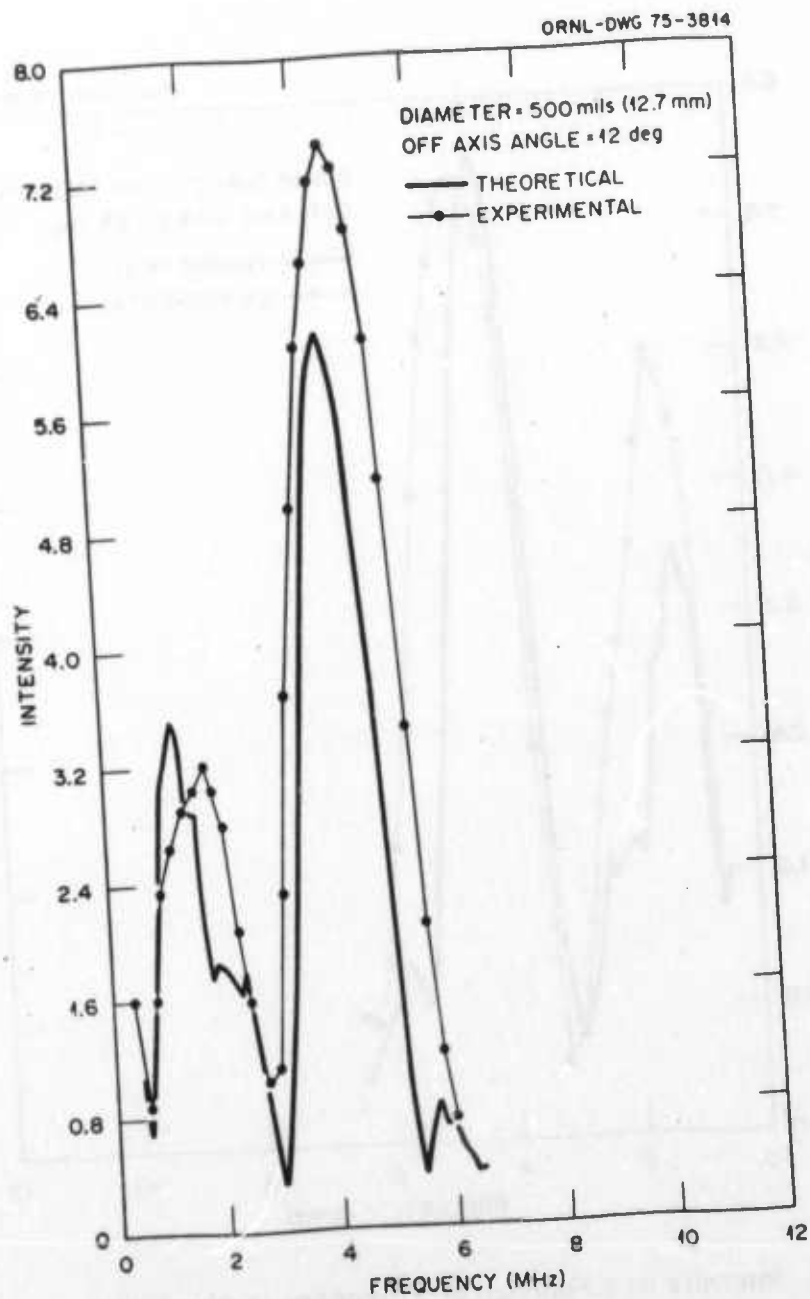
Intensity as a Function of Angle

Figure 9



Intensity as a Function of Frequency in Aluminum.

Figure 10



Intensity as a Function of Frequency in Aluminum.

Figure 11



Science Center
Rockwell International

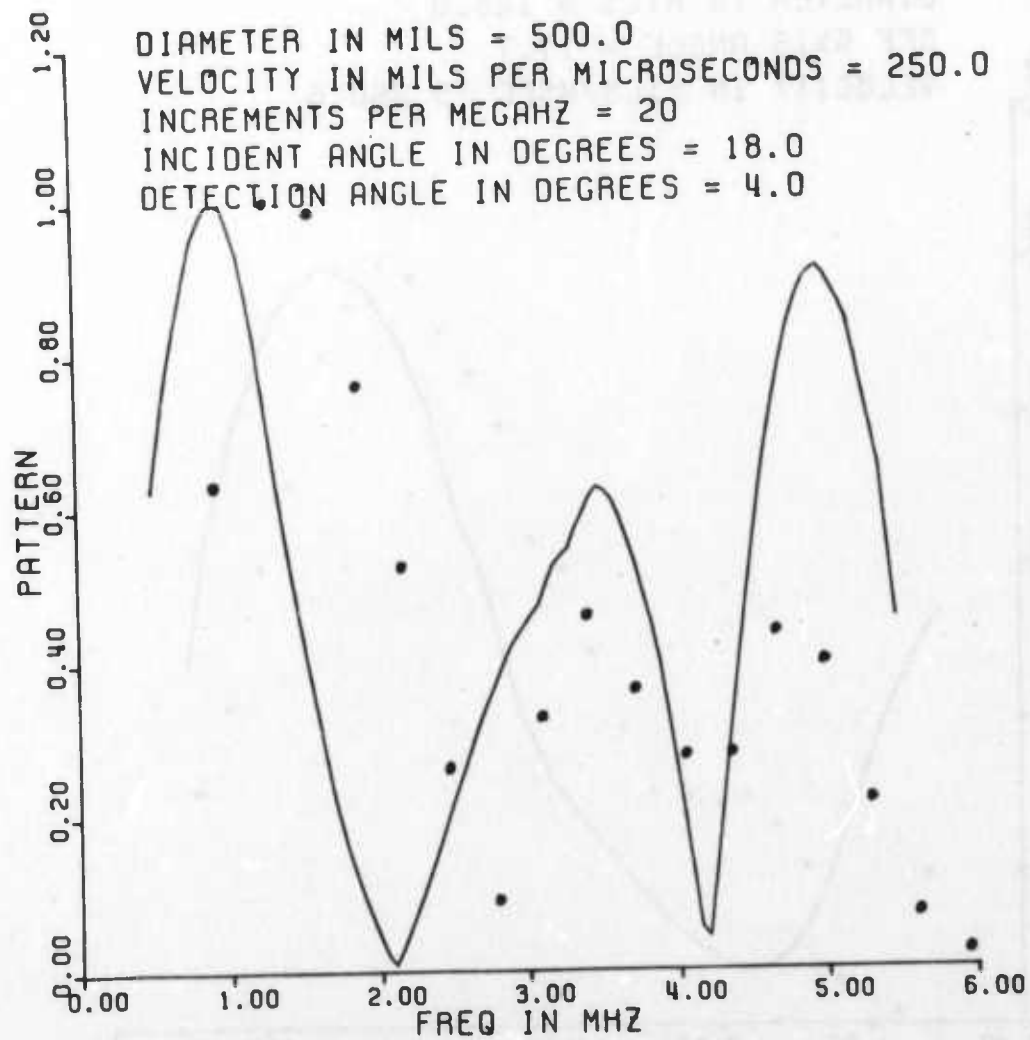


Figure 12. Curved aluminum sample.



Science Center
Rockwell International

PATTERN AS A FUNCTION OF FREQ

DIAMETER IN MILS = 125.0

OFF AXIS ANGLE = 17.7

VELOCITY IN MILS/MSEC IS 250.0

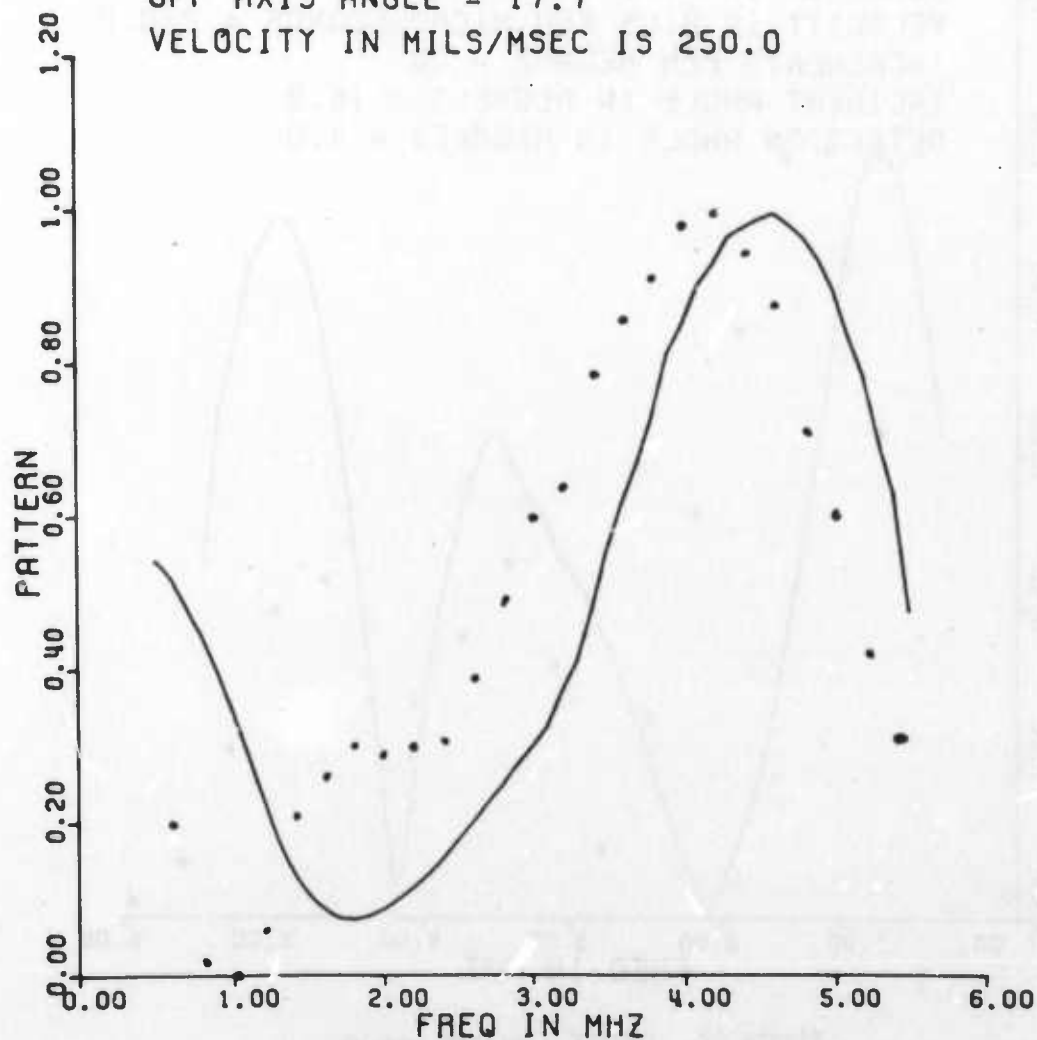


Figure 13. Flat aluminum sample.

PATTERN AS A FUNCTION OF FREQ

DIAMETER IN MILS = 125.0

OFF AXIS ANGLE = 27.1

VELOCITY IN MILS/MSEC IS 250.0

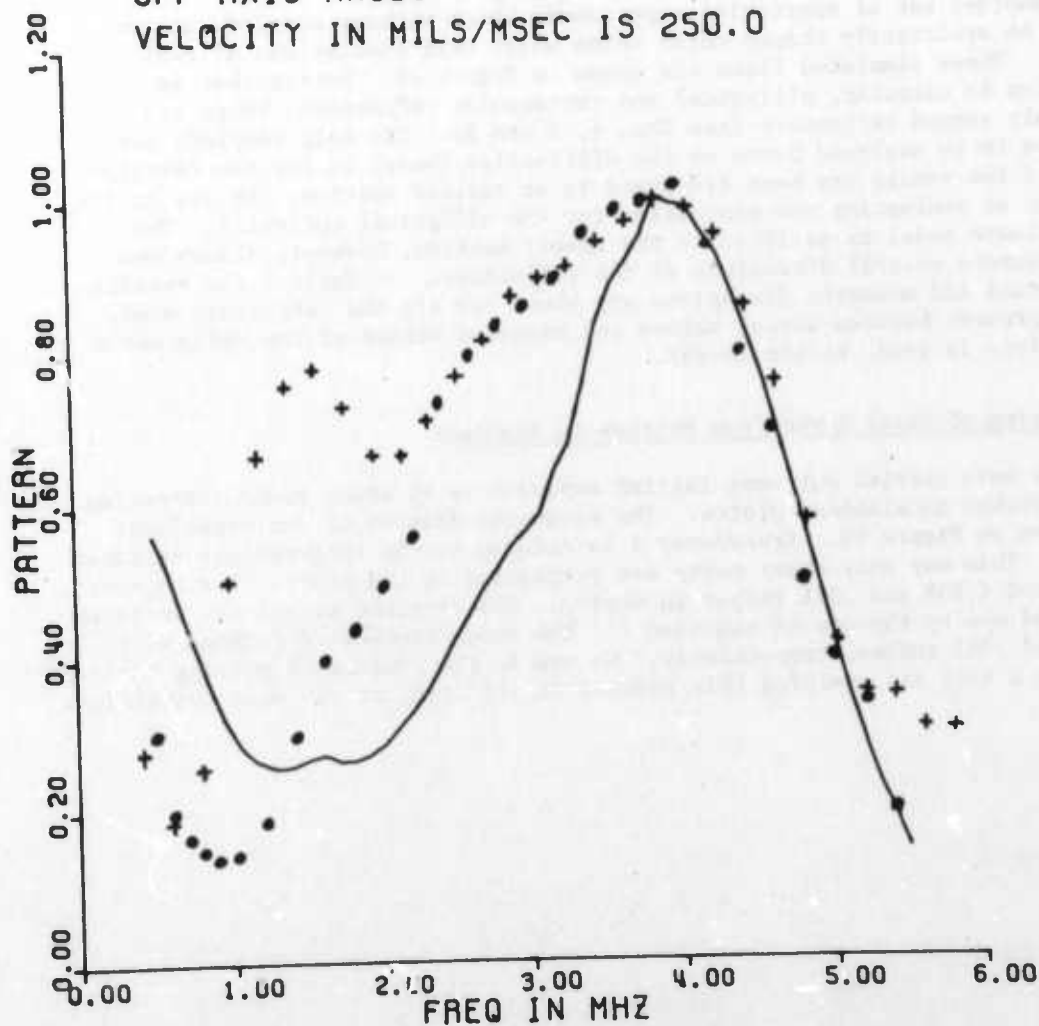


Figure 14. Comparison of effects of surface shape on spectrum. Dots for curved surface and crosses for flat surface.

scattered angle, Figure 15; amplitude-frequency-flaw size, Figure 16, and amplitude-frequency-distance between flaw and transducer, Figure 17.

Simulated Real Flaws

Another set of scattering experiments which we have carried out are those on arbitrarily shaped metal shims which were simulations of real flaws. These simulated flaws are shown on Figure 18. Notice that in addition to circular, elliptical and rectangular reflectors, there are randomly shaped reflectors (see Nos. 4, 5 and 8). The only complete set of data to be analyzed based on the diffraction theory is for the circular one and the result has been discussed in an earlier section. We are in the process of evaluating the expression for the elliptical reflector. The approximate model as outlined in the theory section, however, allows one to determine several dimensions of the reflectors. On Table 1 the results for actual and measured dimensions are shown for all the reflectors used. The agreement between actual values and measured values of the reflector's dimensions is good, within 10-15%.

Scattering of Shear Waves from Notches in Aluminum

We have carried out some initial experiments to study sound scattering from notches in aluminum plates. The schematic diagram of the experiment is shown on Figure 19. Transducer 1 is rotated to the longitudinal critical angle. This way only shear waves are propagated in the plate. Two notches were used (.058 and .091 inches in depth). The received signal was spectrum analyzed and by the use of equation (4) the notch sizes were determined to be .061 and .082 inches, respectively. We are in the process of solving equation (1) for a slit and applying this problem to the study of the mode conversion.



Science Center
Rockwell International

X IS FREQ FROM 0.5 TO 5.5 MHZ
Y IS OFF AXIS ANGLE FROM 10.0 TO 40.0 DEGREES
DIAMETER IN MILS = 245.0
VELOCITY IN 10⁶ MILS/SEC IS 57.1
FIGURE IS ROTATED FROM XZ PLANE BY - 300.0 DEGREES
FROM XY PLANE BY - 60.0 DEGREES

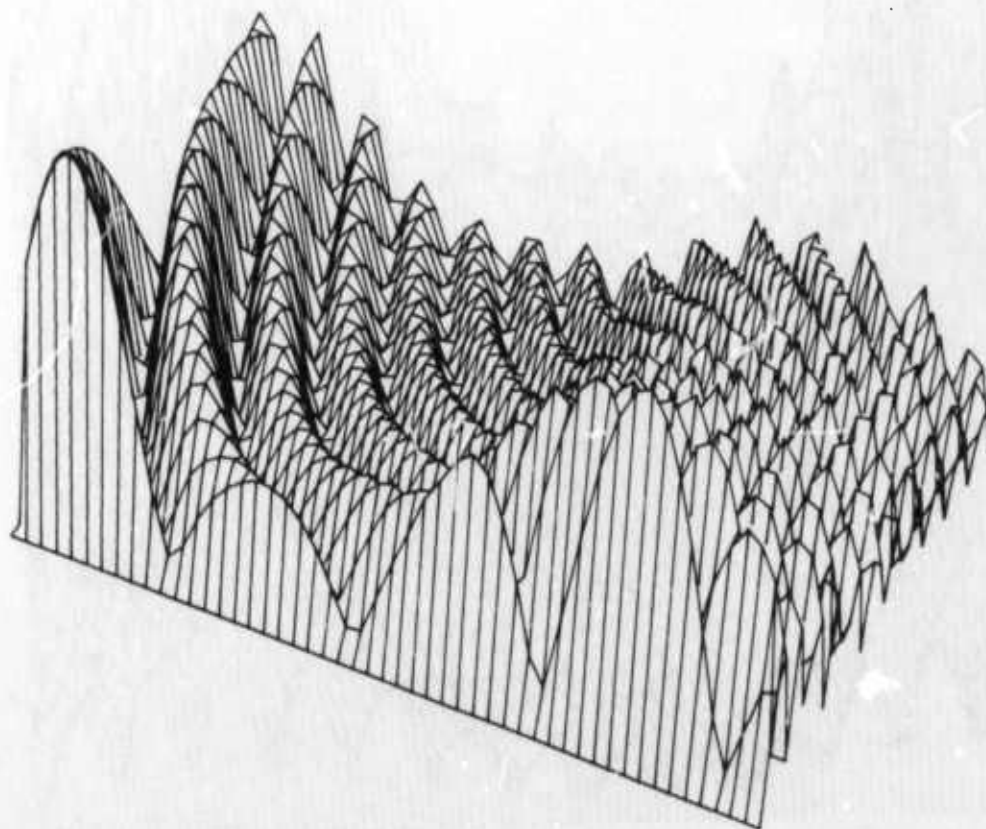


Figure 15. 3D plot, amplitude-frequency-angle.



Science Center
Rockwell International

X IS FREQ FROM 0.5 TO 5.5 MHZ

VELOCITY IN 10° MILS/SEC IS 57.1

FIGURE IS ROTATED FROM XZ PLANE BY - 270.0 DEGREES
FROM XY PLANE BY - 60.0 DEGREES

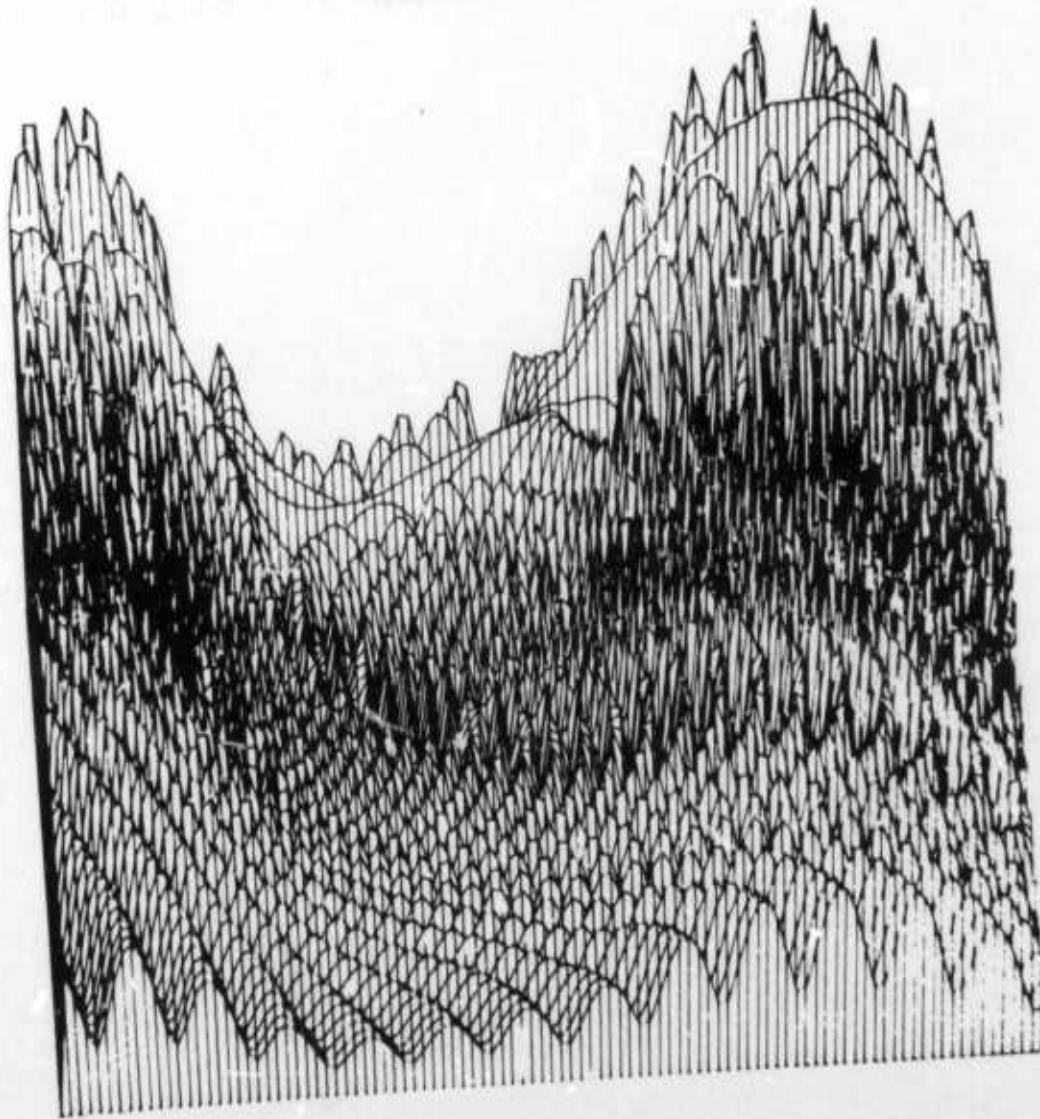


Figure 16. 3D plot. amplitude-frequency-flaw size.

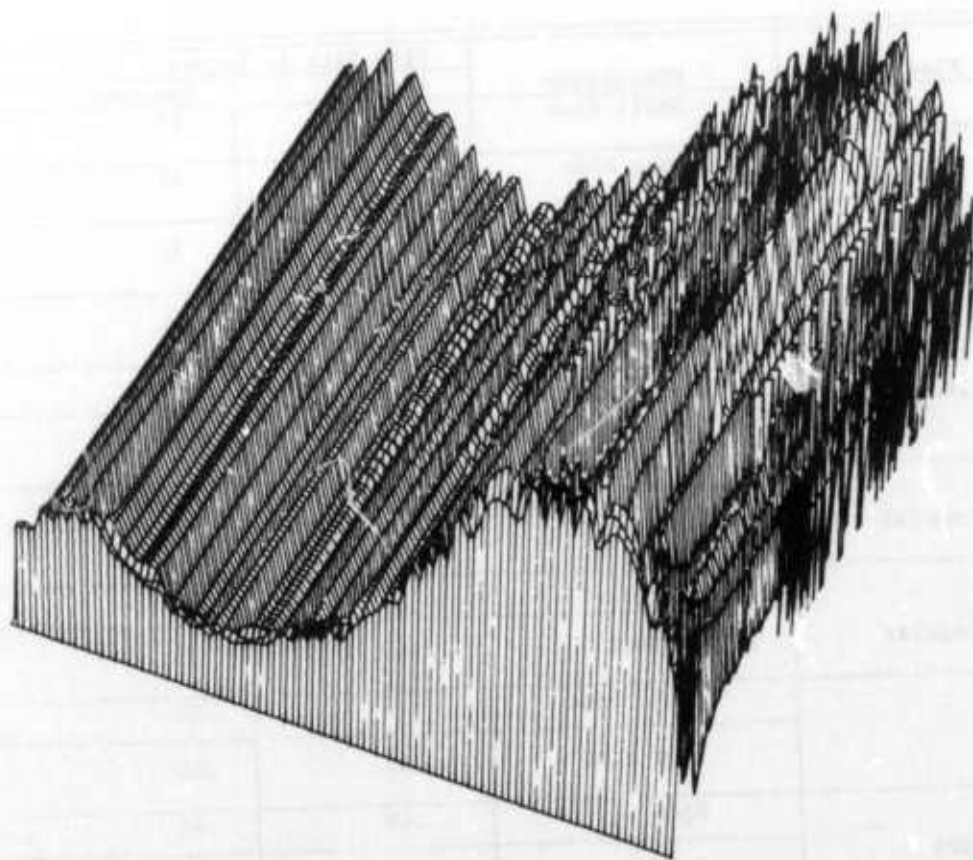


Figure 17. 3D plot, amplitude-frequency-distance.

TABLE 1
COMPARISON OF ACTUAL AND MEASURED SIZES FOR
SIMULATED "REAL FLAWS"

Flaw Type	Dimensions	Flaw Size in Inches	
		Actual	Measured
1. Rectangular	Small Side	.25	.23
	Long Side	.43	.48
2. Ellipse	Small Diameter	.2	.25
	Long Diameter	.55	.53
3. Ellipse	Small Diameter	.46	.41
	Long Diameter	.85	.75
4. Irregular	Smallest	.26	.29
	Largest	.81	.74
5. Irregular	Smallest	.23	.23
	Largest	.29	.26
6. Irregular	Small Side	.19	.29
	Long Side	.63	.60
7. Square	Side	.48	.45
	Smaller	.42	.37
8. Irregular	Smaller	.42	.37
	Largest	.69	.62
9. Circle	Diameter	.52	.53

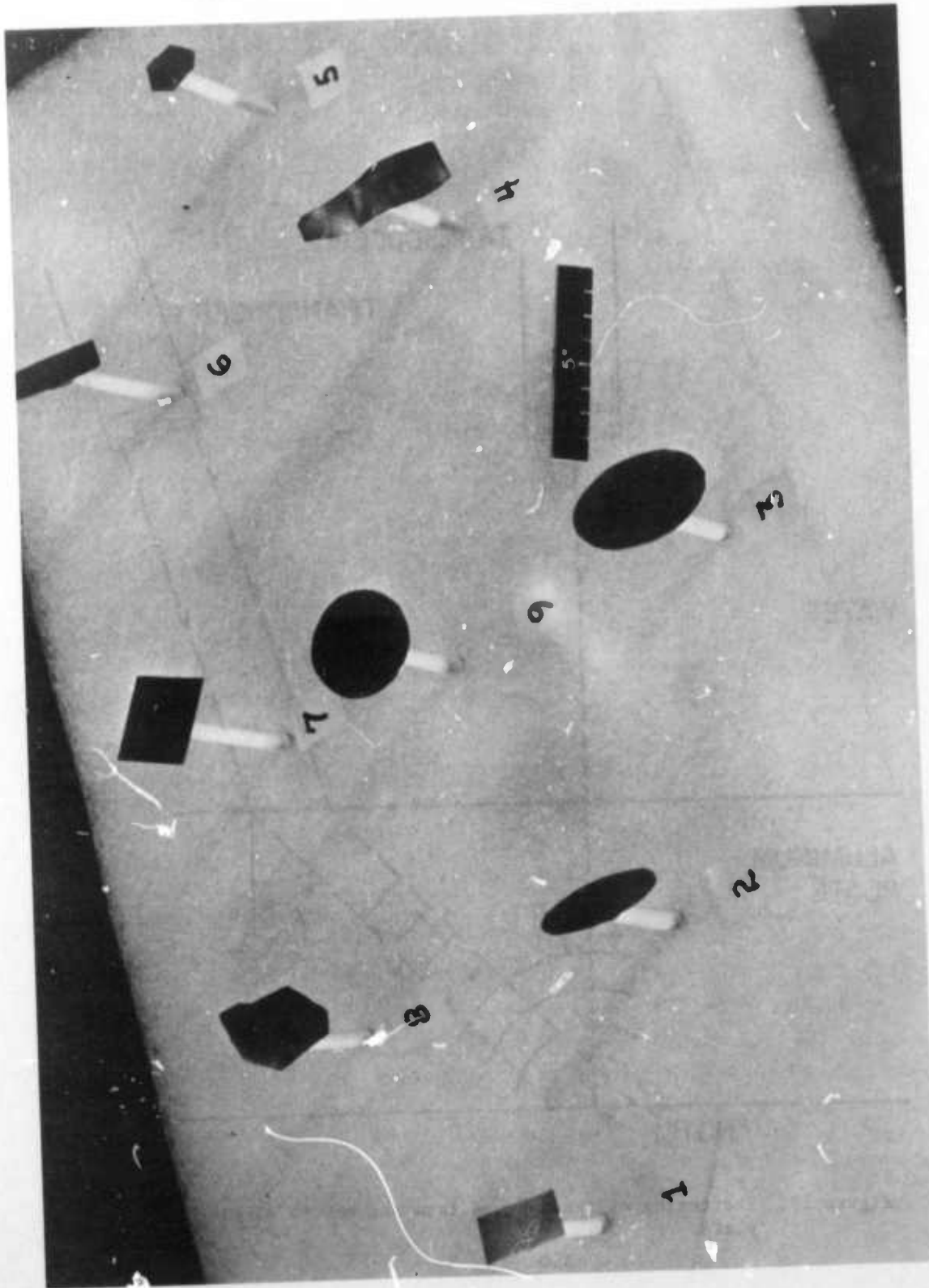


Figure 18. Simulated "real flaws."

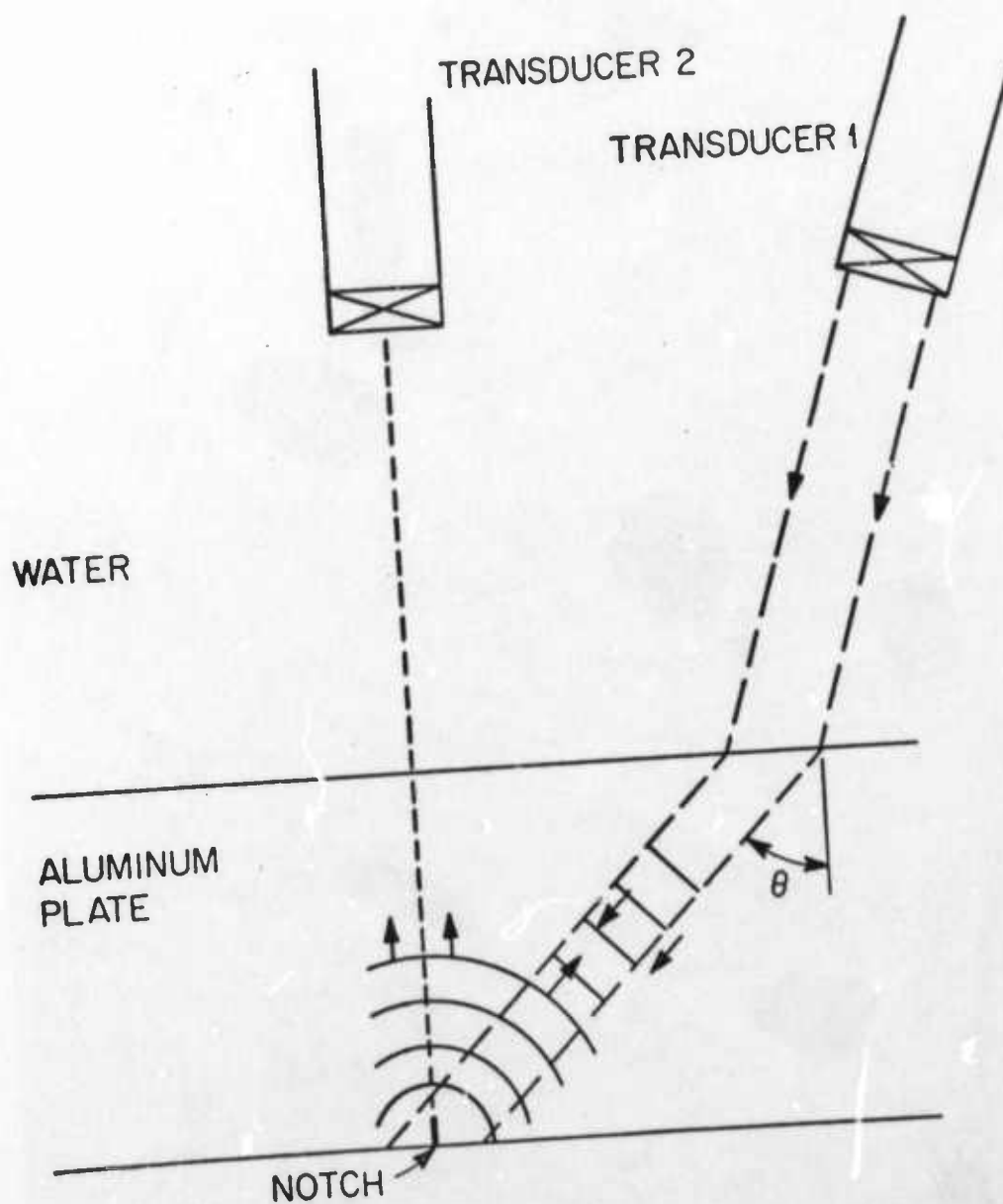


Figure 19. Scattering of shear waves from notches in aluminum plate.



APPENDIX

A study of the flat bottomed hole on axis is presently carried out at the Science Center using an expression derived by Ermolov based on Kirchhoff's approximation. Ermolov's expression is complementary to the expression we obtained from Keller's theory although Equation (2) blows up on the axis. Keller also derives¹ an expression which holds for near the axis and it is in the form of

$$U(P) = \frac{kA}{2r} \pi a^2 J_0(ka \sin \theta) \quad (J_0 \text{ is the zeroth order Bessel function}) \quad (5)$$

instead of Equation (2). Equation (5) holds only for small angles in the farfield. At the same time, Ermolov's⁴ expression is in the form:

$$U = 4A_0 e^{-\delta R} \frac{\beta}{\alpha} \sin^2 \frac{\alpha}{2} \left[1 - \alpha\beta + \beta^2 \left(\frac{\alpha^2}{2} - \frac{\alpha}{3} \operatorname{ctg} \frac{\alpha}{2} + \frac{\alpha^2}{12 \sin^2 \alpha/2} + \dots \right) \right] \quad (6)$$

where $\alpha = \frac{ka^2}{2R}$, $\beta = \frac{kb^2}{2R}$, a is the radius of the disk, b is the radius of the transducer, and R is the distance between the transducer and the disk. For $R \gg ka^2$, U is proportional to a^2 from Equation (6). At the same time, for the on axis case, i.e., $\theta = 0$, the same relationship is obtained from Equation (5).

References

1. J. B. Keller, Journ. of Applied Physics 28, 426 (1957).
2. J. B. Keller, R. M. Lewis, and B. D. Seakler, Journal of Applied Physics 28, 571 (1957).
3. Laszlo Adler and H. L. Whaley, Journal of Acoustical Society of America 51, 61 (1972).
4. I. N. Ermolov, Soviet Physics - Acoustics 5, 248 (1959).

PROJECT I, UNIT III, TASK 2

DEFECT CHARACTERIZATION BY SPATIAL DISTRIBUTION
OF ULTRASONIC SCATTERED ENERGYP. F. Packman and E. J. Coyne
Vanderbilt UniversityIntroduction

The ultrasonic pulse echo technique is a highly sensitive nondestructive method for detecting small defects within the bulk of a structure. The technique is capable of reliably finding small volumetric defects when the defect size is approximately 0.030 inches in diameter and the specimen thicknesses are not too great. If the distance between the transducer and the defect is large, greater than 2 near field distances, the minimum value of volumetric flaw sizes that can be reliably detected rises considerably. For 6-8" thick plates, it is not too surprising to occasionally miss volumetric defects such as slag inclusions of considerable length.

If the defects are planar in nature, and tightly closed such as fatigue cracks, the sensitivity of the ultrasonic technique is such that flaws smaller than 0.10 inches long by 0.050 deep cannot be detected to high degree of probability. Table I lists some of the currently available reliability data on flaw detection of fatigue cracks by production UT methods.(-6)

There are several reasons for this drop in sensitivity for tight cracks. These can be summarized as follows:

1. The tightness of the crack does not reflect as much ultrasonic energy as a volumetric defect of the same apparent projected area.(7)
2. Adjacent portions of the crack faces are in contact with each other, transmitting portions of the impinging ultrasonic energy.(8)
3. The surface roughness of the crack, particularly the fatigue striations and angularity changes due to crossing metallurgical boundaries, disperse some of the initial energy.(9)
4. Plastic deformation associated with the stress field surrounding the crack may diffuse the initial energy.
5. The gross orientation of the crack plane may not be directly perpendicular to the initial pulse wave, and curvature of the crack faces may reflect a portion of the energy back to other portions of the specimen.(10)



SC595.10AR

TABLE 1
ULTRASONIC FATIGUE CRACK DETECTION DATA

Technique/Matl'l	Flaw Size Length & Depth inches	Prob of Detection %	Confidence Level %	Reference
Ultrasonics 2219-T87 0.2" or 0.36"	.186 x .038	90%	95%	(1)
Ultrasonics Shear Wave 2219-T87	.07 .18	90% 95%	95% (set 2) 95% (set 2)	(2)
	.07 .10	90% 95%	95% (set 3) 95% (set 3)	(2)
	.125 .33	90% 95%	95% (set 2) 95% (set 2)	(2)
	.80 .15	90% 95%	95% (set 1) 95% (set 1)	(2)
Shear Wave 7075-T6511	.25	90%		(3)
4340 V Mod.	.20	90%		(3)
Ultrasonic Surface Wave 2219-T87	.20	90%	preproof	(4)
Ultrasonic Shear 5A1-2.5Sn Titanium 0.125" Thick	.09 .03	99% 50%		(5) (5)
Ultrasonic Shear 5A1-2.5Sn Titanium 0.5" Thick	0.07 0.05 0.07	99% 97% 50%		(5) (5) (5)
Ultrasonic Shear 2219 Al 0.50" Thick	.28 .05	99% 50%		(5) (5)
0.02" Thick	.05	99%		(5)
Delta Scan D6AC	.150	90%	induced flaws	(6)
Duplex inspection	.030-075.	90%	95%	(6)



Science Center
Rockwell International

The problem of determining the degree of criticality of the flaw size, shape and orientation is very difficult.(11) Few studies have been conducted on the measurement of the size of small defects by UT. For the case of defects whose size is considerably larger than the diameter of the transducer, several techniques are available. (12), (13), (14) These include the AVG diagrams developed by Krautkramer (15) and the position scanning methods developed by Giacomo, Crisci and Goldspiel.(16) Both techniques are relatively accurate for larger defects. The Giacomo technique uses the motion of the transducer to determine the size of the defect. The transducer is moved slowly across the defect until the reflected signal reaches some lower threshold edge, passes through a maximum and diminishes as it passes beyond the crack plane. Geometric analysis of the diverging ray pattern emanating from the transducer is used to estimate the size of the flaw. In almost all cases the ultrasonic signal analysis underestimates the size of the flaw. These underestimates are attributed to 1) tightness of the flaw, 2) multiple reflections from the rough surfaces of the crack and 3) diffraction effects.(16)

The AVG diagram introduced in 1959, (15) relates the distance of the flaw from the probe (A), the amplification of the signal (V) in db and the equivalent reflector diameter (G). A reference graph is drawn for a transducer by plotting the amplitude in db from a series of flaw disc shaped reflectors as a function of the distance of the reflector disc to the transducer probe in a water bath immersion system. The ultrasonic attenuation of the water is then subtracted out and typical graphs show the reflection conditions without the immersion attenuation. The backwall echo shows that the reflection of large defects becomes nearly linear with the distance when in the far field of the transducer (approximately three field distances). The radiation laws for small reflectors show decreases more nearly proportional to $1/\text{distance}^2$.

Measurements of the equivalent area of the flaw by consideration of reflected amplitude gives information about the possible minimum dimensional values and not about the actual dimension of the flaw. It is apparent that flaws of different geometric configuration can produce the same maximum reflection height, and hence appear to the ultrasonic beam to be the same equivalent area. Excentric elliptical-crack like defects and circular flaw defects of the same area are two typical examples.

The amount of information about the revealed flaw can be substantially increased by considering two aspects of the reflected signal, namely the frequency content and the indicatrix of scattering.

Considerable information is available on the use of frequency analysis of ultrasonics as a tool for the characterization of defects.(17,18) In this type of analysis the frequency content of the ultrasonic pulse is examined, and found to change with shape of the defect. This technique was initially proposed by Gericke.

The use of the indicatrix or indicia as a method of determining information about the shape of the flaw was initially proposed by Gurvich and

Shchukin(19) and further developed by Gurvich and Yermelov(2) The indicia is defined as the standardized function which describes the field of the ultrasonic waves reflected by the defect to the receiver. Thus the indicia measures the totality of reflected energy from a defect associated with the scattering of the ultrasonic waves from a transmitter, as picked up by a receiver when both transmitter and receiver are moving in a prescribed path.

A typical example of an indicia is shown in Figure 1. Here the magnitude of reflected energy I_r is shown as a function of the position of the transmitter/receiver. The particular signal recorded is that found within a gated position selected previously by considering the reflections from a known defective sample. As the transducer scans across the specimen the reflected energy slowly rises from zero to a maximum and decreases. This scan is of a 0.5" diameter straight shank drilled and reamed hole. If there is a crack growing out of the drilled hole, the ultrasonic waves are perturbed by the additional reflections associated with the crack as well as the original reflections associated with the straight shank hole. Hence, the indicia associated with the ultrasonic scan of the hole plus the crack will look typically as shown in Figure 2. Here the crack is located perpendicular to the scan direction.(21) Thus, the indicia gives information regarding the presence of the crack in the vicinity of the drilled hole.

The technique used by Gurvich and Yermolov measures the width of the indicia at a predetermined level and the skewness of the curves. Consequently the characteristic of the scattering does not precisely determine the shape of the flaw, but it becomes important to determine the known scattering from ideal reflectors such as spheres, spheroids and discs, etc.

Experimental Program

The purpose of the experimental program was to develop a series of indicia for scattering from known, well characterized defects imbedded in the interior of right circular cylinders. The specimens were prepared by Rockwell International as part of the ARPA/AFML interdisciplinary program on flaw characterization. The procedures and techniques used to measure and characterize the defect type, size and base material have been described elsewhere.(22)

Ultrasonic indicia were run for all specimens examined, as well as for 1, 2, 3, 4, and 5 sixtyfourths flat and conical bottom holes prepared in our laboratory from 6061 Aluminum. In all cases a 3/8 dia. 5 mh Automation SFZ ultrasonic transducer was used. The ultrasonic system was a Sperry UM 715 with a transigate H gate system. All scans were produced on a specially designed fixture. In this fixture the position can be recorded directly using a 10" slide wire position transducer and scanning speeds controlled with a variable speed screw drive mechanism for one axis. The other axis was indexed using a micrometer drive that is manually operated. The amplified DC signal from the transigate was fed into the Y axis of an X-Y recorder while the position signal was used as the X axis. At least two series were

FIGURE 1 TYPICAL ULTRASONIC SHEAR WAVE INDICIA
OF GOOD HOLE (0.5 DIA)

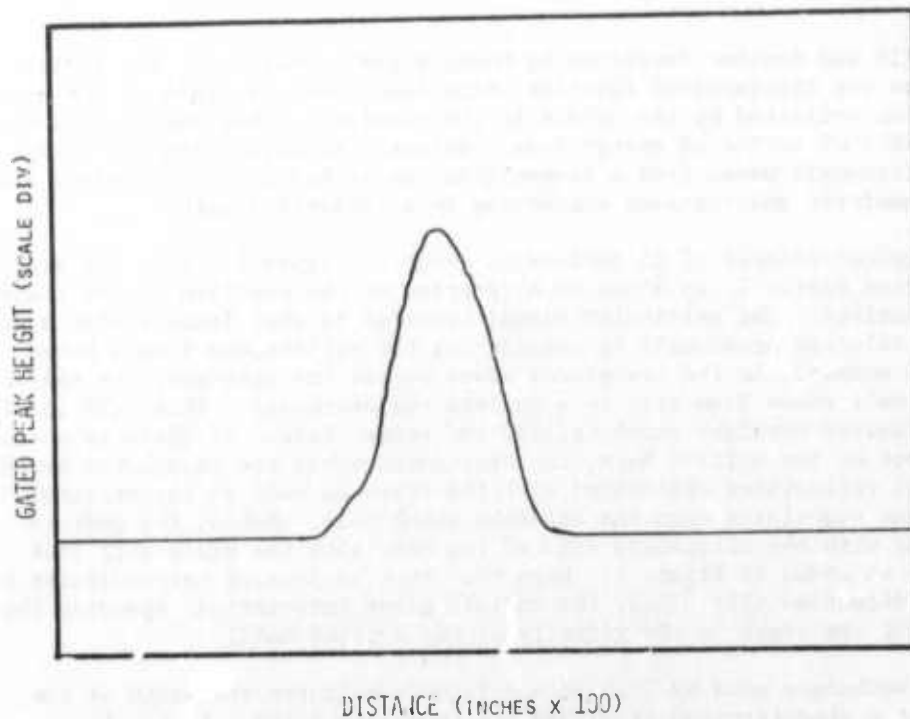
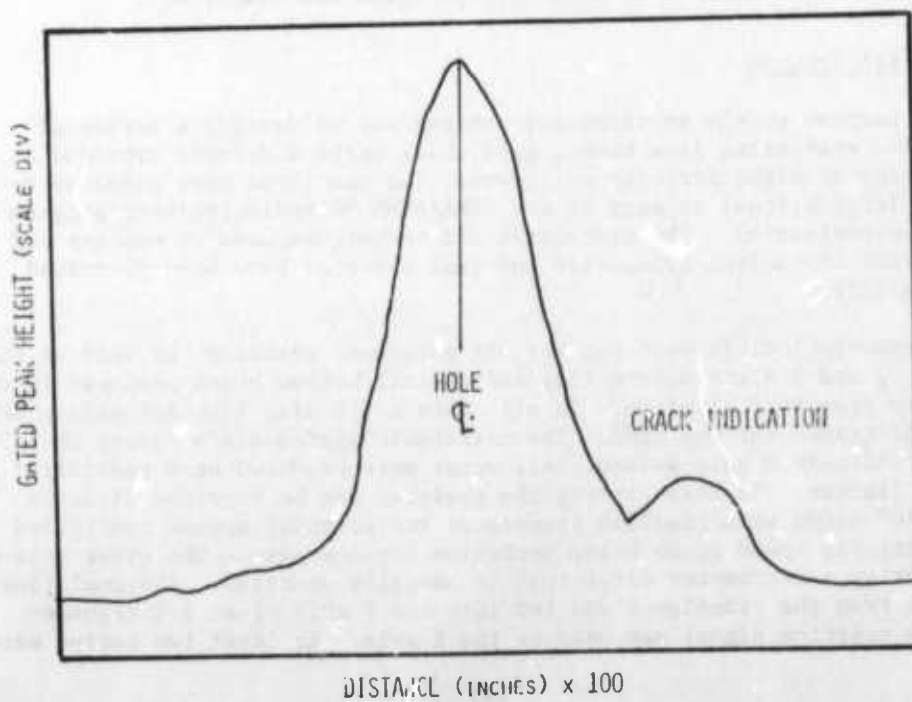


FIGURE 2 TYPICAL ULTRASONIC SHEAR WAVE INDICIA
OF HOLE WITH CRACK (0.5 DIA)





run for each specimen examined; 1) a low sensitivity position scan to obtain the general configuration for the indicia and 2) a high sensitivity position scan to obtain suitable indicia for subsequent digitizing for signal analysis.

The scanning unit also had provisions for micrometer movements in x, y and z directions. Typically the z position was set so that sufficient oil contact was maintained during a scan, and subsequently unchanged. A typical series of scans would be made by first indexing the x-y positions to obtain the supposedly largest reflected signal from the defect within the pre-selected gated position. Scans were then produced with the screw drive unit automatically moving the transducer in the y direction. When a trace was completed, hand step scanning was used in the x direction. Thus, a series of indicia could be developed from a trace that indicated no defect within the ultrasonic gate, pass through a maximum and then decrease as y varied, for each position. Typical indicia obtained are shown in Figure 3 and 4, for .025" x position changes.

Since both indicia were made using the same sensitivity for the y motion, and an equal .025 step position for the x position of the transducer, the difference in the indicia can be attributed only to the shape of the flaw. It thus appears that one specimen is not symmetrical about the vertical axis, since the number of indicia obtained is considerably smaller than that obtained on the second specimen. The apparent area of the defects are roughly the same, since the maximum peak heights of the (maximum indicia) are roughly the same. Hence, one must conclude that one defect shape is elliptical in nature and is elongated along the transverse scan axis. If both defects were circular, the scans would be roughly the same, and there would be approximately the same number of x traverses.

Experimental Results

The simplest method of describing the indicia is to consider the amplitude-distance pulse to be the equivalent of an amplitude-time pulse. (23) If this mechanical shock or impulse is applied to a linear system, and the response of the system to a unit impulse is known, the response of the system to the pulse in question can be estimated by the following:

$$X(t) = \int_{-\infty}^{+\infty} f(\tau)h(t-\tau) d\tau \quad (1)$$

where $X(t)$ is the response

$f(t)$ is the forcing function

$h(t-\tau)$ the unit impulse response of the system

t a dummy time variable

FIGURE 3 TYPICAL ULTRASONIC NORMAL WAVE INDICIA OF
IMBEDDED DEFECT. EACH SCAN IS STEP
INDEX OF 0.025 IN.

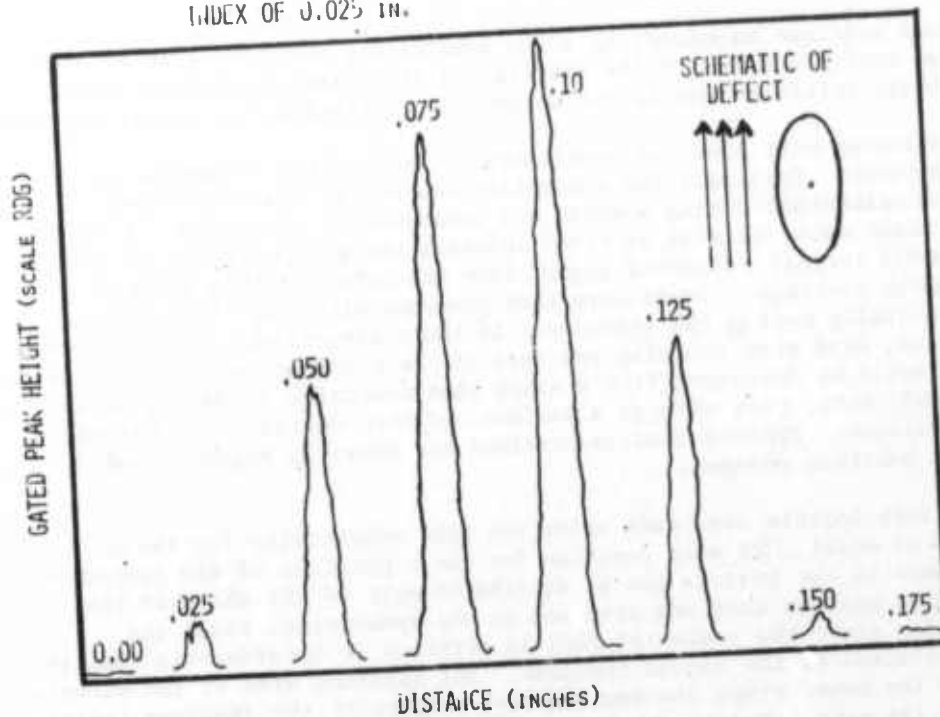
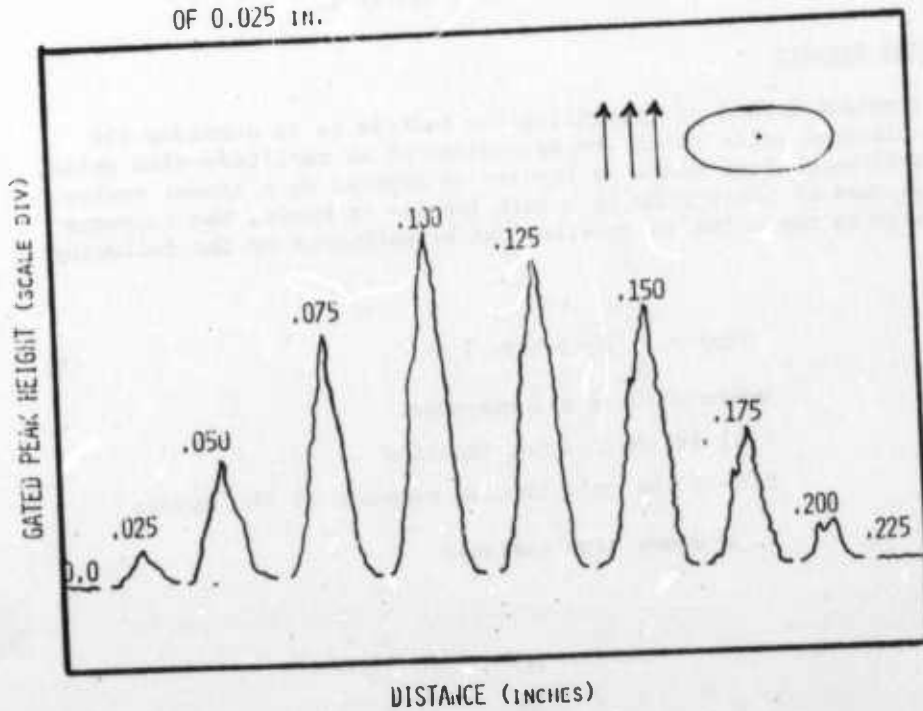


FIGURE 4 TYPICAL ULTRASONIC NORMAL WAVE INDICIA OF
IMBEDDED DEFECT. EACH SCAN IS STEP INDEX
OF 0.025 IN.



The integral involves the convolution of two complicated functions and the exact solution usually poses formidable difficulties. The analysis can be simplified by applying the Fourier Transform to the phenomena and describing the transformation in the frequency domain. It should be emphasized that with the Fourier transform analysis of the indicia, the impulse is space-like instead of time-like as with the more commonly accepted pulses.

The Fourier transform is defined as

$$A(f) = \int_{-\infty}^{+\infty} f(t)e^{-i2\pi ft} dt \quad (2)$$

with the additional requirement that $f(t)$ is finite. When $f(t)$ is a shock or indicia the latter requirement is automatically satisfied since at $t = 0$, and $t-f$, $f(t) = 0$.

If the driving function is given by a short duration square pulse of duration T , and amplitude A , shown in Figure 5, the Fourier spectrum of the rectangular pulse is given by:

$$A(f) = AT \frac{\sin \pi ft}{\pi ft} \quad (3)$$

This is shown in Figure 6. Thus, it appears that driving functions that are Dirac in nature, transform into a series of loops whose frequency between nodes (zeros) is inversely proportional to the width of the pulse T . Similar results can be obtained for sinusoidal driving pulses and triangular pulses. (23)

Since the observed indicia are all pulse-like in nature, an analysis was made to determine the Fourier spectrum of the indicia. A typical Fourier spectrum of an indicia is shown in Figure 7. For some indicia it was found that the nodes did not necessarily pass through zero, but had minimum which could be associated with the width of the pulse. This means that in contrast to the Dirac or Square pulse which is missing energy at certain frequencies, these pulses contained energy in these positions.

A plot could then be made of the "order of the node" vs. the frequency at which the node passed through zero, or through a minimum. For most of the specimens examined this resulted in a straight line, indicating that the general shape of the indicia was that of a space-like pulse, whose shape could be described in terms of some idealized width related to the equivalent width that the ultrasonic probe believes the defect to be.

Since the actual width of the defect is known and the number of passes needed in the step scanning system is also known, the width of the largest peak indicia can be taken to correspond to the transducer scanning the defect at its widest point. Hence, a graph of the slope of the node order-frequency

FIGURE 5 SQUARE PULSE FOR DRIVING FUNCTION FOR
IMPULSE ANALYSIS

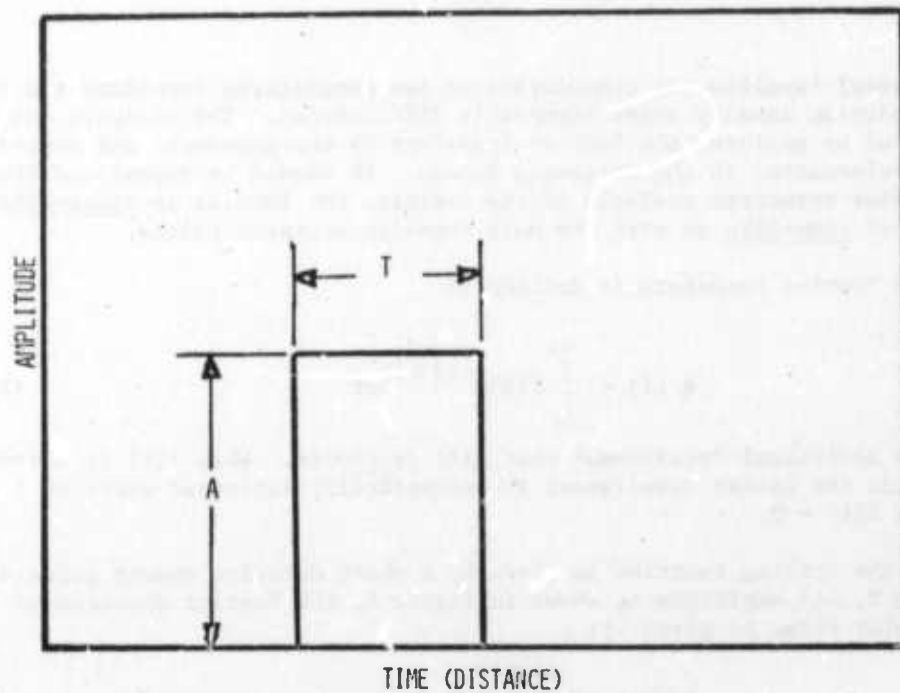
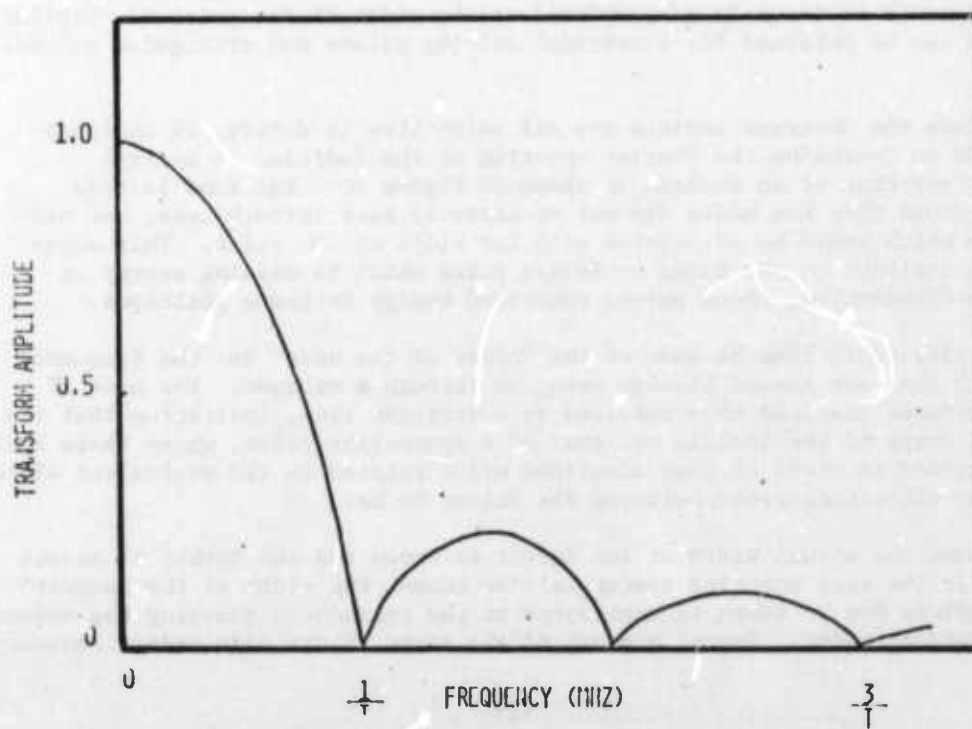


FIGURE 6 FOURIER SPECTRA FOR PULSE SHOWN IN
FIGURE 5



plot could be determined as a function of the known maximum width of the series of defects. This is shown in Figure 8. Using a least squares fit, a straight line has been drawn through the experimental points.

The analysis of an unknown defect would then proceed as follows: 1) the maximum indicia height pulse would be transformed into frequency space. The position of the nodes would be determined, and the slope of the order-frequency plot determined for this unknown. Entering Figure 8 the width of the unknown could then be determined. If a series of scans are made for an unknown, and the position of the Y axis known, then the value of the ultrasonic indication of the width of the specimen could be determined at each scan position. The first and last indicia are essentially straight lines, of Figure 3 and 4, (when the probe field no longer interacts with the defect). Hence, the maximum of the indicia for each scan in the step variable X positions of the scan unit could also be considered as an indicia of the scan in the X direction. This is reasonable for if the scan were made in a direction 90° to the original scan, the value of the ultrasonic width of the defect could be determined in a more straight forward manner by examining Figure 8.

Following this reasoning, one can reconstruct the shape of the defect from the analysis of the indicia. The reconstruction of typical spherical defect, specimens N, O and P are shown in Figure 9. The major problem with these results appear to be that the inherent scatter in the slope curve, Figure 8 results in uncertainties in the ultrasonic width and hence, the exact shape of the defect. It would be difficult to determine if the defect were truly ellipsoidal in shape or circular.

This method of measuring the shape of the defect depends strongly on the shape of the pattern of the lobes of the pressure pattern generated by the transducer. It has been observed that if the transducer is rotated slightly, the pressure pattern of the transducer changes and can influence the shape of the indicia; hence, the analysis of the size of the defect. The process must be repeated for each transducer.

A more direct method of determining the shape of the defect can be made following Gurvich and Shchukin and Gurvich and Yermolov. (19,20) These authors give an impression for the shape of the indicia when the probe sonic axis and the scattering axis of the defect (assumed to be spherical or disc like) are aligned during the scan. The standardized function for the envelope sequence of echo signals or the shape of the maximum indicia is given by:

$$F(x) = \phi_0 \left(\arctg \frac{X_1}{H} \right) \cos^2 \left[\frac{\pi}{5\phi_0} \left(\arctg \left| \frac{X_1}{H} - \alpha_0 \right| \right) \right] x$$

$$\phi_0 \left(\arctg \frac{X_1}{H} \right) \cos^2 \left[\frac{\pi}{5\phi_0} \left(\arctg \frac{X_1}{H} - \alpha_0 \right) (X_1^2 + H^2)^{-n/2} \exp \left[-2\delta (X_1^2 + H^2)^{1/2} \right] \right] \quad (4)$$

FIGURE 7 TYPICAL POWLR SPECTRA OF DEFECT INDICIA

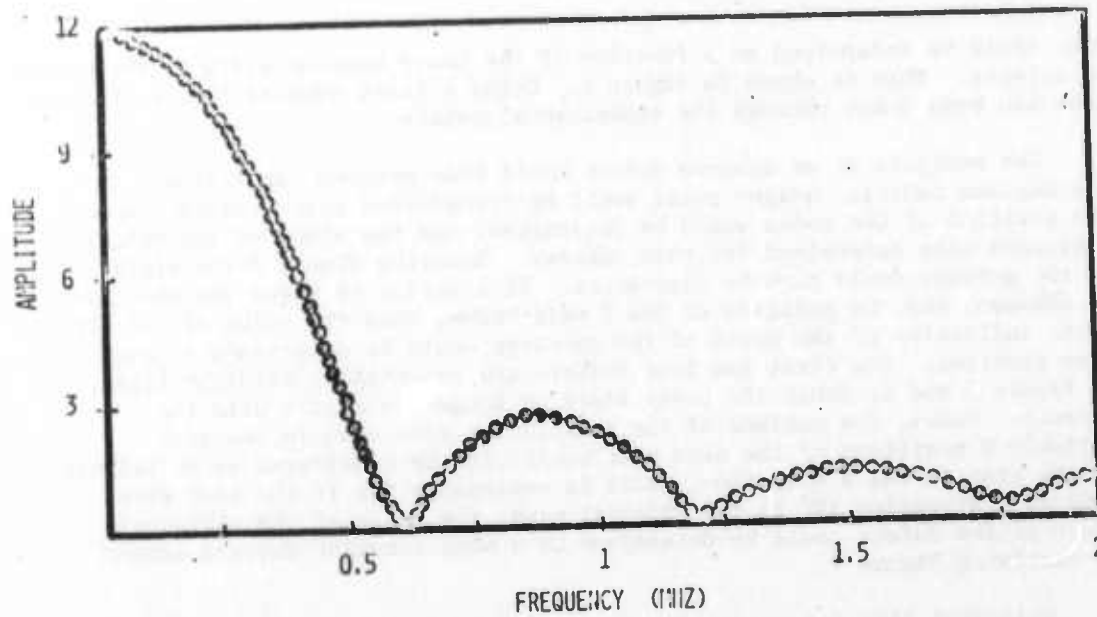


FIGURE 8 SLOPE OF FRINGE ORDER VS FREQUENCY PLOT
(H) VS ACTUAL DEFECT WIDTH

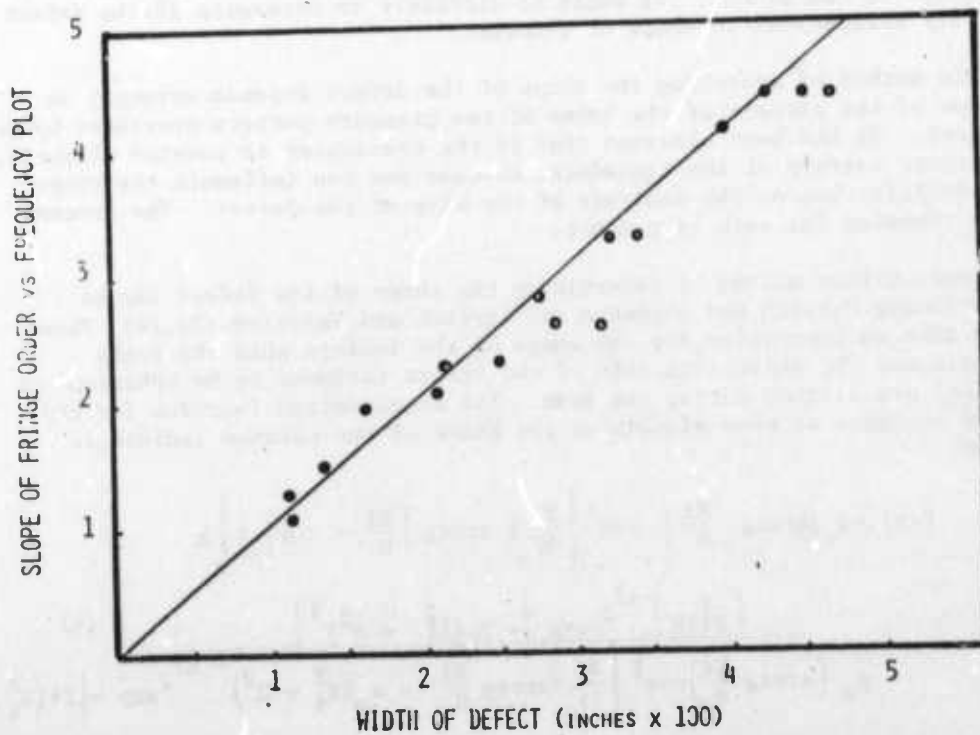


FIGURE 9 PLOT OF ULTRASONIC INDICIA DEFECT SHAPE
(RH. SIDE) vs ACTUAL DEFECT SHAPE (LH. SIDE)

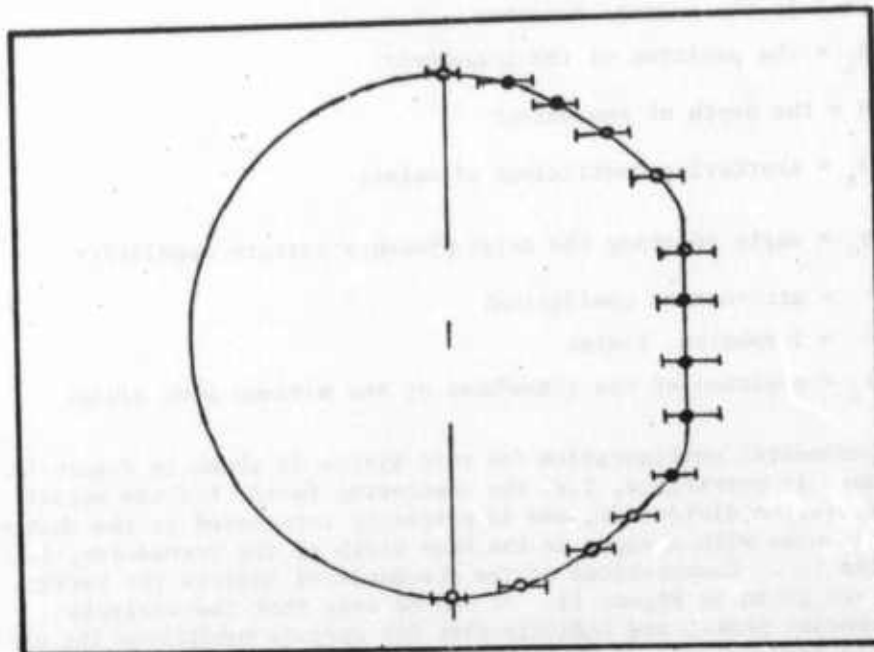
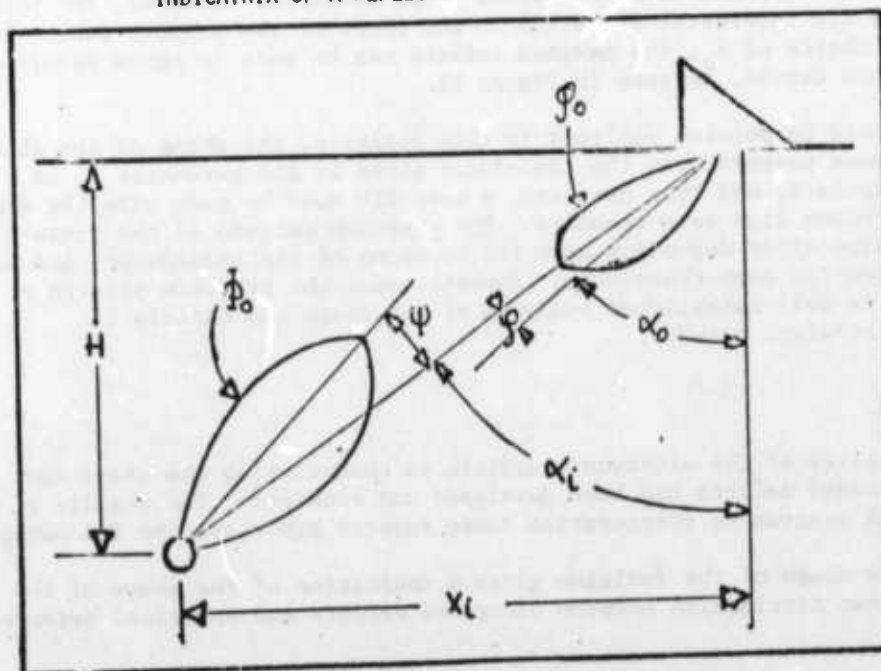


FIGURE 10 SCHEMATIC FOR CALCULATING SCATTERING
INDICATRIX OF A REFLECTOR



Where $f(x)$ is the indicia function

X_1 = the position of the transducer

H = the depth of the defect

ϕ_0 = scattering coefficient of defect

ϕ_0 = angle relating the major pressure pattern angularity

δ = attenuation coefficient

n = 2-spheres, 1-disc

X_1 = position of the transducer at the maximum echo signal

The experimental configuration for this system is shown in Figure 10. Since the shape is normalized, i.e. the scattering factor for the actual defect configuration divide out, one is primarily interested in the changes of shape that occur with changes in the beam width of the transducer, i.e. changes in the ϕ_0 . Computations of the standardized indicia for various values of ϕ_0 are given in Figure 11. It can be seen that the analysis predicts secondary peaks, and indicate that for certain conditions the ultrasonic signals should drop and rise again with further motion of the transducer. This has been observed with 45° shear wave transducers (21) and is due to the formation of multiple reflections from the defect with the gated position as the transducer moves over a large distance. However, for this analysis we are interested primarily in the shape of the primary peak. By a suitable choice of ϕ_0 , the maximum indicia can be made to agree nicely with the predicted curves, as seen in Figure 12.

It should be pointed out that in this analysis, the shape of the ultrasonic pressure pattern from the transducer given by the parameter ϕ_0 is not known apriori, and that here too, a best fit must be made with the data using some known flaw as a standard. The pressure pattern of the transducer may also alter depending upon the rotation of the transducer, and must be determined for each transducer. However, once the pressure pattern of the transducer is well established analysis of the shape and indicia is relatively straight forward.

Conclusions

The ability of the ultrasonic indicia to characterize the shape and size of imbedded defects has been developed and examined. The results of an experimental program to characterize these defects has shown the following:

1. The shape of the indicium gives an indication of the shape of the defect and can distinguish between elongated defects and spherical defects.

FIGURE 11 EFFECT OF PROBE PRESSURE PATTERN ANGLE
ON INDICIA OF SPHERE

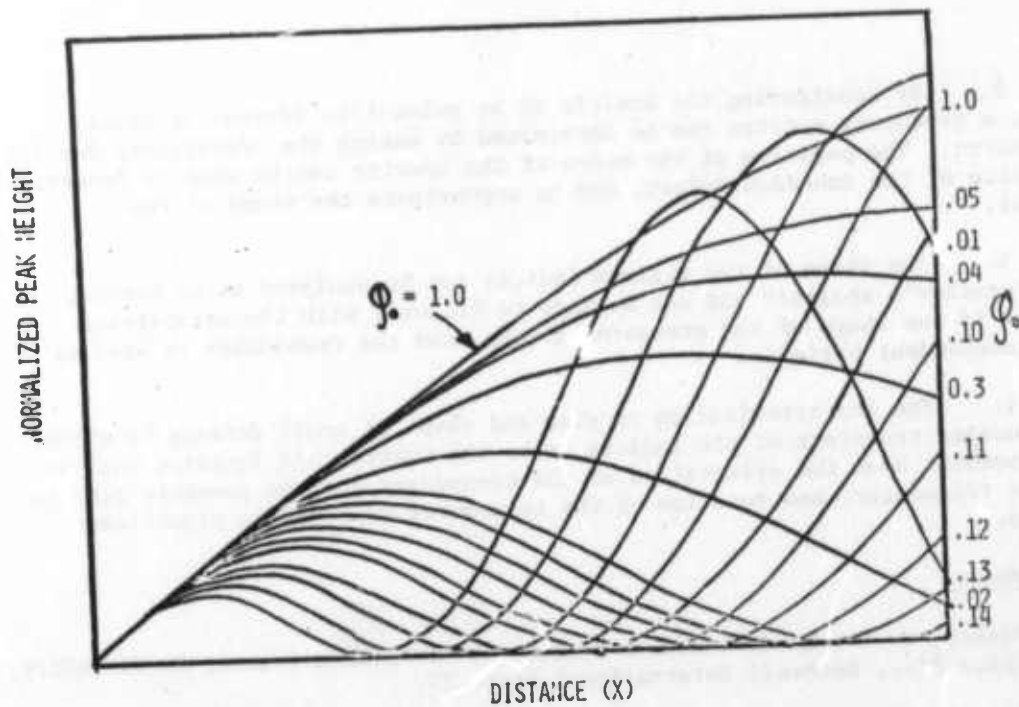
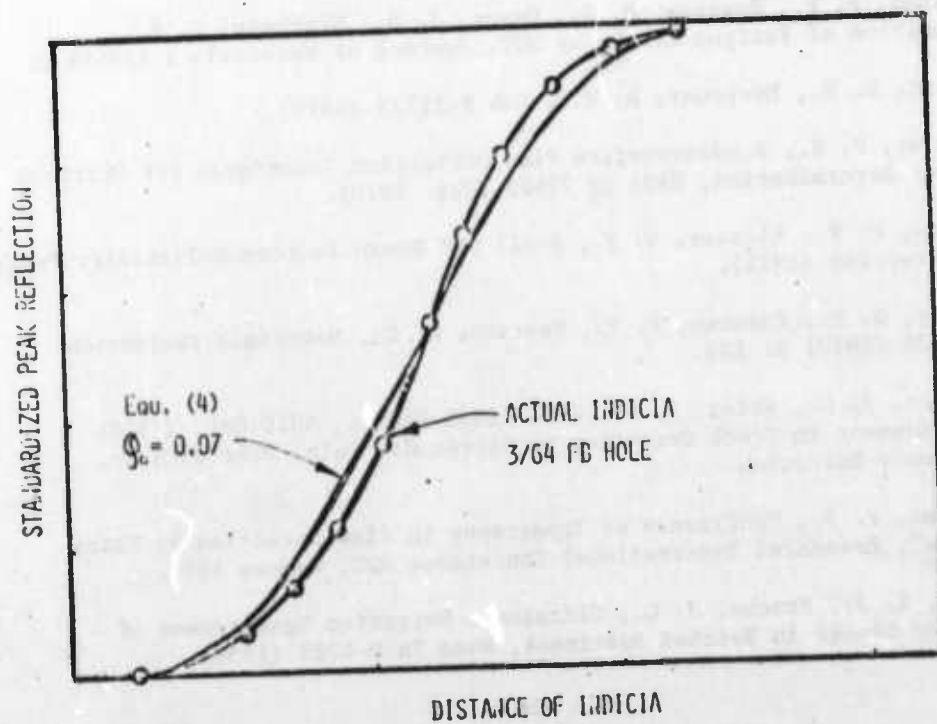


FIGURE 12 COMPARISON OF EQUATION 4 $\phi_0 = 0.07$ WITH
ACTUAL INDICIA OF 3/64 FB HOLE



2. By considering the indicia to be pulse-like instead of space-like, a frequency spectra can be determined by making the appropriate Fourier transform. The position of the nodes of the spectra can be used to determine the size of the imbedded defect, and to approximate the shape of the defect.

3. The shape of the maximum indicia can be analyzed using Gurvich and Yermelov's analysis and can be made to fit well with the established curves if the shape of the pressure pattern from the transducer is used as the independent variable.

4. The characterization of size and shape of small defects by either the Fourier transform of the indicia or by the Gurvich and Yermelov analysis is dependent upon the orientation of the transducer and the pressure pattern of the transducer, and rotation of the transducer can lead to significant errors.

References

1. Bishop, C. R., Nondestructive Evaluation of Fatigue Cracks, SH 73-SH0219, Space Div., Rockwell International Sept., 73.
2. Rummel, W. D. Todd, P. H., Frecska, S. P., Kathke, R. A., The Detection of Fatigue Cracks by Nondestructive Testing Methods, NASA CR 2369, Feb. 1974.
3. Packman, P. F., Pearson, H. S., Owens, J. S., Marchese, G. B., Definition of Fatigue Cracks by NDT, Journal of Materials 4 (1963) 3.
4. Pettit, D. E., Hoepfner, D. W., NAS 9-11722 (1972).
5. Sattler, F. S., Nondestructive Flaw Definition Techniques for Critical Defect Determination, NASA CR 72602 (Jan. 1970).
6. Thomas, E. F., Kloster, W. E., F-111 NDT Human Factors Reliability Program ASM Preprint (1971).
7. Corbly, D. M., Packman, P. F., Pearson, H. S., Materials Evaluation Vol. 28 (1970) p. 103.
8. Sessler, J. G., Weiss, V. W., ARPA Final Report, 8010 Oct. (1970) "Improvement in Crack Detection by Ultrasonic Pulse Echo with Low Frequency Excitation.
9. Packman, P. F., "Influence of Topography in Flaw Detection by Ultrasonics", Presented International Conference NDT, Warsaw 1973.
10. Klima, S. J., Freche, J. C., Ultrasonic Detection Measurement of Fatigue Cracks in Notched Specimens, Nasa Tn D-4782 (1968).



11. ANON: Ultrasonics; Vol. 1 Basic Principles. NASA CR-61209 (1967)
Vol. III Applications NASA CR-6141, Bastien, P., Difficulties in
the Ultrasonic Evaluation of defect size, Nondestructive Testing,
Feb. (1968) p. 147
12. Makara, A.M., Tsechal, V.A., Zhovnitskii I.P., Avtomatich-eskaya
Svorka, Vol. 5 (1961) p.3.
13. Tietz, H. D., "Contribution to the Flaw Detection in the Ultrasonic
Pulse Echo Technique by Investigation of Model Like Flaws," 7th
International Conference in NDT, Warsaw June 1973.
14. Opel, P., Ivens, G., "Determination of Flaw Size with Ultrasonics in
Forgings", Rept. 1320, Material's Committee Union of German Iron
Workers, Sept. 1961, Reprinted by Krautkramer Ultrasonics Reprint
906.
15. Krautkramer, J., Krantkramer, H., Ultrasonic Testing of Materials,
Springer-Verlag, N.Y. (1969).
16. Giacombo, G. D., Crisa, J. R., Goldspiel, S., Materials Evaluation
(1971) p. 189.
17. Whaley, H. L., Cook, K. V., "Ultrasonic Frequency Analysis", Materials
Evaluation 28 (1970) 61.
18. Redwood, M., "A Study of Waveforms in the Generation and Detection
of Short Ultrasonic Pulses", Applied Materials Research April (1963).
19. Gurvich, A. K., Shchukin, V. A., Defektoskopia, Nov., Dec. (1970)
p. 685.
20. Gurvich, A. K., Vermelov, I. N., Ultrasonics Flaw Detection in
Welded Joints, Izdvo Tekhinka, Kiev (1972).
21. Packman, P. F., Impulse Analysis of Ultrasonic Indicia, Proceedings
of Interdisciplinary Workshop for Quantitative Flaw Definition,
AFML TR-74-238, June 1974.
22. Proceedings of Interdisciplinary Workshop for Quantitative Flaw
Definition, July 1975, to be published.
23. Broch, J. T., Olesen, H. P., "On the Frequency Analysis of Mechanical
Shocks and Single Impulses", Presented 78th Meeting of Acoustical
Society of America, Nov. 1969. B & K Technical Review #3 (197).

PROJECT I, UNIT III, TASK 3

COMPARISON OF THEORY AND EXPERIMENT FOR
ULTRASONIC SCATTERING FROM SPHERICAL AND FLAT-BOTTOM CAVITIESB. R. Tittmann
Science Center, Rockwell InternationalObjective

The objective of this task has been to perform those ultrasonic experiments and analyses required to interpret the electrical signals derived from the pulse-echo scattering from defects in terms of the characteristics of the defect. The work has been done in the context of evaluating standards as currently encountered and utilized in the industrial NDE community.

Summary

Experimental data are compared with theoretical calculations for the scattering of short-duration ultrasonic pulses from a single spherical cavity embedded in a metallic solid. Emphasis has been placed on the influence which a defect has on a wavepacket containing many frequency components as is used in practical NDT applications. The angular dependence of the scattered longitudinal and mode converted shear waves generated by an incident longitudinal wave pulse has been measured over the frequency range from 2.25 to 10 MHz. These data are found to be in reasonable agreement with theoretical angular-dependence results obtained with two alternate schemes of synthesizing the scattered wave packet out of each of the frequencies making up the incident pulse.

The study of scattering from flat-bottom holes emphasized normal incidence of an ultrasonic beam onto the flat bottom of a drill hole. The measurements have been carried out under a variety of conditions to test the range of relevance or Ermolov's theory and more generally to shed light on the range of applicability of the flat-bottom hole as a reference standard. Effects of liquid versus solid propagation medium, large versus small bandwidth ultrasonic pulses, stress-free versus clamped boundary conditions for the scatterer, near-zone versus far-zone scattering ranges have been considered for a variety of transducers and frequencies. For most situations, Ermolov's theory adequately describes the scattering characteristics and, therefore, provides a useful tool for predicting the behavior of the flat bottom hole.

A. Procedure for the Theoretical and Experimental Treatment of Ultrasonic Pulses of Wide Frequency and Band Width

(1) Introduction

Approximately half of the effort during the last year concentrated on the quantitative evaluation of the scattering of short-duration-pulses from spherical voids¹ in order to study the influence of a defect on a wavepacket containing many frequency components as is used in practical NDT applications. These results are unique and different from those of another program (AFOSR Contract No. F44620-74-C-0057) which seeks to develop a detailed theoretical and experimental description of the interaction of plane, monochromatic waves with spheroids of revolution of arbitrary density and elastic moduli. The interpretation of the results obtained with short pulses discussed here benefited from the detailed calculations generated by the AFOSR program.

(2) Procedural Techniques

The ultrasonic pulses used in many NDT experiments have a high bandwidth and a comparison between our data obtained with these pulses and calculations based on monochromatic waves showed severe deviations. In order to resolve this dilemma we developed technique to take into account, in the calculations, the frequency content of the short-duration pulses. Here we briefly summarize the results of this effort in such a way as to suggest procedures for applying present scattering theory to laboratory and field practice.

As example, Figure 1 shows the angular dependence of a 7.5 MHz ultrasonic pulse scattered from an 800 μ diameter spherical cavity. The data is compared (by fitting at one point, i.e., $\theta \approx 40^\circ$) to the results of three theoretical calculations. One of these is the result for monochromatic waves² which is not in good agreement because of the wide frequency band width in the short-duration pulses used in the experiment. Another result (the curve labeled "Synthesized") is an attempt to take into account the frequency spectrum of the pulse by first theoretically spectrum-analyzing the incident pulse and then summing the power intensities for each frequency component with a weighting factor deduced from the differential cross-section at each frequency. Because of the particular nature of this procedure the final result is actually a calculation of the area under the square of the scattered signal and not the peak height of the rectified RF pulse as was measured in the experiment.

The curve labeled "Simulated" represents an improved calculation procedure in which the experimental signal is simulated theoretically as nearly as possible. Here, the transmitted ultrasonic pulse is theoretically spectrum analyzed, as before, and then the scattered RF burst waveform is calculated for each angle. This signal is then "rectified" by theoretically fitting its envelope with a parabola and the peak height of the envelope is used to calculate the scattered power for each angle to be compared with the experiment. This result gave nearly the same angular dependence as the previous

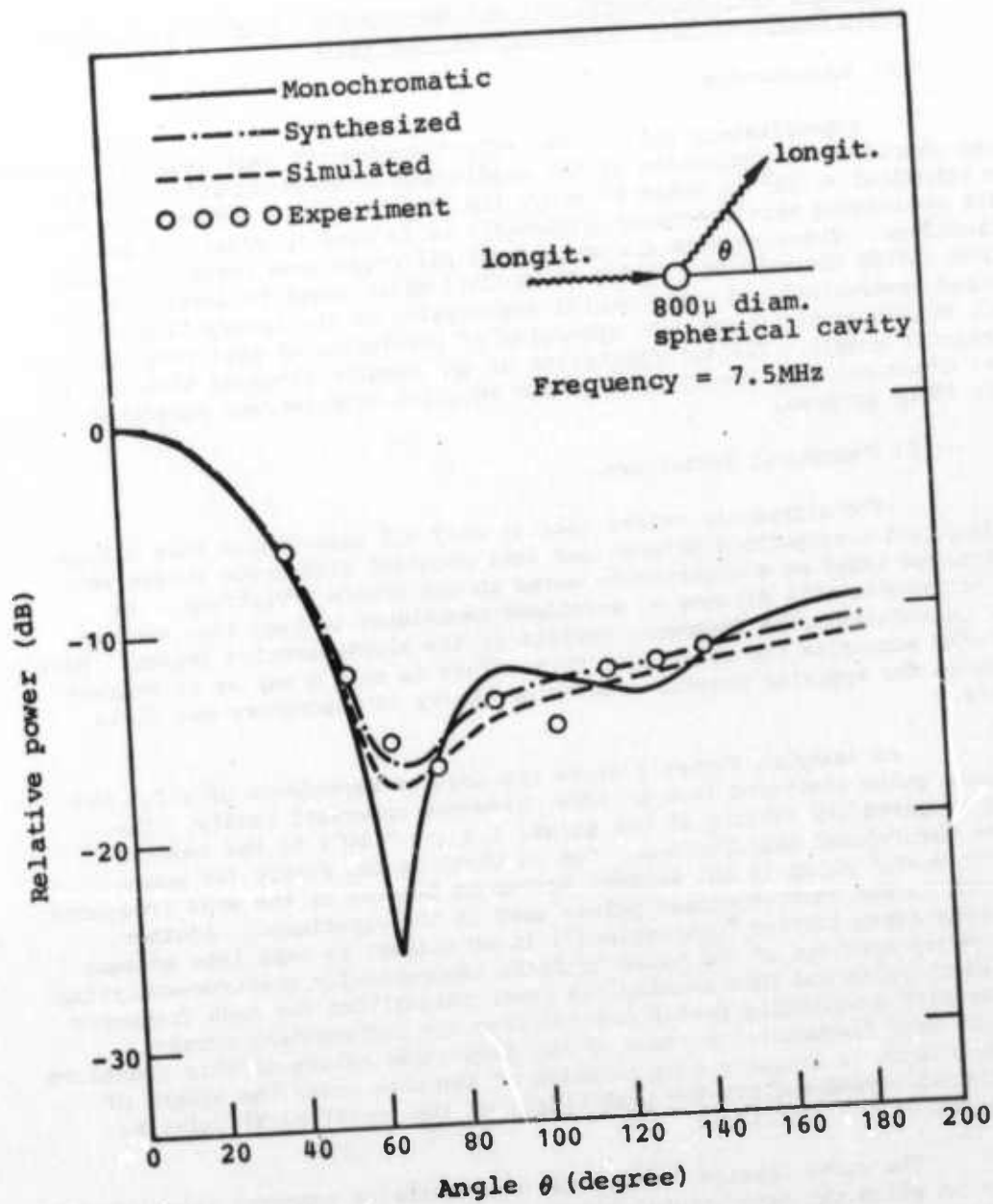


Fig. 1. Data and calculations on the angular dependence of ultrasonic pulses scattered from an 800 μ diameter spherical cavity.

technique, but was found to consume considerably more computer time.

(3) Results and Conclusions

Figures 2 and 3 present some representative results for the angular dependence of scattered longitudinal and mode-converted shear waves respectively associated with a 800 μ diam. spherical cavity upon which are incident longitudinal waves. The lines are those theoretically calculated by the method which gave the "Synthesized" result in Fig. 1. Three points emerge from this study: namely; one, that the technique is sufficiently accurate to give good agreement between theory and experiment for a wide range of frequencies and transducers (model numbers listed below respective frequency); secondly, that each curve is sufficiently different that a few measurements points in the angular range, say from $\theta = 40$ to $\theta = 60$ should be sufficient to determine the size of the spherical cavity, and; thirdly, the technique is adequately treating the mode conversion of the scattered waves, which plays an important role in the unique identification of defects.

B. Comparison of Ermolov's Theory with a Variety of Experimental Procedures

(1) Introduction

Ermolov's theory³ is the solution of a scalar potential equation for normal incidence of longitudinal waves on a rigid, motionless disk in a fluid. This treatment is only one of several addressing the scattering from disks and although Ermolov's is not as general as some of the other, his solution enjoys the advantage of being simple and convenient to use. Since his solution does not take into account mode conversion to shear waves, the question arises of how well his solution describes situations other than the highly idealized situation of a disk in a fluid. Of the several cases studied, only three will be considered here: a rigid, motionless flat-topped rod in a water bath; a flat-bottom drill hole in a metal block immersed in a water bath; and a flat-bottom drill hole in a metal block with the transducer in solid bond with the metal so as to allow reception of mode-converted shear waves.

(2) Comparison for three test cases.

(a) Rod in water bath

Figure 4 shows the relative amplitude of the signal reflected from a 5/64" diameter flat-topped rod in a water-bath when the separation R between the transducer and rod was varied. Here a 3/4" diameter, 1.0 MHz transducer was used as transmitter and receiver with very long pulseslengths (10.15 cycles) to simulate the monochromaticity basic to the theory. Also

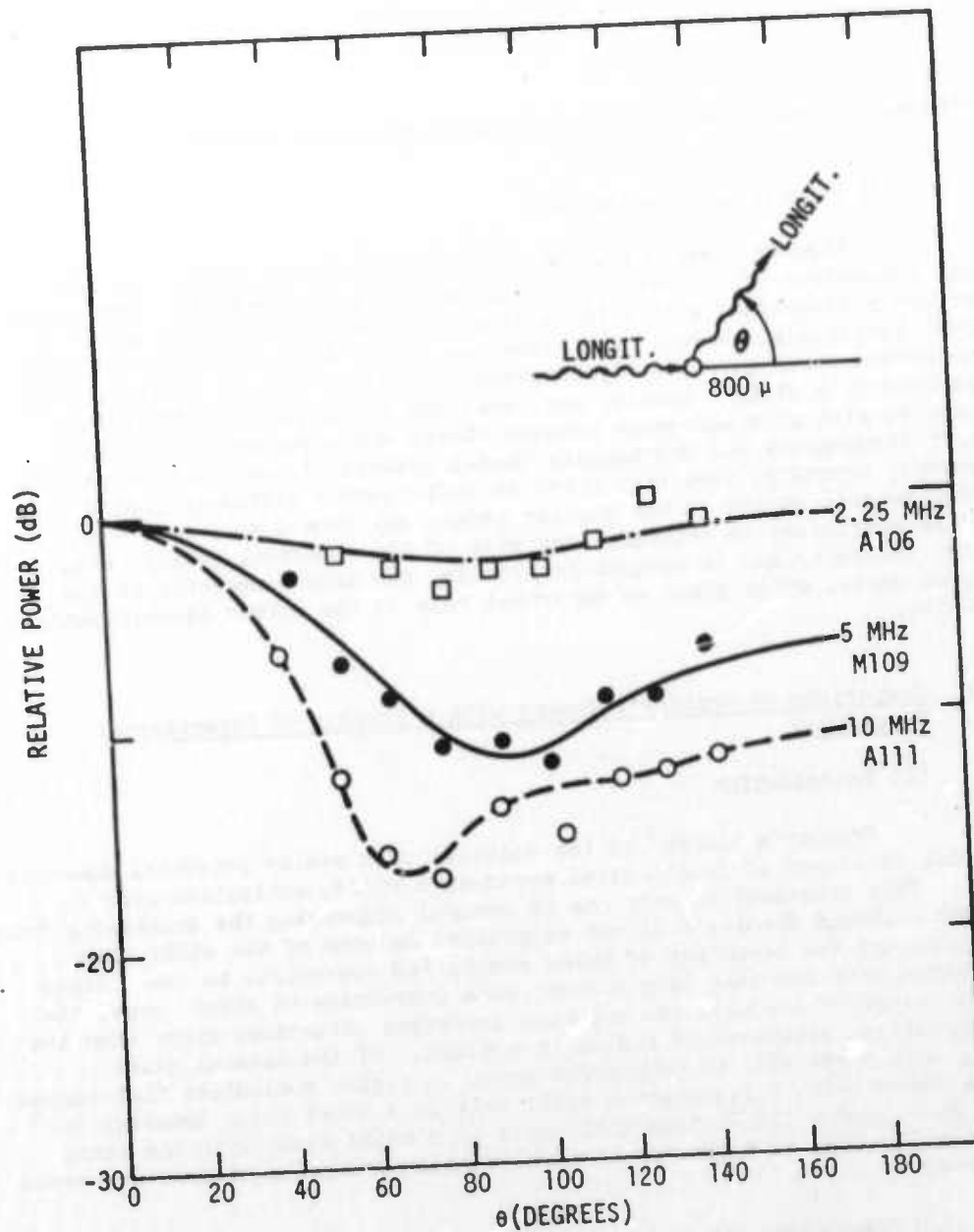


Fig. 2. Angular dependence of scattered pulses for several different frequencies.

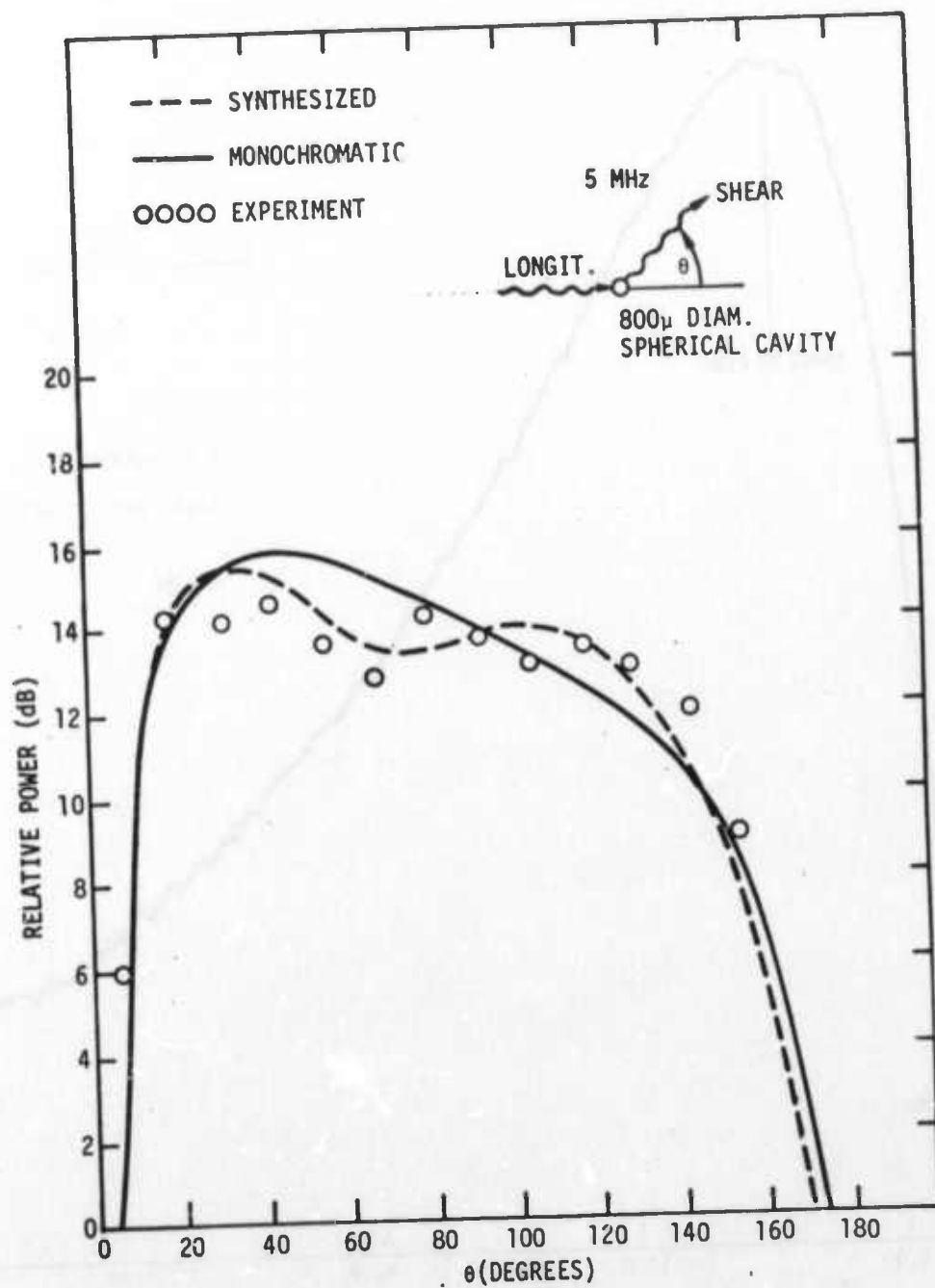


Fig. 3. Angular dependence of mode-converted shear wave pulses for 800 μ diameter void at 5 MHz.

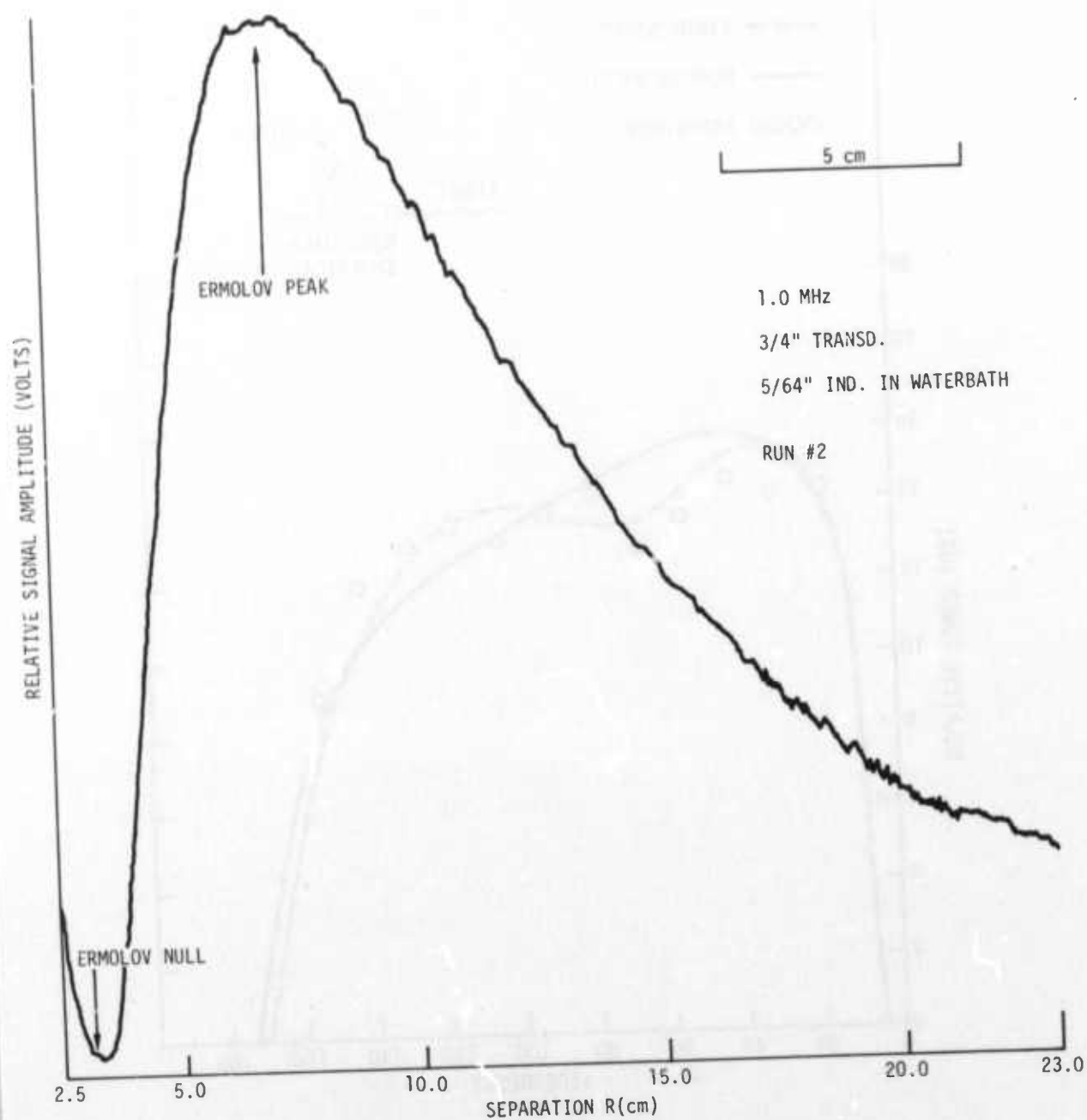


Fig. 4. Chart recording of amplitude of signal scattered from flat top of rod in waterbath as separation between rod and transducer is varied.



shown in the figure are the theoretically calculated positions of the first peak and null marking the transition between the far-zone (high values of R) and the near-zone (small values of R). The agreement between theory and experiment is good even though in this case any effects from the sides of the rod (the shaft) are clearly not taken into account in the theory. A more stringent test of this comparison is afforded by the plot shown in Fig. 5 which graphs the information in terms of normalized parameters.⁴ Here also, the data from a few runs with different diameter transducers show reasonably good agreement with the theoretical plots represented by the continuous lines. These lines show both the far-zone (Fraunhofer) and near-zone (Fresnel) regimes over a very large range of the separation R . In this plot R enters into the denominator of the abscissa, so that by contrast with Fig. 4 the separation increases from right to left.

A noticeable characteristic of the graph is the smoothing of the near-zone peaks and nulls as the ratio of the disk diameter b to transducer diameter a increases. This result is plausible on physical grounds when one considers the phase relationship between waves arriving at the center of the transducer with those arriving at the edge. If the source is almost a point source (b/a small), the two waves could add in or out of phase and the integrated response of the transducer would give sharp peaks and nulls, respectively. When the source becomes the same size as the transducer, the source can be thought of as consisting of many point sources distributed over a relatively large area. Consequently, the waves arriving at the transducer no longer have a well-defined phase relationship and the sharp features become smooth and disappear. The same result must be expected to occur when the waves lose their plane-wave character as would be the case for a pulse containing a large frequency band-width. The partial rounding of the peak and null in the data in the vicinity of $a/\sqrt{R} = 1.5$ is most likely due to both of these effects.

(b) Flat-bottom hole in metal block immersed in water.

When the rod was replaced by a block of metal with a flat-bottom drill hole, our data, as well as published data, again gave reasonable agreement with theory. As example, Fig. 6 presents data in normalized form for the case of Al Ultrasonic Standard Reference blocks of various lengths and containing holes of various sizes (data taken from the 1974 Annual Book of ASTM Standards⁵). Here the transducer is maintained a fixed distance (3 inches) from the face of the block containing the flat-bottom-hole such that the waves are incident at right angles to the block face and the flat bottom of the drill hole. Any effects of mode conversion taking place in the solid metallic sample are not detected by the transducer, since the shear waves are not propagated in the water. As seen in the figure, the agreement between theory and experiment is reasonable in spite of the fact that the waves are encountering two layers of material and the flat-bottom-hole (backed up by air) no longer satisfies the boundary conditions assumed in the theory, i.e., that of a motionless (clamped) disk.

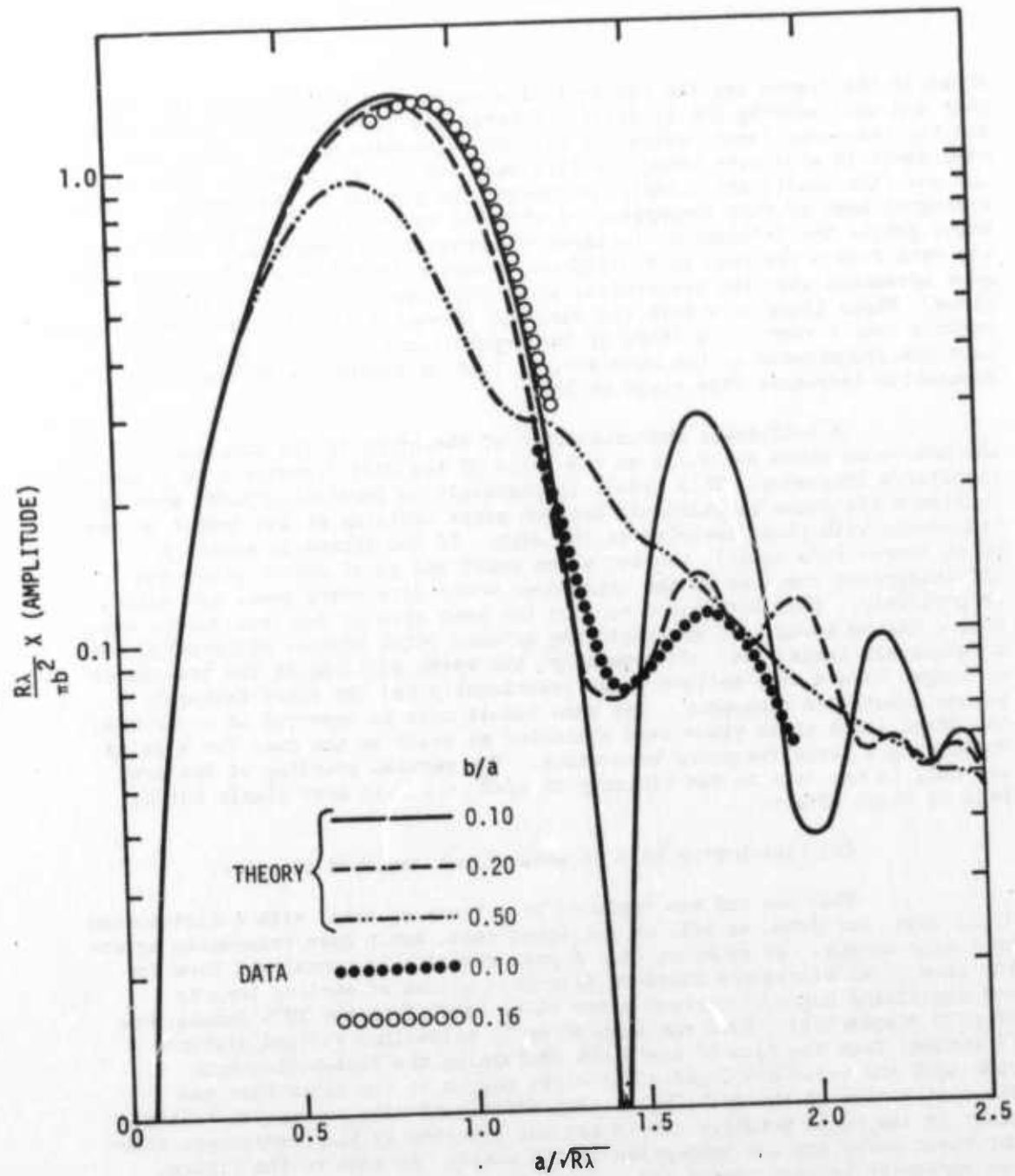


Fig. 5. Scattering from rod in water bath. Plot of data and Ermolov's predictions in terms of normalized coordinate.

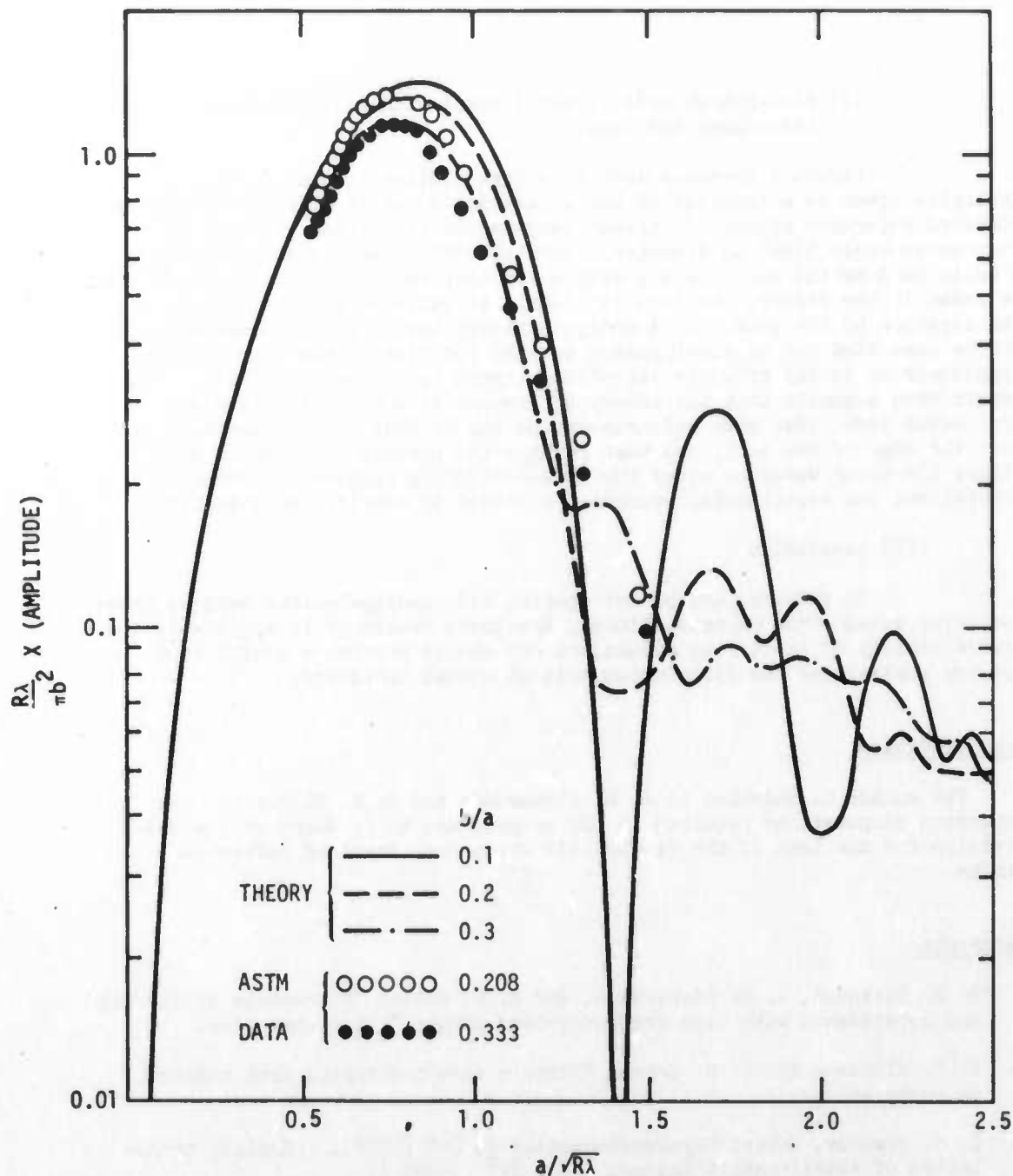


Fig. 6. Comparison of theory and experiment (normalized coordinates) for scattering from flat-bottom hole in Al block immersed in water. The travel path in water is fixed (3 inches) whereas travel path in Al changes with different block lengths. The experimental points were obtained from data published for Ultrasonic Standard Reference blocks.⁵

(c) Flat-bottom hole in metal block with solid between transducer and sample.

Figure 7 presents data in a form similar to that in Fig. 4 (relative power as a function of the separation R) on Ti-6%Al-4%V Ultrasonic Standard Reference blocks of various lengths all containing the same size flat-bottom-hole 5/64" in diameter. Special effort was placed on assuring a solid bond by the use of a wax with a low temperature melting point ($\sim 50^{\circ}\text{C}$). As shown in the figure, the data is clearly at variance with the theory for the location of the peak. Data analysis showed that this disagreement could not be accounted for by misalignment between the flat-bottom hole and the transducer or in any property variation between the reference blocks. The result then suggests that the theory of Ermolov is not quantitatively applicable here, that some mode-conversion may in fact occur - probably near the edge of the hole, and that perhaps the presence of a solid bond allows the shear waves to alter the back-scattering problem. Further theoretical and experimental evidence is needed to clarify the situation.

(5) Conclusion

In summary, except for special test configurations such as those involving solid bonds on metal blocks, Ermolov's treatment is applicable to a wide variety of scattering situations and should provide a useful tool for the analysis of the flat-bottom hole at normal incidence.

Acknowledgement

The author is indebted to J. M. Richardson and R. K. Elsley for the extensive computations required in the program and to J. Moore of the B-1 Division for the loan of the Ti-6%Al-4%V Ultrasonic Standard Reference blocks.

References

1. B. R. Tittmann, J. M. Richardson, and E. R. Cohen, "Ultrasonic scattering and experiments with wide frequency-band pulses," in preparation.
2. B. R. Tittmann and E. R. Cohen, "Elastic wave scattering from spheres," in preparation.
3. I. N. Ermolov, Soviet Physics-Acoustics 5, 248 (1959). [English translation of Akusticheskii Zhurnal 5(2), 247 (1959).]
4. E. R. Cohen, "Acoustic scattering by discs," Science Center Report SCTR-73-15 (1973).
5. 1974 Annual Book of ASTM Standards, Part II, Metallography; Nondestructive Tests, American Society for Testing and Materials, Philadelphia, Pa., pp. 229-242 (1974).

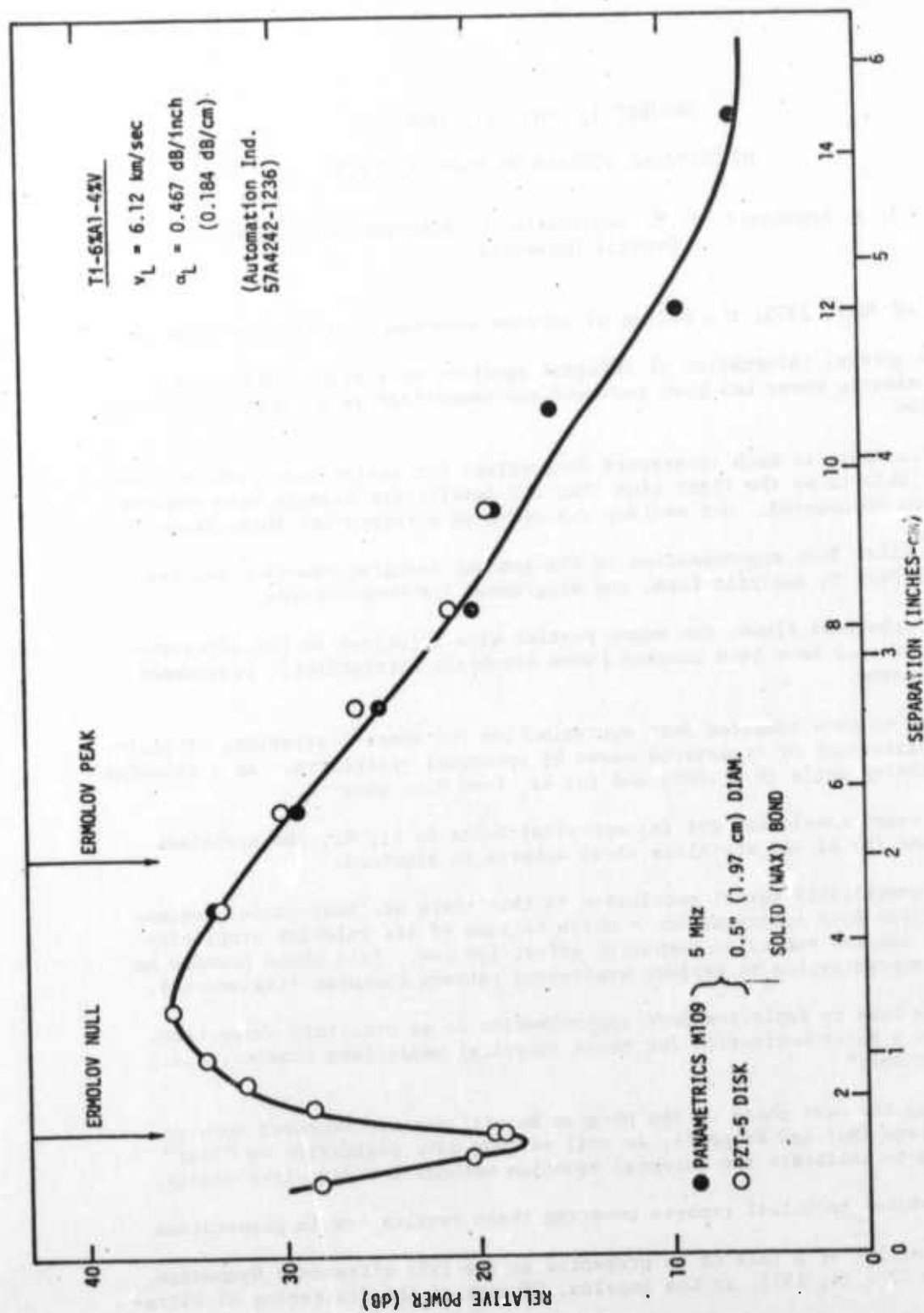


Fig. 7. Relative power of signal scattered from 5/64" diameter flat-bottom-holes in series of T1-6%Al-4%V Ultrasonic Standard Reference blocks. The theoretical positions calculated for the null and peak are indicated by arrows.

PROJECT I, UNIT III, TASK 4
THEORETICAL STUDIES OF FLAWS AND NDE

J. A. Krumhansl, J. E. Gubernatis, M. Huberman and E. Domany
Cornell University

As of July, 1975, the status of various components of this program is:

1. The general information of integral equation scattering theory for vector elastic waves has been reviewed and summarized in a report just being completed.

While there is much literature (acoustics) for scalar wave problems, we believe this to be the first time that the details for elastic wave systems have been documented. Our writeup can serve as a source for this theory.

2. The first Born approximation to the general integral equation has been obtained both in analytic form, and programmed for computations.
3. For spherical flaws, the exact partial wave solutions in the literature (Truell et al.) have been checked [some algebraic corrections], programmed, and evaluated.
4. Thus, we have computed Born approximation and exact scattering, of incident longitudinal or transverse waves by spherical scatterers - as a function of scattering angle ($0 - 180^\circ$) and for kr_s from 0 to about 6.

The cases considered are (a) spherical holes in Al, Ti, and stainless steel, and (b) Al and stainless steel spheres in aluminum.

5. The practically useful conclusion is that there are many useful regimes of the first Born approximation - which because of its relative simplicity does not require extensive computing effort for use. This shows promise as a first approximation to explore scattering pattern features (signatures).

It is easy to apply the Born approximation to an arbitrary shape flaw, which was a major motivation for these numerical comparison studies, i.e., "calibrations."

During the next phase of the program we will explore improved Born approximations (Mal and Knopoff), as well as long wave scattering by "flat" spheroids to calibrate the integral equation methods for disc-like cracks.

Individual technical reports covering these results are in preparation.

An abstract of a talk to be presented at the 1975 ultrasonic Symposium, September 22 - 24, 1975, at Los Angeles, "Theory of the Scattering of Ultra-



sound by Flaws," J. A. Krumhansl, J. E. Gubernatis, M. Huberman, and E. Domany, Laboratory of Atomic and Solid State Physics, Cornell University, is attached.

Although publications are planned, results from this first year's work are just now being assembled in our reports.

A more detailed overview of the program is attached.

Overview

Ultrasonic methods are of great importance in the study of structural and elastic properties of materials, particularly for non-destructive testing. A tremendous body of experimental work exists and has been interpreted to varying degrees. However, these interpretations have frequently been based upon theoretical methods which, in terms of modern concepts, have not advanced nearly as far as have the experimental techniques.

Beyond the experimental aspects of signal production and processing, the central question is that of specifying how flaws, i.e., inhomogeneities, scatter ultrasonic waves. Several experimental programs are now under way to lay a basic foundation for engineering applications, by measuring and analyzing the behavior of specific, well-controlled, prototype defects in a few representative materials.

We have addressed ourselves to the theoretical problems encountered in this controlled, experimental study. Two lines of development have been emphasized, representing substantial advances in the theoretical and analytical capability of theory for interpretive purposes: First, integral equation methods adapted from quantum scattering theory are susceptible to a wider variety of practical approximation methods than are the traditional differential equation approach; second, modern computer capability is vastly greater than that available a decade or more ago when much of the last serious study of elastic wave scattering in solids was done. In both respects, new results have been obtained.

Thus, we plan to write a series of reports for record and for use by the experimental community; in part, these reports will be a review of theory, but much of what we report is new and is not to be found elsewhere, to our knowledge. In addition, computer programs have been produced and results obtained for several representative (single) flaw situations in titanium, aluminum, and stainless steel.

Another set of introductory remarks, for perspective, concerns the broader view of the experimental situation. Scattering problems are encountered at several levels:

- 1) Even the normal "good" material is usually polycrystalline, so that when looked at with sufficient resolution there is a "noise" source not present in single-crystal material.

2) When a well-defined flaw in a polycrystalline medium scatters, both incoming and outgoing waves must usually propagate through the host heterogeneous medium, which certainly modifies the signal.

3) In some instances, multiple scattering between flaws requires analysis. In all of these cases, the traditional differential equation methods have been intractable, whereas the general integral equation methods which we emphasize have already been found usable in some applications, and show reasonable potential for wider applicability.

Of considerable interest is the fact that very complete computations of scattering from simple flaws now can be carried out at a fraction of the cost of an experimental run to obtain similar data.

In order to help visualize these interrelated remarks, as well as to serve as a prospectus of topics on which subsequent report sections will be presented, a topical and application chart is useful.

ULTRASONIC SCATTERING THEORY AND SITUATIONS

Krumhansl, Gubernatis, Domany, and Huberman
July 1975

Physics: Constitutive Relations (Elasticity)
Dynamics (Newton's Laws)

Equations of Motion:

Differential Equations: Wave Equation
Polynomial Expansions
Boundary Matching
Partial Wave Scattering Basis

Integral Equation:

Fredholm Equation
Iteration Solutions
Boundary Matching Automatic
Approximation Options: Born, Modified
Born, Variational
General Scattering Cross Section
Formula
Asymptotic and Conservation Laws

Regimes:

Diffraction Limit:

$ka_{\text{flaw}} \ll 1$
Scattering Pattern Signature



Science Center
Rockwell International

Geometric Optics Limit: $ka_{\text{flaw}} \gg 1$
Ray Theory; Edge, Surface Waves

Applications:

Single Scatterer & Diffraction Limit:

A. Diffraction Limit: Exact results for sphere, partial wave basis
Born approximation for sphere, comparison
Exact results ($ka_f < 1$) for spheroid, "flat crack limit," integral equation method
Born approximation for spheroidal crack
Born approximation for flat bottom and cylindrical holes
Improved Born approximation
Distorted wave method for nonspherical shape
Variational approximations

B. Multiple Scatterers: Polycrystalline media, integral equation method
Attenuation, spectral modification
Flaw structure correlations, integral equation method



Science Center
Rockwell International

THEORY OF THE SCATTERING OF ULTRASOUND BY FLAWS

J. A. Krumhansl, J. E. Gubernatis, M. Huberman, and E. Domany,
Laboratory of Atomic and Solid State Physics, Cornell University, Ithaca,
NY 14853

An integral equation governing the scattering of ultrasound by an arbitrarily shaped flaw is presented, and features of the scattered displacement and stress fields are discussed for the case of a flaw embedded in an isotropic medium. Also discussed are the total and partial differential cross sections for the scattered power. These cross sections for a spherical flaw (cavity and inclusion) are evaluated by two approximations: one analogous to the first Born approximation in quantum mechanical scattering, the other analogous to the Mie-Debye approximation for the scattering of electromagnetic waves. The results of the calculations are compared with exact results for scattering of ultrasound by spheres. The relevance of this comparison to NDE, i.e., flaw identification, is discussed.

THEORY OF THE SCATTERING OF ULTRASOUND BY FLAWS

J. A. Krumhansl, J. E. Gubernatis, M. Huberman, and E. Domany,
Laboratory of Atomic and Solid State Physics, Cornell University, Ithaca,
NY 14853



Science Center
Rockwell International

REVIEW OF THEORIES OF SCATTERING OF ELASTIC WAVES BY CRACKS

Edgar A. Kraut
Science Center, Rockwell International
Thousand Oaks, California

ABSTRACT

The detection of cracks with the aid of ultrasonics is an important NDE technique. The corresponding theoretical problem of the scattering of elastic waves by cracks has also been studied by scientists working in many different fields. Contributions to our knowledge of the subject have come from such diverse areas as geophysics, and applied mathematics, electrical engineering, and continuum mechanics. Many of the results obtained by workers in those fields are also of interest to the NDE Community and for that reason a review is presented here of current results and profitable directions for future research.

PROJECT I, UNIT IV, TASK 1
REVIEW OF THEORIES OF SCATTERING
OF ELASTIC WAVES BY CRACKS

E. A. Kraut
Science Center, Rockwell International

Introduction

The ultrasonic detection of cracks in the interior of an elastic solid by the use of surface transducers is a fundamental NDE problem. The presence of cracks may be detected either by observing the back scattered elastic waves using the launching transducer as a receiver or by observing obliquely scattered waves with a separate receiving transducer located elsewhere on the surface. Unfortunately, most of the theoretical work on the scattering of elastic waves from cracks has been confined to the case of a crack in an unbound elastic solid, a situation far different from the experimental one. Even in that case, exact results are available only for a crack occupying a half plane. Exact results for cracks having a finite surface area, such as a penny shaped crack, are not available, although many approximate calculations have been published, particularly in the low frequency limit. Before delving into the mathematical details of scattering from cracks it is important to recognize that idealized cracks and real cracks may differ substantially in their behavior. For example, a cracked specimen may show different ultrasonic scattering characteristics depending on whether it is loaded or not. Such differences may be attributable to the closing of cracks under compression or the opening of cracks under tension. Important as such considerations are, they have received little attention from theorists. Consequently, until a better description of the boundary conditions at a crack becomes available, the idealized theory must be employed.

Idealized Description of Cracks

From the theoretical point of view, a crack is a two dimensional surface of finite or infinite area located in the interior of an elastic solid. For example, a penny shaped crack can be thought of as the result of removing a thin disc shaped section of material from the interior of a solid. Boundary conditions are now applied at the surfaces of the void which has been created. In the case of a weak crack the surfaces of the void are taken as free surfaces where the stress must vanish. In the case of a rigid crack, the void is imagined to be filled with a completely rigid material which pins the walls of the crack so that the displacement is zero everywhere. In each case the finite thickness of the disc is neglected and both faces are thought of as occupying the same plane. This approach, while mathematically convenient, avoids the question of how the faces of the crack interact with one another and whether the crack is open or closed. Typical examples of two dimensional cracks are shown in Figures (1) and (2).

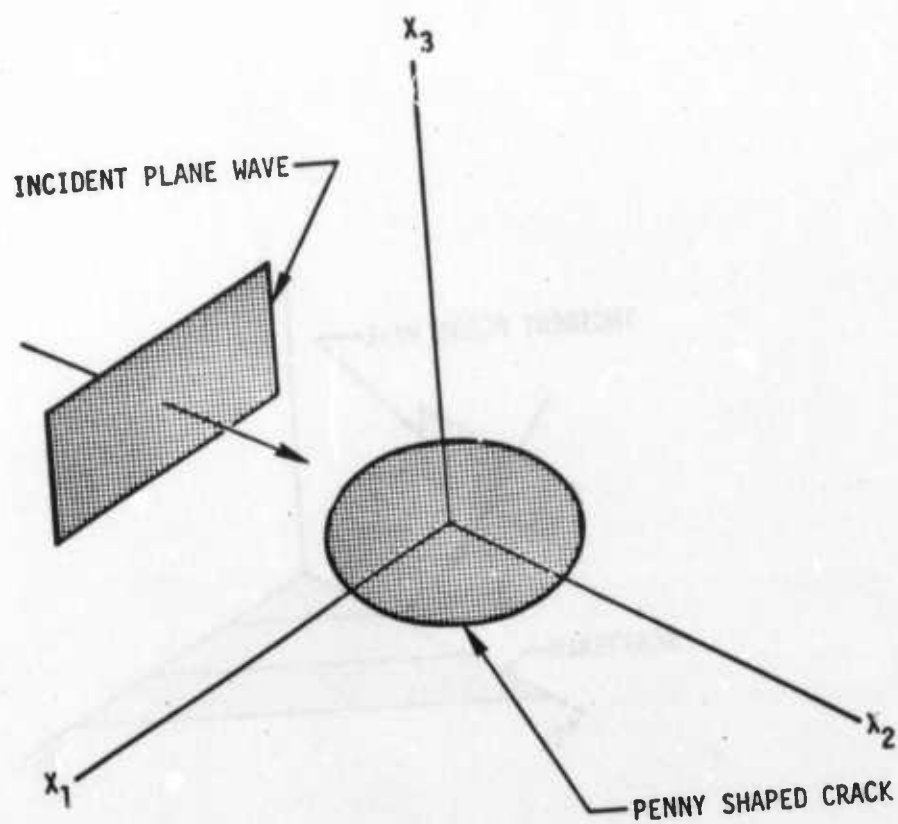


Fig. 1 Geometry of the Scattering Problem for A
Penny Shaped Crack.

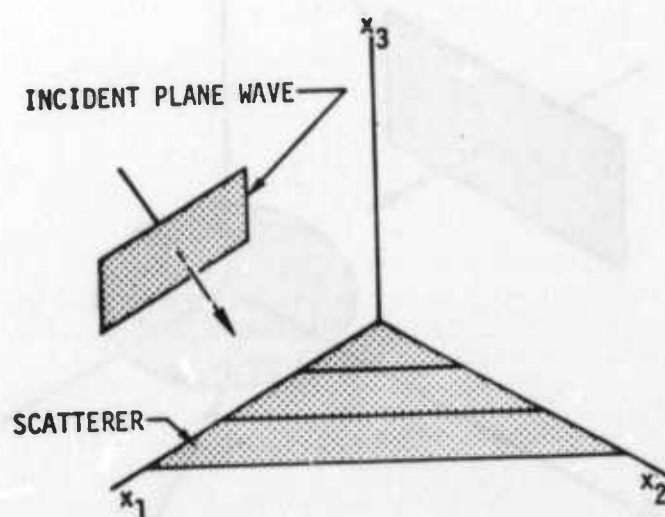


Figure 2

Geometry of the Scattering Problem for a crack
occupying a quarter plane

Scattering of Elastic Waves by a Crack Occupying a Half Plane

There are two features of a crack that are essential in determining its behavior as a scatterer of elastic waves. The first is that a crack represents a two dimensional surface across which the stress or displacement (or both) can be discontinuous. The second is that cracks have edges which generate diffracted waves. The scattered waves produced by an incident compressional wave striking a half plane crack are shown in Figure (3). For the case of a weak crack in addition to the wave fronts shown, there will also be a Rayleigh wave propagating away from the edge of the crack and confined to the plane of the crack. The first exact solution for scattering by a rigid half plane crack was given by Fridman⁽¹⁾ in 1948. The corresponding problem of the scattering of time harmonic shear and compressional waves by a weak half plane was solved exactly by Maue⁽²⁾ in 1953. A very detailed exact treatment of the diffraction of incident shear and compressional pulses by weak and rigid half planes was presented by DeHoop⁽³⁾ in 1958. The half plane problem is particularly simple because displacements parallel to the edge of the half plane are decoupled, making the remaining problem two dimensional. Since the exact solution is known, the half plane problem provides a convenient means of testing various approximate solutions such as the Kirchoff approximation. Experimentally, scattering from a half plane can be modelled as shown in Figure (4). This corresponds to the theoretical problem of scattering from a half plane at a finite depth beneath the free surface of an elastic half space. In addition to the types of scattered waves shown in Figure (3), there is now also the possibility of multiple scattering, waveguiding and the excitation of Lamb waves in the region between the half plane and the free surface. The corresponding theory does not seem to have been worked out in any detail and because of the ease with which the problem can be modelled further work seems worthwhile.

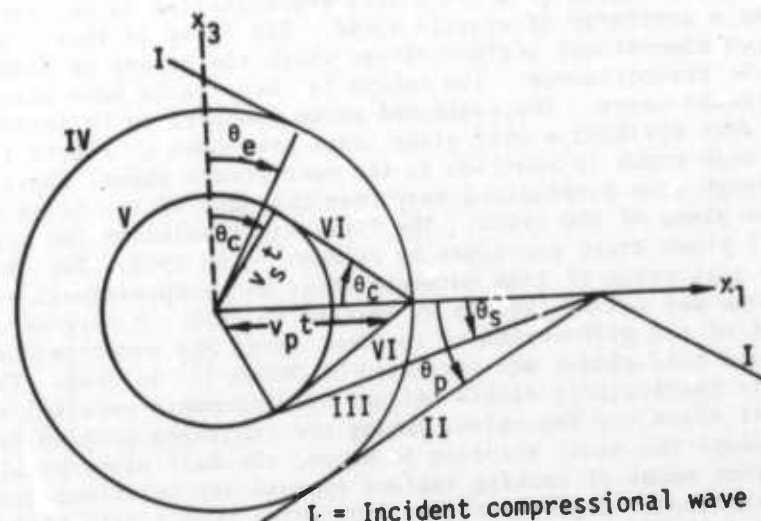
Scattering of Elastic Waves by a Two Dimensional Crack of Arbitrary Shape in an Unbounded Elastic Medium

Consider the scattering of an arbitrary incident wave by a crack Σ of finite extent and vanishing thickness. In an elastic solid Σ is a two dimensional region across which the displacement and stress may be discontinuous. Both the incident and scattered elastic waves satisfy the homogeneous wave equation

$$c_{ijpq} \left(\frac{\partial^2 u_p}{\partial x_j \partial x_q} \right) - \rho \frac{\partial^2 u_i}{\partial t^2} = 0 \quad (4.1)$$

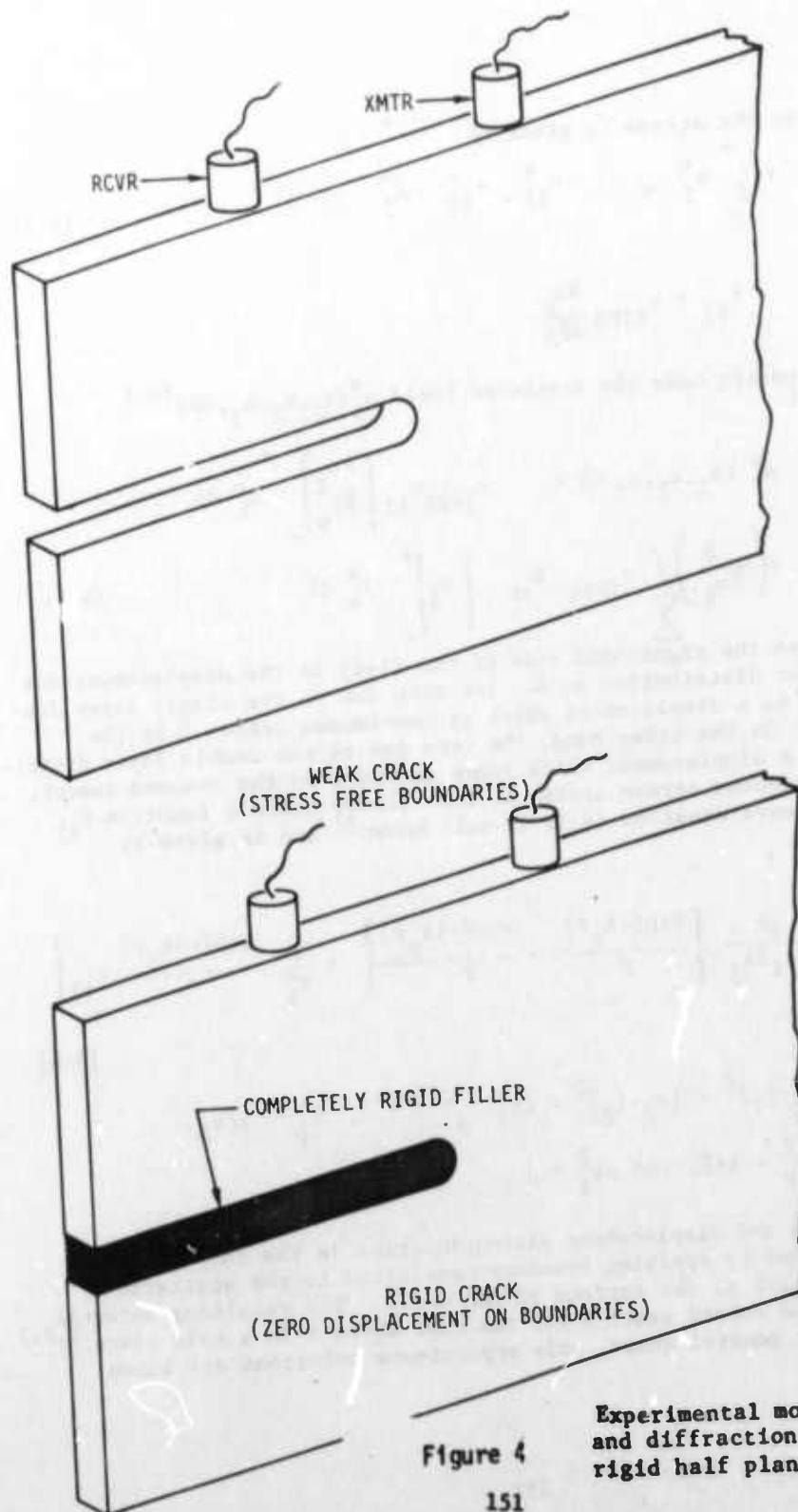
With the aid of Green's theorem, the scattered displacement field u_i^s can be expressed in terms of the jumps across Σ in the displacement and stress. Let n_i^+ and n_i^- denote the unit vectors in the direction of the normal to Σ^+ and Σ^- respectively; Σ^+ is one face of Σ and Σ^- is the other face. The positive sense of n_i^+ and n_i^- is taken towards Σ ; hence, $n_i^+ = -n_i^-$. The jump in displacement is given by

$$[u_i]^+ = u_i^+ - u_i^- \quad (4.2)$$



- I = Incident compressional wave
- II = Reflected compressional wave
- III = Reflected shear wave
- IV = Diffracted compressional wave
- V = Diffracted shear wave
- VI = Diffracted conical wave

Figure 3
Diffracted and reflected wavefronts produced an
incident compressional wave on a half plane crack.



Experimental models for scattering
and diffraction from stress free and
rigid half plane cracks.

Figure 4

and the jump in the stress is given by

$$\tau_{ij}^+ n_j^+ - \tau_{ij}^- n_j^- = \tau_{ij}^+ - \tau_{ij}^- \quad (4.3)$$

where

$$\tau_{ij} = c_{ijpq} \frac{\partial u_p}{\partial x_q}$$

In the time harmonic case the scattered field $u_1^s(x_1, x_2, x_3, \omega) e^{i\omega t}$ is given by (3)

$$u_1^s(x_1, x_2, x_3, \omega) = c_{jkpq} G_{ij} \left[\frac{\partial u_p}{\partial x_q} \right]^+ n_k^+ dS + \left(\frac{\partial}{\partial x_q} \right) \int \sum c_{jkpq} G_{ip} \left[u_j \right]^+ j_k^+ dS \quad (4.4)$$

The first term on the right-hand side of the (4-4) is the displacement due to a single layer distribution on Σ . The term due to the single layer distribution leads to a displacement which is continuous across Σ by the assumed amount. On the other hand, the term due to the double layer distribution leads to a displacement which jumps across Σ by the assumed amount, but gives a continuous stress across Σ . The tensor Green's function G_{ij} for the elastic wave equation (4.1) is well known³ and is given by

$$G_{ij}(x-\xi, \omega) = \frac{1}{4\pi\rho} \left\{ \frac{1}{\omega^2} \frac{\partial^2}{\partial x_i \partial x_j} \left\{ \frac{\exp(-ik_s r)}{r} - \frac{\exp(-ik_p r)}{r} \right\} + \frac{1}{v_s^2} \frac{\exp(-ik_s r)}{r} \delta_{ij} \right\} \quad (4.5)$$

$$\text{where } r = \left\{ (x_1 - \xi_1)^2 + (x_2 - \xi_2)^2 + (x_3 - \xi_3)^2 \right\}^{1/2}, \quad k_p = \omega/v_p,$$

$$k_s = \omega/v_s, \quad \rho v_p^2 = \lambda + 2\mu \text{ and } \rho v_s^2 = \mu.$$

The unknown stress and displacement discontinuities in the integrands of (4.4) are determined by applying boundary conditions to the scattered field $u_1^s(x_1, x_2, x_3, \omega)$ at the surface of the crack. The resulting integral equations have been solved exactly for the case where Σ is a half plane.^{1,2,3} For cracks of more general shape, only approximate solutions are known.

Kirchoff's Approximation

In the Kirchoff approximation, specific assumptions are made about the jumps in the stress and displacement across a crack. This permits the direct evaluation of (4.4) without having to solve any integral equations. We are interested here in the errors introduced by this approximation. In Kirchoff's original theory; on the illuminated part of the scatterer (in the sense of geometrical optics) the wave function and its normal derivative are equal to their corresponding values as if the scatterer were absent, on the dark part of the scatterer the wave function and its normal derivative vanish. The corresponding assumptions for the scattering of elastic waves are that the amounts by which the stress and displacement jump across a crack are numerically equal to the corresponding values of the incident wave at the illuminated surface of the crack. When this assumption is made it is found³⁾ that all the reflected waves are lost in the solution. The critical angle head wave is also lost. Only the incident wave and the diffracted waves generated by the edge of the crack are obtained. This explains why the Kirchoff assumptions are supposed to solve diffraction by a perfectly absorbing scatterer (in optical terms a black screen). The Kirchoff approximation can be modified in such a way that the correct reflected waves are obtained,^{3,4)} however, the critical angle head waves are always lost. One can think of the Kirchoff approximation as a method of specifying the physical properties of a crack in terms of the jumps in displacement and stress across it. If these jumps are numerically equal to the corresponding values of the incident wave at the crack surface, the crack is perfectly absorbing or "black". In general, however, the theories of Kirchoff and modifications of it are poor substitutes for rigorous diffraction theory (wave equation plus boundary conditions) because they do not correctly describe the field in the vicinity of the scatterer and in the long wavelength limit because they entirely fail to predict the correct order of magnitude of the field far from the scatterer.⁴⁾

Scattering from a Penny Shaped Crack

The scattering of elastic waves by a penny shaped crack in an unbounded elastic solid has been treated by several investigators.⁵⁻¹⁵⁾ Some of the earliest work is that of Filipczynski⁵⁾ (1961) who treated the problem by separation of variables in an axially symmetric oblate spheroidal coordinate system. Use of that coordinate system permits a simple statement of the boundary conditions on the surface of a disc since a disc is one of the coordinate surfaces. The case considered by Filipczynski⁵⁾ is that of the scattering of a normally incident plane compressional wave by a disc in the limit in which the radius of the disc is much shorter than the wavelength of the incident wave (long wavelength or Rayleigh limit $ka \rightarrow 0$). In this case the Kirchoff approximation is expected to be poor. Far away from the disc in Figure (1), the reflected waves can be referred to a set of spherical coordinates



$$\begin{aligned}x_3 &= R \cos \theta \\x_2 &= R \sin \theta \sin \phi \\x_1 &= R \sin \theta \cos \phi\end{aligned}\quad (6.1)$$

When a plane compressional wave is normally incident on the penny shaped crack in Figure (1), then axial symmetry permits the scattered displacement field to be represented by the gradient of a scalar potential $\vec{A} = \vec{e}_\phi A_\phi$ so that,

$$\vec{U} = \nabla \varphi + \nabla \times (\vec{e}_\phi A_\phi) \quad (6.2)$$

Filipczynski's expressions⁵⁾ for φ and A_ϕ in the long wavelength, far field limit are

$$\varphi = \varphi_0 \frac{e}{R} \frac{-ik_L R}{\cos \theta} \quad (6.3)$$

$$A_\phi = A_0 \frac{e}{R} \frac{-ik_T R}{\sin \theta} \quad (6.4)$$

where

$$\varphi_0 = -\frac{2a}{3\pi} \frac{\left(\frac{k_L a}{1 + \frac{3}{4} \frac{k_T}{k_L}}\right)^2}{\left(\frac{k_T}{k_L}\right)} \quad (6.5)$$

$$A_0 = -\frac{2a}{3\pi} \frac{\left(\frac{k_T a}{1 + \frac{3}{4} \left(\frac{k_T}{k_L}\right)}\right)^2}{\left(\frac{k_T}{k_L}\right)} \quad (6.6)$$

The longitudinal and transverse wave numbers are k_L and k_T respectively. The corresponding displacement components u_R , u_θ , and u_ϕ to order R^{-1}

$$u_R = -ik_L \varphi_0 \frac{e}{R} \frac{-ik_L R}{\cos \theta}, \quad (6.7)$$

$$u_\theta = ik_T A_0 \frac{e}{R} \frac{-ik_T R}{\sin \theta}, \quad (6.8)$$

$$u_\phi = 0_\phi \quad (6.9)$$



Different expressions for the far field displacements due to diffraction of elastic waves by rigid and weak circular discs have been obtained by MAL,⁷⁻¹¹⁾ and formulas for the corresponding scattering cross-sections appear in the works of Robertson⁶⁾ and Filipczynski.⁵⁾ Details of the computation of the scattering cross section when plane time harmonic compressional or shear waves are incident on two or three dimensional obstacles in an infinite elastic solid have been discussed by several authors.¹⁶⁻¹⁹⁾ Except for Filipczynski's work, all the other cited results have been obtained in cylindrical coordinates by iteratively solving integral equations for the scattered field in the long wavelength limit. The work of Robertson⁶⁾ is particularly interesting. He assumed that the scattered field due to a plane compressional wave normally incident on a penny shaped crack could be modelled by a harmonically oscillating piston on the surface of a semi-infinite elastic solid. He thus replaced the problem of calculating the scattered field from a disc shaped flaw in an unbounded elastic medium by the problem of calculating the radiation field of a disc shaped transducer on the surface of an elastic half space. Robertson considered the case where a time harmonic normal stress is prescribed at the disc surface and the displacements are zero elsewhere on the boundary.⁶⁾ He also treated the complementary case where the displacement is prescribed at the disc surface and the stresses are zero elsewhere on the boundary.²⁰⁾ In both of these cases, the fact that stress is prescribed over one portion of the boundary and the displacement is prescribed over the remaining portion leads to integral equations which have only been solved approximately in the long wavelength limit.

There is another kind of disc shaped transducer problem that has been solved exactly by Miller and Pursey.²¹⁾ It is the problem of the field due to an oscillating normal stress applied over a disc shaped region on an otherwise free surface of a semi-infinite elastic solid. Since in this case the stress alone is specified on the boundary, the problem can be solved exactly. The solution obtained by Miller and Pursey²¹⁾ given in terms of the potentials $\phi(r, z)$ and $\psi(r, z)$ is

$$\begin{aligned}\phi(r, z) &= \frac{a}{v} \int_0^\infty \frac{(2k^2 - k_\beta^2)}{F(k)} \exp(-vz) J_1(ka) J_0(kr) dk \\ \psi(r, z) &= \frac{a}{v} \int_0^\infty \frac{2v}{F(k)} \exp(-v'z) J_1(ka) J_0(kr) dk\end{aligned}\quad (6.10)$$

where

$$\begin{aligned}v &= \sqrt{k^2 - k_\alpha^2} \\ v' &= \sqrt{k^2 - k_\beta^2} \\ F(k) &= (2k^2 - k_\beta^2)^2 - 4k^2 v v'\end{aligned}\quad (6.11)$$



and k_α , k_β are the compressional and shear wave numbers respectively. The radius of the disc is $r = a$ and the modulus of rigidity of the solid is μ . The displacement u_r , and u_z and the stresses T_{rz} and T_{zz} are related to the potentials by

$$\begin{aligned} u_r &= \frac{\partial \phi}{\partial z} + \frac{\partial^2 \psi}{\partial r \partial z} \\ u_z &= \frac{\partial \phi}{\partial z} \left(\frac{\partial^2}{\partial z^2} + k_\beta^2 \right) \psi \\ T_{rz} &= \mu \left(\frac{\partial u_r}{\partial z} + \frac{\partial u_z}{\partial r} \right) \\ T_{zz} &= -\lambda k_p^2 \phi + 2\mu \frac{\partial u_z}{\partial z} \end{aligned} \quad (6.12)$$

The boundary conditions satisfied by this solution are

$$\begin{aligned} \left[\begin{matrix} T_{zz} \\ z = 0 \end{matrix} \right] &= 1 \quad \text{for } r \leq a \\ \left[\begin{matrix} T_{zz} \\ z = 0 \end{matrix} \right] &= 0 \quad \text{for } r > a \\ \left[\begin{matrix} T_{rz} \\ z = 0 \end{matrix} \right] &= 0 \quad \text{for } 0 \leq r < \infty \end{aligned} \quad (6.13)$$

In the spherical coordinate system of (6.1), the far field asymptotic form of the solution valid for large R and small a is given by

$$u_R = -\frac{a^2}{2} \frac{e^{-1R}}{R} \frac{\cos \theta (\xi^2 - 2 \sin^2 \theta)}{F_0(\sin \theta)} \quad (6.14)$$

$$u_\theta = \frac{-1a^2 \xi^3}{2\mu} \frac{e^{-1\xi R}}{R} \frac{\sin 2\theta (\xi^2 \sin^2 \theta - 1)^{1/2}}{F_0(\xi \sin \theta)} \quad (6.15)$$

where the compressional wave number k_α has been replaced by unity in (6.14) and the new shear wave number is given by $\xi = k_\beta/k_\alpha$. The function $F_0(\xi) = (2\xi^2 - \xi^2)^2 - 4\xi^2(\xi^2 - 1)^{1/2}(\xi^2 - 2)^{1/2}$. (6.16)

The corresponding expressions obtained by Mal^{7,11)} for the asymptotic scattered fields due to rigid and weak discs in unbounded elastic solids are



$$\begin{aligned} u_R &= -\frac{1}{\rho \alpha^2} \cos \theta P(k_\alpha \sin \theta) \frac{e^{-ik_\alpha R}}{R} \\ u_\theta &= \frac{1}{\rho \beta^2} \sin \theta p(k_\beta \sin \theta) \frac{e^{-ik_\beta R}}{R} \end{aligned} \quad (6.17)$$

for rigid discs,⁷⁾ and

$$\begin{aligned} u_R &= \text{const.} \frac{e}{R} \frac{ik_\alpha R}{(\xi^2 - 2 \sin^2)} \frac{P(k_\alpha \sin \theta)}{\sin \theta} \\ u_\theta &= \text{const.} \frac{e}{R} \frac{ik_\beta R}{\sin 2\theta} \frac{P(k_\beta \sin \theta)}{\sin \theta} \end{aligned} \quad (6.18)$$

for weak discs.¹¹⁾

The amplitude factor $P(k)$ is obtained from the approximate or numerical solution of the integral equations for the scattered field. In these expressions, ρ is the density of the solid and α and β are the compressional and shear wave velocities respectively. The far field radiation pattern and the amplitude factor $P(k)$ obtained by Mal¹¹⁾ are shown in Figures 5 and 6.

Related Diffraction and Scattering Problems

The diffraction of plane elastic waves by two dimensional straight strips or cracks of finite width has been treated by Ang and Knopoff^{22,23)} and by Loeber and Sih.^{24,25)} More recently, Keer and Luong²⁶⁾ have considered the diffraction of waves and stress intensity factors in cracked layered composites. Non-axisymmetric scattering of plane compressional elastic waves by a rigid disc has also been examined by Datta.²⁷⁾ Related numerical work using the finite-element approach to acoustic scattering from elastic and rigid discs immersed in water has recently been published by Hunt et al.²⁸⁾ Their results complement those of Ermolov²⁹⁾ and Cohen³⁰⁾ based on analytical approximations to acoustic scattering by discs. A comprehensive review of acoustic (and electromagnetic) scattering from discs and other simple shapes has been compiled by Bowman, Senior, and Uslenghi³¹⁾ and some useful information on the diffraction of elastic waves is contained in a selected review by Pao and Mow.³²⁾ In addition to the problems of scattering of elastic waves from half-planes, discs, and strips, another two dimensional scattering surface of interest is a crack occupying a quarter plane, i.e. one quadrant of an (x,y) plane. This problem and the solution of related integral equations has been discussed in a series of papers by Kraut.³³⁻³⁶⁾ Unfortunately, an exact analytical solution of the quarter plane scattering problem for elastic waves does not appear to be possible.

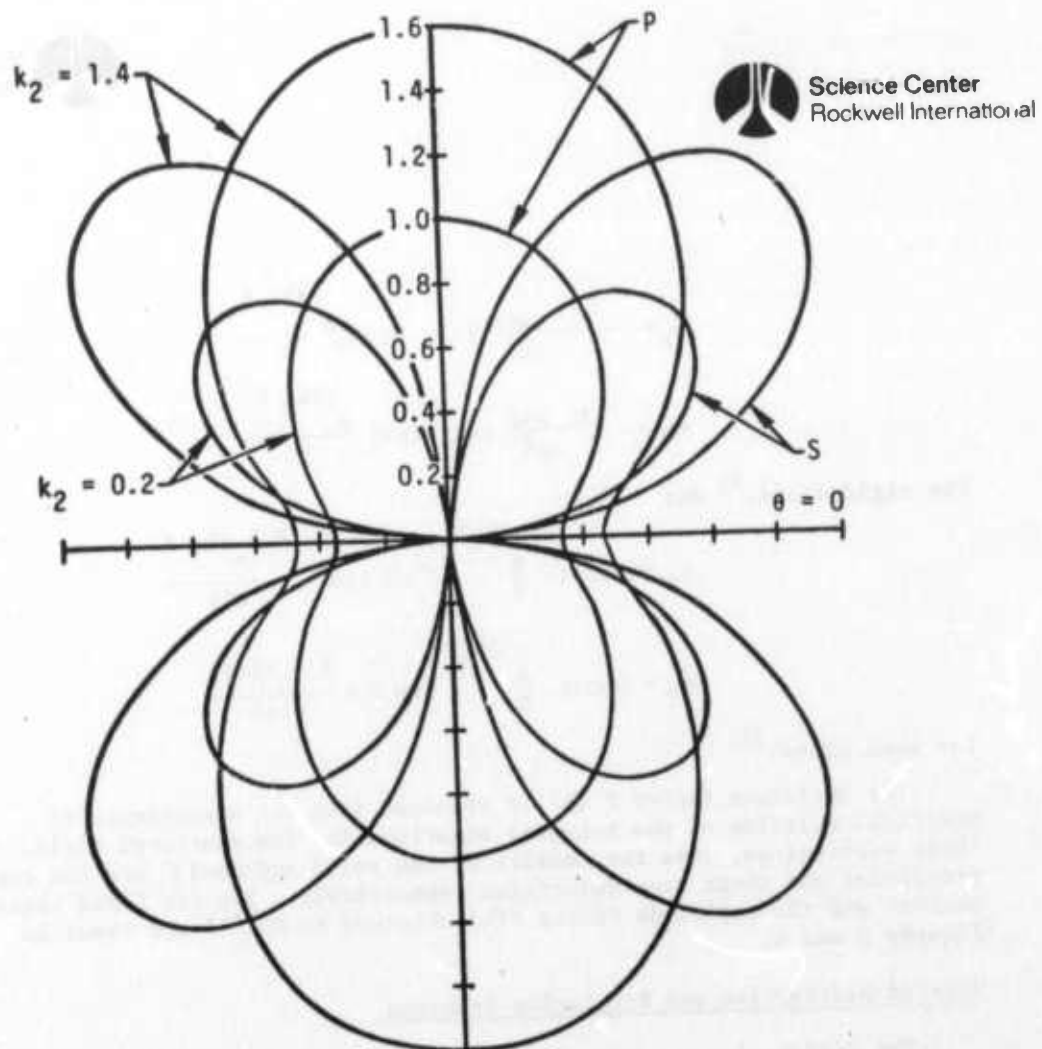


Fig. 5. Radiation field of the diffracted P and S waves for incident P waves.

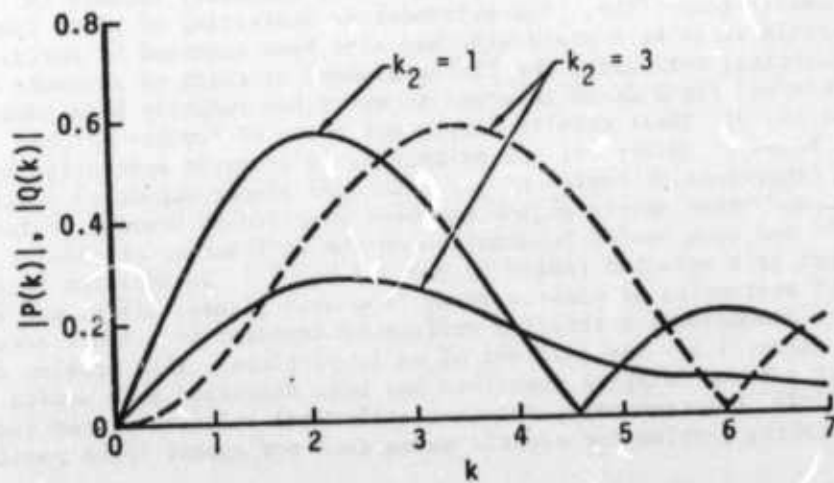


Fig. 6. Amplitudes of $P(k)$ (solid curves) and $Q(k)$ (dashed curves). For $k_2 = 1$, the amplitudes of $P(k)$ and $Q(k)$ are almost identical.

Conclusion

In a brief review such as this a great many topics of current interest in elastic wave propagation have to be omitted. These include recent advances in finite difference ^{37,38)} and finite element methods, ³⁹⁾ application of Keller's geometric theory of diffraction ^{40,41)} to elastic wave propagation problems, ⁴²⁾ first motion methods in the scattering of elastic pulses, ⁴³⁾ variational methods, ⁴⁴⁾ numerical solution of integral equations arising in scattering problems, applications of the W.K.B. and Born approximations to elasticity, use of the Watson transformation, ³¹⁾ asymptotic expansions, perturbation methods, as well as long, short and intermediate wavelength approximations in general.

Many problems of interest to NDE involve scattering from cracks and flat bottom holes in bounded or semi-infinite elastic solids as opposed to unbounded solids. The presence, in addition to a crack, of one or more extra free surfaces greatly complicates the mathematics of the scattering problem. The development of effective approximate methods to solve such problems and comparison of the results obtained with experiment can contribute significantly to progress in NDE.

References

1. M. M. Fridman, The Diffraction of a plane elastic wave by a semi-infinite rigid plane, Dokl. Akad. Nauk., U.S.S.R., 60, 1145 (1948).
2. A. W. Maue, The Diffraction of Elastic Waves by a Half Plane, Z. Fur Agnew. Math. U. Mech. 33, 1 (1953).
3. A. T. De Hoop, Representation Theorems for the Displacement in an Elastic Solid and Their Application to Elastodynamic Diffraction Theory, Sc.D. Thesis, Technische Hogeschool, Delft, Holland (1958).
4. C. J. Bouwkamp, Diffraction Theory, Repts. on Progress in Phys. XVII, 35 (1954).
5. L. Filipczynski, Scattering of a plane longitudinal wave on a free surface of a disc in a solid medium, Proc. of Vibration Problems, Volume 2, No. 1 (6), p. 41, Warsaw (1961).
6. I. A. Robertson, Diffraction of a plane longitudinal wave by a penny shaped crack, Proc. Camb. Phil. Soc. 63, 229 (1967).
7. A. K. Mal, D. D. Ang, and L. Knopoff, Diffraction of Elastic Waves By a Rigid Circular Disc, Proc. Camb. Phil. Soc. 64, 237 (1968).
8. A. K. Mal, Diffraction of Elastic Waves by a Penny Shaped Crack, Q. Appl. Math. 26, 231 (1968).



9. A. K. Mal, Dynamic Stress Intensity Factor for an Axisymmetric Loading of The Penny Shaped Crack, *Int. J. Eng. Sci.* 6, 623 (1968).
10. A. K. Mal, Dynamic Stress Intensity Factor for a non-axisymmetric Loading of The Penny Shaped Crack, *Int. J. Eng. Sci.* 6, 725 (1968).
11. A. K. Mal, Interaction of Elastic Waves With a Penny Shaped Crack, *Int. J. Eng. Sci.*, 8, 381 (1970).
12. G. C. Sih and J. F. Loeber, Normal Compression and Radial Shear Waves Scattering at a Penny Shaped Crack in An Elastic solid, *J. Acoust. Soc. Am* 46, 711 (1969).
13. H. D. Garbin and L. Knopoff, The Compressional Modulus of a Material Permeated By A Random Distribution of Circular Cracks; *Q. of Appl. Math.* 30, 453 (1973).
14. H. D. Garbin and L. Knopoff, The Shear Modulus of a Material Permeated by A Random Distribution of Free Circular Cracks, Publication No. 1311, *Inst. of Geophysics and Planetary Physics, Univ. of Calif., Los Angeles.*
15. H. D. Garbin and L. Knopoff, Elastic Moduli of a Medium With Liquid Filled Cracks, Publication No. 1312, *Inst. of Geophysics and Planetary Physics, Univ. of Calif., Los Angeles.*
16. P. J. Barratt and W. D. Collins, The Scattering Cross-Section of an Obstacle in an Elastic Solid For Plane Harmonic Waves, *Proc. Camb. Phil. Soc.* 61, 969 (1965).
17. C. F. Ying and R. Truell, Scattering of a Plane Longitudinal Wave by a Spherical Obstacle in an Isotropically Elastic Solid, *J. Appl. Physics* 27, 1086 (1956).
18. N. G. Einspruch, E. J. Witterholt and R. Truell, Scattering of a Plane Transverse Wave by a Spherical Obstacle in an Elastic Medium, *J. Appl. Phys.* 31, 806 (1960).
19. I. A. Robertson, Forced Vertical Vibration of a Rigid Circular Disc on a Semi-Infinite Elastic Solid, *Proc. Camb. Phil. Soc.* 62, 547 (1966).
20. G. Johnson and R. Truell, Numerical Computations of Elastic Scattering Cross-Sections, *J. Appl. Phys.* 36, 3466 (1965).
21. G. F. Miller and H. Pursey, The Field and Radiation Impedance of Mechanical Radiators on the Free Surface of a Semi-Infinite Isotropic Solid, *Proc. Roy. Soc. London, Ser. A.*, 223, 521 (1954).
22. D. D. Ang and L. Knopoff, Diffraction of Vector Elastic Waves by a Clamped Finite Strip, *Proc. Natl. Acad. Sci., U.S.A.*, 52, 201 (1964).

23. D. D. Ang and L. Knopoff, Diffraction of Vector Elastic Waves by a Finite Crack, Proc. Nat. Acad. Sci. U.S.A., 52, 1075 (1964).
24. J. F. Loeber, and G. C. Sih, Diffraction of Antiplane Shear Waves by a Finite Crack, J.A.S.A. 44, 90 (1968).
25. G. C. Sih and J. F. Loeber, Wave Propagation in An Elastic Solid With a Line Discontinuity or Finite Crack, Quart. Appl. Math 27, 193 (1969).
26. L. M. Keer and W. C. Luong, Diffraction of Waves and Stress Intensity Factors in a Cracked Layered Composite, J. A. S. A., 56, 1681 (1974).
27. S. K. Datta, The Diffraction of a Plane Compressional Elastic Wave by a Rigid Circular Disc, Quart. Appl. Math. 28, 1 (1970).
28. J. T. Hunt, M. R. Knittel, C. S. Nichols, and D. Barach, Finite-element approach to acoustic scattering from elastic structures, J.A.S.A., 57, 287 (1975).
29. I. N. ERmolov, Application of the Theory of a Scalar Sound Field For the Analysis of the Acoustic Path of an Ultrasonic Flow Detector, Society Physics-Acoustics 5, 248 (1959).
30. F. R. Cohen, Acoustic Scattering by Discs, SCTR-73-15, Science Center/Rockwell International, Thousand Oaks, Calif. 91360, November 13, 1973. (Unpublished).
31. J. J. Bowman, T. B. A. Senior, and P. L. E. Uslenghi, Electromagnetic and Acoustic Scattering by Simple Shapes, North Holland Publishing Co.- Amsterdam, 1969.
32. Y. H. Pao, and C.C. Mow, Diffraction of Elastic Waves and Dynamic Stress Concentrations, Crane, Russak and Company, Publishers, New York, 1973.
33. E. A. Kraut, Diffraction of Elastic Waves by a Rigid 90° Wedge. Part I, Bull. Seism. Soc. of Amer. 58 (3), 1083 (1968).
34. E. A. Kraut, Diffraction of Elastic Waves by a Rigid 90° Wedge, Part II, Bull. Seism. Soc. Amer. 58 (3), 1097 (1968).
35. E. A. Kraut, Elastic Wave Propagation and the Factorization of Matrix-Valued Functions of Several Complex Variables, J. Math. Phys. 9 (9), 1481 (1968).
36. E. A. Kraut, On Equations of the Wiener-Hopf type in Several Complex Variables, Proc. Amer. Math. Soc. 23 (1), 24 (1969).

37. Z. Alterman and D. Loewenthal, Computer Generated Seismograms, Methods of Computational Physics, Vol. 12, pg. 35, Academic Press; N.Y., 1972.
38. D. M. Boore, Finite Difference Methods for Seismic Wave Propagation In Heterogeneous Materials, Methods of Computational Physics, Vol. 11, p. 1, Academic Press, N.Y., 1972.
39. J. Lysmer and L. A. Drake, A finite Element Method for Seismology, Methods of Computational Physics, Vol. 11, p. 181, Academic Press, N.Y., 1972.
40. J. B. Keller, Diffraction by an Aperture, J. Appl. Physics 28, 426 (1957).
41. J. B. Keller, Geometrical Acoustics, The Theory of Weak Shock Waves, J. Appl. Physics 25, 938 (1954).
42. F. C. Karal, Jr. and J. B. Keller, Elastic Wave Propagation in Homogeneous and Inhomogeneous Media, J.A.S.A. 31, 694 (1959).
43. L. Knopoff and F. Gilbert, First Motion Methods in Theoretical Seismology, J.A.S.A. 31, 1161 (1959).
44. H. H. Demarest, Jr., Cube Resonance Method to Determine the Elastic Constants of Solids, J.A.S.A. 49, 768 (1971).



Science Center
Rockwell International

SAMPLE PREPARATION

N. E. Paton
Science Center, Rockwell International

ABSTRACT

Standard NDE samples of various metals and alloys containing defects of known geometry were fabricated. Some conventional flat bottom hole samples were made, but the majority of the samples contained internal defects of known size, shape and location and were fabricated by a diffusion bonding technique. The material used for the diffusion bonded samples was exclusively Ti-6Al-4V since the bonding conditions for this alloy are well characterized. Methods for successfully diffusion bonding steel and aluminum alloys have been investigated, with the ultimate aim of making NDE standard samples from these materials by diffusion bonding.

PROJECT I, UNIT V, TASK 1

SAMPLE PREPARATION

N. E. Paton
Science Center, Rockwell International

Objectives

The following objectives were established for this task at the initiation of the program.

1. To fabricate a set of standard NDE samples containing defects of known size, shape and location, the metals and alloys used for sample preparation to be structural engineering materials. Diffusion bonding to be used to fabricate internal defects in suitable materials such as titanium alloys.
2. To develop methods of preparing standard NDE samples from metals such as steels and aluminum alloys which cannot currently be diffusion bonded by accepted techniques.

Background and Introduction

In a previous effort⁽¹⁾ techniques were developed for introducing internal defects -either voids or inclusions- into bulk samples of titanium alloys by diffusion bonding. In order to avoid changing the shape and volume of an internal defect it is important to keep the bulk strains low, and consequently the pressure used in the diffusion bonding process must also be low. This can be successfully accomplished only by careful attention to surface preparation, but techniques for achieving the desired results have already been developed⁽¹⁾. A typical example of the types of defect which can be produced is shown in Fig. 1. These techniques have been further developed for Ti alloys under the present program and also extend to certain steels.

Sample Preparation Methods

Methods used for preparing standard samples for ultrasonic non-destructive testing depended on the type of defect desired and the alloy. Four types of defects have been made so far, and these are illustrated in Figure 2. The defects are characterized as to their geometry; Type 1 being a flat-bottomed-hole, Type 2 a sphere, Type 3 an oblate spheroid and Type 4 a prolate spheroid. The flat-bottom-hole was made by conventional machining techniques, and the accuracy with which a flat bottom was obtained in different materials was checked by sectioning trial samples. These results are shown in Fig. 3 and demonstrate that an acceptable flat geometry was obtained.

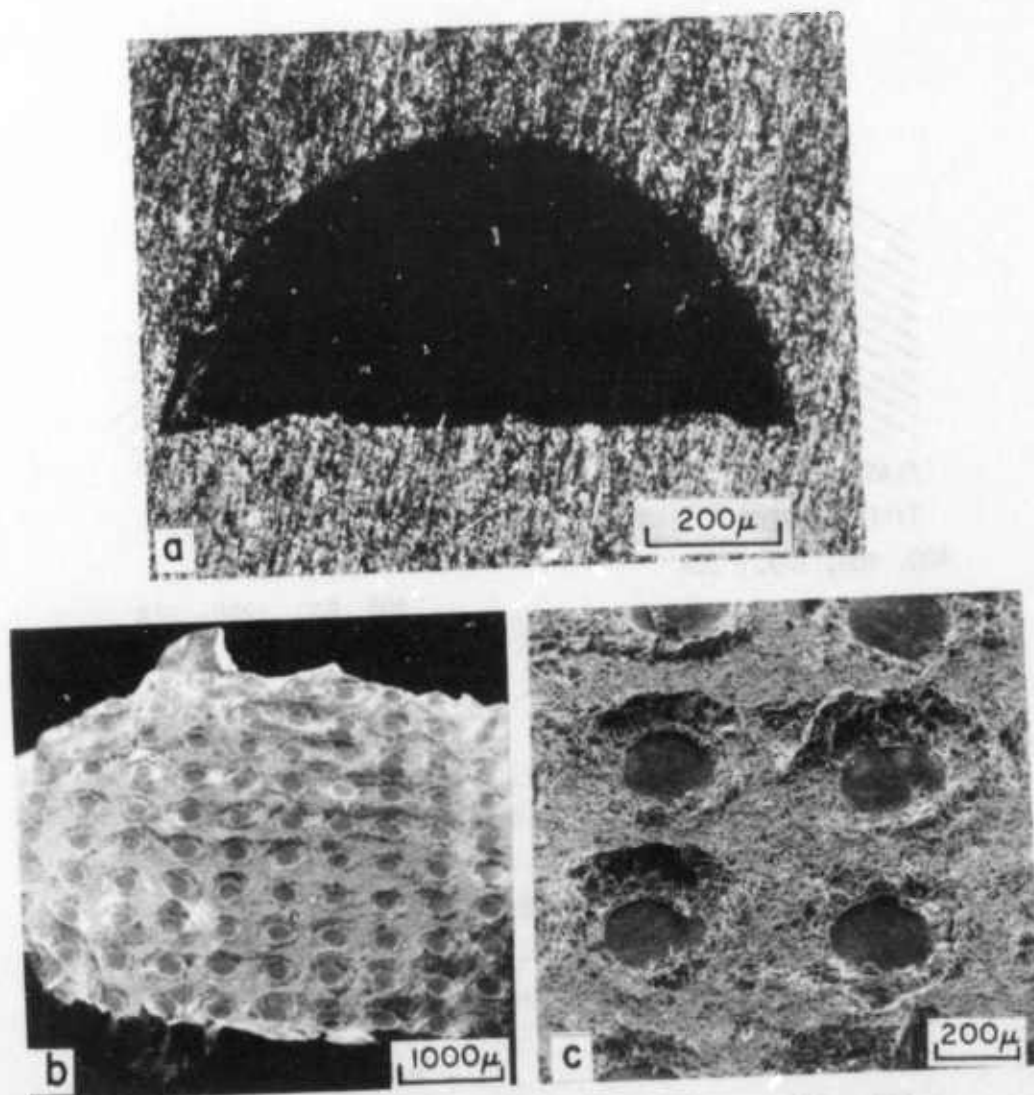
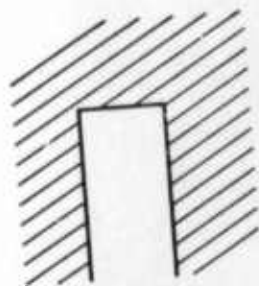
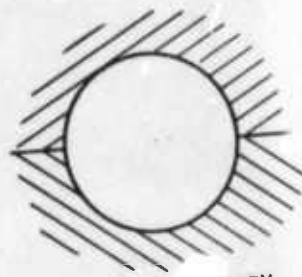


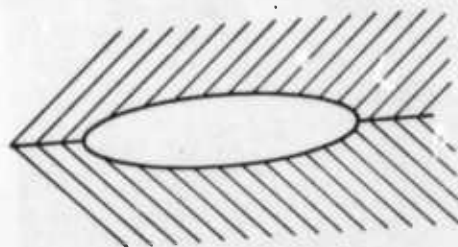
Fig. 1 Examples of internal defect geometries made by diffusion bonding
 (a) cross section of a hemispherical defect ~ 38 mils in diameter,
 (b) fracture surface of a tensile specimen containing a 10×10
 array of .008 inch (200 μ m) dia hemispheres, with a .020 inch (500 μ m)
 spacing. (c) Same as (b) at a higher magnification.



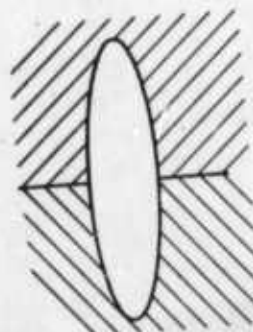
FLAT BOTTOM HOLE
TYPE 1 DEFECT
400, 800, 1200 μ DIA



SPHERICAL CAVITY
TYPE 2 DEFECT
400, 800, 1200 μ DIA

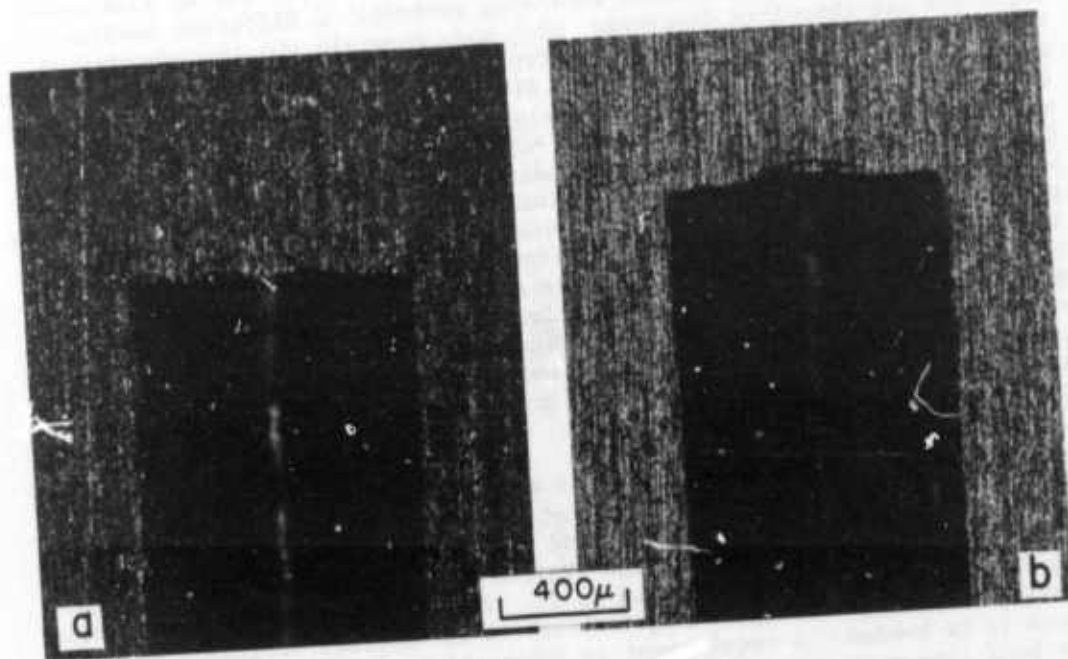


OBLATE SPHEROID
TYPE 3 DEFECT
800 μ DIA.
200, 400 μ HIGH



PROLATE SPHEROID
TYPE 4 DEFECT
1600 μ HIGH
400, 800 μ DIA

Fig. 2 Defect geometries produced during the program.



2024AL

FLAT BOTTOM HOLES

Ti-6Al-4V

Fig. 3 Flat bottom holes 800 μ m in diameter in (a) 2024Al (b) Ti-6Al-4V.

All of the other defects made were internal defects and as such could not be produced by conventional machining methods. A diffusion bonding technique was therefore developed which made possible the introduction of internal defects of controlled geometry. With present methods only titanium and its alloys can be satisfactorily diffusion bonded. With titanium alloys, the oxide, which is always formed during surface preparation, goes into solution during the high temperature bonding cycle. This yields an oxide free, high quality, bond which is indistinguishable from the parent metal both ultrasonically and metallographically. In addition, failure of tensile tested samples did not occur in the bond plane. Thus high quality NDE samples can be produced containing internal defects. Unfortunately, this process cannot presently be applied to Al and steel alloys because of the difficulty encountered with oxide inclusions at the bond line. This results from the inability of these metals to dissolve their oxides, in contrast to the situation with titanium. Efforts are being made to find a solution to this problem, and a section on bonding of Al and steel alloys included at the end of this report.

One further important requirement must be met in the production of internal defects of controlled size and geometry, and that is the bonding pressures must be low in order to limit the macroscopic specimen strain, and in turn, prevent changes in the desired defect geometry. In practice, the macroscopic strain was limited to 2%. This requirement for low bonding pressures enforces stringent requirements on the surface roughness of the faces to be bonded. A requirement in fabrication of such samples is that the bond line must contain no defects such as voids, apart from those introduced intentionally. This, of course, conflicts with the requirement to use a low bond pressure, and special surface preparation techniques must be employed to satisfy these conflicting conditions.

Recent work by Garmong and Paton⁽²⁾ on the theory of diffusion bonding provides a method of calculating the minimum bonding time and pressure for a void-free bond, from a knowledge of the constitutive behavior of the material to be bonded. They showed that two features of the surfaces to be bonded are important factors in controlling the time and pressure for a satisfactory bond. They are first, the overall surface flatness (or long wavelength asperity height) and second, the fine scale surface roughness (or short wavelength asperity height). Of these two, the first was found to be the most important factor. Thus, short bond times and low pressures can most readily be employed with an optically flat, but not necessarily mirror finish. These criteria were successfully followed in preparing surfaces prior to diffusion bonding.

Bonding of titanium Ti-6Al-4V was successfully accomplished by first lapping the surfaces to be bonded to a flatness tolerance of four optical bands. This procedure resulted in void-free bonds whereas conventional machining or grinding was most unsatisfactory yielding bonds with a high void density under the pressures and temperatures employed.

A typical sample after bonding is shown in Fig. 4(a), while the sample halves and locating ring ensuring their correct alignment are shown in Fig. 4(b), (c) and (d) respectively. The lack of a mirror finish on the lapped surfaces is evident in Figures 4(b) and 4(c).

The specific conditions used for sample surface preparation and bonding are listed in Table II, together with details, the cleaning procedure and the parameters used for diffusion bonding. The precise bonding conditions employed depend on the alloy chemistry and microstructure, and satisfactory results cannot necessarily be obtained by simply reproducing the conditions quoted here⁽²⁾.

TABLE I

Surface Preparation and Diffusion Bonding Procedures

<u>Lapping</u>	Surface ground and lapped to #4 finish, flat to within four optical bands.
<u>Cleaning</u>	<ol style="list-style-type: none"> 1. Wash in alcohol 2. Rinse in distilled water 3. Ultrasonic clean in detergent 4. Rinse in distilled water 5. Ultrasonic clean in distilled water 6. Dry dust free
<u>Diffusion Bonding</u>	<ol style="list-style-type: none"> 1. Heat in vacuum of better than 10^{-5} torr to specified temperature (900 or 926°C)- see Table III. 2. Load to 500 psi for 30 m/ns. 3. Cool in vacuum

Material Specifications

Samples were made from 2024 Al, 1100 Al, Commercial Purity Ti, Ti-6Al-4V, and A533B steel. The compositions of these alloys are shown in Table III.

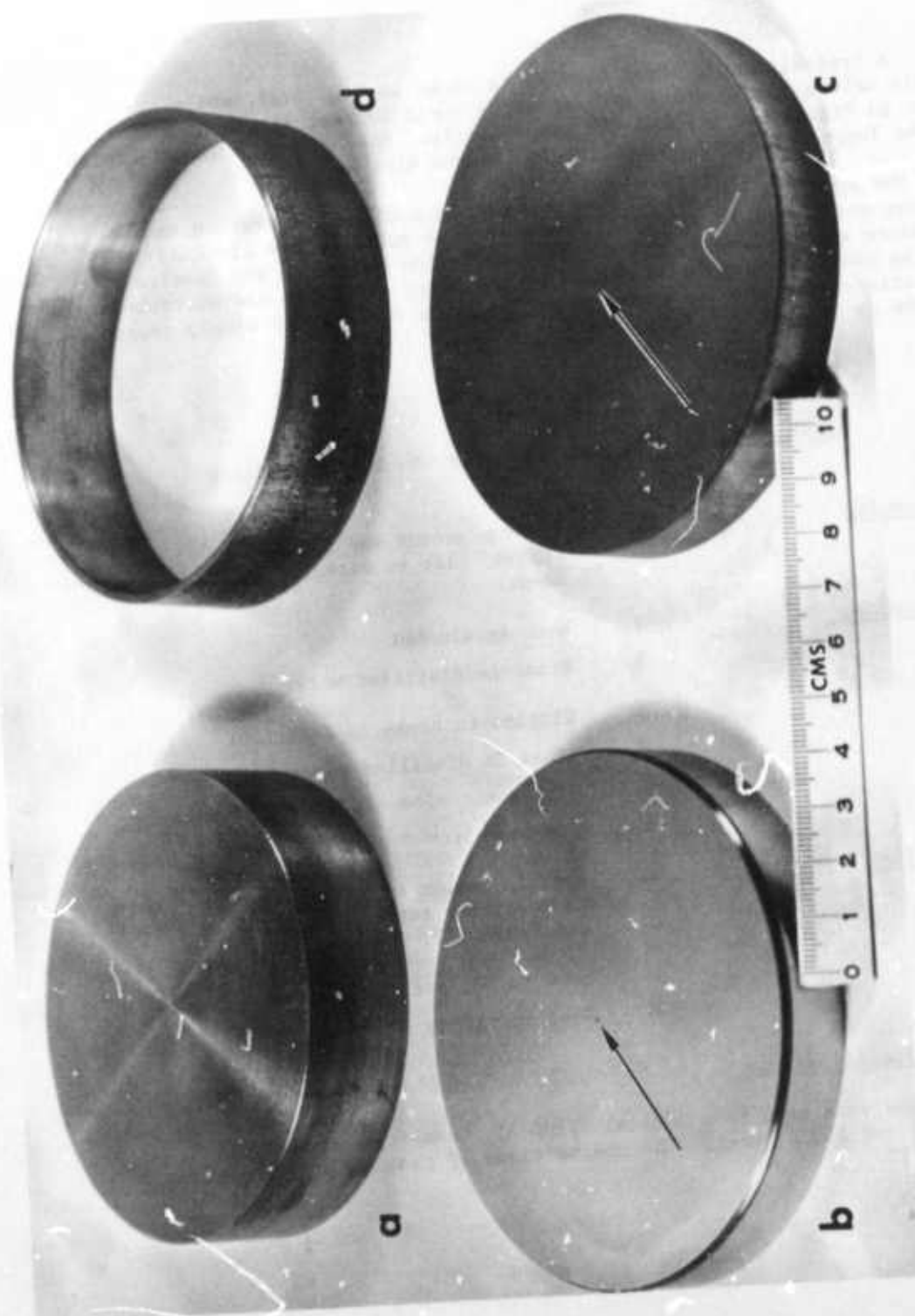


Fig. 4 Typical diffusion bonded sample (a) finished sample (b) and (c) lapped top and bottom halves containing a prolate spheroid (arrowed) (d) 4130 steel alignment ring.

TABLE II

Alloy Compositions

2024 Al	Al - 4.5% Cu - 1.5% Mg - 0.6% Mn
1100 Al	99.0% Al
75A Ti	99.0% Ti
Ti-6Al-4V (Heat #D4781)	Ti - 6.32% Al - 4.15% V - 0.15% O ₂ 0.16% Fe*
Ti-6Al-4V (Heat #D4705B)	Ti - 6.30% Al - 4.09% V - 0.17% O ₂ 0.14% Fe*
A533B Steel	Fe - 0.25% C - 1.3% Mn - 0.5% Mo - 0.5% Ni

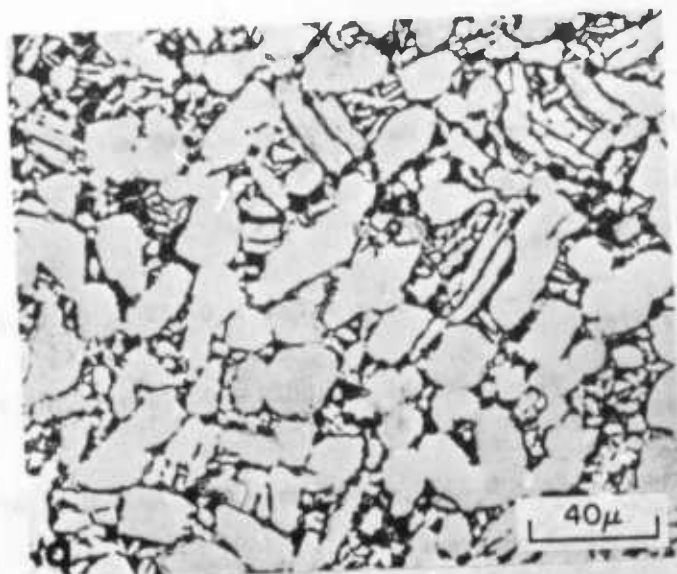
* Actual chemical analyses

Since most of the diffusion bonded samples were made from Ti-6Al-4V, the microstructure and texture of this material was carefully characterized. The microstructures of the two heats of Ti-6Al-4V, after a heat treatment cycle duplicating that used in the diffusion bonding are shown in Fig. 5. The equiaxed, two phase ($\alpha + \beta$) microstructure with a grain size of $\sim 20 \mu$ is evident. In the micrographs the hexagonal α phase appears light while the bcc β phase appears dark.

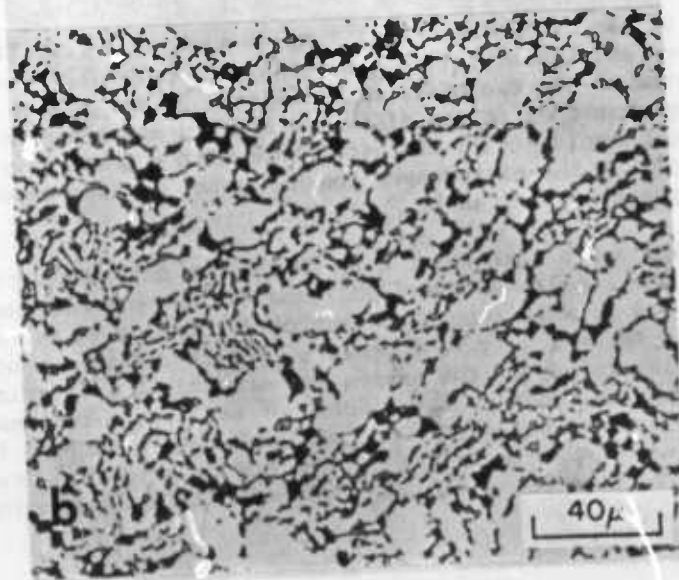
The crystallographic texture of heat #D4781 was determined by a standard x-ray method and the results of the (0002) and (10 $\bar{1}$ 0) pole figures showed that the texture was no more than a maximum of 2 x random in either case. This is considered to be a very weak texture, and therefore was not considered a problem in any of the subsequent acoustic NDI experiments. In a further attempt to minimize the effects of texture, a reference mark was placed on the side of both heats of bar stock before cutting into sections for the samples. The sample top and bottom were then reassembled without rotation relative to one-another prior to diffusion bonding.

Sample Inventory

Samples having three different external geometries were fabricated during the course of this program, depending on experimental requirements. These are shown in Figures 6, 7 and 8. Figures 6 and 7 are the 2 $\frac{1}{4}$ " diameter samples made at the beginning of the program, Fig. 7 showing the longer sample (3 11/16 inches high) intended to be machined at a later date into a sphere centered on the defect for investigation of the angular

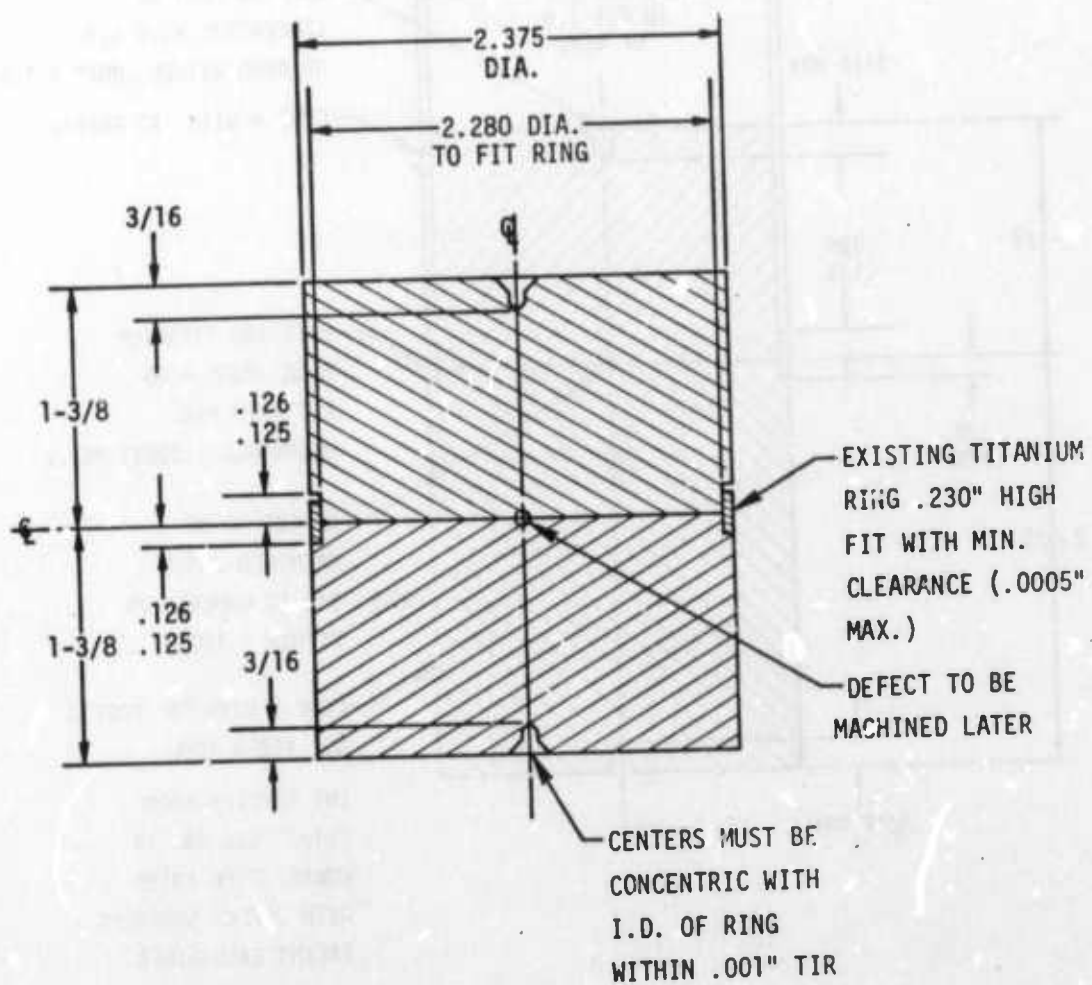


D4705B



D4781

Fig. 5 Microstructures of the two heats of Ti-6Al-4V (a) Heat D4705B used for 4 inch diameter samples. (b) Heat D4781 used for 2 ½ inch diameter samples.



NDE DEFECT SAMPLE ASSEMBLY

FINISHED DIMENSIONS 2.250 ± .002 in DIA
2.250" HIGH

MATERIAL Ti-6Al-4V HEAT # D4781 (TIMET)

Fig. 6 Sample assembly for 2 1/4 inch diameter specimen.



MATERIAL - Ti-6Al-4V HEAT # D4781 (TIMET)

174

dependence of scattering from spheroidal defects. Fig. 8 shows the larger diameter (4 inch) samples made later in the program. An inventory of all samples made during the course of the program is given in Table III. This table includes information on flat-bottom-hole samples as well as the external dimensions, serial number, sample code number, heat treatment and date delivered. Details of the sample code number, which permits identification of the alloy and defect geometry, are given at the end of the Table III.

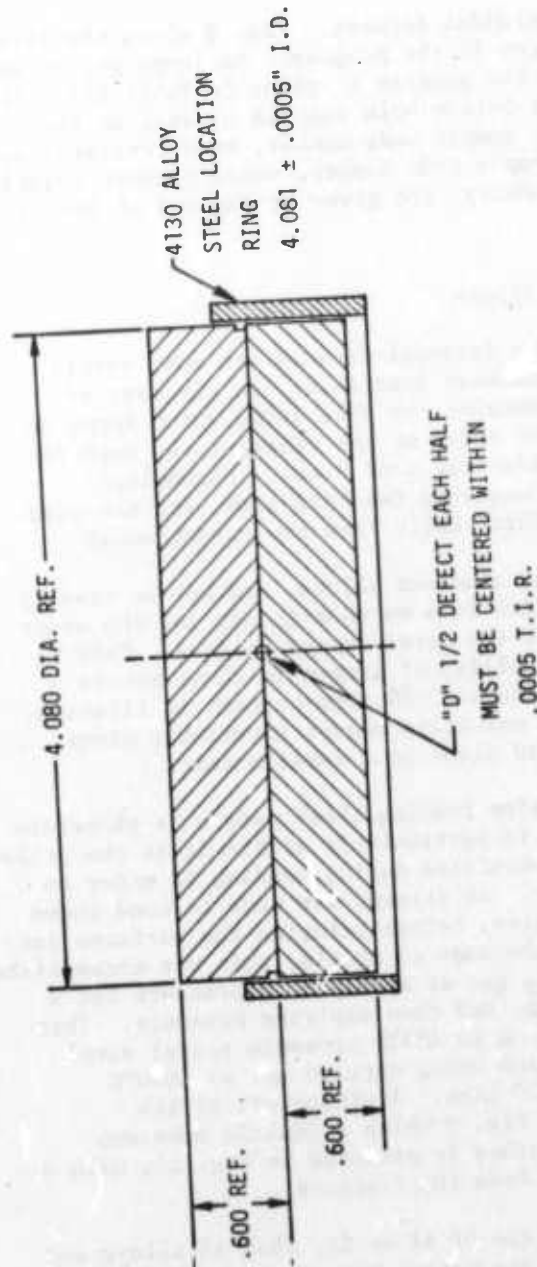
Diffusion Bonding of Steel and Al Alloys

Standard test blocks containing internal defects are most easily produced by the diffusion bonding methods described. In the case of titanium, this method works well, because the thin oxide which forms on the surface dissolves readily in the metal at the temperatures used for bonding, giving rise to a clean oxide-free bond plane. Mechanical failure in a tensile test does not occur in the bond line, and the bond plane is metallographically indistinguishable from the parent metal.

Other metals, such as steel and aluminum alloys, are not so readily bonded however, since the oxides which form on them in air (of the order of 100 Å thick) do not dissolve into the metal during bonding. This is on account of the limited solid solubility of oxygen in these metals - a few hundred ppm at most, as compared to ~30 atom percent in titanium. The resulting planar array of oxide particles almost invariably gives rise to premature failure at the bond plane in a tensile test.

A method of successfully diffusion bonding these metals is therefore needed. A solution to this problem is particularly difficult in the present case, where only 1 to 2% strain is permitted during bonding in order to preserve the desired defect geometry. An attempt was made to bond these materials by removing the surface oxide, before bringing the surfaces into contact and applying pressure. In the case of steels, this was accomplished by flushing the vacuum system with H₂ gas at atmospheric pressure for a period of time, evacuating the system, and then applying pressure. This procedure proved entirely successful on an A533B pressure vessel steel with the H₂ flush and bonding operation being carried out at 1000°C and a bond pressure of 5000 psi for 30 mins. A micrograph of the resulting diffusion bond is shown in Fig. 9 which a tensile specimen containing a bond produced by this method is pictured in Fig. 10, with a pencil indicating the bond line away from the fracture.

Hydrogen gas will not reduce oxides of Al or Cr, thus Al alloys and stainless steels cannot be bonded in the manner described above, and attempts are being made to use Ar sputtering to clean the surfaces of these metals prior to bonding. It is anticipated that such methods will work on these alloys, but at a considerable cost in experimental complexity.



NDE DEFECT SAMPLE ASSEMBLY

FINISHED DIMENSIONS	4.000 ± .002 in DIA.
	1.000 in HIGH
MATERIAL	Ti-6Al-4V
	HEAT # 047058 (ORMET)

Fig. 8 Sample assembly for 4 inch diameter specimen.

TABLE III
Sample Inventory
NDE SAMPLES DELIVERED OCTOBER 1, 1974 TO JULY 10, 1975

Serial No.	Code *	Height (in.)	Diameter (in.)	Date	Heat Treatment (Heat No.)
1	0-0-64	1	2½	10/1/74	None (D4781)
2	0-0-64	1	2½	10/1/74	None (D4781)
3	0-0-T	1	2½	10/1/74	None (D4781)
4	0-0-T	1	2½	10/1/74	None (D4781)
5	0-0-24	1	2½	10/1/74	None (D4781)
6	0-0-24	1	2½	10/1/74	None (D4781)
7	0-0-A	1	2½	10/1/74	None (D4781)
8	0-0-A	1	2½	10/1/74	None (D4781)
10	1-12-T	2	2½	10/1/74	None
11	1-12-24	2	2½	10/1/74	None
12	2-4-64	2	2½	10/1/74	DB, 1700°F (D4781)
13	2-8-64	2	2½	10/1/74	DB, 1700°F (D4781)
14	2-12-64	2	2½	10/1/74	DB, 1700°F (D4781)
15	1-8-64	2	2½	10/8/74	DB, 1700°F (D4781)
16	1-8-64	2	2½	10/8/74	DB, 1700°F (D4781)
17	1-8-T	2	2½	10/8/74	None
18	1-8-T	2	2½	10/8/74	None
19	1-8-24	2	2½	10/8/74	None
20	1-8-24	2	2½	10/8/74	None
21	1-8-A	2	2½	10/8/74	None
22	1-8-A	2	2½	10/8/74	None
23	1-4-24	2	2½	10/8/74	None
24	1-8-24	2	4	10/18/74	None
25	1-12-24	2	4	10/18/74	None
26	1-24-24	2	4	10/18/74	None
27	1-32-24	2	4	10/18/74	None
28	0-0-64	2	2½	1/15/75	None (D4781)
29	0-0-64	2	2½	1/15/75	None (D4781)
30	2-8-64	2	2½	1/15/75	DB, 1700°F (D4781)



Science Center
Rockwell International

TABLE III (Continued)

Serial No.	Code *	Height (in.)	Diameter (in.)	Date	Heat Treatment (Heat No.)
31	1-4-T	1½	2¼	2/18/75	None
32	1-4-64	1½	2¼	2/18/75	None (D4781)
33	2-4-64	2¼	2¼	3/3/75	DB, 1700°F (D4781)
34	2-8-64	2¼	2¼	3/3/75	DB, 1700°F (D4781)
35	B-2-4-64	3 11/16	2¼	3/7/75	DB, 1700°F (D4781)
36	B-2-8-64	3 11/16	2¼	3/7/75	DB, 1700°F (D4781)
37	B-2-12-64	3 11/16	2¼	3/7/75	DB, 1700°F (D4781)
38	B-3-2-64	3 11/16	2¼	3/24/75	DB, 1700°F (D4781)
39	B-3-4-64	3 11/16	2¼	3/24/75	DB, 1700°F (D4781)
40	B-4-4-64	3 11/16	2¼	3/27/75	DB, 1700°F (D4781)
41	B-4-8-64	3 11/16	2¼	3/28/75	DB, 1700°F (D4781)
42	0-0-64	6	2¼	4/28/75	1700°F, 30 min. (D4781)
43	0-0-64	1	4	4/28/75	1700°F, 30 min. (D4781)
44	0-4-64	1	4	4/28/75	1700°F, 30 min. (D4705B)
45	1-8-64	1	4	4/28/75	1700°F, 30 min. (D4705B)
46	1-12-64	1	4	4/28/75	1700°F, 30 min. (D4705B)
47	2-4-64	1	4	6/20/75	DB1650°F (D4705B)
48	2-8-64	1	4	6/20/75	DB1650°F (D4705B)
49	2-12-64	1	4	6/30/75	DB1650°F (D4705B)
50	3-12-64	1	4	7/7/75	DB1650°F (D4705B)
51	3-4-64	1	4	7/8/75	DB1650°F (D4705B)
52	4-4-64	1	4	7/9/75	DB1650°F (D4705B)
53	4-8-64	1	4	7/10/75	DB1650°F (D4705B)
54	2-8-64	1	4	7/10/75	DB1650°F (D4705B)

*Sample code describes defect type, size and material as follows:

Defect Type	Defect Size μm x 100	Material
0 - No defect		T - CP Titanium
1 - Flat Bottom Hole		64 - Ti-6Al-4V
2 - Spherical Cavity		A - 1100 Al
3 - Oblate Spheroid		24 - 2024 Al
4 - Prolate Spheroid		
B - Defect displaced from mirror plane		

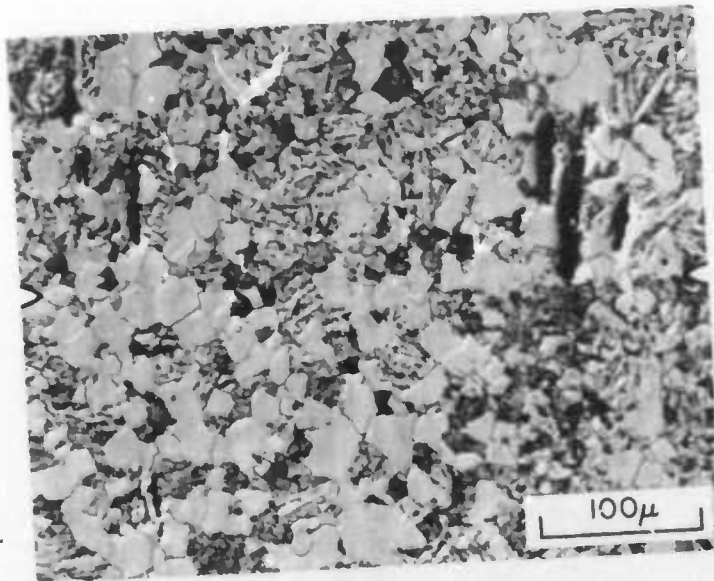


Fig. 9 Bond line (arrowed) in A5333 steel produced by reducing the surface oxide in H_2 at $1000^\circ C$ and then bonding at 500 psi for 30 mins.

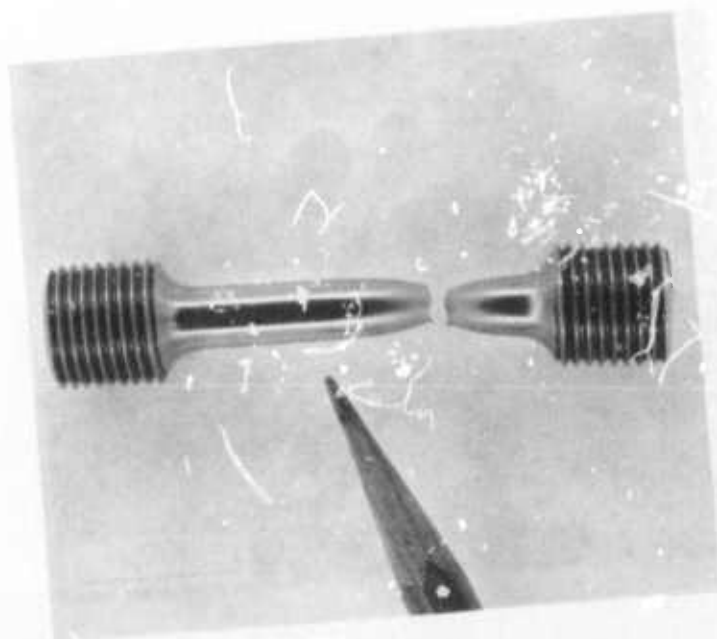


Fig. 10 Failed tensile test specimen with a bond line produced as described in the Fig. 7 caption at the location indicated by the pencil.

References

1. B. R. Tittmann, H. Nadler and N. E. Paton, "A Technique For Studies of Ductile Fracture in Metals Containing Voids or Inclusions," Submitted to Met. Trans.
2. G. Garmong, N. E. Paton and A. S. Argon, "Attainment of Full Interfacial Contact During Diffusion Bonding," Met. Trans., 6A, 1269 (1975).

Acknowledgments

The author is grateful for the assistance of the Science Center Machine Shop, P. Q. Sauers, Dr. G. Garmong, H. Nadler, F. Nevarez and E. Wright and J. C. Chesnutt during the course of this program.



Science Center
Rockwell International

PROJECT II

BOND STRENGTH

UNIT I - Acoustical Interactions At Thin Interfaces

Task 1 Measurement of Adhesive Bond Strength With
 Ultrasonic Wave Interactions
 G. Alers, Science Center, Rockwell International

Task 2 Ultrasonic Signal Processing Methods For
 Adhesive Bond Strength Measurement
 J. Rose and P. A. Meyer, Drexel University

UNIT II - Nature of Bonded Interface Degradation in Composites

Task 1 Development of a Nondestructive Test For
 Strength Degradation Composites
 D. H. Kaelble, Science Center, Rockwell International



Science Center
Rockwell International

PROJECT 11, UNIT I, TASK 1

ULTRASONIC WAVE INTERACTION WITH INTERFACES

G. A. Alers and L. J. Graham
Science Center, Rockwell International

Summary and Conclusions

Adhesive bonds of different mechanical strength between identical materials were fabricated by both chemical and thermal means. Table I summarizes the results obtained by listing the measured mechanical strength and the corresponding amplitude of the ultrasonic signal reflected directly backwards from the bond plane relative to a planar Lucite-to-air interface. It can be concluded that:

- (1) Chemically formed bonds that use a solvent at the interface form a layer approximately 60 microns thick whose acoustic properties differ from the surroundings.
- (2) The strength of the chemically formed bond can be measured by the amplitude of the ultrasonic wave reflected from the layer which, in turn, is determined by the degree of acoustic mismatch between the layer and the surroundings.
- (3) The strength of the thermally formed bonds was found to be independent of the ultrasonic reflection characteristics of the bond plane.
- (4) The ultrasonic reflection strength of the thermally formed bonds was largely frequency independent over the frequency range examined (2 to 10 MHz). The mathematical models available for predicting this frequency dependence could not be made to fit the observed frequency independent data.
- (5) Either the observed reflection characteristics were caused by an artifact at the interface that was common to all specimens or the direct back reflection of ultrasonic energy from an adhesive bond does not contain adequate information to predict the mechanical strength of the bond.

Introduction

The structure of the boundary between an adhesive and an adherend (usually a metal or a high-strength fiber) plays an important role in determining the mechanical strength of an adhesive bond. In order to measure this interfacial bond strength with a nondestructive technique such as an ultrasonic wave, it is important to know how the wave interacts with the structure at the boundary and how different structures can be expected to modify the waves that are reflected from or transmitted through this thin layer. Two fundamental aspects

Table I. Mechanical strengths and ultrasonic reflection coefficients (relative to an air interface) observed for adhesive bonds formed in different ways between Lucite blocks.

BONDING METHOD	MEAN BOND STRENGTH kg/cm ²	CHARACTERISTIC ULTRASONIC REFLECTION STRENGTH dB
<u>CHEMICAL:</u>		
60% METHYLENE CHLORIDE 40% ETHYLENE DICHLORIDE		
REGION A	364 \pm 36	-10.5
C	383 \pm 39	-14.5
B	409 \pm 24	-25.0
ACRYLIC ADHESIVE PS-30	94 \pm 16	-12.5
<u>THERMAL:</u>		
120°C, 15 MIN.	0 - 10	-48.0
130°C, 15 MIN.	17	-48.0
140°C, 15 MIN.	76 \pm 7	-48.0
160°C, 15 MIN.	69 \pm 9	-48.0
190°C, 15 MIN.	310 \pm 50	-48.0
200°C, 15 MIN.	408 \pm 30	-48.0



of the boundary make the experimental study of this interaction very difficult. These are: (1) the bond line or interface is very thin compared to the wave length so that distinctive features must be looked for in the long wave length limit of any mathematical model, and (2) the interfacial structure of interest usually separates two media of quite different acoustic impedance so that the observations of the ultrasonic interaction will be dominated by a large impedance mismatch and the interface effects will appear only as a small perturbation.

The objective of the experiments described in this report was to avoid the complications caused by the second difficulty by making measurements on a chemically-formed bond line between two media of identical acoustic impedance. In this way, the interaction of an ultrasonic wave with a very thin bond plane could be studied all by itself. The resulting data could then be used to establish a mathematical model for the interface that could be applied either to more general models of interfaces between media of different acoustic impedance or to suggest unusual ultrasonic techniques that would enhance special characteristics of the interface.

Possible Interface Models

It is valuable to consider the predictions of various possible models for the interaction of a sound wave with a thin layer separating two identical media in order to expose qualitative features to be looked for in the data.

The most common model describes the interface as a planar region of different acoustic impedance with a discontinuity of impedance at its boundaries. In this case, the reflected amplitude is a periodic function of frequency with a first maximum at the frequency where the thickness equals one quarter of the wavelength in the layer. Figure 1 (top) shows this periodic function and the impedance versus distance curve that generated it.

If the boundaries of the layer are not discontinuities in impedance, but are characterized by a gradual change in impedance spread over a finite distance, the reflection amplitude versus frequency curve is modified³ as shown in the example given in the middle diagram in Fig. 1. The zero in the periodic function has been moved to higher frequency and the maximum reflection has become spread over a broad frequency range.

The third model for describing a thin interface goes to the extreme of thinness by treating the bond plane as a region of infinitesimal width across which special boundary conditions apply. These boundary conditions are that the stress is continuous across the boundary while the displacement undergoes a discontinuous jump whose magnitude is proportional to the stress. that is,

$$\sigma_2 = \sigma_1 \quad (1)$$

$$u_2 = u_1 + k_1 \sigma_1 \quad (2)$$

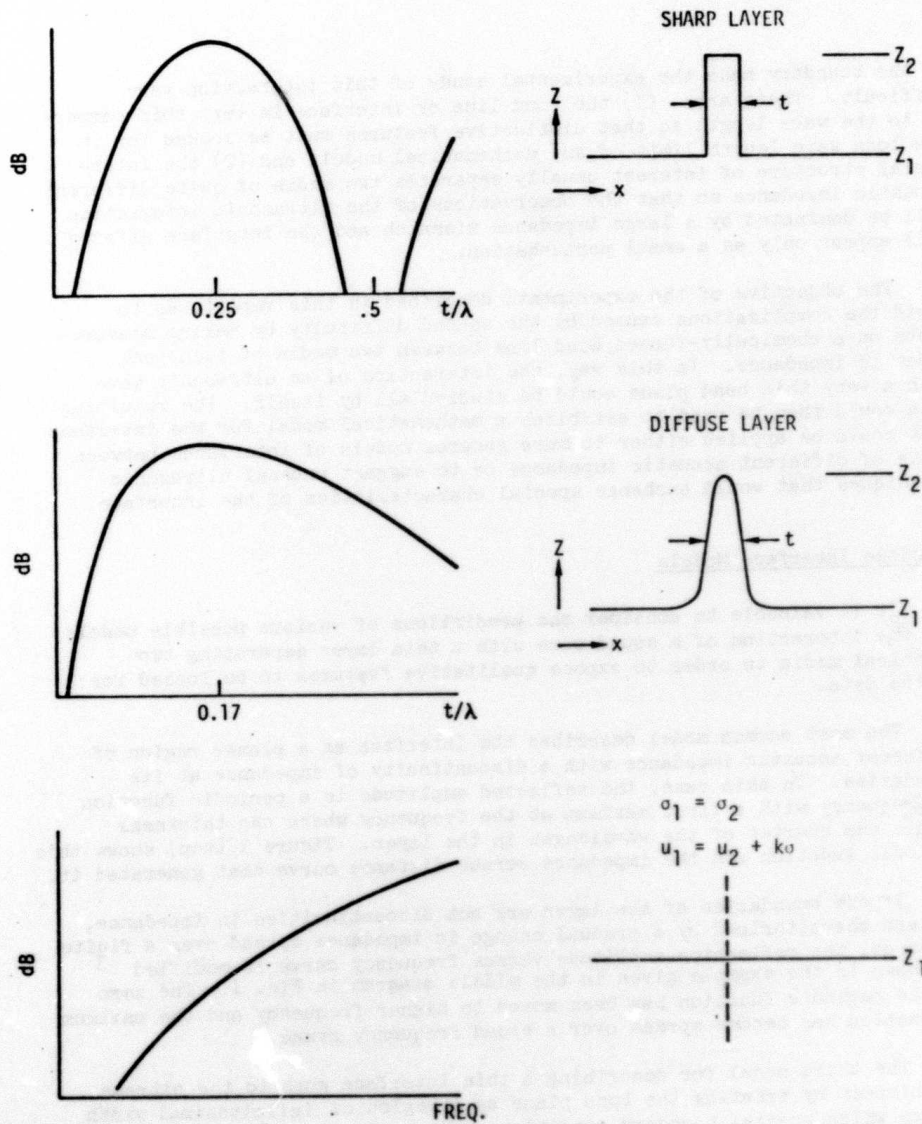


Fig. 1. Schematic diagrams of the frequency dependence of the reflected amplitude of ultrasonic waves reflected from the various impedance versus distance functions shown on the right.



As a consequence of these boundary conditions, Tattersall⁴, and also Thompson⁵, have derived the frequency dependence for the reflection coefficient sketched at the bottom of Fig. 1.

The primary objective of the measurements on thin bonds between identical materials is to determine which of the qualitatively different shaped reflection coefficient curves shown in Fig. 1 describes the experimental data.

Fabrication Of Bond Planes

In order to fabricate ultrasonic specimens containing a chemical bond across a planar interface separating two media of identical acoustic impedance, two techniques were employed. Both of them utilized clear plastic blocks for the two media and formed the bond by either painting a chemical solvent on the two surfaces just before joining or by mechanically pressing the surfaces together in a vacuum at elevated temperature. The former method, called the chemical method, dissolves and softens a thin layer on the surface of each block with a solvent so that when the blocks are pressed together at room temperature the molecules on each side of the interface can interact and cross-link in a localized, semi-liquid region. As the solvent diffuses into the bulk of each block, the interface region subsequently "solidifies" into a rigid joint whose thickness and mechanical strength are determined by the amount of solvent used and the time allowed for diffusion to take place. The thermal joints were formed by heating the two blocks to a temperature above their glass transition temperature at a fixed amount of pressure and time, joints of different strengths can be achieved¹. Table II describes these two methods in detail.

After the bonds were formed and all of the ultrasonic tests had been completed, the specimens were sliced into 1/8" thick slabs with the bond plane running across the center of each slab. The two outermost slabs were used for optical examination of the bond plane under a microscope equipped with crossed polarizers. The four innermost slabs were machined into flat tensile specimens with a 3.2 mm x 4.8 mm cross-section and a 12.5 mm gage length. These tensile specimens were pulled to failure in an Instron testing machine and the stress for fracture at the bond plane was measured. In all but two cases, the failure occurred at the bond planes and the failure stresses were lower than those which are characteristic of the virgin material. Figure 2 displays the observed fracture strengths as a function of the temperature at which the thermal bond was formed. Obviously, the technique yielded a set of specimens containing bond planes of different mechanical strengths.



Table II. Details of the fabrication procedures used to form the chemical interfaces studied in this report.

Method	Block Material	Surface Preparation	Joint Fabrication	Specimen Name	Remarks
Chemical	3/4" thick Polystyrene 1-1/2" Square	Dip in Methylene Chloride	Room Temperature	P	Transparent interface. Two interfaces, 0.8 mm apart. Clearly resolved ultrasonically.
	1/2" thick Plexiglass; Odd Shapes	Dip blocks in 60% Methylene Chloride 40% Ethylene Dichloride ----- Acrylic Adhesive PS-30 (Cedillac Plastics Co.)	Room Temperature Press in Hydraulic press -----	A B C ----- D	All transparent interfaces 180 μ m thick layer. 18 μ m layer. 60 μ m layer. ----- 117 μ m sharply defined layer.
Thermal	1/2" thick Plexiglass, 1" dia.	Alcohol wash; ultrasonic clean; in detergent, in water.	Vacuum press at 40 Kg/cm ² for 15 min. at 120°C 130°C 140°C 160°C 190°C 200°C	E F G H J K	Transparent interface. No layer visible under microscope. Frequency independent ultrasonic reflection coefficient.

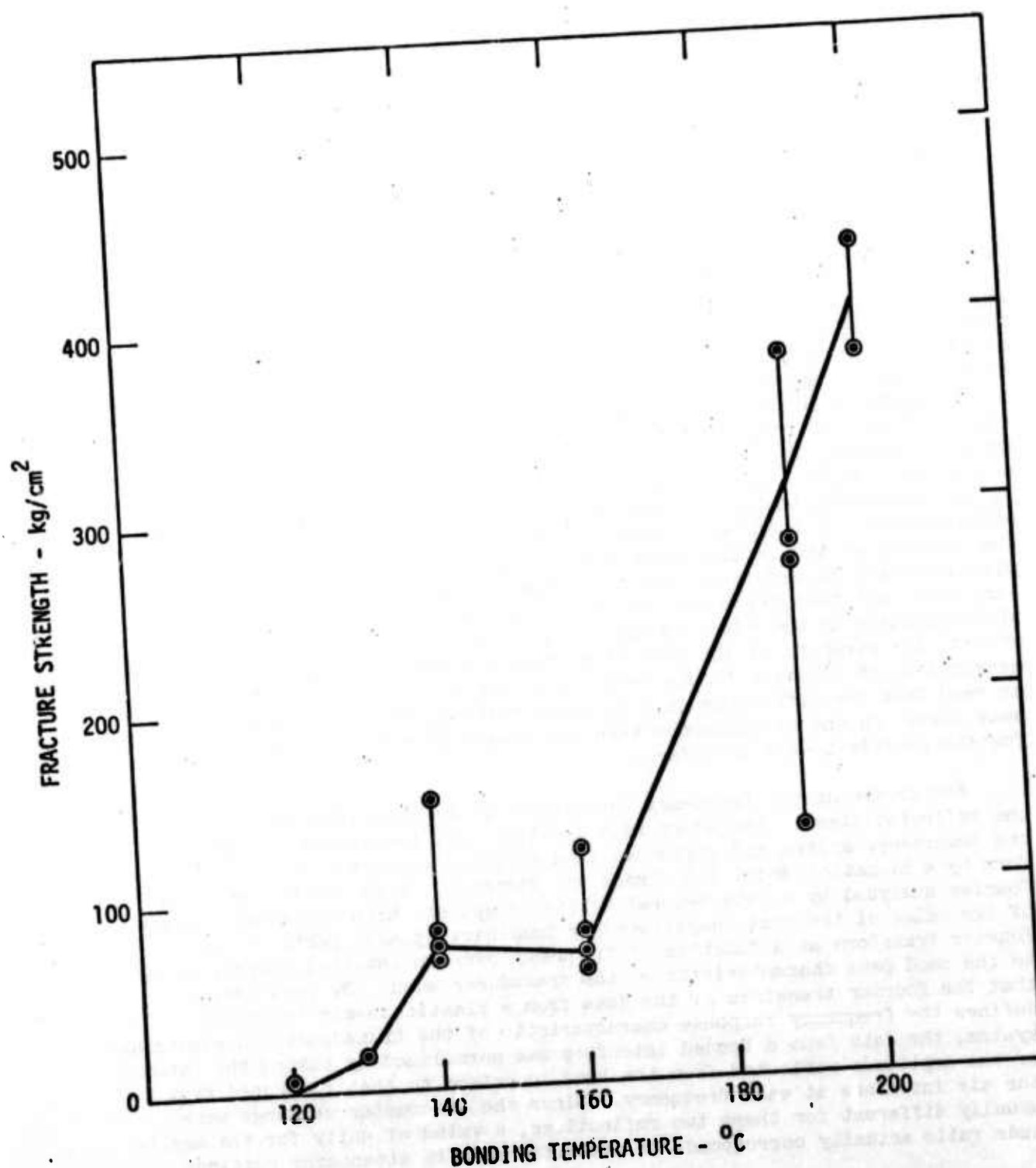


Fig. 2. Variation of the fracture strength of adhesive bonds formed by pressing Lucite blocks together with a pressure of 40 Kg/cm² in a vacuum for 15 minutes at the temperatures plotted along the abscissa.

Ultrasonic Technique

Two different ultrasonic techniques were employed to measure the frequency dependence of the amplitude and the phase of ultrasonic pulse signals reflected directly backward from the bond plane in the plastic samples. The most precise technique used a Matec Model 5100 gated amplifier to generate long R. F. bursts of well defined frequency to be applied to the sample through narrow band transducers (Panametrics A Series) at 2.25, 5.0, and 10.0 MHz. These same transducers detected the reflected signal which was displayed on an oscilloscope after passing through a calibrated attenuator and a Matec Model 615 tuneable receiver. The less precise, but more versatile technique employed a commercial ultrasonic NDT instrument (Immerscope) to apply a very short, high voltage electrical pulse to a broad band transducer (Panametrics V Series) so that a short duration RF burst, rich in different frequency components was generated in the sample. The same transducer also detected the reflection from the bond plane and generated an electrical signal which passed through an attenuator and broad band amplifier in the instrument to be displayed as an R.F. tone burst on an external oscilloscope. In both techniques, the attenuator was adjusted to give the same display on the oscilloscope when the signal was reflected from a planar plastic-to-air interface or from the bonded interface. It was found to be very important that the plastic-to-air interface be at the same distance from the transducer as the adhesive interface. For all the data given in this report, the strength of the reflection from a given adhesive bond line was measured in dB relative to the reflection from the air-to-plastic interface as read from the difference in attenuator settings needed to produce the same signal on the oscilloscope when the bonded interface was substituted for the plastic-to-air interface.

For obtaining the frequency dependence of the amplitude and phase of the reflected signal, the short time duration R.F. tone burst generated by the Immerscope system and reflected from an interface were put into digital form by a Biomation Model 8100 Transient Recorder. This digital data was Fourier analyzed by a Data General Eclipse computer which generated a graph of the value of the real (amplitude) or imaginary (phase) parts of the Fourier transform as a function of frequency over an interval corresponding to the band pass characteristic of the transducer used. By postulating that the Fourier transform of the data from a plastic-to-air interface defines the frequency response characteristic of the transducer and electronic system, the data from a bonded interface was normalized by taking the ratio of the amplitude reflected from the bond interface to that reflected from the air interface at each frequency. Since the attenuator settings were usually different for these two reflections, a value of unity for the amplitude ratio actually corresponds to the difference in attenuator settings.

By taking the difference in the imaginary parts of the Fourier transform for the bond interface and the air interface the phase shift upon reflection



from the bond plane can be deduced. Unfortunately, this phase difference contains a factor that varies linearly with frequency and measures the difference in arrival time between the echo from the air interface and that from the bond interface. Since this time difference cannot be measured independently to sufficient accuracy, the phase shift data is useful only in cases where the phase shift is a non-linear function of frequency within the band pass of the transducers used. Some effort was expended at obtaining phase shift data by directly comparing the relative positions of zero crossings within a long R.F. signal reflected from the air interface and from the bond line, but this was found to be very tedious and subject to large errors introduced by the inability to define the time at which the R.F. signal actually appears out of the background noise. Thus, the phase shift produced by reflection from an interface is correct to within an arbitrary linear function of frequency.

In order to test these methods of generating reflection coefficient data, two interfaces having known properties were fabricated and analyzed with the techniques described above. The simplest interface exhibiting a well-defined amplitude and phase variation with frequency is that produced by a thin layer of liquid between two flat, parallel metal plates. Reflection from such an interface or layer predicts a phase shift going rapidly from $+\pi/2$ to $-\pi/2$, and a sharp minimum in reflection amplitude when the frequency is such that the wave length is equal to twice the thickness of the liquid layer. Figure 3 shows the results of the computer performed Fourier analysis of the signal reflected from a water layer trapped between two parallel steel blocks. The thickness of the water layer was adjusted to put the dip in reflection amplitude in the middle of the frequency band pass of the transducer used.

In order to test the apparatus from measuring small reflections from a very thin layer at a set of fixed frequencies, the ultrasonic signal reflected from a piece of 2000 Angstrom thick gold leaf sandwiched between two Lucite blocks was measured. The thickness of the thin gold layer was measured before fabricating the sandwich by measuring the area of a sample of the gold leaf whose total mass was known. From a knowledge of the density of gold, an average thickness value could then be deduced. Figure 4 shows the dB difference between the amplitude of a narrow-band ultrasonic wave reflected from the gold and that reflected from an air interface as a function of frequency. The data points delineate a reflection coefficient that increases with increasing frequency. Since the acoustic impedance of both gold and Lucite are known, the reflection coefficient was calculated from Eqn. (1) with a layer thickness chosen to best fit the data. This theoretical thickness for the solid line curve in Fig. 4 was 2600 Angstroms in satisfactory agreement with the actual thickness.

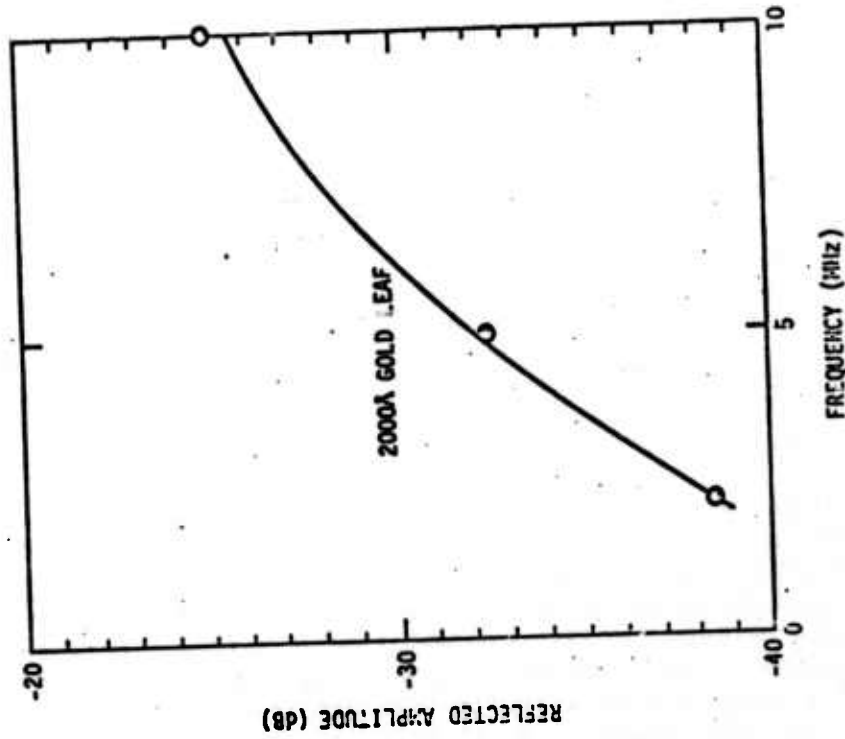


Fig. 4.

Frequency dependence of the amplitude of ultrasonic signal reflected from a 2000 Angstrom thick gold film between two blocks of Lucite. The data points were obtained at three fixed frequencies and are in dB relative to reflection from a Lucite to air interface. The solid line is reflected by eqn. (1).

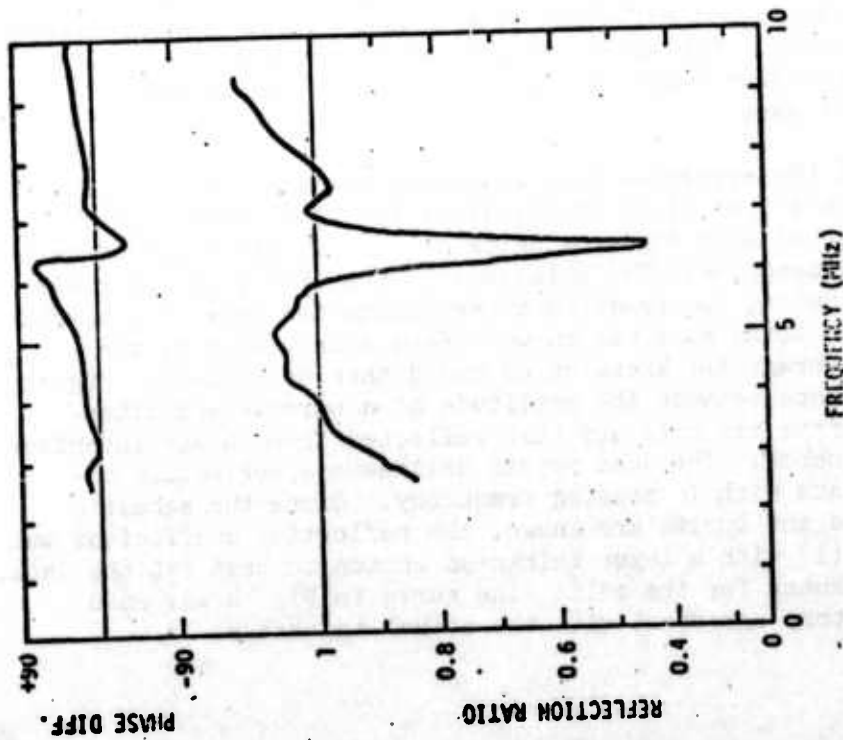


Fig. 3.

Frequency dependence of the amplitude and phase of the ultrasonic signal reflected from a thin layer of water held between parallel steel blocks.

Experimental Results

A. Chemically Formed Bond

As described in Section III on specimen fabrication, some large slabs of 1/2-inch thick Lucite were bonded together with Methylene-Ethylene Chloride mixtures placed at the interface. The ultrasonic reflections from different regions of these bonded slabs differed somewhat so three regions were marked out as representative of two extremes of reflection coefficient and the average reflection coefficient. These regions were labeled A, B, and C and form a commercial adhesive joint labeled D in Table II (all relative to an air interface). Associated with each curve is the strength of the bond determined by subsequent destructive mechanical tests. It can be seen from the qualitative shapes of the curves that these chemical bonds behave acoustically like layers with well-defined boundaries as shown in the top drawing in Fig. 1. From the frequency at which the maxima occur, it can be estimated that the adhesive layers have a thickness of approximately 60 microns. It is also noteworthy that the value of the reflected energy at the maximum correlates well with the strength of the bond for the same bonding material. Thus, on the basis of the limited data presented in Fig. 5, it would appear possible to predict the bond strength of chemically formed joints from a nondestructive ultrasonic test.

B. Thermally Formed Bonds

The bonds formed by mechanically pressing the Lucite blocks together at elevated temperature were also studied by taking the Fourier transform of the ultrasonic pulses reflected back from the bond plane. Figure 6 shows the frequency dependence of this reflected amplitude for three bond planes that exhibited the different strengths noted on the graph. Note that the ordinate scale is linear (not the usual logarithmic, dB scale) and that there is no reliable difference in reflection characteristics that correlate with the strength.

In order to more accurately establish this lack of correlations with strength and the rather small frequency dependence, careful measurements of the reflection amplitude difference between an air interface and the bond plane were made at three fixed frequencies (2.25 MHz, 5 MHz and 10 MHz) using narrow band transducers and the Matec signal generator. These results are shown in Fig. 7 where each temperature for forming the bond is denoted by a different symbol. It can be seen that there is neither a systematic variation with the temperature at which the bond was formed (and hence bond strength) nor is there a frequency dependence that exceeds the experimental scatter in the data. All of which is in agreement with the results obtained by the Fourier analysis of a broad band width ultrasonic pulse.

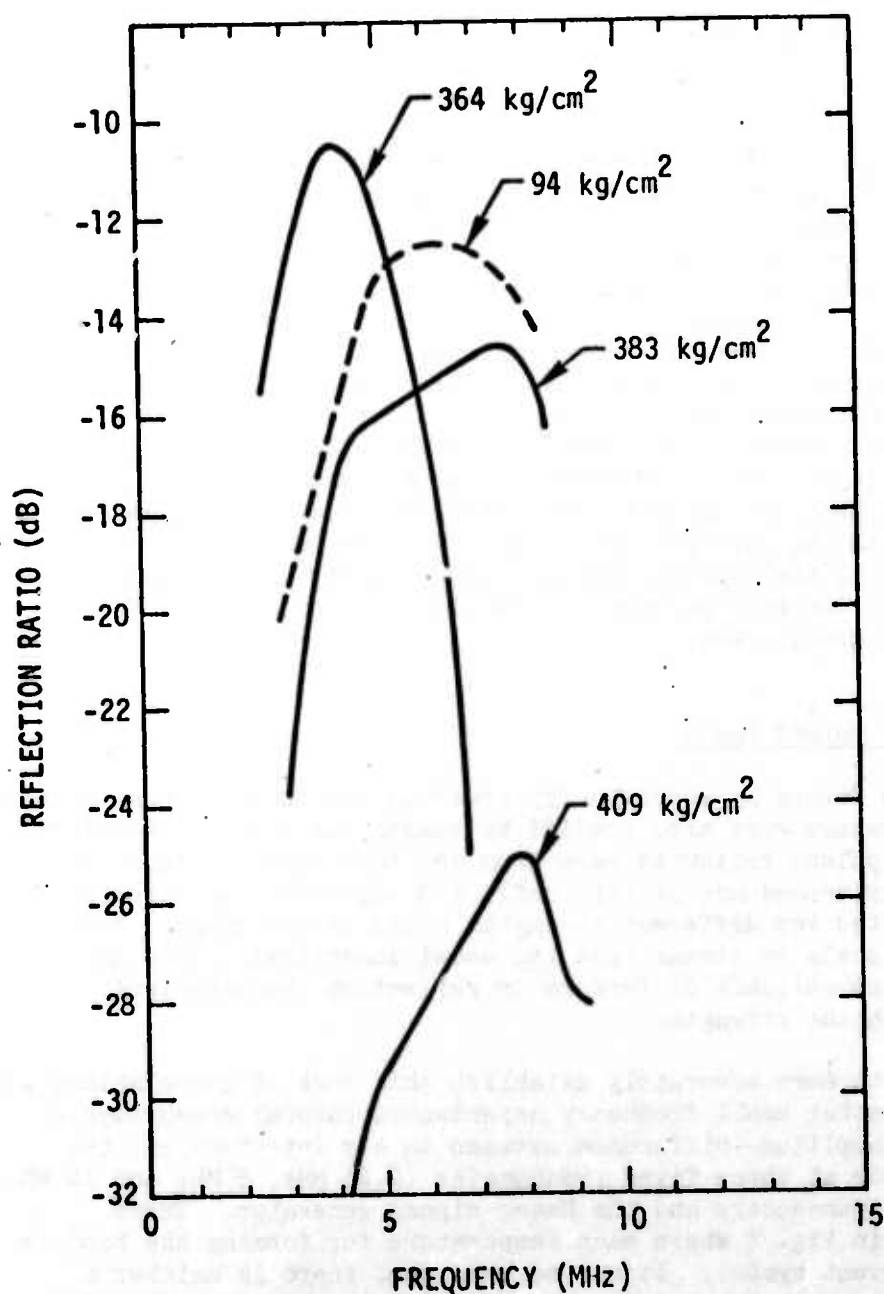


Fig. 5. Graphs of the frequency dependence of the ultrasonic energy reflected from adhesive bonds between Lucite blocks formed by placing an adhesive or solvent at the interface. These data were deduced from Fourier transforms of the RF signal reflected from the bond line.

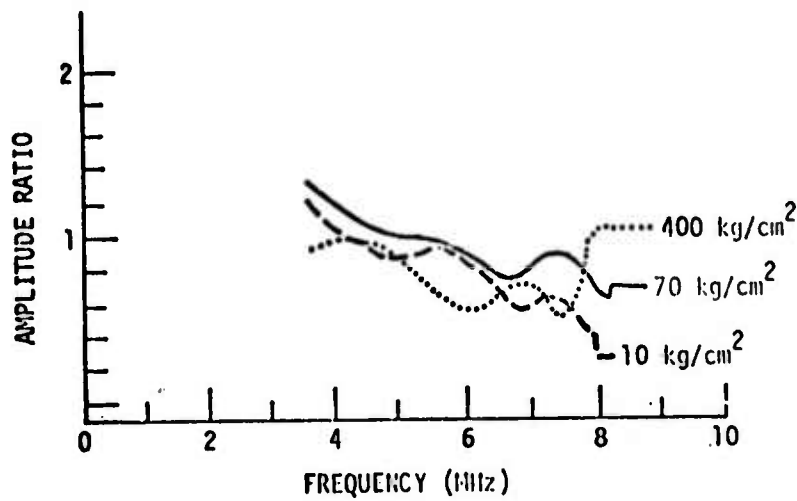


Fig. 6. Frequency dependence of the amplitude of ultrasonic signals reflected from three bonds between Lucite blocks whose failure strengths are indicated. These data were deduced from a Fourier transform of a broad band ultrasonic pulse.

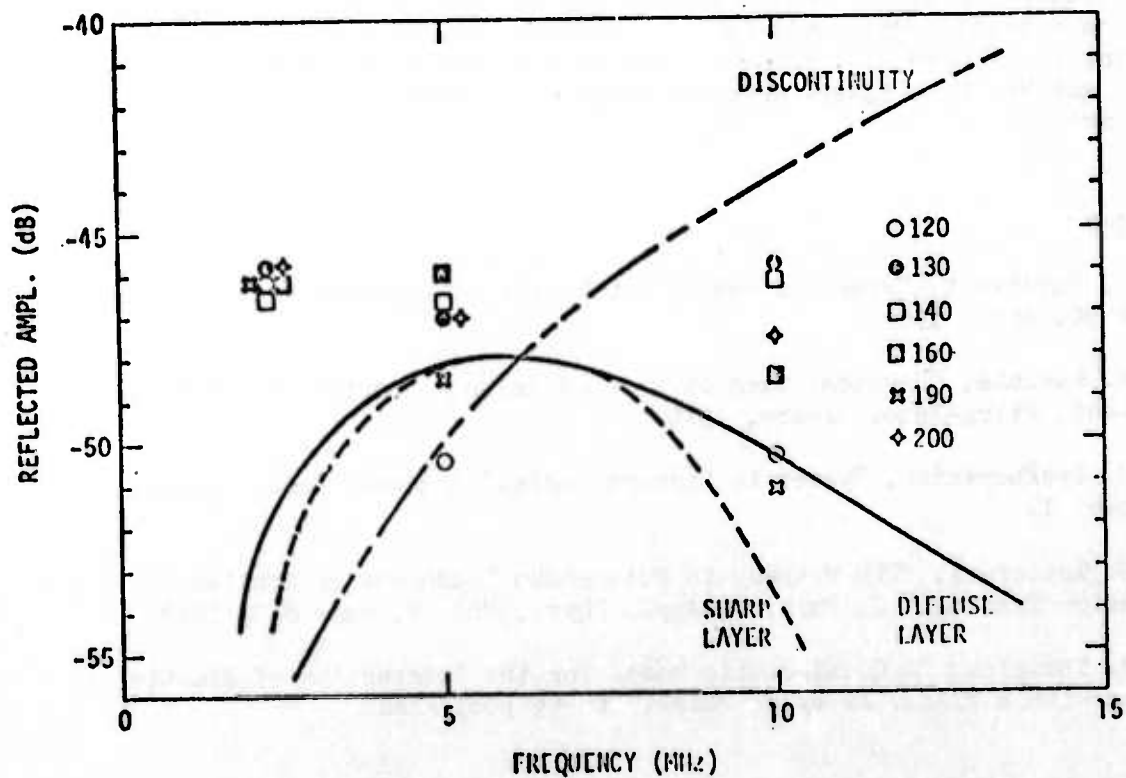


Fig. 7. Comparison between various theoretical models for the frequency dependence of the reflection of ultrasonic energy by a planar impedance variation with measurements made on a bond between Lucite blocks formed at the different temperatures indicated.



The original motivation for measuring the frequency dependence of the ultrasonic energy reflected from a thin adhesive layer was to obtain data from which to deduce a mathematical model that describes the interface. Figure 7 shows the functional form of the reflection amplitude versus frequency to be expected from various commonly considered models. These same models were used to fit the 5 MHz data in the results obtained on the thermally formed bonds shown in Fig. 7. Obviously, none of the anticipated models adequately describes the data because the models predict either a rising frequency dependence or a maximum in the middle of the frequency range examined. The experimental data is largely frequency independent or decreasing slightly at high frequency.

Acknowledgements

The authors would like to express their thanks to Dr. R. K. Elsley for performing the almost real time Fourier analysis of the ultrasonic reflection signals. Mr. David Kaelble deserves special recognition for suggesting the method of forming the adhesive bonds of controlled mechanical strength and Mr. Pete Sauers deserves thanks for producing the specimens by this method.

References

1. S. S. Voyutskii, "Adhesion and A Sutohesion of Polymers," Adhesives age, page 30, April 1962.
2. D. H. Kaelble, "Physical Chemistry of Adhesion," Chapter 12, pages 396-448, Wiley-Interscience, 1970.
3. L. M. Brekhovskikh, "Waves in Layered Media," Academic Press, 1960, Chapter 1.
4. H. G. Tattersal, "The Ultrasonic Pulse-Echo Technique as Applied to Adhesion Testing," J. Phys. D. Appl. Phys., Vol. 6, page 819, 1973.
5. R. B. Thompson, "A Quasi-Static Model for the Interaction of Elastic Waves with a Planar Array of Voids," to be published.



Science Center
Rockwell International

ULTRASONIC SIGNAL PROCESSING METHODS FOR ADHESIVE BOND STRENGTH MEASUREMENT

J. L. Rose and P. A. Meyer
Drexel University

ABSTRACT

The purpose of this work is to examine the effects of selected attenuation functions in adhesive bond modeling problems so that the attenuation in signal processing and interpretation can be treated adequately. Bond models are presently being used to study such problems as improper substrate surface preparation, improper adhesive cure, or chemical segregation of the adhesive. Specific attenuation functions used include some experimentally measured values for real materials, such as polystyrene, lucite, and rubber, and also a few hypothesized resonant functions based on observed attenuation phenomena in polymeric materials. Results indicate that attenuation effects can substantially alter the ultrasonic reflection even though the bondline is relatively thin. As a result of the study, it will then become possible either to select suitable transducers and signal processing techniques for bond inspection or perhaps to develop more sophisticated adhesive bond models with more accurate attenuation functions that would ultimately lead to criteria for transducer and signal processing selection.



Science Center
Rockwell International

PROJECT II, UNIT I, TASK 2

ULTRASONIC SIGNAL PROCESSING METHODS FOR ADHESIVE BOND STRENGTH MEASUREMENT

J. L. Rose and P. A. Meyer
Drexel University

Introduction

Adhesive bonding is rapidly becoming a very useful fastening technique. More uniform stress transfer, increased fatigue life and a reduction in structural weight are just a few of the possible benefits of using adhesive bonding. Concurrent with this increase in the use of adhesives is the research in developing an effective NDT technique for evaluating bond strength. One of the potential methods is ultrasonic bond evaluation. Zurbrick [1,2], for example, discusses the many variables that can affect the ultimate strength of an adhesive bond. Typical variables include bondline thickness, substrate surface roughness, surface chemical condition, adhesive type, humidity, and various degradation or aging effects. Rose and Meyer [3] have shown that the overall bond strength for an aluminum-Scotchweld-aluminum step-lap joint can be related to the echo amplitude from the bondline. Thompson, Alers and Thompson [4] have shown that it is feasible to relate the bond strength characteristics of the adhesive used to attach the skin to the honeycomb core in sandwich panels to the damping characteristics of panel vibrations and the propagation velocity of surface waves on the panel. Rose and Meyer [5] have demonstrated the capability of detecting surface preparation ultrasonically in an Aluminum-FM-47-Aluminum bonding system. They have also extended the ultrasonic signal interpretation work by developing analytical models that can be used to determine the theoretical reflection from a bondline as a function of the incident pulse and the particular adhesive system being used. The work in [5], however, does not consider attenuative effects in the adhesive system. The purpose of this work is therefore, to examine the effects of selected attenuation functions in adhesive bond modeling problems so that the attenuation in signal interpretation and processing can be treated adequately. It would then be desirable to establish signal interpretation and processing criteria that would allow us to evaluate good and bad areas of a bond as a function of selected signal characteristics. Before examining the amplitude-time profiles and frequency or phase profiles or other transform profiles, however, it is necessary to examine the variation in these signals as a function of the various attenuation characteristics of adhesive bond materials as well as the parameter adjustments in the models presented in [5]. As a result of the study, it will then become possible to either select suitable transducers and signal processing techniques for bond inspection or perhaps to develop more sophisticated adhesive bond models with more accurate attenuation function that would ultimately lead to criteria for transducer and signal processing selection.



Approaches

A classical solution for the reflection of an ultrasonic pulse from a viscoelastic bondline would proceed as follows. First, the time dependent constitutive equations would be selected that accurately describe the mechanical behavior of the adhesive and substrate materials. After matching stresses and displacements at the interfaces, a dynamic wave response equation would be developed for the system. In spite of the potential validity of this approach, the technique would become a very tedious and time consuming numerical computation process regardless of the approximate nature of the viscoelastic parameters selected for the study. Rather than study the attenuative effects of the adhesive on the ultrasonic signal reflection using the above method, it was decided to pursue a physical modeling approach to the problem similar to that presented by Rose and Meyer [5]. In this method, parameters can be adjusted to represent typical properties of the system as well as to include possible bondline defects. For instance, an ideal adhesive bond system might be considered a system of three isotropic layers,--substrate, adhesive, substrate--while interfacial defects could be interpreted as an equivalent area reduction at the interface. An elastic modulus variation through the thickness of the adhesive could be modeled as a system of sub-layers each having different mechanical properties. In this method, the analytical models are assigned certain experimentally observable or physically reasonable parameters which are used in the calculation of the ultrasonic reflection signals based on the input boundary conditions. Sample problems are discussed by Rose and Meyer [5].

Note that in both of the above techniques, such ultrasonic signal variations as amplitude changes due to reflection factor, amplitude changes due to attenuation, and dispersion or pulse spreading due to layering are physically generated as a result of the mathematical solution procedure. A choice of parameters in the viscoelastic constitutive equation could very well provide identical results to a corresponding set of parameters used in the physical modeling approach. Both approaches could be used to provide qualitative aspects of various signal changes from good and bad bonds and ultimately lead to parameter optimization in correlation considerations of the theoretical and experimental results of ultrasonic signal comparisons with bond performance of flaw type.

Attenuation Functions for Bond Model Analysis

Several studies were made using the analytical models for bondlines having various attenuative characteristics. The attenuation function is introduced as a frequency and distance dependent dissipation of energy in the adhesive bondline. Some of these functions were taken from experimental studies of real materials while others were established based on qualitative aspects of the attenuation phenomenon as discussed by other researchers in this field. A discussion of the motivation for the selection of the particular attenuation functions used in the models follows.

Since the purpose of this work is to determine the variation in the reflection due to the consideration of attenuation, a reflection from a non-attenuative material is needed. The reference used for this study is uniform property bondline having perfect wave coupling at the interfaces and zero attenuation and is shown as material "a" in Fig. 1a. Other bondline test cases can be compared with the result from this reference. Of the attenuative bondlines materials considered, the simplest is one having a frequency independent attenuation value. Such a function is shown in Fig. 1a and is labeled material "b". It was decided that 2 db/cm is a reasonable value for this study. A second attenuation bond-line considered is identical to the reference bondline except that the adhesive is assigned a frequency dependent bondline function, shown as material "c" in Fig. 1a. The attenuation function used was that determined experimentally by Mason (6) for polystyrene over a frequency range of 0-8 MHz. This function was chosen because many of the adhesives used industrially exhibit mechanical properties which are very similar to polystyrene. In addition, there is little experimental data available for other than a few common materials. A few other attenuation functions were used in order to investigate the effect of increasing the magnitude of the attenuation function on the reflected signal. These functions are those determined by Mason (6) for Lucite, (material "d") two times the magnitude of the Lucite function. (material "e"), and Mason's (6) function for rubber (material "f"). These functions are shown in Fig. 1a. Physically, these curves could simulate various states of cure for the adhesive bondline. Adhesives are usually applied as liquids or low modulus semi-liquids. During the cure process, the adhesive is transformed into a relatively high modulus material capable of transmitting the load from one substrate to the other. If we can assume the uncured adhesive can be represented by an attenuation function similar to that of rubber and after cure the adhesive is similar to polystyrene, then the ultrasonic reflection can be related to the cure state through the attenuation functions.

Attenuation studies in polymer solutions by Ferry (7) and in plastic by Auberger and Rinehart (8) have shown peaks in the attenuation functions. Some researchers (9) mention that this phenomenon may be due to resonance in the material at the molecular level. Since empirical data is limited for adhesive-like materials in the ultrasonic frequency range, it was decided to use the peaking attenuation functions shown in Fig. 1b. The first of these (material "g") has a relatively constant value of 2 db/cm with a peak of 8 db/cm occurring at 4 MHz while the next function (material "h") shows a similar peak located at 2 MHz. The remaining two functions (materials "i" and "j") are simple sine function demonstrating the occurrence of multiple peaks. Results of employing these attenuation functions in the bond model work is reviewed on the following pages.

Solution Technique

The computer program used to generate the ultrasonic reflection from the various modeled non-attenuative bondlines is described in detail by

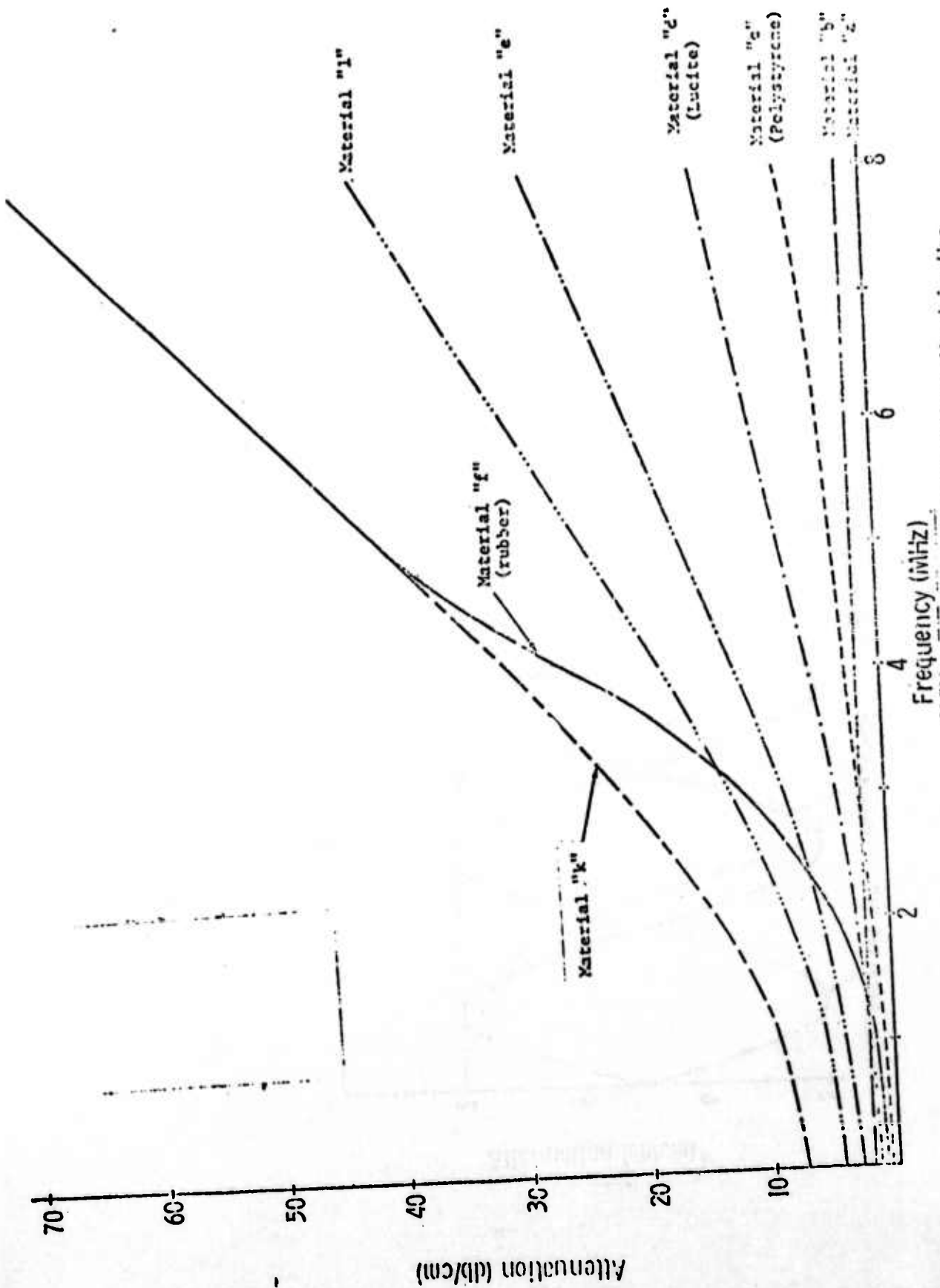


Fig. 1a - Monotonically Increasing Attenuation Functions Used in the
Broad Bandwidth Analysis

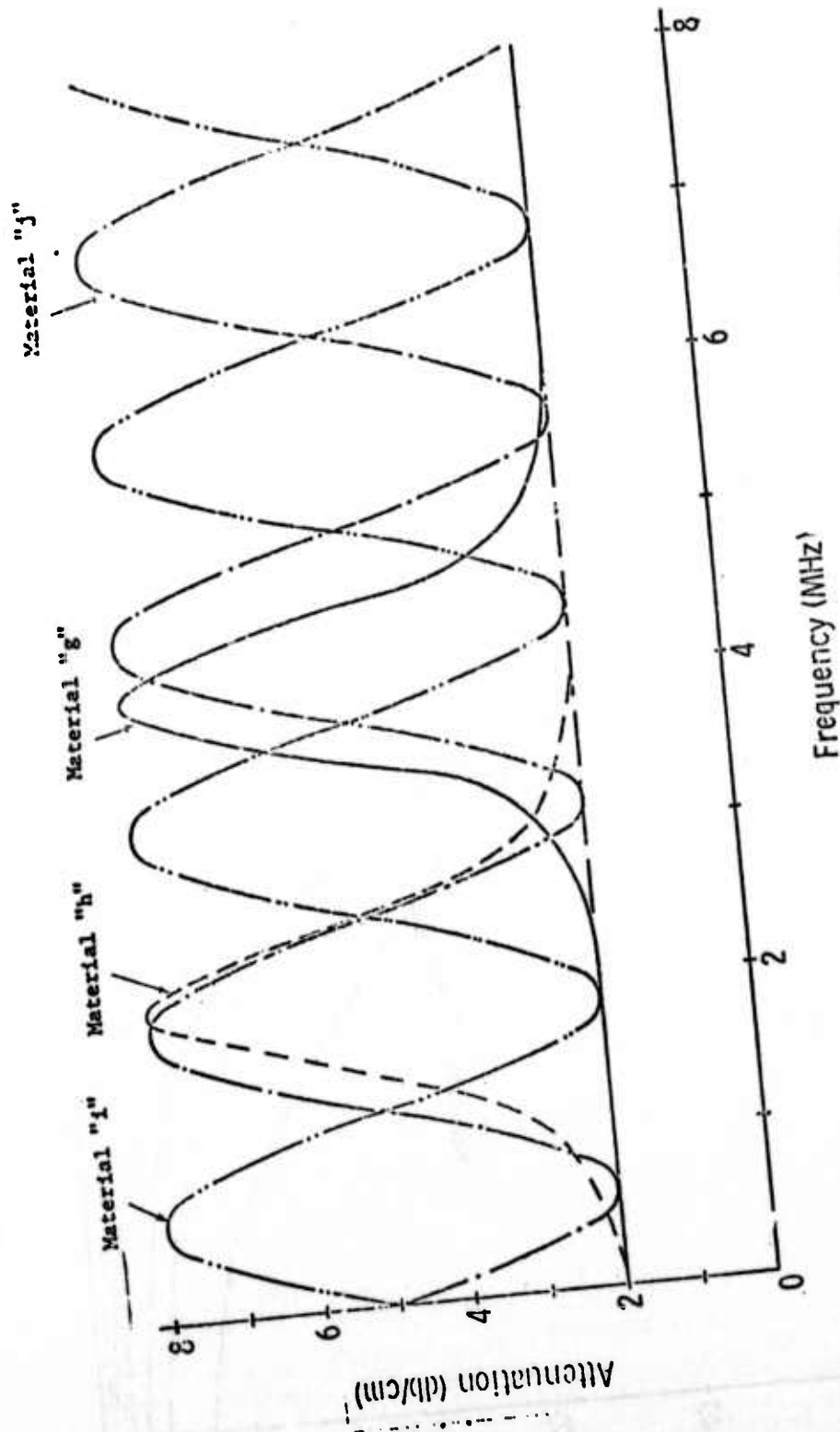


Fig. 1b - Resonant Attenuation Functions Used in the Bond Model Analysis.



Rose and Meyer [5]. The major difference in this study is the addition of the attenuation function. These values are read into the program as a function of frequency in units of (db/cm). The distance travelled by each internal reflection is computed and loss (L) for the frequency components of that signal are computed. The amplitude of each resulting internal reflection can then be determined by

$$\text{Amplitude}_{\text{out}} = \text{Amplitude}_{\text{initial}} \left(-\frac{L}{20}\right)^{(10)} \quad (10)$$

Thirty-three cases were studied as outlined in Table 1. A reference bondline and 10 attenuative bondlines were considered, each for three different thicknesses selected as follows. The largest bondline thickness (.32 cm) yields separate internal reflections allowing the attenuation effects on the pulse characteristics in the time domain to be studied readily. The two thinner bondlines (.029 cm and .025 cm) permit various degrees of superposition of the internal reflections. The input signal to the bondline in all cases is an 8 MHz bandwidth 'white noise' pulse having a constant Fourier amplitude of unit magnitude and a zero amplitude phase profile as shown in Figure 2. Using this form of input function simplifies the reflection analysis in the frequency domain and also allows the reflection for an arbitrary input pulse to be generated. For example, the Fourier spectrum of the reflection of an arbitrary input pulse is the product of that input spectrum and the reflected spectrum for the white noise pulse. The geometric characteristics of the bondline models are shown in Figure 3. The reference bondline and single attenuation function bondlines are represented as a simple three-layer system shown in Fig. 3a. As mentioned earlier, Rose and Meyer [5] suggested the use of an equivalent area reduction at the adhesive interfaces to represent such flaws as improper substrate surface preparation or surface contamination prior to bonding. In this study, it was decided to consider an alternative approach to such an interface condition by treating the interface as a very thin highly attenuative layer as shown in Figure 3b. A variation in adhesive cure through the thickness of the adhesive possibly due to an improper cure procedure could be represented as a multiple layer adhesive bondline as shown in Figure 3c. Each layer would be assigned different mechanical properties approximating a continuous variation.

Results

Monotonically Increasing Attenuation Functions

A comparison of the computer generated reflections from bondlines having monotonically increasing attenuation functions can be conducted using the two approaches described below, one of visual signal evaluation and one of mathematical preprocessing.

Computer Run	Bondline Thickness (cm)	Attenuation Function
1a	.025	Material "a"
1b	.029	"
1c	.033	"
2a	.025	Material "b"
2b	.029	"
2c	.033	"
3a	.025	Material "c"
3b	.029	"
3c	.033	"
4a	.025	Material "d"
4b	.029	"
4c	.033	"
5a	.025	Material "e"
5b	.029	"
5c	.033	"
6a	.025	Material "f"
6b	.029	"
6c	.033	"
7a	.025	Material "g"
7b	.029	"
7c	.033	"
8a	.025	Material "h"
8b	.029	"
8c	.033	"
9a	.025	Material "i"
9b	.029	"
9c	.033	"
10a	.025	Material "j"
10b	.029	"
10c	.033	"

Table 1a - Data for Computer Runs Made with the Bondline Geometry
Shown in Figure 3a.



Science Center
Rockwell International

Computer Run	Bondline thickness (cm)	Attenuation Function
11a	.0025(interfaces) .020 (adhesive)	Material "k"(interfaces) Material "d"(adhesive)
11b	.0029(interfaces) .0232(adhesive)	Material "k"(interfaces) Material "d"(adhesive)
11c	.0033(interfaces) .0264(adhesive)	Material "k"(interf. s) Material "d"(adhesive)

Table 1 b - Data for Computer Runs Made for
the Bondline Geometry Shown in Fig. 3 b.

Bondline Thickness	Bondline Properties
12a 6 bond layers .0042 cm each	Layers 1,6 c = $2.67 \times 10^5 \frac{\text{cm}}{\text{sec}}$ α = material "d" Layers 2,5 c = $2.53 \times 10^5 \frac{\text{cm}}{\text{sec}}$ α = material "e" Layers 3,4 c = $2.39 \times 10^5 \frac{\text{cm}}{\text{sec}}$ α = material "l"
12b 6 bond layers .0048 cm each	Layers 1,6 c = 2.53×10^5 α = material "d" Layers 2,5 c = 2.53×10^5 α = material "e" Layers 3,4 c = 2.39×10^5 α = material "l"
12c 6 bond layers .0054 cm each	Layers 1,6 c = 2.67×10^5 α = material "d" Layers 2,5 c = 2.53×10^5 α = material "e" Layers 3,4 c = 2.39×10^5 α = material "l"

Table 1c - Data for Computer Runs Made for the Bondline Geometry
Shown in Figure 3 c.

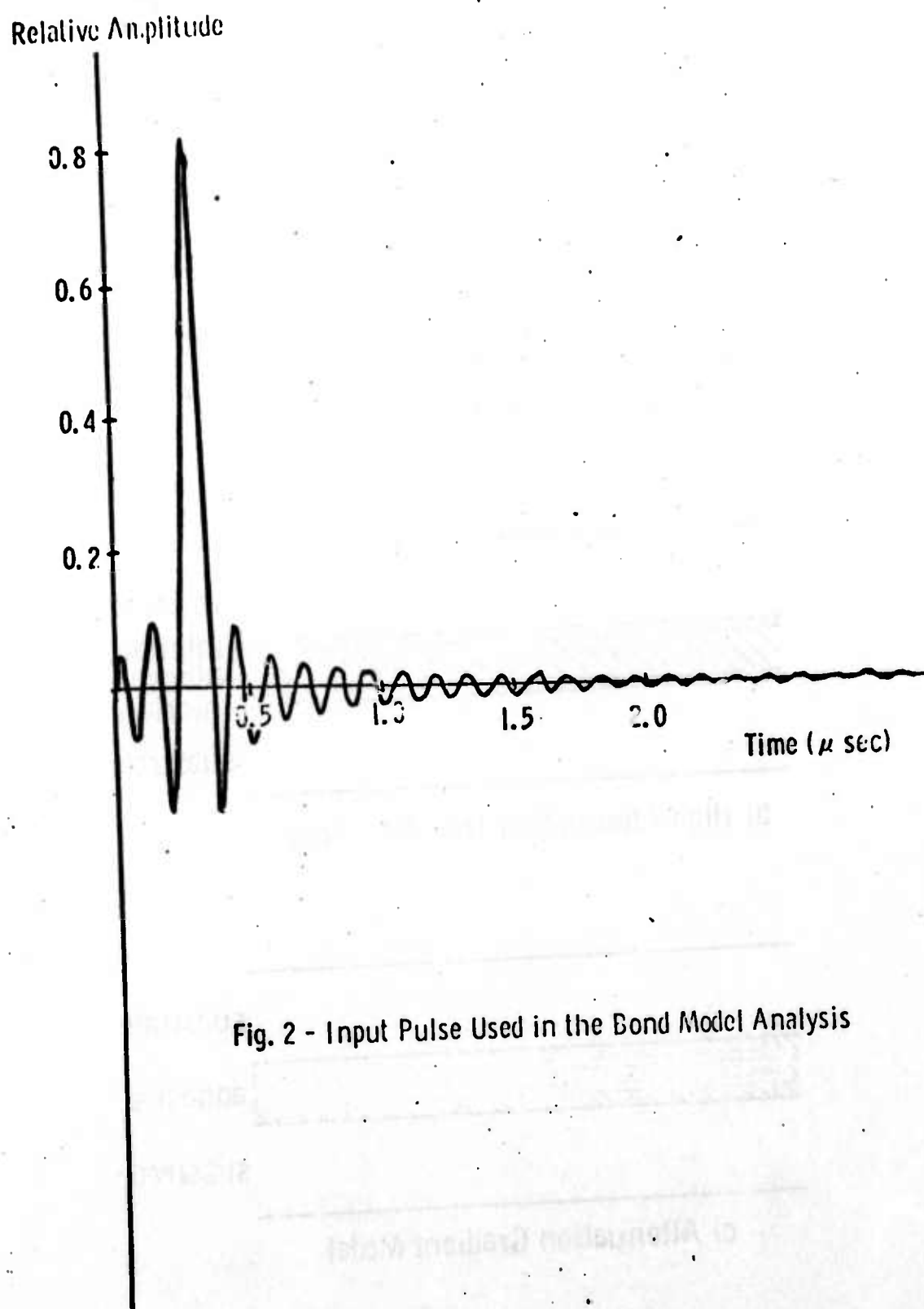
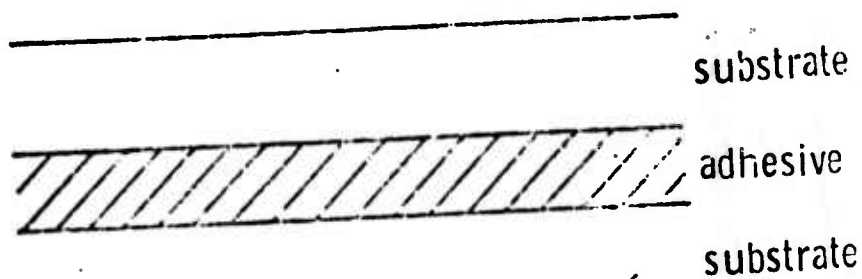
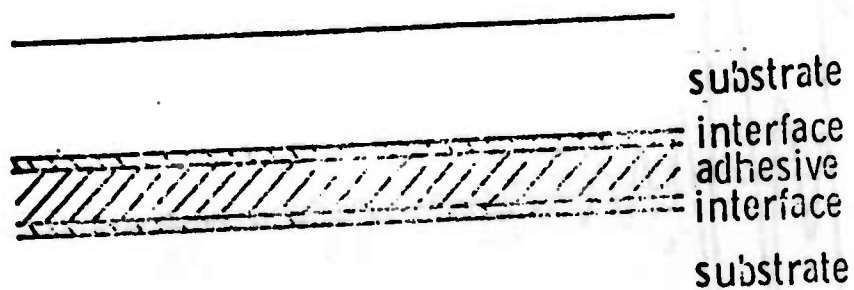


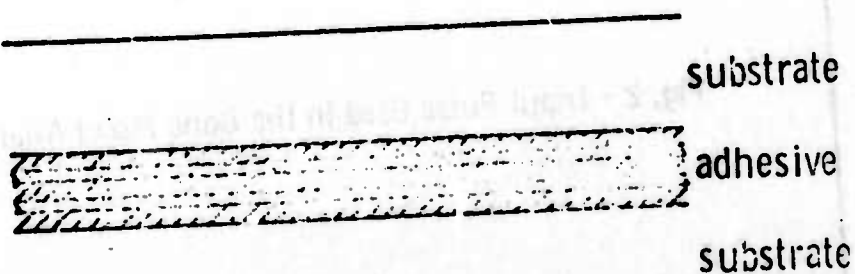
Fig. 2 - Input Pulse Used in the Bond Model Analysis



a) Single Layer Bond Model



b) High Attenuation Interface Model



c) Attenuation Gradient Model

Fig. 3 - Bondline Geometries Used in Adhesive Bond Analysis

1) Visual Signal Evaluation

The amplitude-time reflections for the six monotonically increasing attenuation cases are shown in Fig. 4. In studying the signals in the time domain, it can be seen that as the attenuation function is increased in magnitude, the amplitude of the internal reflections from the bondline decreases as might be expected. Other differences such as minor alterations of signal shape are also noticeable.

In the frequency domain, however, the attenuation consideration has a more pronounced effect. A comparison of the Fourier amplitude and phase profiles for cases 1 to 6 is shown in Fig. 5. The "spectral depressions" caused by the destructive interference of the multiple internal reflections for frequency components satisfying the relation

$$d = \frac{n \lambda}{2}$$

are altered. As the attenuation function is increased, the amplitude of the frequency profile at the spectral depression location is increased while the amplitude at other locations is decreased. This phenomenon is due to the decreased effect of the multiple reflections caused by attenuative losses in the adhesive. An extreme case using the attenuation function for material "f" (rubber) shows that the depression almost disappears completely leaving a spectrum resembling a reflection of the incident pulse from a single interface. Corresponding to the spectral depression in the Fourier amplitude profile is a well defined inflection point at the same frequency location in the phase profile. The effect of increasing attenuation is to decrease the magnitude of this inflection as shown in Fig. 5.

2) Preprocessing Considerations of the Results

A tabulation of certain preprocessing features or characteristics of the reflections could prove useful in analyzing the results. Table 2 gives the peak-to-peak amplitude of the reflection in the time domain. Computer runs 1 to 6 represent the monotonically increasing attenuation functions. The trend of decreasing signal amplitude with increasing attenuation is evident here for the three bondline thickness with the exception of run 6 for material "f" (rubber). This appears, however, to be due to a change in the location of the maximum positive peak in the signal.

Two characteristics of the frequency reflection profiles, the spectral depression location and the ratio of amplitude at the spectral depression and maximum value, are tabulated in Tables 3 and 4. The amplitude ratio measurement quantitatively depicts

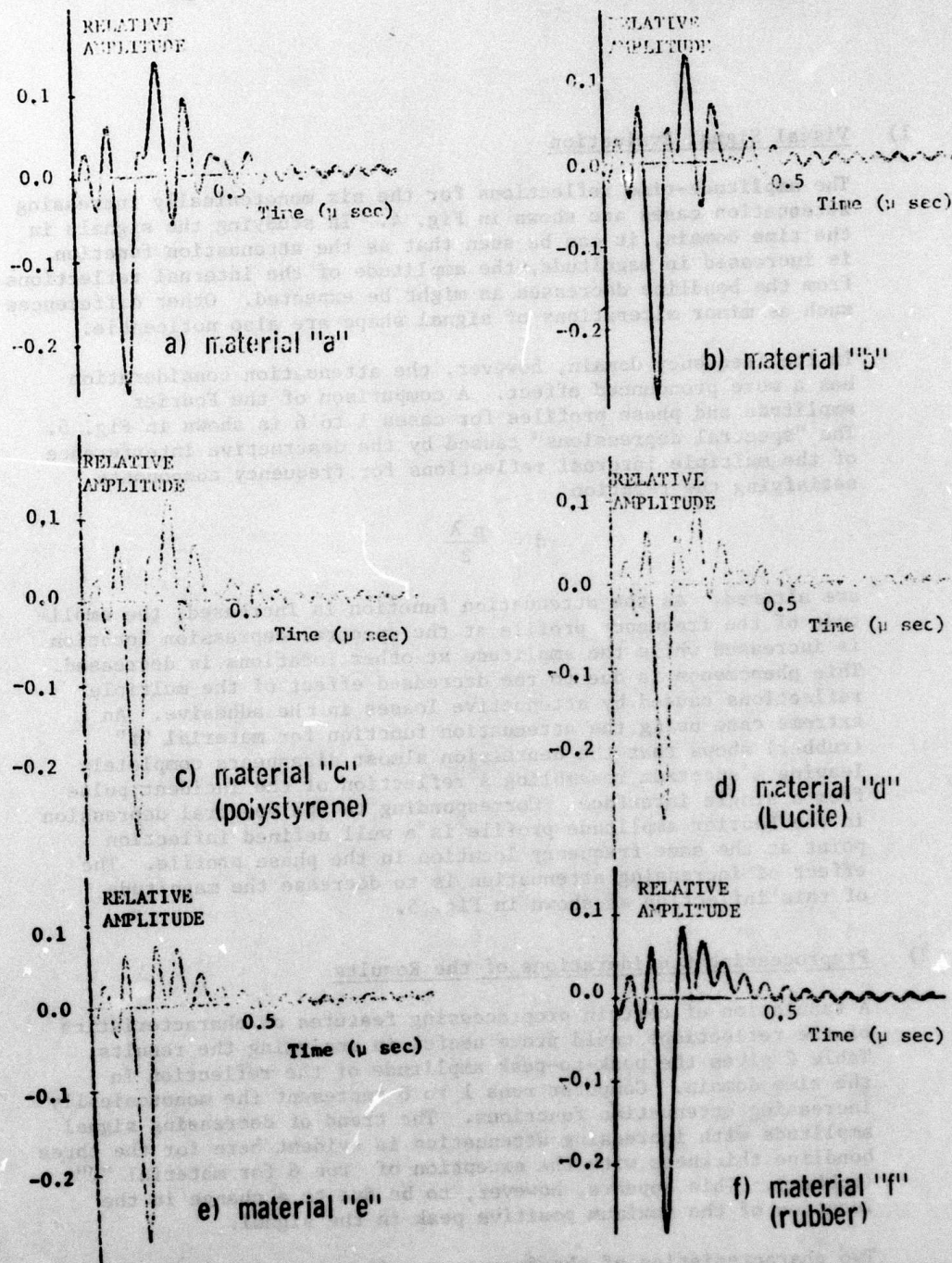


Fig. 4a - Ultrasonic Reflections from .025 cm Bondlines Having Monotonically Increasing Attenuation Function.

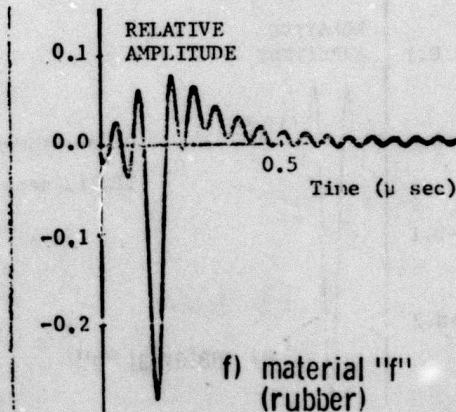
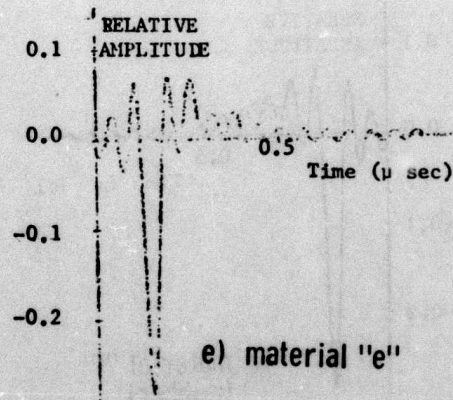
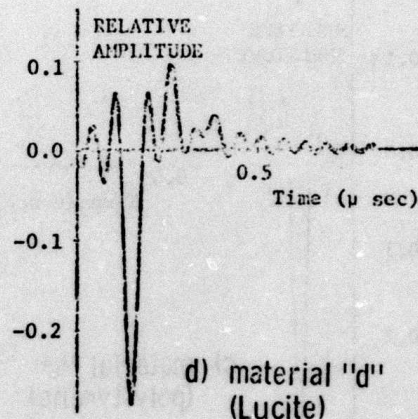
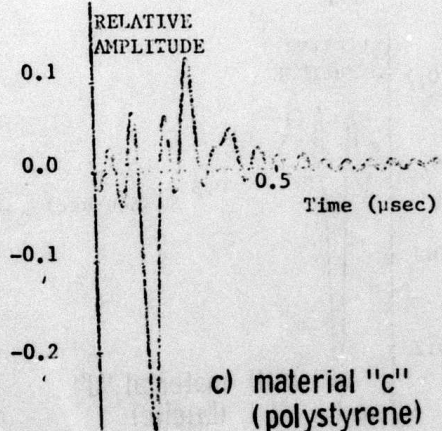
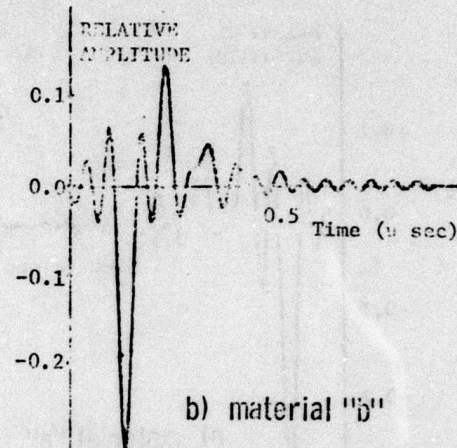
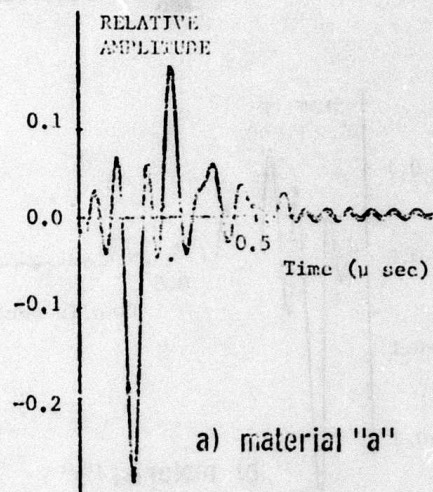


Fig. 4b - Ultrasonic Reflections from .029 cm Bondlines Having Monotonically Increasing Attenuation Function.

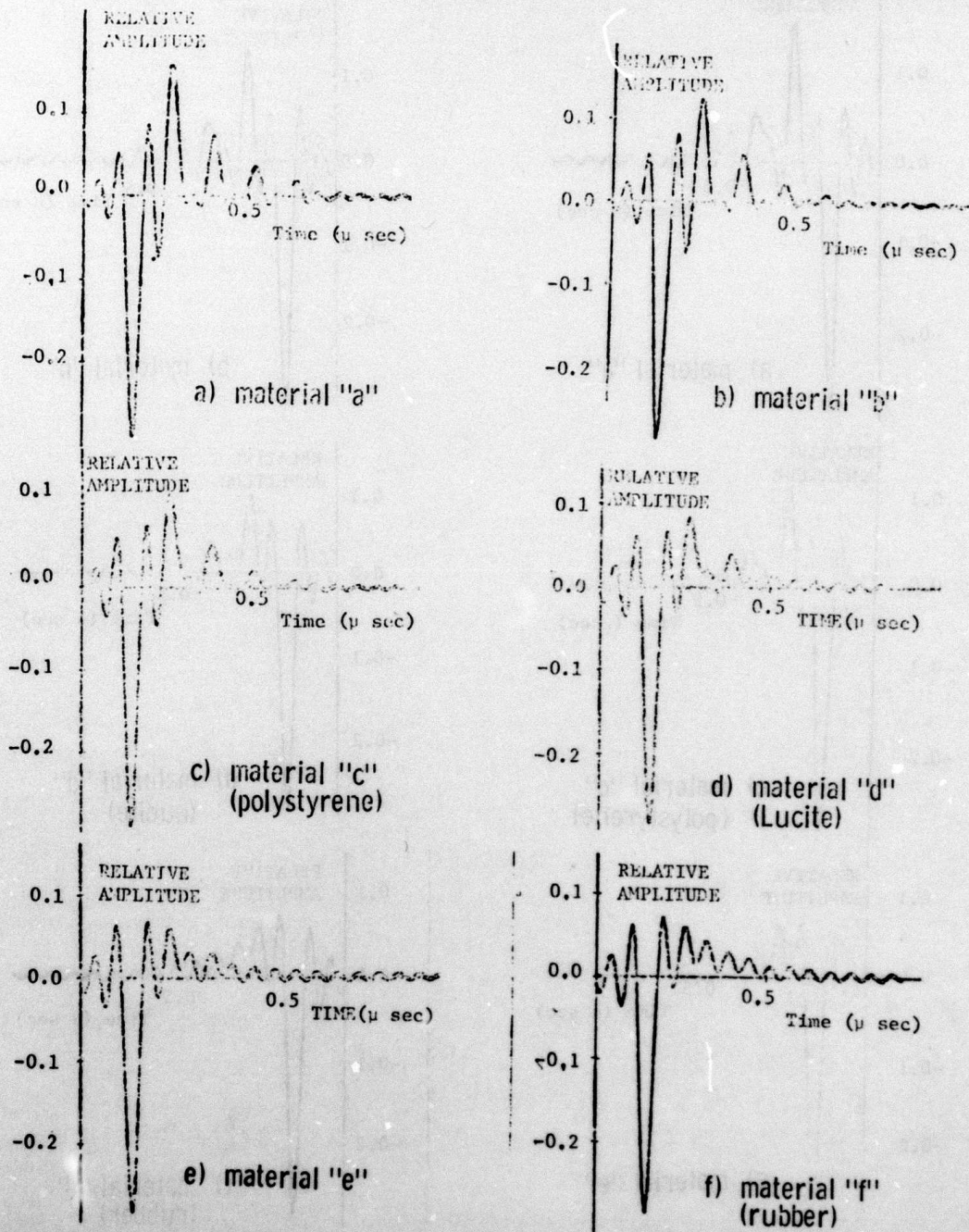


Fig. 4c - Ultrasonic Reflections from .033 cm Bondlines Having Monotonically Increasing Attenuation Function.

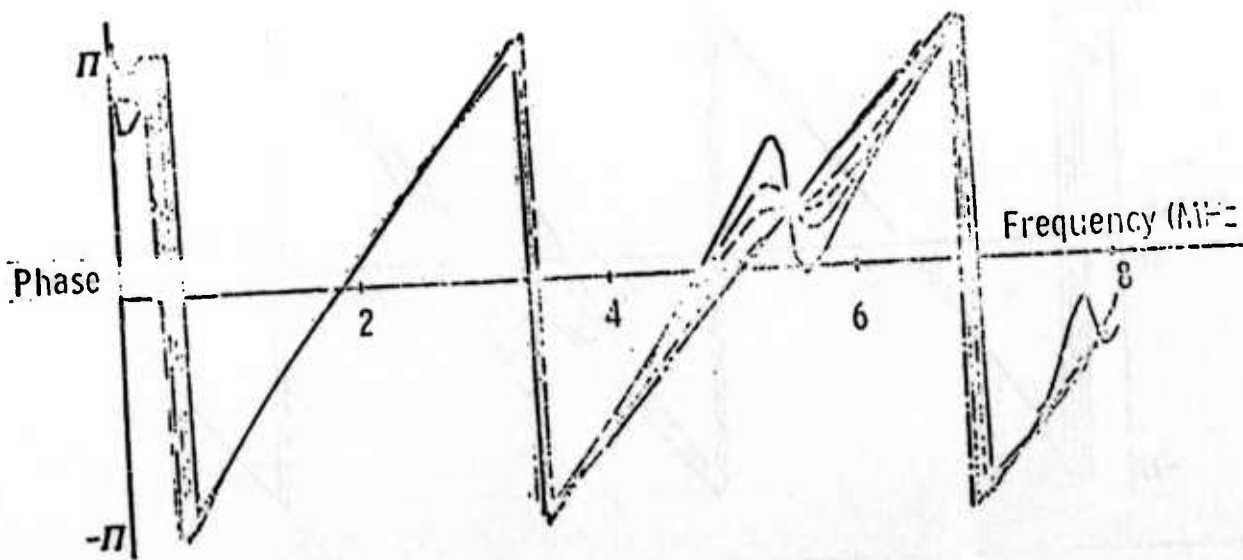
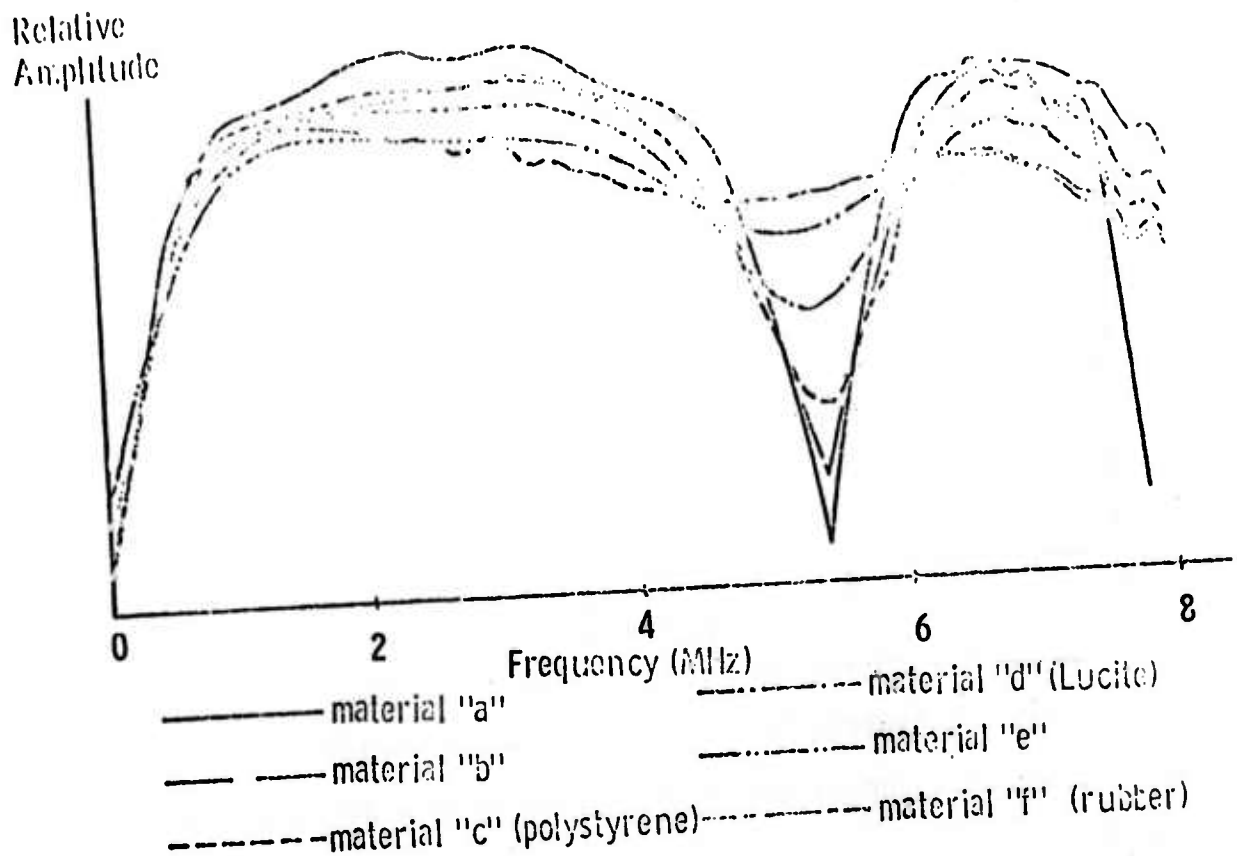
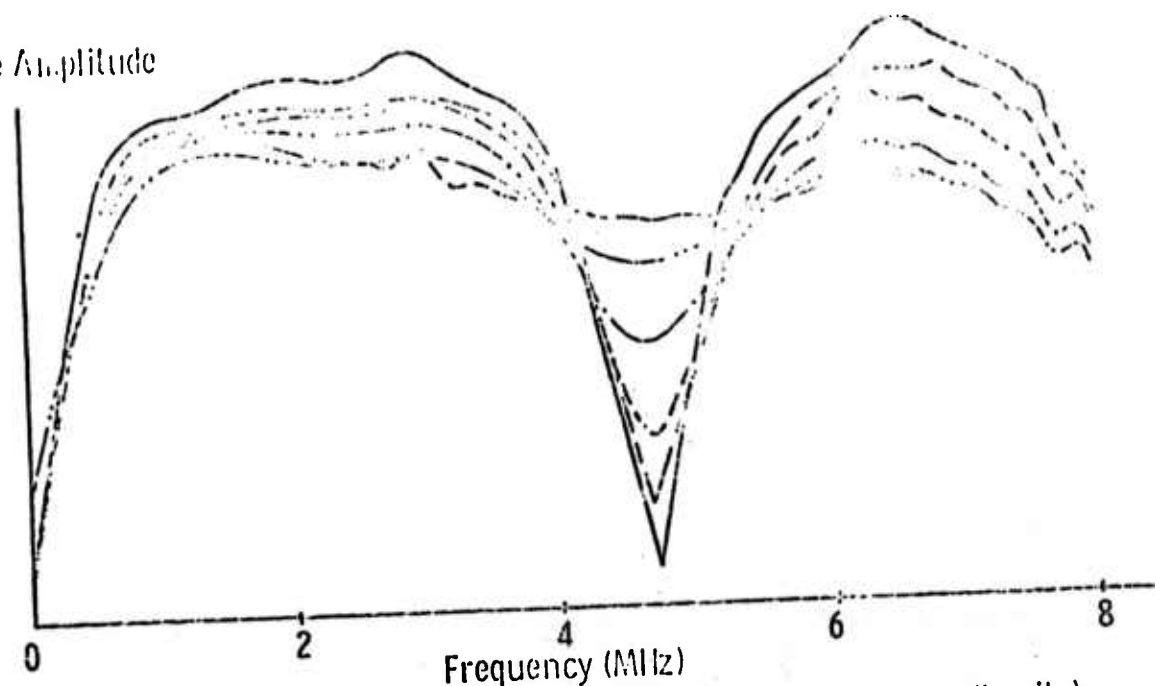


Fig. 5a - Frequency Characteristics of the Ultrasonic Reflections from .025 cm Bondlines Having Monotonically Increasing Attenuation Functions.

Relative Amplitude



material "a"
 material "b"
 material "c"(polystyrene)
 material "d" (Lucite)
 material "e"
 material "f" (rubber)

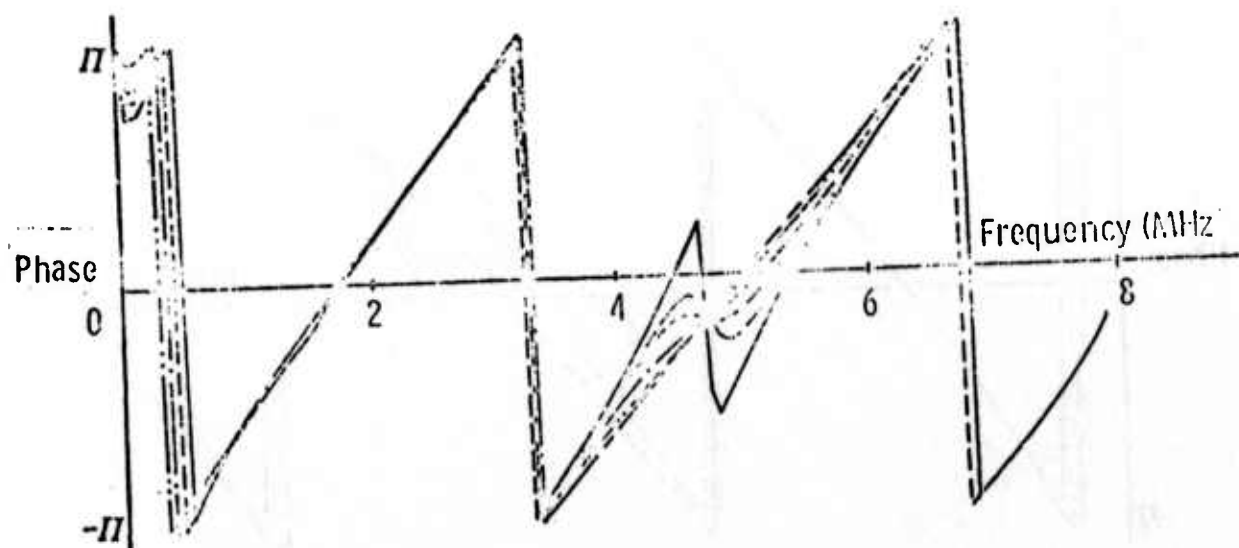


Fig. 5b - Frequency Characteristics of the Ultrasonic Reflections from .029 cm Bondlines Having Monotonically Increasing Attenuation Functions.

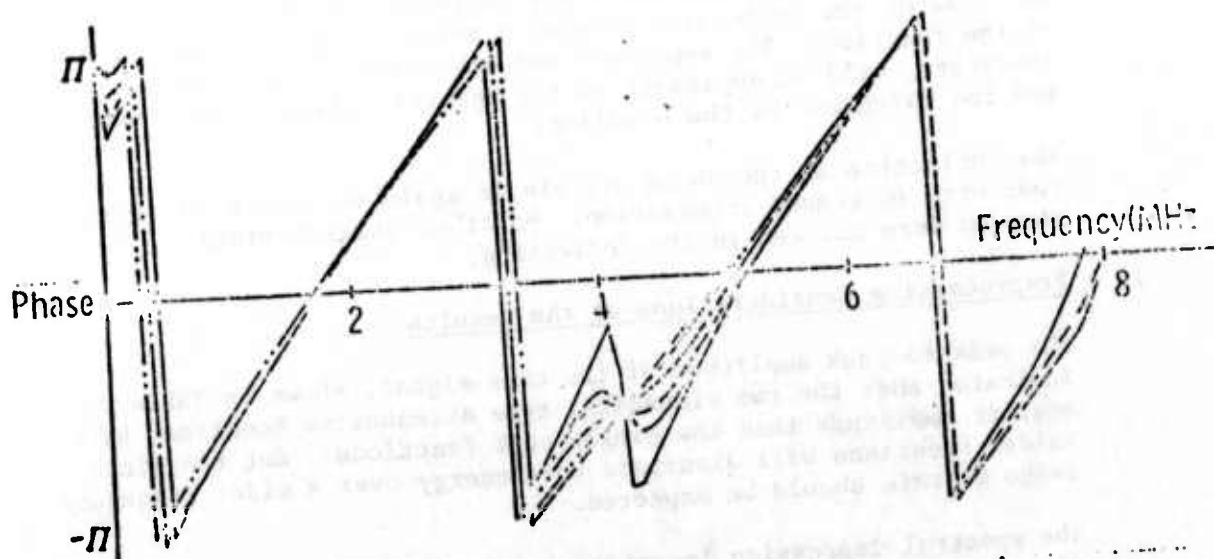
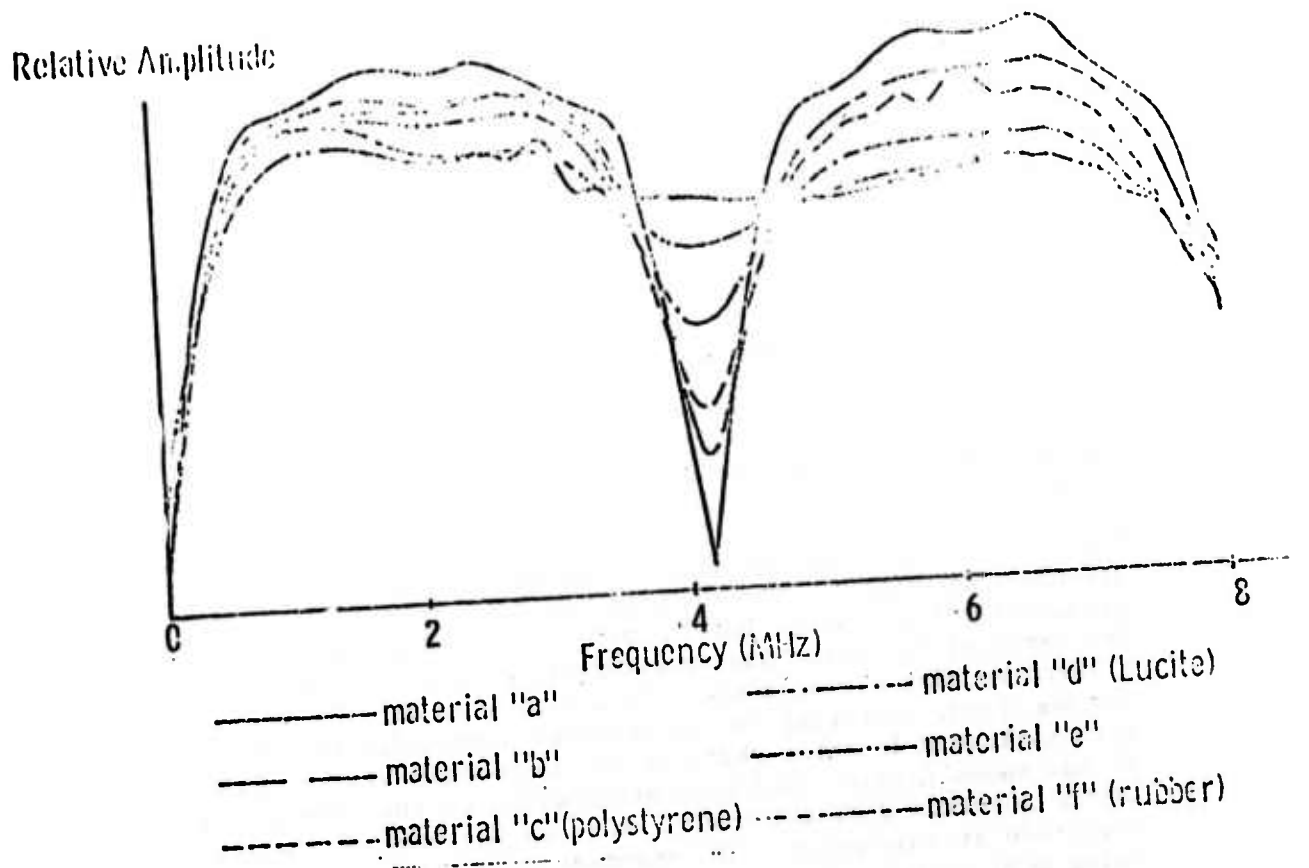


Fig. 5c - Frequency Characteristics of the Ultrasonic Reflections from .333 cm. Bondlines Having Monotonically Increasing Attenuation Functions.



the change in the depth of the spectral depression which was observed earlier. The spectral depression location do vary, however, correlations with the attenuation functions are not conclusive.

Resonant Type Attenuation Functions

1) Visual Signal Evaluation

The amplitude-time profiles for computer runs 7 to 10 (materials "g" to "j") are shown in Fig. 6. The variations among these signals are not so obvious as in the previous set but careful inspection will establish the differences.

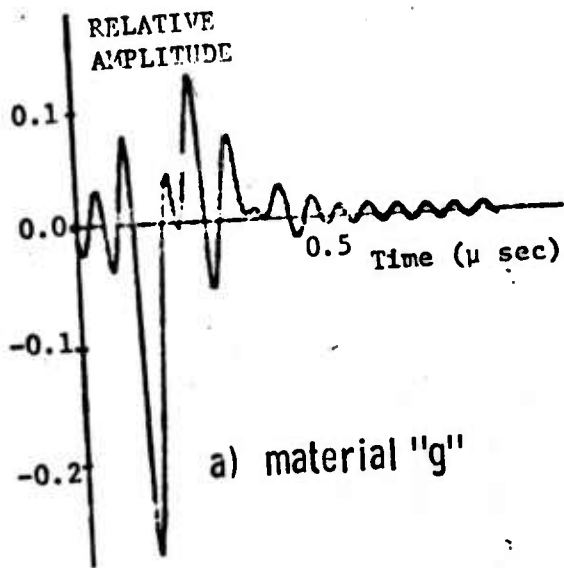
The Fourier amplitude and phase profiles for these reflections are shown in Fig. 7. These curves are more indicative of the attenuation functions. For instance, the Fourier amplitude curve for material "g" which has an attenuation peak at 2 MHz, shows a corresponding dip at 2 MHz. In addition to the increase of the amplitude occurring at the spectral depression location, a more noticable location shift of the depression can be observed. It was shown earlier that high attenuation in the frequency range of the spectral depression will cause an increase in the Fourier amplitude at this point. The resonant type attenuation functions being used contain peaks which may increase the amplitude more on one side of the depression causing a shift in the minimum value of the function. The magnitude and direction of this shift, therefore, will be dependent on the specific attenuation function and the thickness of the bondline.

The inflection in the phase profile is again decreased in magnitude with increased attenuation. No other characteristic changes were noticed in the inflection.

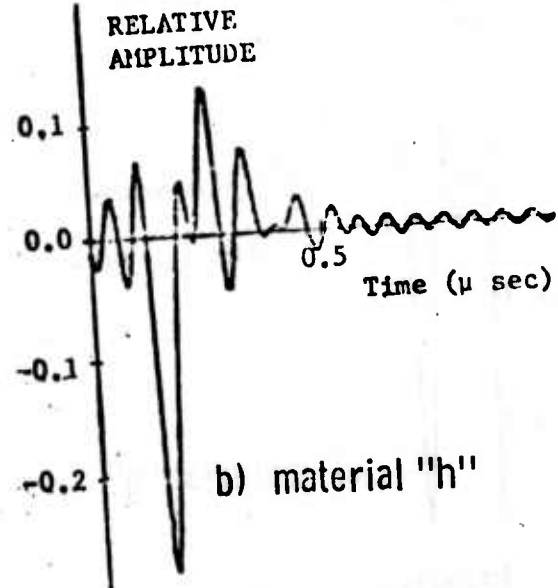
2) Preprocessing Considerations of the Results

The peak-to-peak amplitude of the time signal, shown in Table 2, indicates that the two sinusoidal type attenuative bondlines have smaller amplitude than the single peak functions. But the sinusoidal functions will dissipate more energy over a wider frequency range so this should be expected.

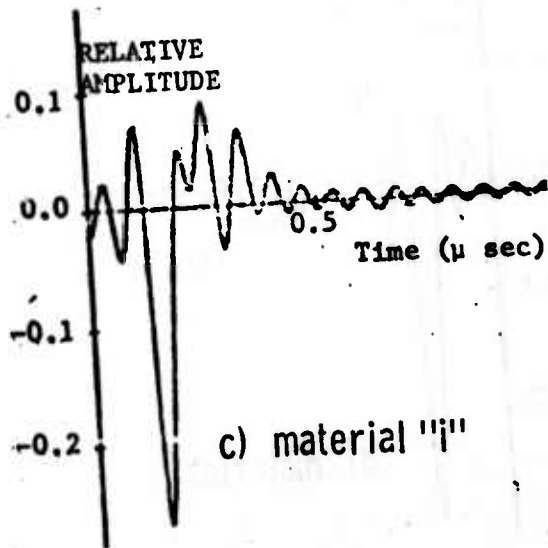
The spectral depression locations and frequency amplitude ratios given in Tables 3 and 4 could be misleading without considering other data. The spectral depression shift due to attenuation should not be confused with an indication of a change in bondline thickness. However, if the thickness of the bondline is known, the minimum amplitude frequency location could be useful in determining characteristics of the attenuation function. Some characteristics



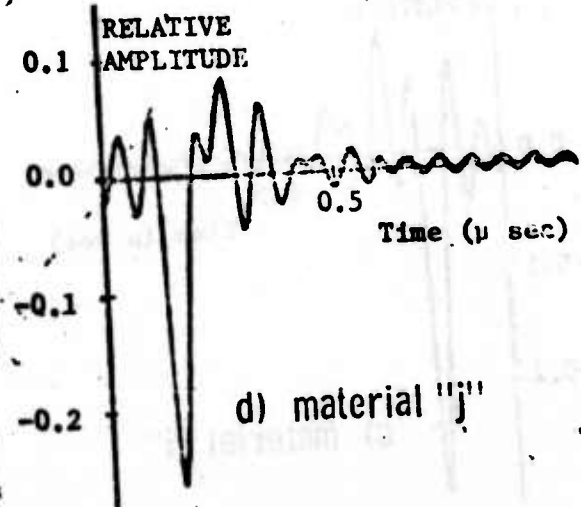
a) material "g"



b) material "h"

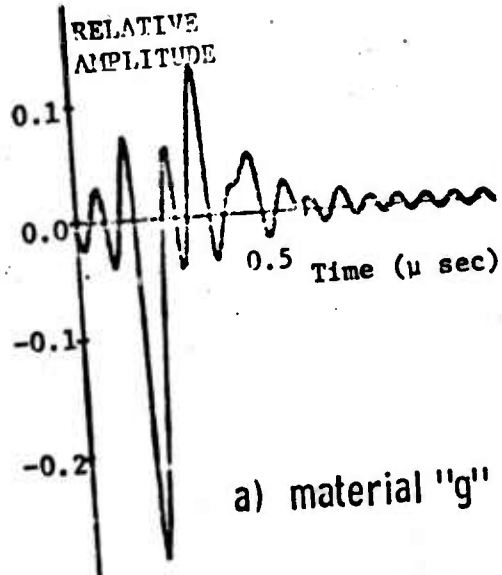


c) material "i"

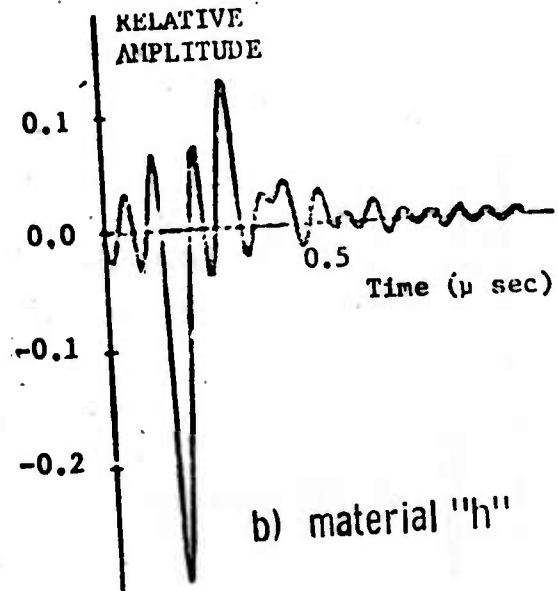


d) material "j"

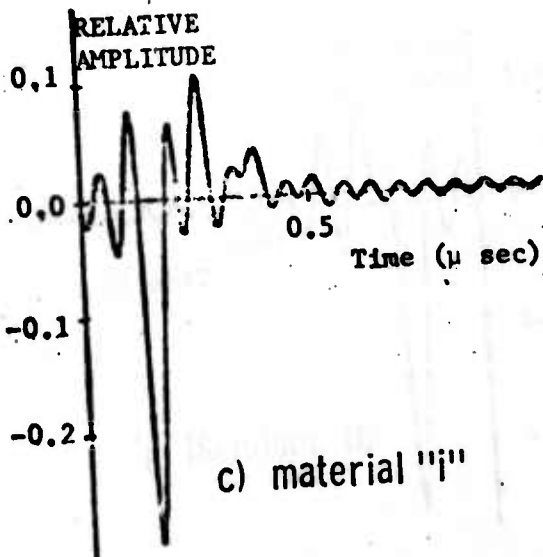
Fig. 6a - Ultrasonic Reflections from .025 cm Bondlines Having Resonant Type Attenuation Functions.



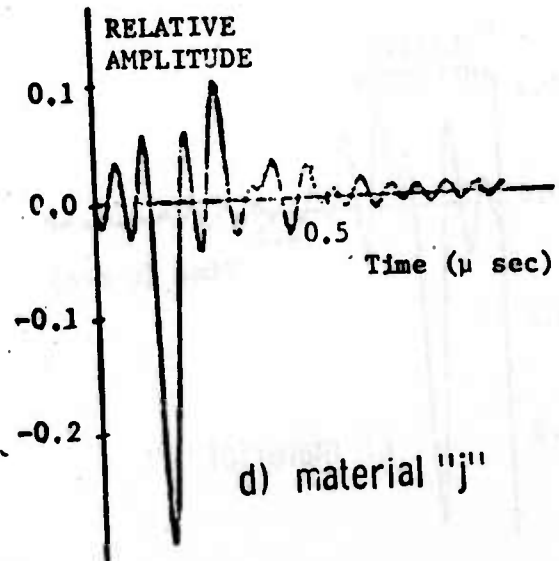
a) material "g"



b) material "h"



c) material "i"



d) material "j"

Fig. 6b - Ultrasonic Reflections from .029 cm Bondlines Having Resonant Type Attenuation Functions.

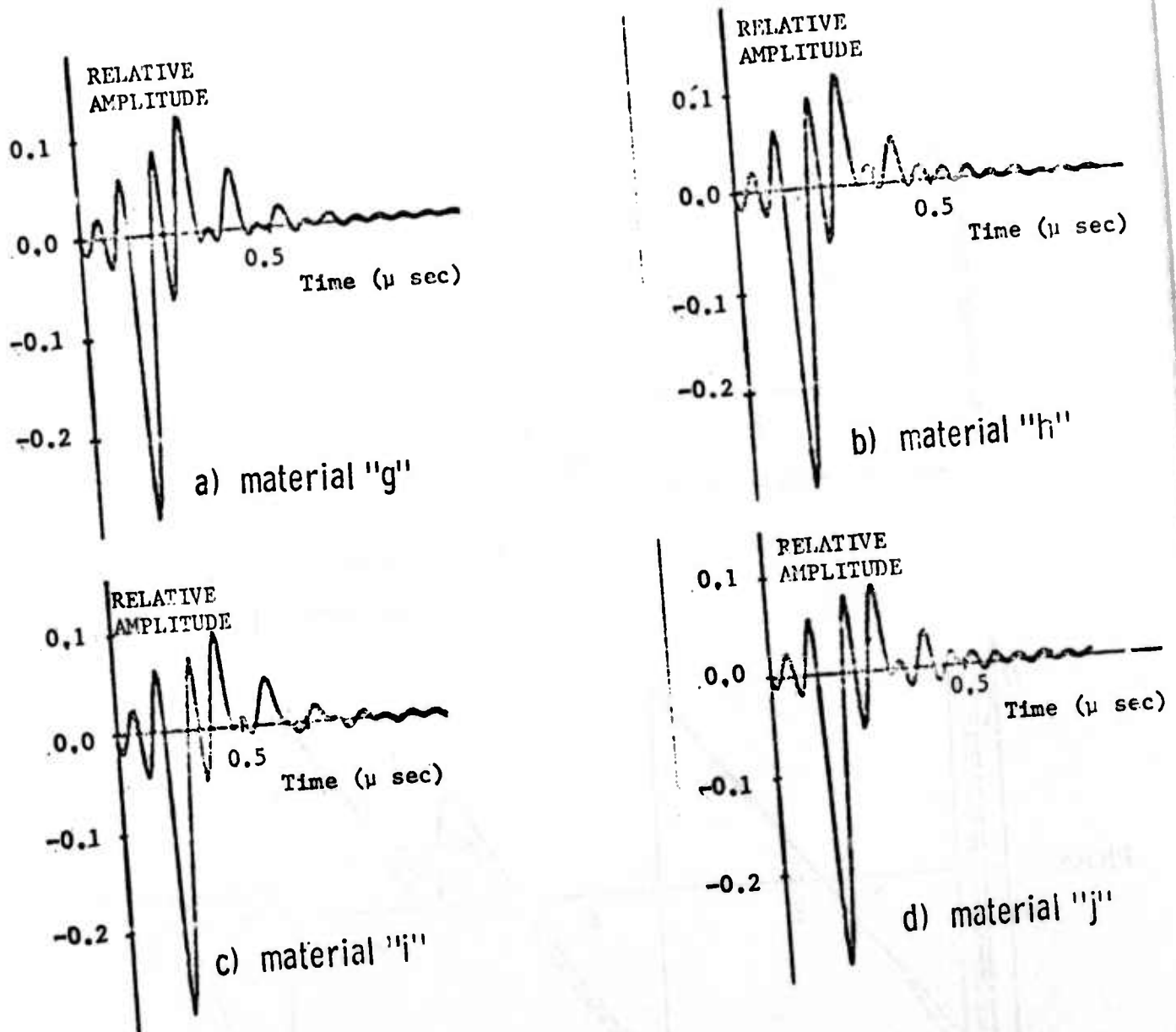


Fig. 6c - Ultrasonic Reflections from .033 cm Bondlines Having Resonant Type Attenuation Functions.

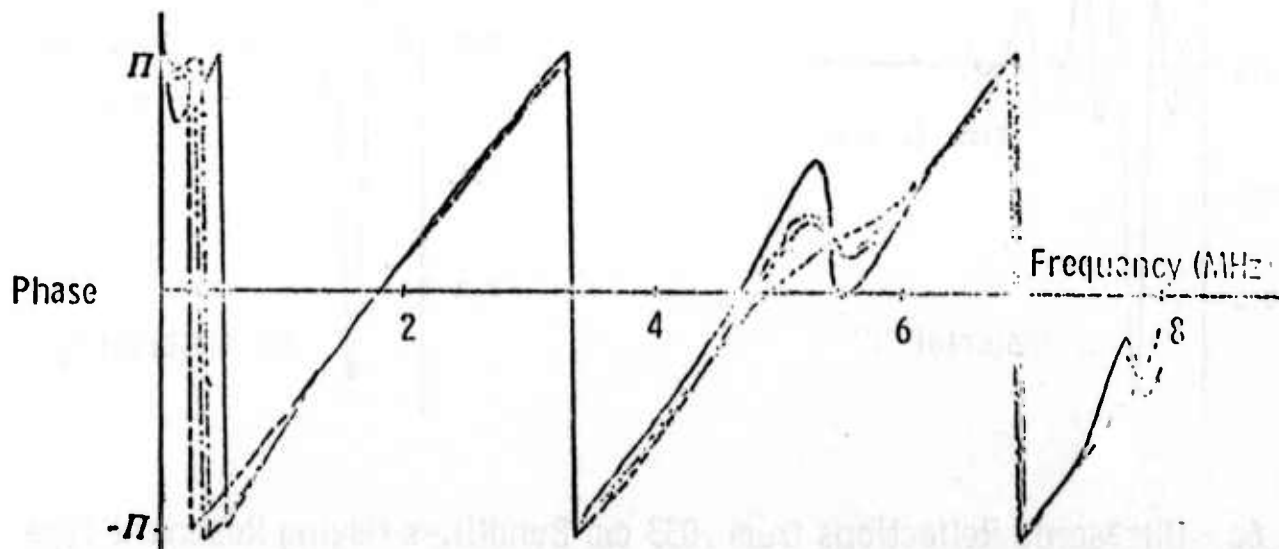
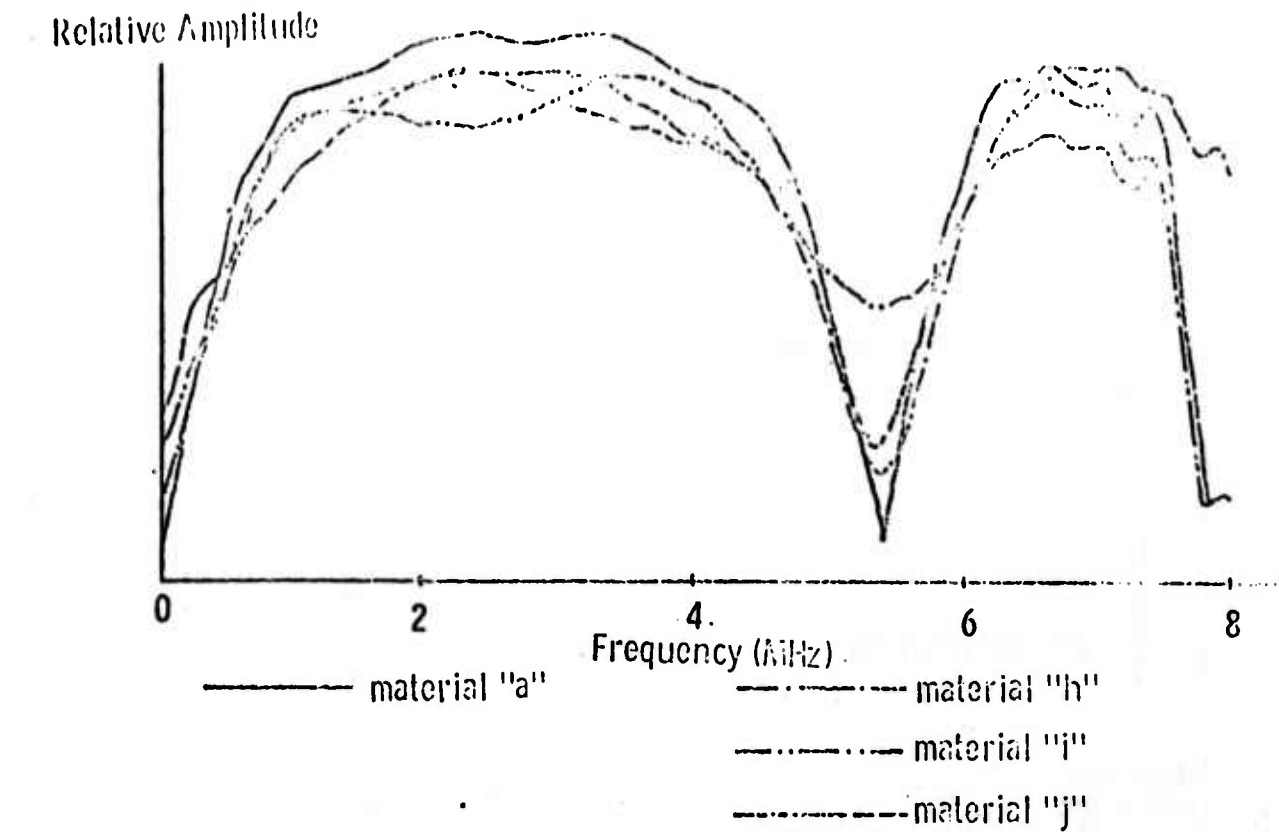


Fig. 7a - Frequency Characteristics of the Ultrasonic Reflections from .025 cm Bondlines Having Resonant Type Attenuation Functions.

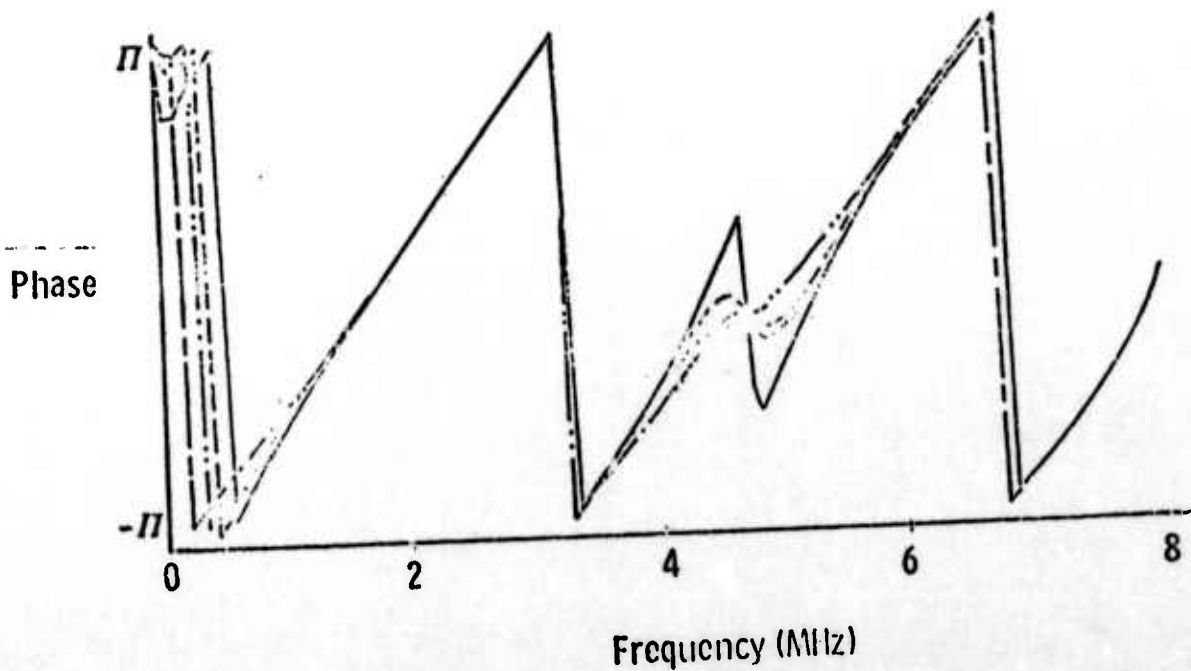
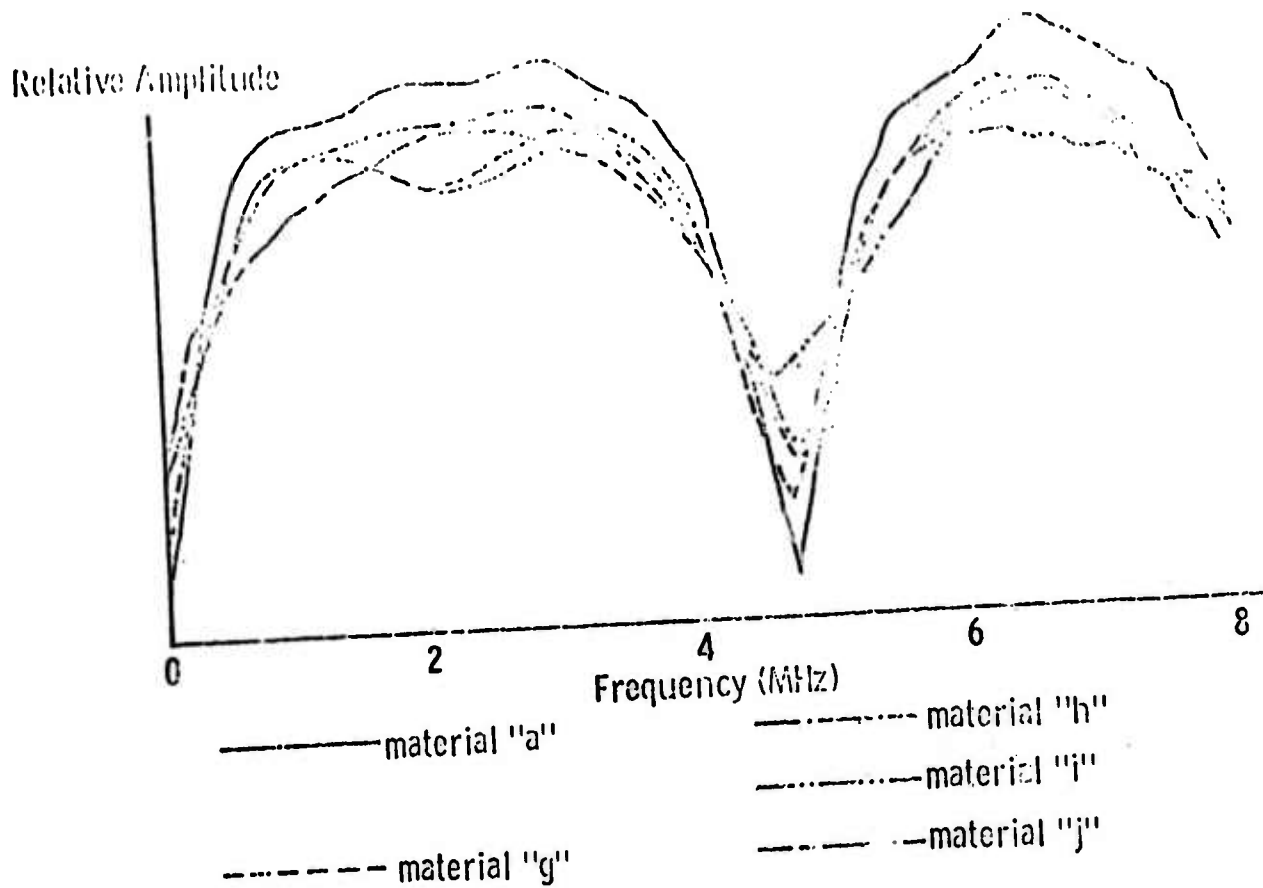


Fig. 7b - Frequency Characteristics of the Ultrasonic Reflections from .529 cm Bondlines Having Resonant Type Attenuation Functions.



Computer Run

	1	2	3	4	5	6	7	8	9	10	11	12
0.025	3.88	4.05	3.94	3.67	3.47	3.58	3.92	3.96	3.45	3.33	3.47	3.47
0.029	4.53	4.17	4.06	3.72	3.43	3.53	4.05	4.10	3.86	3.80	3.45	3.43
0.033	4.37	4.00	3.92	3.60	3.41	3.48	3.88	3.97	3.69	3.61	3.41	3.38

Bondline
Thickness
(cm)

Table 2 - Peak to Peak Reflection Amplitude for the Bond
Model Analysis Computer Runs

Computer Run

	1	2	3	4	5	6	7	8	9	10	11	12
0.025	5.4	5.43	5.40	5.33	5.15	4.95		5.40	5.40	5.40	5.15	5.08
0.029	4.73	4.71	4.71	4.71	4.58	4.83	4.70	4.78	4.50	4.78	4.66	4.46
0.033	4.14	4.12	4.14	4.14	4.14	4.53	4.14	4.28	4.09	4.26	4.09	3.9

Bondline
Thickness
(cm)

Table 3 - Spectral Depression Location (MHz) of the Frequency
Profiles for the Bond Model Analysis Computer Runs

Computer Run

	1	2	3	4	5	6	7	8	9	10	11	12
0.025	0.09	.213	0.32	0.57	0.76	0.82		0.15	0.55	0.27	0.72	0.72
0.029	0.04	.213	0.35	0.54	0.74	0.80	0.22	0.34	0.49	0.33	0.71	0.72
0.033	0.06	.275	0.36	0.55	0.78	0.79	0.29	0.56	0.37	0.55	0.72	0.74

Bondline
Thickness
(cm)

225

Table 4 - Ratio of the Minimum to Maximum Amplitudes
of the Frequency Profiles for the Bond
Model Analysis Computer Runs

of the attenuation function would have to be known if the amplitude ratio in Table 4 is to be useful for these cases. If the peak of an attenuation function having only a single peak were to occur at the depression location, the ratio could be altered significantly. Occurring at a different frequency or for a bond having a different thickness, the ratio might not be changed at all.

Comparison of Results for a High Attenuation Interface With an Attenuation Gradient

This comparison demonstrates that the reflection profile is not a function of the particular attenuation parameters for the bondline but only the average attenuation value of the bondline. For instance, a comparison of the reflections from a bondline having a high attenuation interfaces and one having a 6 layer attenuation gradient across the bondline thickness shown in Fig. 8 indicates only very small differences. A similar comparison in Fig. 9 in the frequency domain shows the same similarity. This similarity should be expected because the total dissipation of energy for each passage through the bondline is the same for both cases even though the distribution of the bondline is the same for both cases even though the distribution of the attenuation parameters is different.

Concluding Remarks

Results of this work indicates that attenuation effects in ultrasonic bond inspection may be quite substantial in altering the reflected pulse shape and amplitude and also characteristics of the Fourier Transform such as the spectral depression depth and Fourier phase profiles. This demonstrates the need for incorporation of attenuation effects into future work as well as more accurate representation of the attenuation characteristics of adhesive materials. An understanding of these variations due to attenuation could prove useful in evaluating adhesive bond quality in ultrasonic inspection programs through the proper selection of the signal generating and signal processing equipment.

With the addition of the attenuation effects to the bond model program, a resource base is now available which is capable of generating analytical reflection data sets for use with various learning machine and pattern recognition theories. One such technique called "simulearning", introduced by Rose, Mast and Niklas (10) could prove beneficial to the bond evaluation program possibly through the elimination of adhesive-substrate interface effects, once the interfaces have been characterized. This would allow the adhesive properties to be characterized separately. In addition, magnification of the attenuation effects might be possible through the incorporation of transform processors other than Fourier. Using a well defined mathematical pattern recognition and indication optimization programs other than, simply the visual inspection of peak-to-peak amplitude or spectral depression shape, bond evaluation could become a more quantitative science.

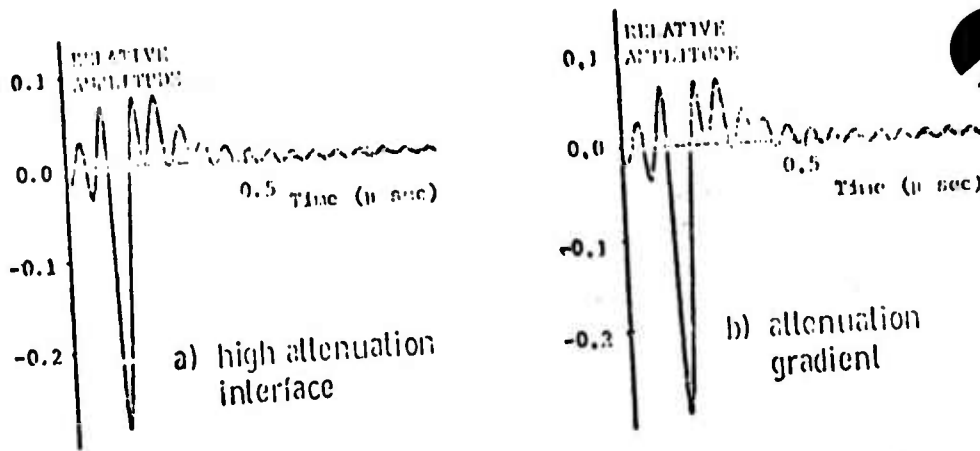


Fig. 8a - A Comparison of Ultrasonic Reflections from a .325 cm Bondline Having a Single Layer High Attenuation Interface versus a 6 Layer Attenuation Gradient across the Bond Thickness.

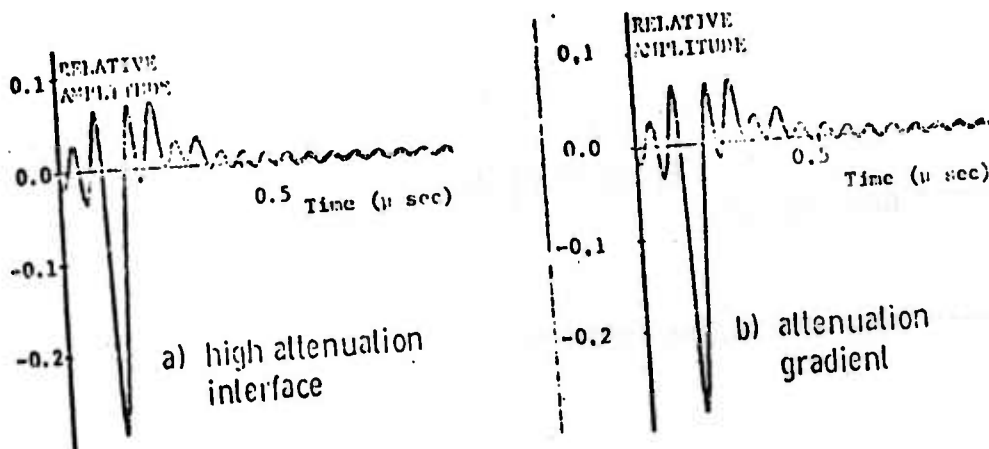


Fig. 8b - A Comparison of Ultrasonic Reflections from a .329 cm Bondline Having a Single Layer High Attenuation Interface versus a 6 Layer Attenuation Gradient across the Bond Thickness.

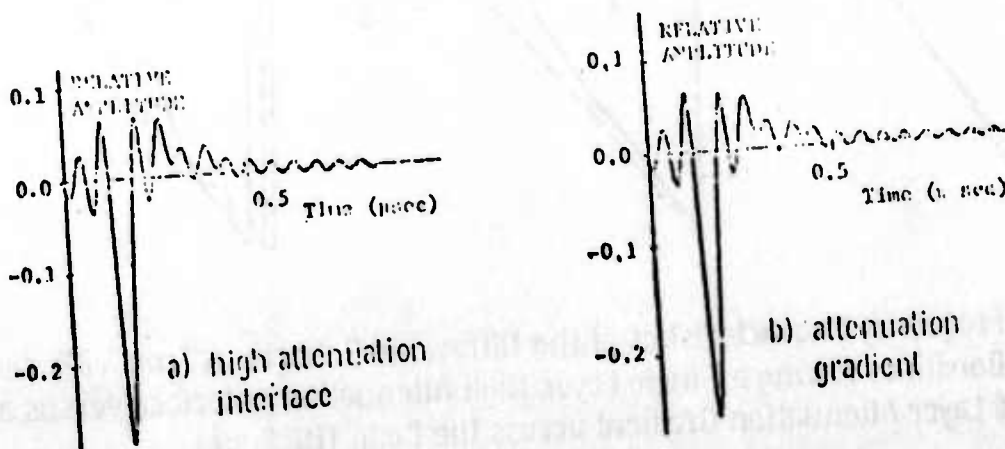


Fig. 8c - A Comparison of Ultrasonic Reflections from a .333 cm Bondline Having a Single Layer High Attenuation Interface versus a 6 Layer Attenuation Gradient Across the Bond Thickness.

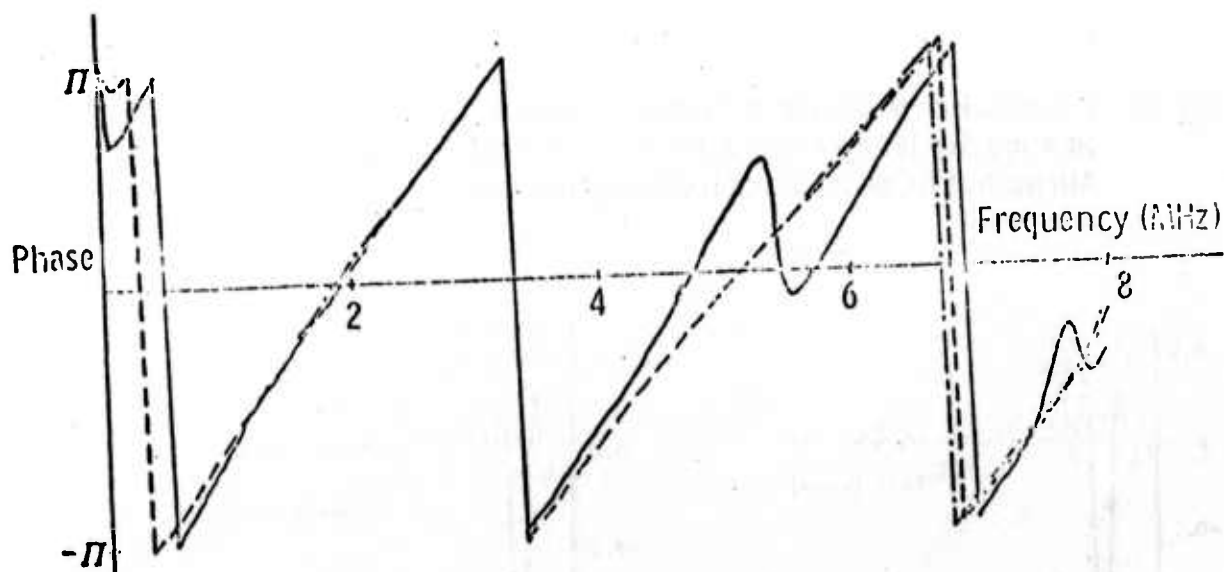
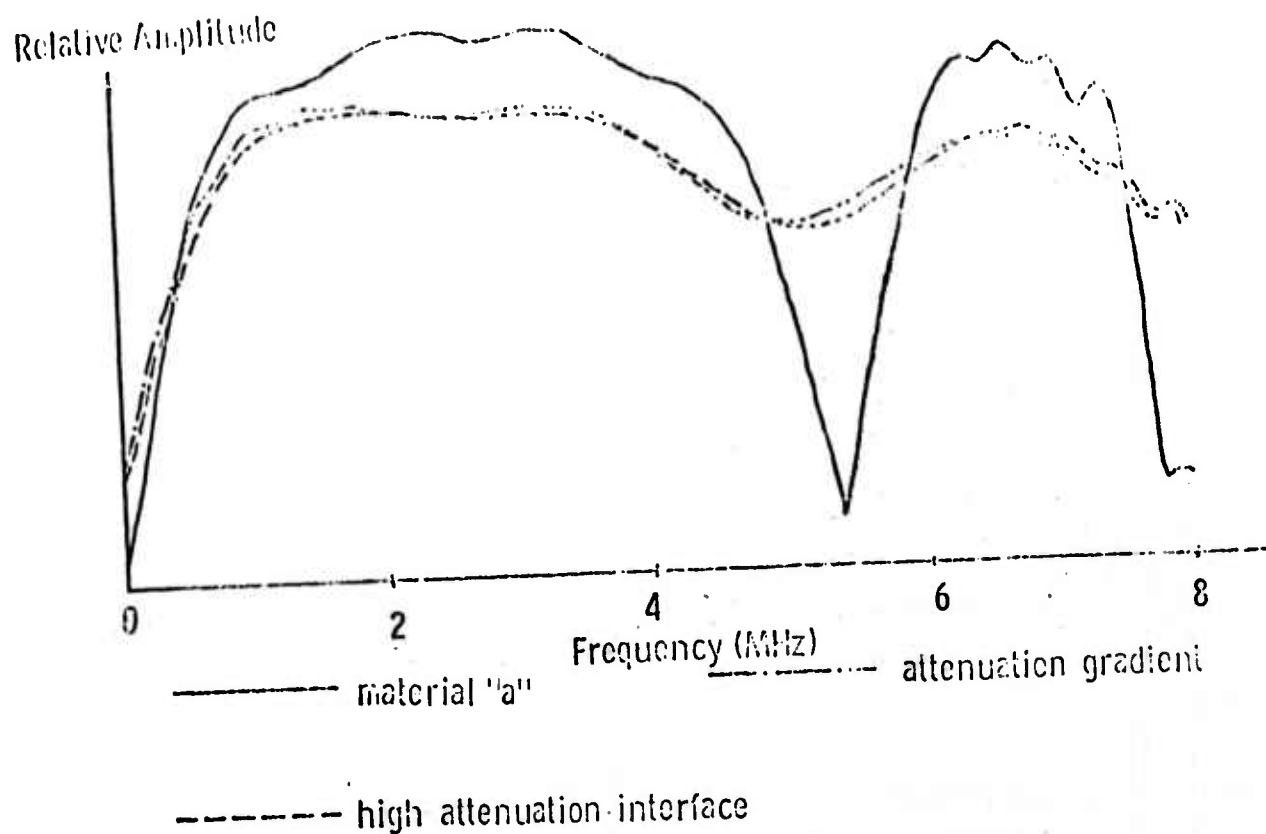


Fig. 9a - Frequency Characteristics of the Ultrasonic Reflections from .025 cm Bondlines Having a Single Layer High Attenuation Interface versus a 6 Layer Attenuation Gradient across the Bond Thickness.

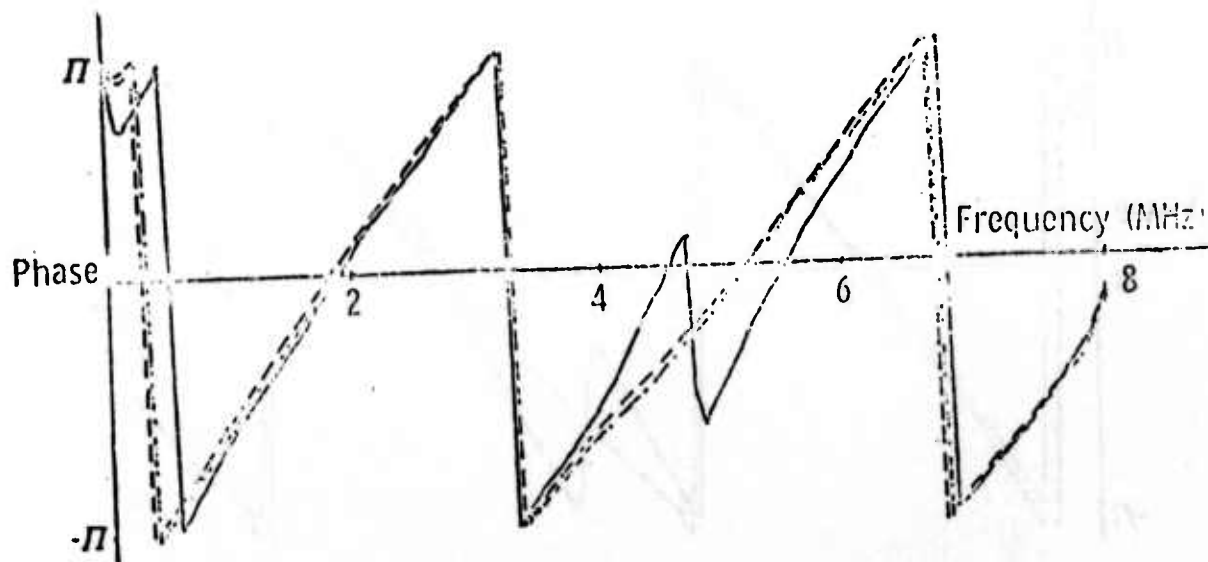
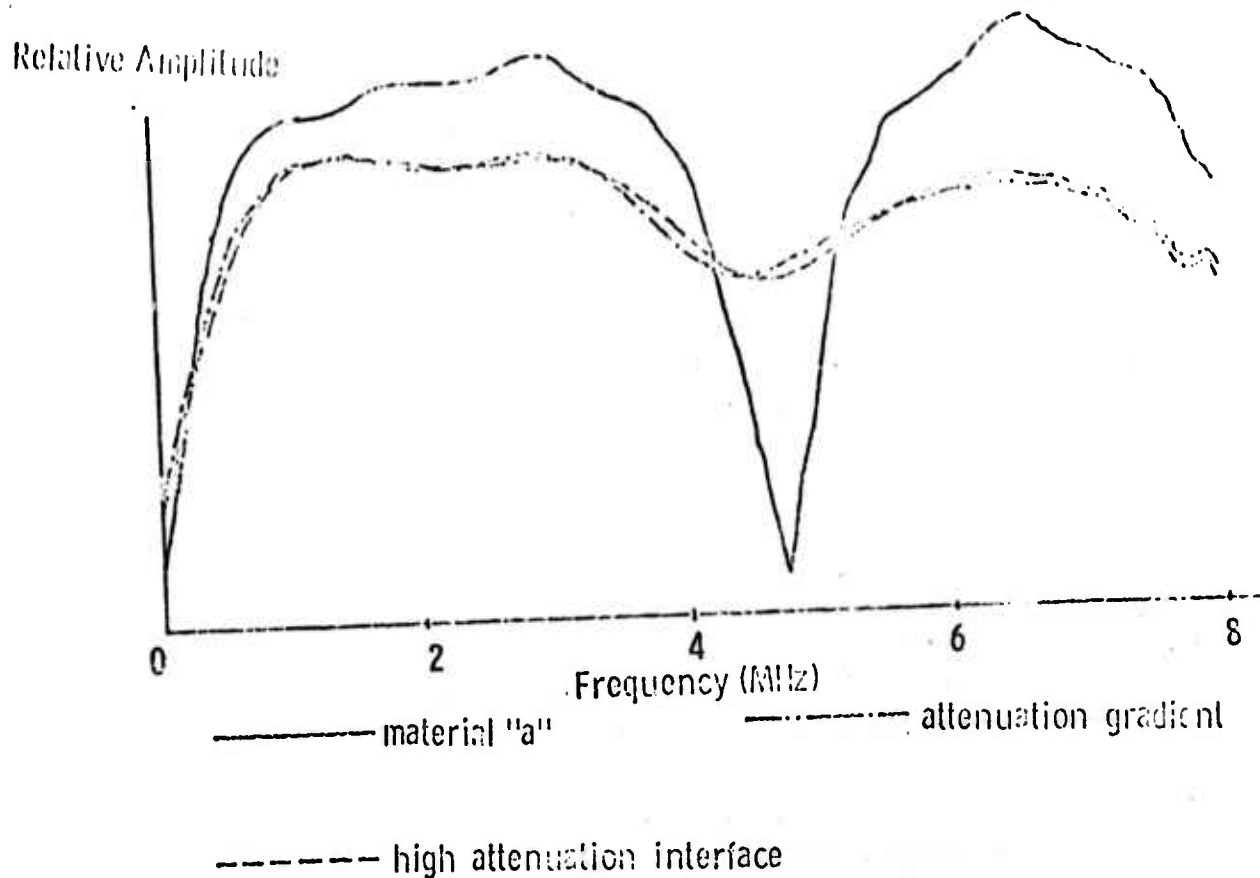


Fig. 9b - Frequency Characteristics of the Ultrasonic Reflections from .029 cm Bondlines Having a Single Layer High Attenuation Interface versus a 6 Layer Attenuation Gradient across the Bond Thickness.

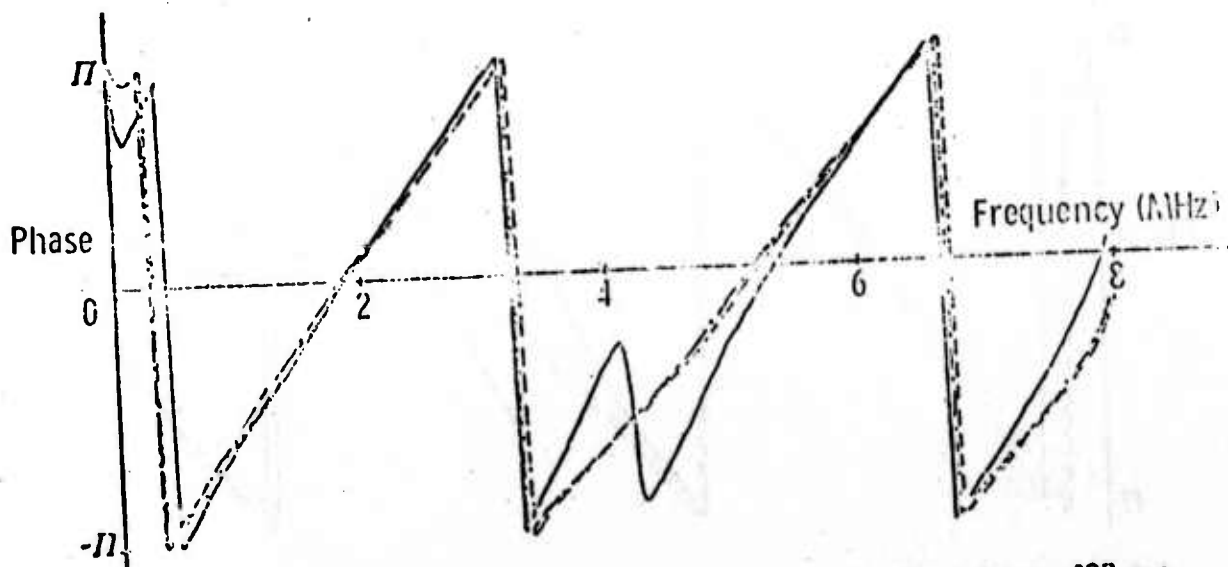
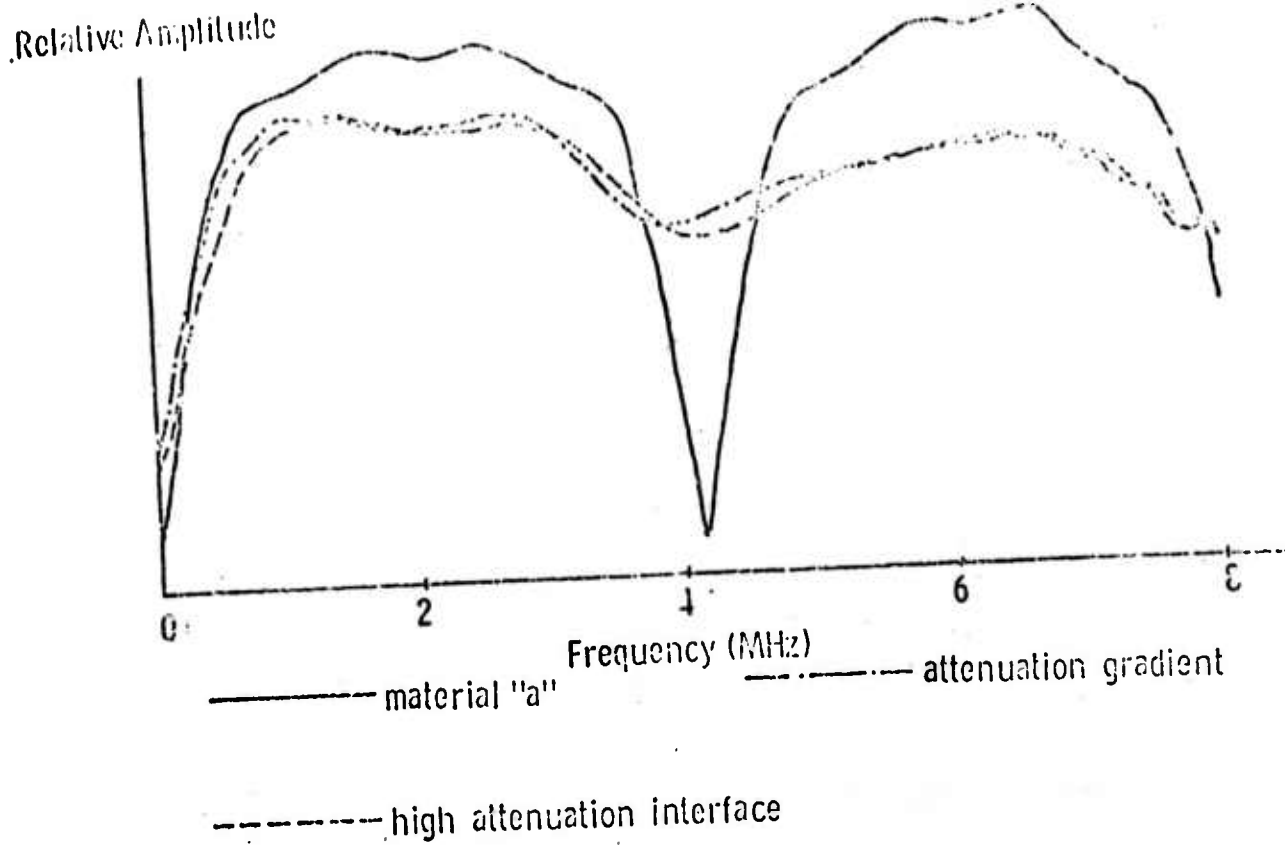


Fig. 9c - Frequency Characteristics of the Ultrasonic Reflections from .033 cm Bondlines Having a Single Layer High Attenuation Interface versus a 6 Layer Attenuation Gradient across the Bond Thickness.

References

1. J. R. Zurbrick, "Nondestructive Test Technique Development Based on The Quantitative Prediction of Bond Adhesive Strength, "AVSD-0331-70-RR, Prepared by Avco Government Products Group 1969, July 21 to 1970, July 20.
2. J. R. Zurbrick, E. A. Proudfoot and C. H. Hastings, "Nondestructive Test Technique Development for Evaluation of Bonded Materials," AVSD-0494-71-CR, Prepared by Avco Government Products Group 1970, Oct. 5 to 1971, Nov. 5.
3. J. L. Rose and Paul A. Meyer, "Ultrasonic procedures for Predicting Adhesive Bond Strength," Materials Evaluation, Vol. 31, June 1973 p. 109-114.
4. R. B. Thompson, G. A. Alers and D. O. Thompson, "Nondestructive Measurement of Adhesive Bond Strength in Honeycomb Panels, "Materials Evaluation, Vol. 32, April 1974, p. 81.
5. J. L. Rose and Paul A. Meyer, "Ultrasonic Procedures for the Determination of Bond Strength," AFOSR-73-2480A, AFOSR Interim Scientific Report.
6. W. P. Mason "Piezoelectric Crystals and Their Application to Ultrasonics," Von Nostrand, 1950.
7. John D. Ferry, "Viscoelastic Properties of Polymers", John Wiley and Sons, Inc. 1970.
8. Michel Auberger and John S. Rinehart, "Ultrasonic Attenuation of Longitudinal Waves in Plastics," Journal of Applied Physics, Vol. 32, Feb. 1961, p. 219-222.
9. Personal communication with Dr. E. Kraut, Science Center, Rockwell International, Thousand Oaks, Calif.
10. Rose, J. L., Mast, P. W., and Niklas, L., "Simulearning Potential in Flaw characterization," presented at a special ASM Conference in San Francisco, July 9, 10, and 11, 1975 on Fracture Mechanics, Flaw Characterization and Nondestructive Testing.

Acknowledgment

This work is supported by the Science Center, Rockwell International. The authors would also like to thank Mr. Graham Thomas for his assistance in this study

NONDESTRUCTIVE TEST FOR STRENGTH DEGRADATION IN COMPOSITES

D. H. Kaelble
Science Center, Rockwell International

ABSTRACT

Hydrothermal (separate or combined high moisture and temperature) aging of graphite fiber reinforced epoxy matrix composites produces irreversible deterioration in interlaminar shear strength λ_b over a range of temperatures from $-150^{\circ}\text{C} \leq T \leq 120^{\circ}\text{C}$. Fiber surface treatments were employed to produce controlled rates and extents of hydrothermal degradation in the laminated composite. A study was conducted to develop methods of specifically detecting and identifying the extent and mechanism of hydrothermal aging. This study shows that hydrothermal aging concurrently degrades the bonded fiber-matrix interface, produces changes in the chemical network structure of the epoxy matrix, and modifies the differential stress balances imposed by fiber constraints upon the epoxy continuum phase. The degradation state of the fiber-matrix interface is detected through correlation of surface energetics analysis, ultrasonic characterization, and moisture take up. The state of the bulk epoxy is evaluated by differential scanning calorimetry (DSC) and specific heat measurements, IR and dynamic mechanical spectroscopy, and thermo-mechanical analysis (TMA). The fiber-matrix stress state is delineated by thermal expansivity, dynamic mechanical spectroscopy, and ultrasonic response. These nondestructive measurement techniques for hydrothermal aging form the basis for detailed analysis of the relations between materials response and composite performance and reliability.

PROJECT II, UNIT II, TASK 1
NONDESTRUCTIVE TEST FOR STRENGTH DEGRADATION
IN COMPOSITES

D. H. Kaelble
Science Center, Rockwell International

Introduction

A number of published reports show that exposure of laminated graphite-epoxy or graphite-polyester composites to water immersion or water vapor at elevated temperatures leads to irreversible degradation of interlaminar shear strength and changes in fracture toughness(1-6). In this study several recent theories of moisture degradation in composite materials⁽³⁻⁶⁾ were employed in conjunction with a range of nondestructive tests on the composite material to accomplish the following three phases of this program.

1. Prepare and degrade reinforced composite specimens with varied moisture susceptibility.
2. Characterize composites by NDE and correlate with mechanical strength.
3. Develop a mathematical model to relate physical property measurements with molecular mechanisms of moisture degradation.

Conclusions

This study of detection of moisture degradation in uniaxially reinforced graphite-epoxy composites provided the following conclusions concerning the response parts of accelerated moisture degradation.

Part 1: Interface

- Surface energy analysis of both fiber and matrix correctly predict moisture degradation.
- Translaminar ultrasonic (2.25 MHz) sound velocity and absorption measures prior moisture exposure and strength degradation.

Part 2: Bulk Matrix

- Changes in chemical network structure produced by aging modify the matrix dynamic mechanical spectrum to lower sound velocity and increase absorption.
- Hydrothermal (100°C in H₂O) aging induces a temporary rubbery response state through water swelling which permits micro-defect growth in the matrix phase.

Part 3: Composite System Response

- Unaged composites display a high degree of locked in strain along fiber axis due to fiber-matrix constraints.

- The fiber-matrix strain relaxation during aging produces major temperature shifts in the glass transition.

Experimental

The graphite-epoxy composite materials utilized in this study are described in Table 1. Composite SC-2-2 was designed with a fiber-matrix interface of high moisture sensitivity and composite SC-2-3 was designed to display a moisture resistant interface. The study of the kinetics and mechanisms for hydrothermal aging effects in the interface, bulk matrix, and composite system response are respectively summarized in Table 2.

Results

1. Interfacial Aspects

The measurement of interlaminar shear strength (λ_b) and moisture uptake (Wt.% H_2O) served as direct indicators of the rate and extent of moisture degradation. The upper curves of Figure 1 plot the averaged values of λ_b as a function of hydrothermal (100°C in H_2O) aging time while the lower curves display Wt.% H_2O which accompanies strength degradation. The fiber surface treatments described in Table 1 provide widely different kinetics and extent of fractional degradation in interlaminar shear strength in these two composites as shown by upper Figure 1. Analysis of these data is made in terms of the following expression: (6)

$$\lambda_b(t) = \lambda_{bo} \left[r + (1-r) \exp(-t/\tau) \right] \quad (1)$$

where $\lambda_b(t)$ and λ_{bo} denote interlaminar shear strength at hydrothermal aging time t and $t = 0$ respectively, $r = \lambda_{b\infty}/\lambda_{bo}$ is a dimensionless degradation ratio and τ the relaxation time for degradation. The moisture sensitivity of composite SC-2-2 is reflected in the low values of $r = 0.37 \pm .11$ and $\tau = 3.15 \pm 1.67$ hr as compared to higher values of $r = 0.67 \pm 0.09$ and $\tau = 52.5 \pm 8.9$ hr for moisture resistant composite SC-2-3.

Ultrasonic (2.25 MHz) measurement of longitudinal sound velocity C_L and acoustic adsorption α_L at 23°C was conducted on the aged and dried interlaminar shear specimens. The upper curves of Figure 2 show that interlaminar sound velocity diminishes in a systematic manner with hydrothermal degradation of shear strength λ_b . The lower curves of Figure 2 show that α_L increases systematically with decreased λ_b . Similar results are obtained for both composite SC-2-2 and SC-2-3 indicating that a single correlation applied for two materials of different interfacial moisture sensitivity.

The data of Figure 1 and Figure 2 represent degradation effects and correlations applicable to ambient test temperature at 23°C. The effect of prior moisture aging and drying of composite SC-2-3 upon λ_b over a range

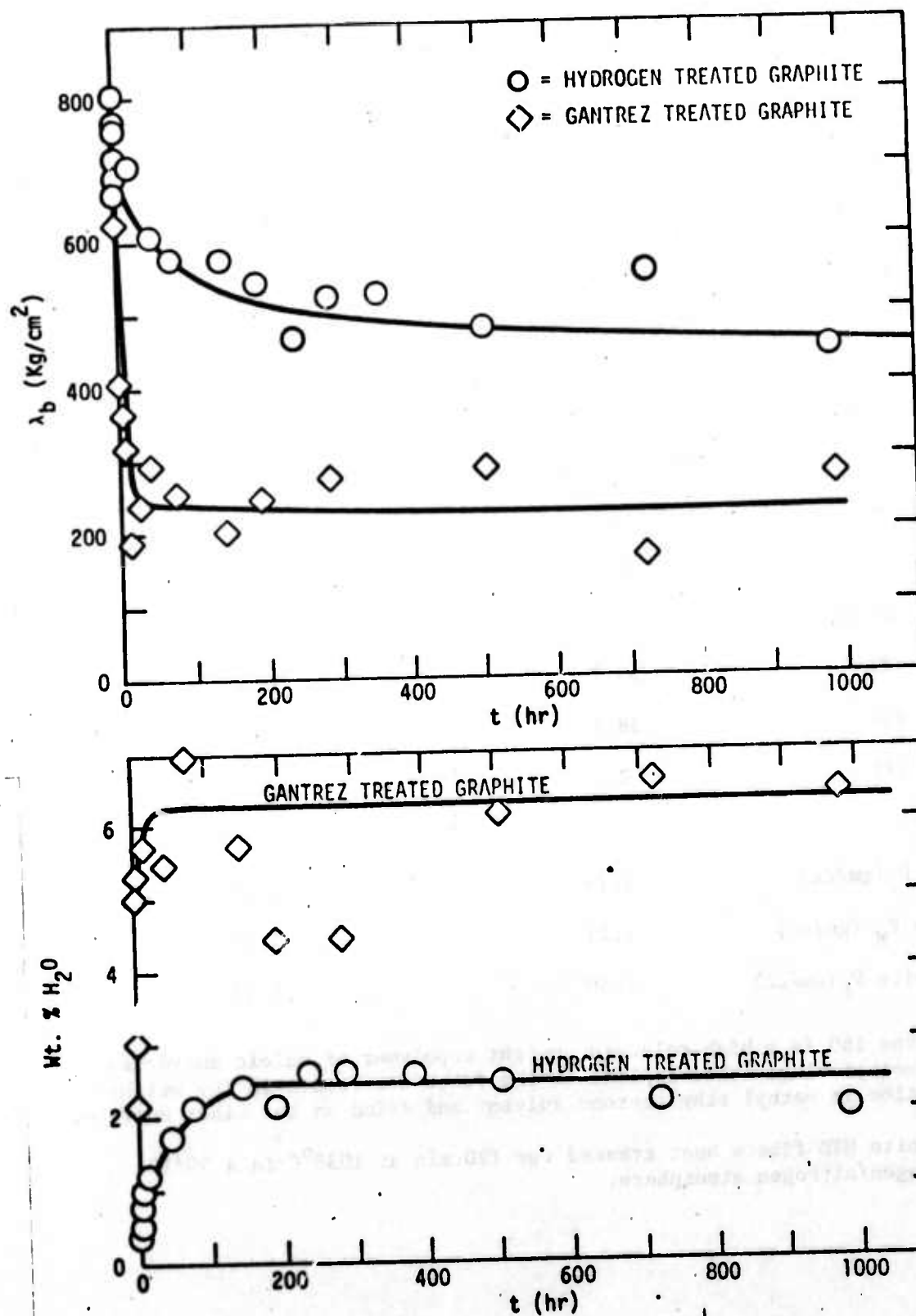


Fig. 1

TABLE 1

Constituents and Volume Fractions of Components
in Uniaxially Reinforced Graphite-Epoxy Panels

Reinforced Composite Panel	SC-2-2 Moisture Sensitive	SC-2-3 Moisture Resistant
Fiber plies/cm	52	52
Fiber	HTS with Gantrez (1) 169 Size	HTS with Hydrogen (2) Surface treatment
Resin	BP907	BP907
Volume Fractions		
Fiber (%)	59.7	57.0
Resin (%)	38.1	43.0
Voids (%)	2.2	0.1
Densities:		
Fiber P_F (gm/cc)	1.74	1.74
Matrix P_M (gm/cc)	1.21	1.21
Composite P_C (gm/cc)	1.50	1.51

(1) Gantrez 169 is a high molecular weight copolymer of maleic anhydride and methyl vinyl ether applied to the fiber tow from a 1% (by weight) solution in methyl ethyl ketone solvent and dried on the fiber surface.

(2) Graphite HTS fibers heat treated for 120 min at 1038°C in a 90/10:: hydrogen/nitrogen atmosphere.

TABLE 2

Experimental Methods for Study of
Moisture Degradation

Part 1: Interface

- Surface energy analysis
- Interlaminar shear strength
- Moisture take up
- Ultrasonics-transverse (2.25 MHz)
- SEM failure surface

Part 2: Bulk Matrix

- Differential scanning calorimetry
- Specific heat
- Infrared spectroscopy
- Dynamic mechanical spectroscopy (1.1-110 Hz)
- Thermomechanical analysis
- SEM failure surface

Part 3: Composite System Response

- Thermal expansivity
- Dynamic mechanical spectroscopy (1.1 - 110 Hz)
- Ultrasonics - longitudinal (30 KHz)
- Ultrasonics - transverse (1-10 MHz)
- SEM failure surface

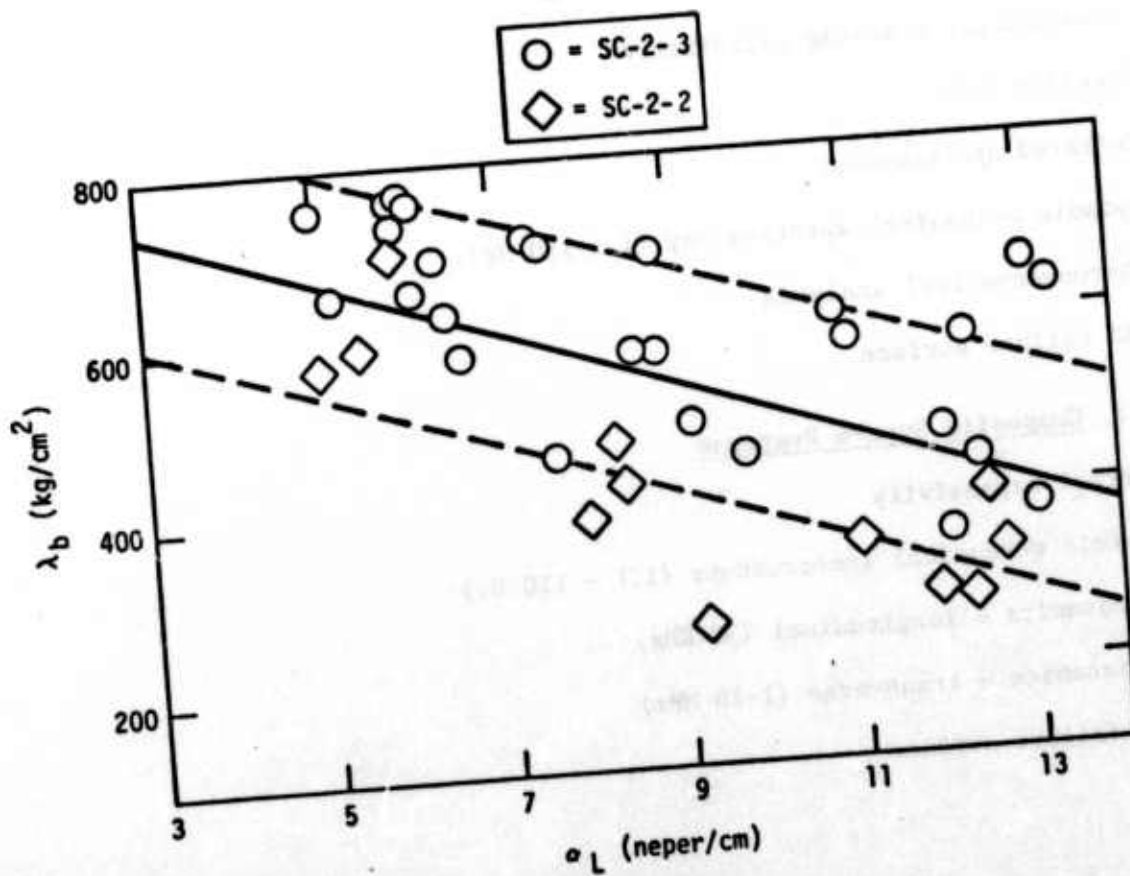
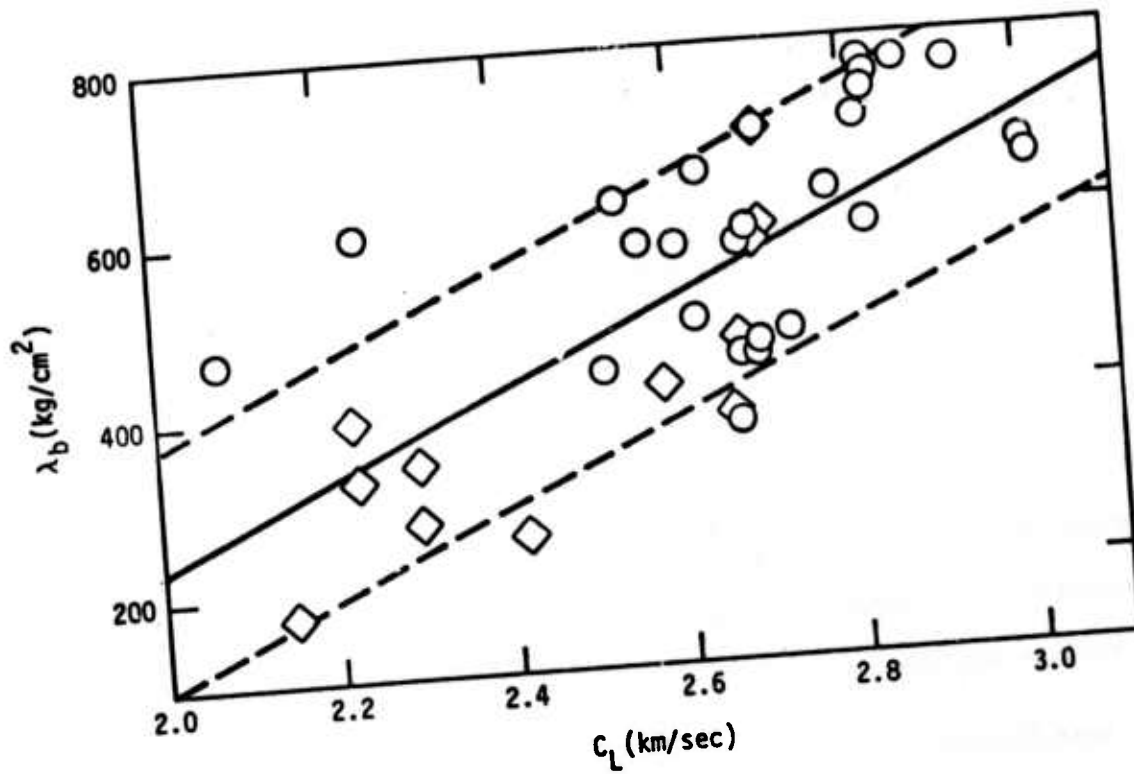


Fig. 2



of test temperatures is shown in Figure 3. These data show that the epoxy β relaxation at $T_{\beta} = -45 \pm 15^{\circ}\text{C}$ marks the point where λ_b becomes temperature dependent in both aged and unaged composite. The values of λ_b in both unaged and aged composites approach $\lambda_b = 0$ at the matrix glass transition temperature $T_g = 122 \pm 15^{\circ}\text{C}$. The data of Figure 3 show that λ_b is importantly influenced by matrix rheology and that analysis of NDT^b data on the pure matrix is required.

2. Matrix Aspects

A combination of chemical analysis by IR spectroscopy combined with a calorimetry study of curing kinetics indicates that BP 907 epoxy matrix displays the curing mechanisms outlined in Table 3. The first reaction indicated by the upper arrow in Table 3 shows four epoxide groups reacting with one molecule of DICY to form a highly polar and hydrogen bonding crosslink. This portion of the epoxy network is highly water susceptible. Further studies of wet and dry aging of the cured epoxy confirmed a second chemical reaction indicated by the lower arrow of Figure 3 in which one portion of the crosslink is modified by the guanyl urea ring structure. These reactions have been reported in the literature for DICY cured epoxy resins^(7,8).

The β viscoelastic transition in BP907 which is produced by motion of the $-\text{O}-\text{CH}_2-\text{CH}(\text{OH})-\text{CH}_2-$ segments shown in the crosslink structure of Table 3 might be expected to change due to the aging reaction which leads to the guanyl urea ring structure. Dynamic mechanical spectroscopy (1.1 - 110 Hz on Rheovibron) measurements confirm this assumption as shown in the curves of mechanical loss tangent $\tan \delta$ versus temperature in Figure 4. The curves of Figure 4 show that at temperatures above $T_{\beta} - 30^{\circ}\text{C}$ the hydrothermally aged and dried BP 907 displays higher values of $\tan \delta$ indicative of lower values for the modulus of elasticity and sound velocity. These property changes in the pure matrix are consistent with aging effects on composite ultrasonic response shown in Figure 2.

Measurement of the 15 second tensile relaxation modulus $E(t)$ as a function of test temperature during thermomechanical analysis (TMA)⁽⁹⁾ was undertaken to correlate hydrothermal aging effects on both the β and α (or glass) transitions of BP907. The curves of Figure 5 show plots of $\log E(t)$ versus test temperature and show that hydrothermal aging does enhance the β transition and lower $E(t)$ at all temperatures above $T_{\beta} \cong -45^{\circ}\text{C}$ even when aged and dried. These results reconfirm the point that hydrothermally aged BP 907 matrix is chemically modified. The curves of Figure 5 also show that hydrothermally aged BP 907 in the wet state (12.2% by Wt. H_2O) shows a transition from glass to rubbery response well below the aging temperature of 100°C . In other words, water is a very effective plasticizer for the molecular motions which dominate the T_g response of BP907. Subsequent drying as shown in Figure 5 returns the $E(t)$ versus T curve nearly back to that shown for the unaged BP 907 α transition. Thus, the effects of moisture on the α transition response appear much more reversible

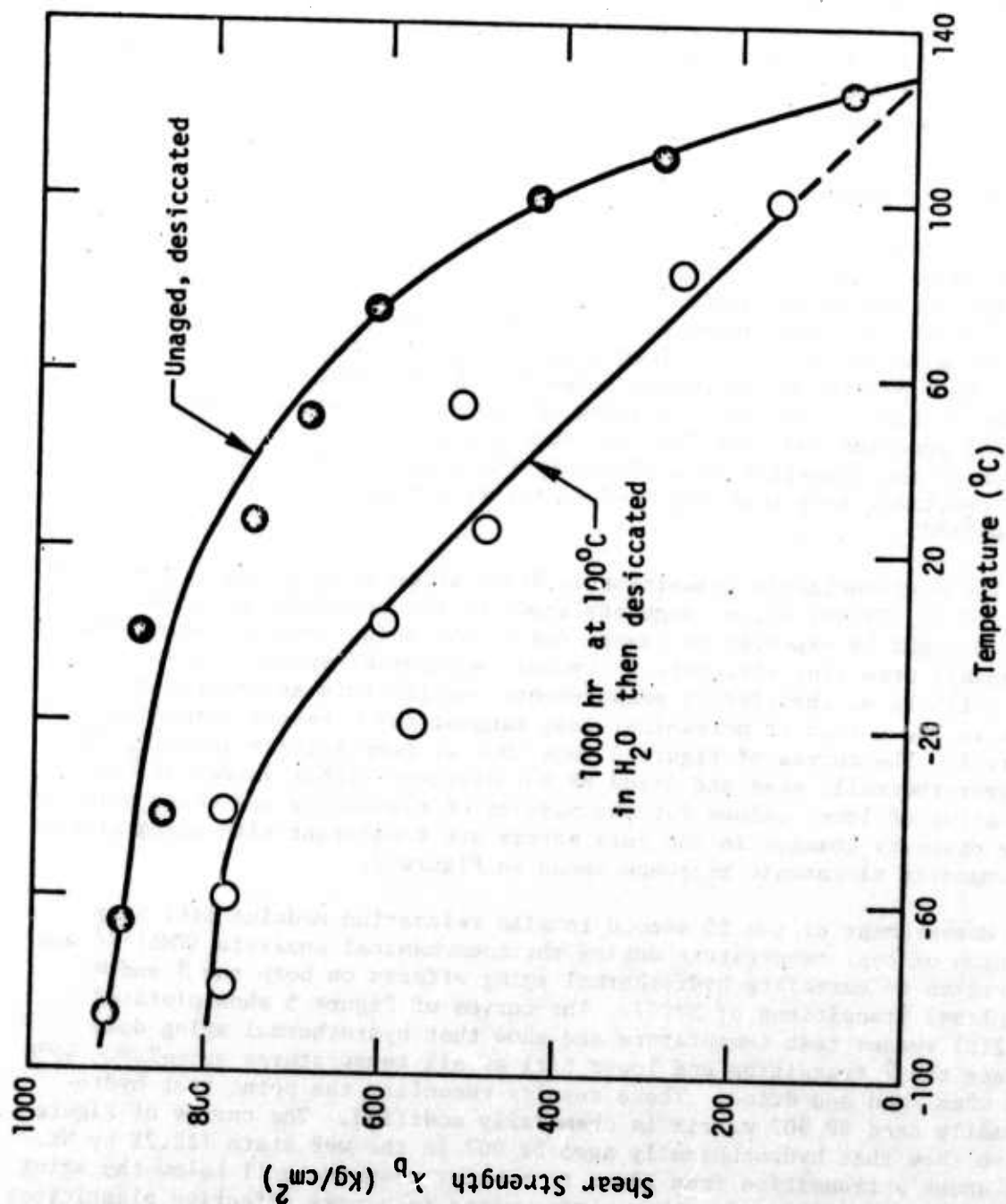


Fig. 3

Epoxy + Dicyanodiamide (DICY)

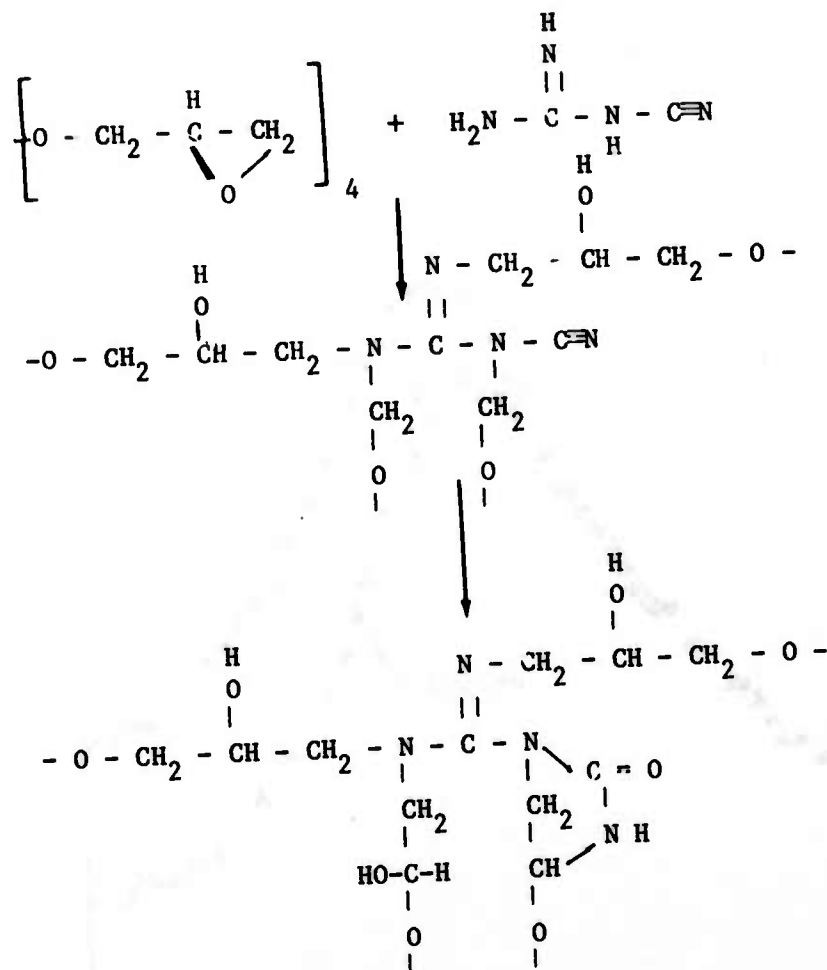


Table 3: Suggested Curing Mechanisms for Epoxy BP 907 Resin

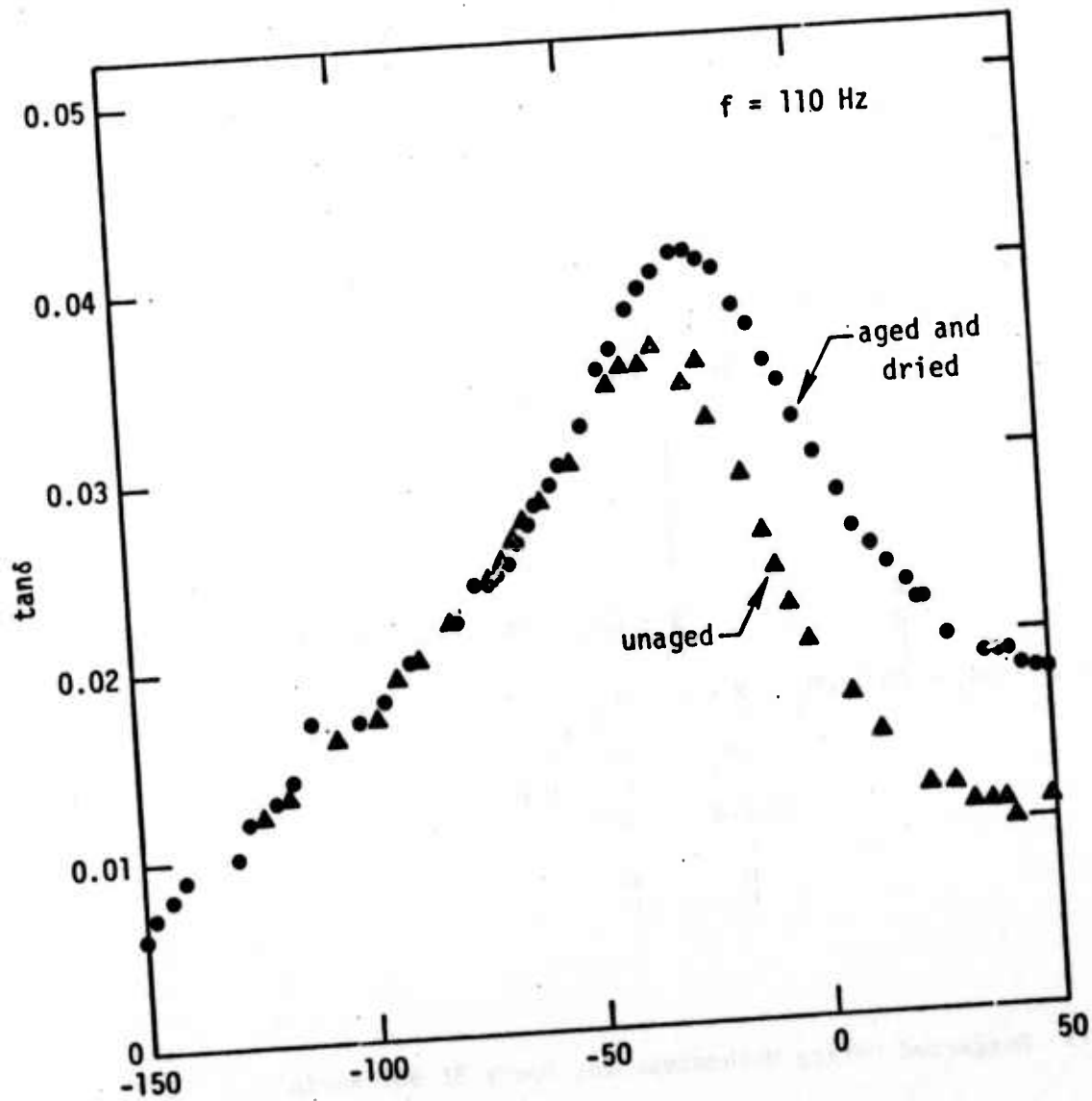


Fig. 4



than for β transition response.

The fact that the BP 907 matrix is temporarily plasticized to display rubbery response at 100°C was shown in subsequent studies to stimulate the growth of defects in the bulk resin which substantially lower the cohesive fracture toughness. All of the aging effects discussed above for the pure matrix phase contribute to the overall changes in composite interlaminar shear strength as reported in Figure 1 and Figure 3. The temperature dependence of λ_b in Figure 3 is clearly correlated with the $E(\tau)$ versus T functions of the pure BP 907 shown in Figure 5.

Composite System Response

Fabrication of polymer composite laminates invariably involves temperature differentials of over 100°C wherein significant internal (curing) stresses are developed within the composite. In some cases these stresses are reported to cause interlaminar failure or modified thermal expansivity. (10-14) In this study we observe what appears to be a new and important internal stress effect evidently produced by the specific history of hydrothermal aging. When composite SC-2-2 and SC-2-3 are hydrothermally aged at 100°C in H₂O the curves of Figure 5 shows that the matrix achieves a rubbery state where $T_g < 100^\circ\text{C}$. These swollen samples are removed to 23°C in the swollen state and thus the swollen matrix is returned to a glassy state where $T_g > 23^\circ\text{C}$. Subsequent desiccation removes the water from the glassy matrix and evidently this drying process leaves a state of excess free volume in the matrix phase. The internal stresses produced by this moisture uptake and drying cycle are sufficient to produce interlaminar failure in moisture sensitive composite SC-2-2. In moisture resistant composite SC-2-3 failure was not observed but large hysteresis in thermal strain versus temperature functions and suppression of the α transition temperature are clear evidence of the excess free volume state which correlates with a high triaxial tensile stress in the matrix phase.

Measurement of linear thermal strain response curves are illustrated in Figure 6 for composite SC-2-3 which is hydrothermally aged and dried at 23°C. The upper left curve shows the change in length, where initial length $L_0 = 1.000$ in, by first cooling to -95°C then heating to 170°C at constant thermal scan rate $\pm 1^\circ\text{C/min}$ and transverse to the fibers. At about +80°C on the first thermal cycle the curve bends downward and on cooling to 23°C a 0.6% loss in sample length is evident due to free volume collapse in the matrix phase.

The second thermal cycle shown in the upper right portion of Figure 6 still shows evidence of volume collapse accompanied by the expected change in slope at about 100°C characteristics of normal glass transition response for the BP 907 matrix. The third thermal cycle shown in the lower portion of Figure 6 shows that the hysteresis behavior has been essentially removed by the thermal annealing above T_g and the BP 907 displays a normal change in thermal expansivity at $T_g > 100^\circ\text{C}$.

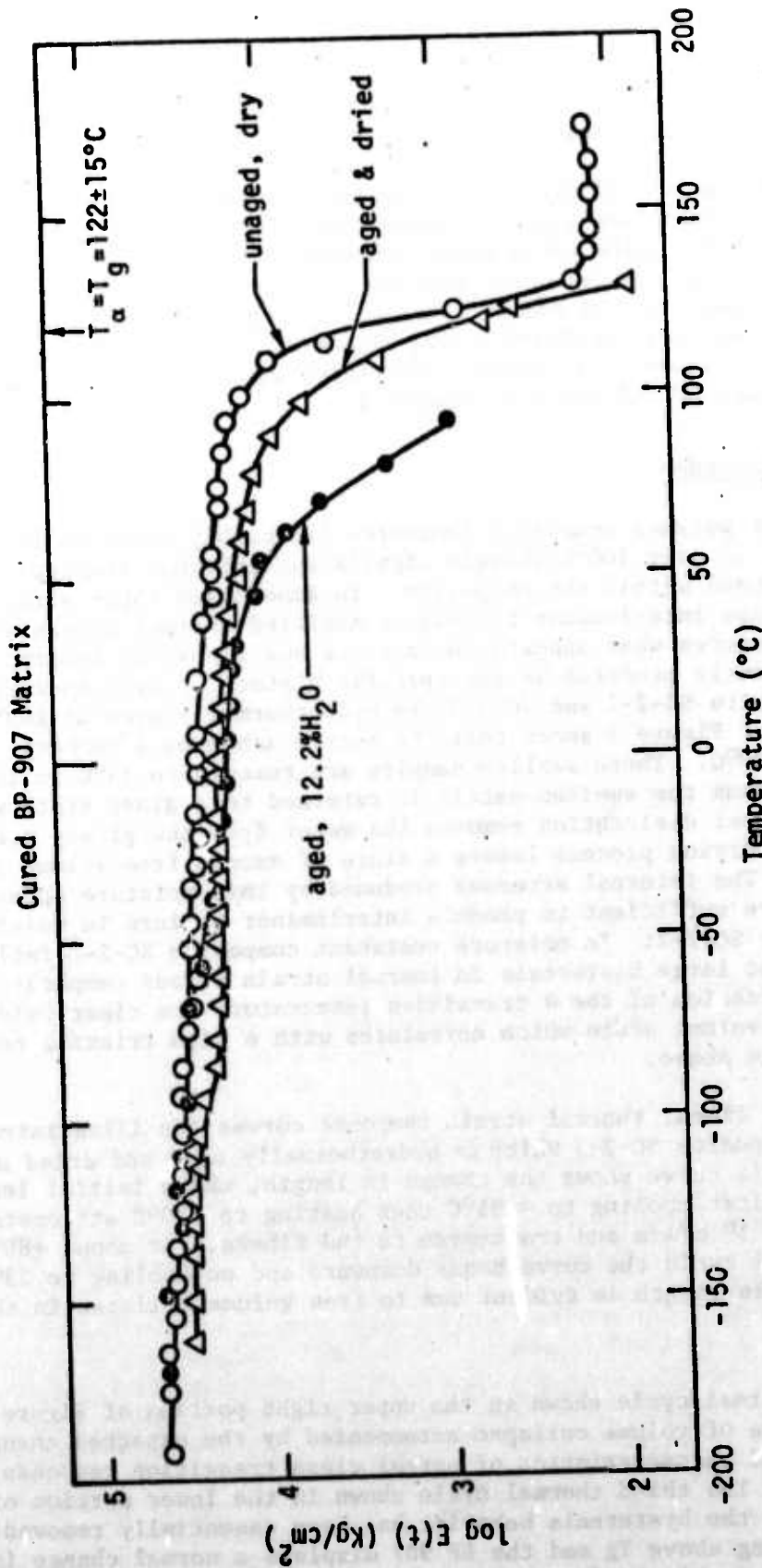


Fig. 5

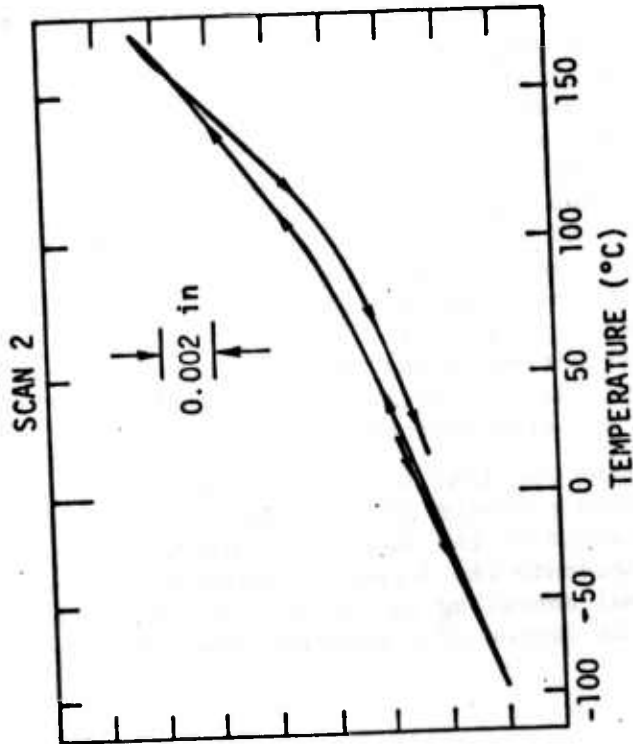
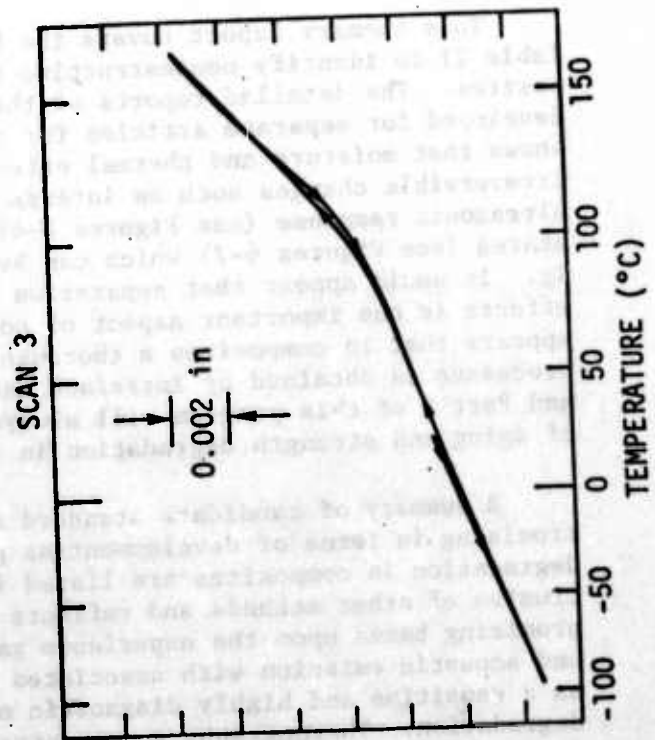
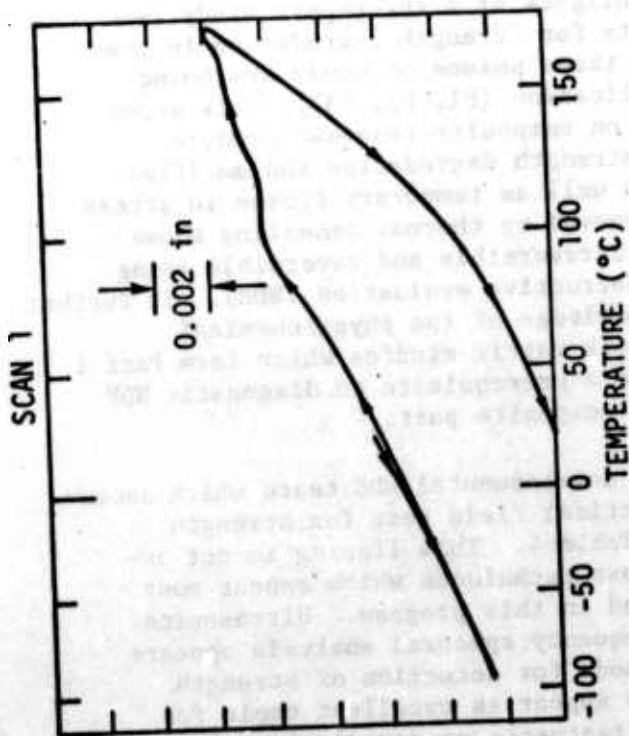


Fig. 6





The multiple curves of Figure 7 display the results of dynamic mechanical (Rheovibron) measurement of $\tan \delta$ at 110 Hz in the fiber axis of the composite. The first, second and third thermal scans (respective data symbols = closed square, closed circle, closed triangle) show successive shifts of the α transition curves of \tan versus T to higher temperature. The first thermal scan of the hydrothermally aged and dried specimen (data symbols = open squares) show onset of the α transition at below 100°C and the $\tan \delta$ versus T function bending over to converge with the thermally annealed response of unaged SC-2-3 at high temperature. The second thermal scan of SC-2-3, aged and dried, (data points = open circles) shows a complete loss of the original hysteresis. Since $\tan \delta$ relates directly with molecular motion in the matrix phase the curves of Figure 7 provide direct evidence that the primary rheological transitions of the composite can be modified by aging history.

The data of Figure 6 and Figure 7 point out that the past moisture state and particularly the time-temperature-moisture states provide important variables in the current internal stress state of the composite material. It further appears that measurements which indicate the degree of internal stress or creep relaxation, as produced by thermal annealing in Figure 6 and Figure 7 provide a basic new tool for evaluating the degree of recovering from prior aging history.

Summary

This summary report covers the highlights of a three-part study (see Table 2) to identify nondestructive tests for strength degradation in composites. The detailed reports of these three phases of study are being developed for separate articles for publication (P1, P2, P3). This study shows that moisture and thermal effects on composite response produce irreversible changes such as interface strength degradation and modified ultrasonic response (see Figures 2-4) as well as temporary frozen in stress states (see Figures 6-7) which can be removed by thermal annealing above T_g . It would appear that separation of irreversible and reversible aging effects is one important aspect of nondestructive evaluation (NDE). It further appears that in composites a thorough knowledge of the physiochemical processes as obtained by interface and bulk matrix studies which form Part 1 and Part 2 of this program will always be a prerequisite to diagnostic NDE of aging and strength degradation in the composite part.

A summary of candidate standard and developmental NDE tests which appear promising in terms of development as practical field test for strength degradation in composites are listed in Table 4. This listing is not exclusive of other methods and reflects those techniques which appear most promising based upon the experience gained in this program. Ultrasonics and acoustic emission with associated frequency spectral analysis appears as a sensitive and highly diagnostic methods for detection of strength degradation. Thermography and penetrants appear as excellent tools for detecting failure of protective surface treatments or degradation of surface structures exposed to environmental extremes.

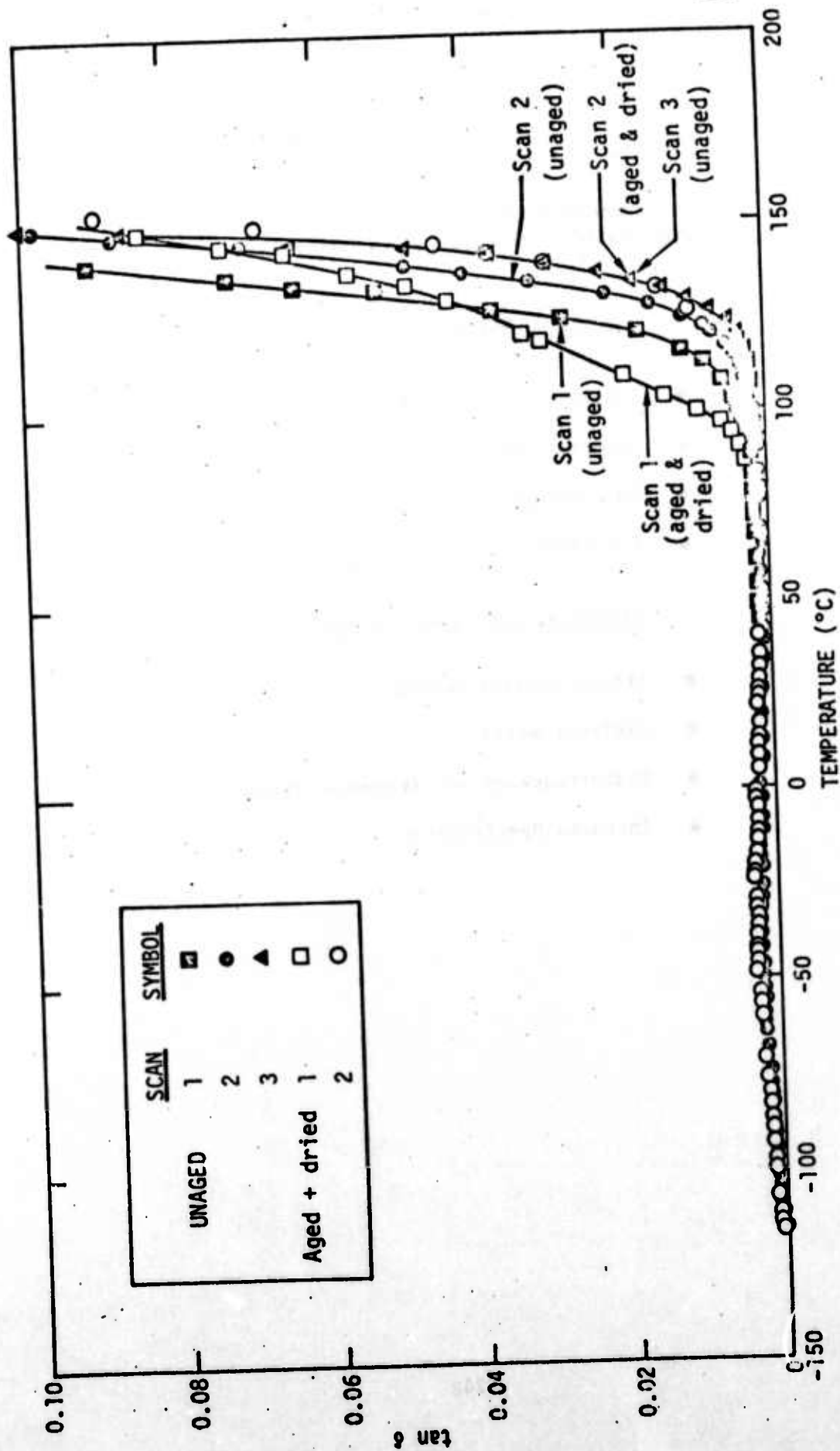


Fig. 7



Science Center
Rockwell International

TABLE 4

CANDIDATE DIAGNOSTIC NDE TESTS
FOR STRENGTH DEGRADATION IN COMPOSITES

CANDIDATE STANDARD NDE TESTS

- Ultrasonics (Frequency Spectra)
- Acoustic Emission
- Thermography
- Penetrants

CANDIDATE DEVELOPMENTAL TESTS

- Strain-density Sensors
- Dielectrometry
- Radiofrequency and Microwave Tests
- Infrared Spectroscopy

Gages such as strain-density sensors or dielectrometer electrodes can, of course, be fabricated into a composite material and operate as valuable new methods for monitoring internal stress and physical response. Specific spectrographic tests that can conduct an analysis of chemical structure state of the composite surface using optical (IR) or microwave response of the polymer matrix phase are also recommended by the very specific information deduced from IR spectroscopy in this study. In conjunction with the methods of Table 4 an appropriate selection of laboratory tests for materials and subsystem response from Table 2 are, of course, required to isolate the physiochemical mechanism of strength degradation.

References

1. B. Harris, P. W. R. Beaumont, and E. M. deFerran, J. Matl. Sci. 6, 238 (1971).
2. P. W. R. Beaumont and B. Harris, J. Comp. Matls., 7, 1265 (1972).
3. E. L. McKague, Jr., J. E. Halkias, and J. D. Reynolds, Ibid., 9, 2 (1975).
4. D. H. Kaelble, Proc. 23rd Intl. Cong. of Pure and Appl. Chem., 8, Butterworths, London (1971) pp. 265-302.
5. D. H. Kaelble, J. Adhesion, 5, 245 (1973); 6, 23 (1974).
6. D. H. Kaelble, P. J. Dynes, L. H. Crane, and L. Maus, Ibid., 7, 25 (1974).
7. G. D. Wagner, Jr. and E. L. Wagner, J. Phys. Chem., 64, 1480 (1960).
8. T. F. Saunders, M. F. Levy, and J. F. Serino, J. Appl. Poly. Sci., Part A-1, 5, 1609 (1967).
9. D. H. Kaelble, and E. H. Cirlin, J. Poly. Sci., Part C, 35, 79 (1971).
10. H. T. Hahn and J. J. Pagano, J. Comp. Matls., 9, 91 (1975).
11. A. A. Fahmy and A. N. Ragai, J. Appl. Phys., 41, 5112 (1970).
12. A. A. Fahmy and A. N. Ragai - Ellozy, J. Comp. Matls., 8, 90 (1974).
13. N. J. Pagano, J. Comp. Matls., 8, 310 (1974).
14. G. Moram and A. Weinberg, J. Matls. Sci., 10, 1005 (1975).

Publications Developed From This Work

- P-1 "Detection of Hydrothermal Aging in Graphite-Epoxy Composites Part 1: Interfacial Aspects", (by D. H. Kaelble, P. J. Dynes, L. Maus) to be published.
- P-2 Detection of Hydrothermal Aging in Graphite-Epoxy Composites Part 2: Matrix Aspect (D. H. Kaelble, P. J. Dynes, to be published).
- P-3 "Detection of Hydrothermal Aging in Graphite-Epoxy Composites, Part 3: Internal Stress Effects"(by D. H. Kaelble, P. J. Dynes, O. Buck, and D. O. Thompson) to be published.

Titles to Figures

- Fig. 1 Dependence of interlaminar shear strength λ_b (upper view) and moisture content as Wt. % H_2O (lower view) on hydrothermal aging time t at $100^\circ C$ in H_2O .
- Fig. 2 Variation of interlaminar shear strength λ_b (aged-hydrated) with sound velocity C_L (upper view) and attenuation α_L (lower view) of of subsequently dried composites SC-2-2 and SC-2-3.
- Fig. 3 Temperature dependence of interlaminar shear strength λ_b for unaged ($t = 0$) and hydrothermally aged ($t = 1000$ hrs) samples of composite SC-2-3.
- Fig. 4 Temperature dependence of $\tan \delta$ for cured BP 907 Epoxy Matrix at 110 Hz.
- Fig. 5 Tensile relaxation modulus $E(t)$ versus temperature T for cured BP 907 Epoxy at $t = 15$ sec.
- Fig. 6 Linear thermal expansivity of composite SC-2-3 transduce to fiber orientation subsequent to hydrothermal aging and drying (initial sample length 1.000 in. at $23^\circ C$).
- Fig. 7 Temperature dependence of $\tan \delta$ for composite SC-2-3 parallel to fiber orientation for unaged and aged-dried specimens.



Science Center
Rockwell International

PROJECT III

FAILURE PREDICTION

UNIT I - Determination of Residual Stresses in Structural Materials

- Task 1 Harmonic Generation by Ultrasonic Surface Waves for Materials Characterization
O. Buck, Science Center, Rockwell International
- Task 2 Detection of Stress Through Magnetostrictive Contribution to Electrodynamic Generation of Ultrasound
R. B. Thompson, Science Center, Rockwell International

UNIT II - Acoustic Emission

- Task 1 Effect of Microstructure on The Frequency Content of Acoustic Emissions
L. J. Graham, Science Center, Rockwell International

PROJECT III, UNIT I, TASK 1
HARMONIC GENERATION BY ULTRASONIC WAVES
FOR INTERNAL STRESS DETERMINATION

O. Buck
Science Center, Rockwell International

Summary

From Elbaum's work¹ it is known that ultrasonic harmonic generation is sensitive to σ_μ , the internal stress of the second kind (microscopic internal stress) which is due to the elastic distortions in the vicinity of the dislocations. σ_μ , to a large degree, determines the yield stress and the work hardening as well as the state of fatigue of metals and, thus, is of great technological importance.

These internal stresses of the second kind should be clearly distinguished from internal stresses of the first kind (macroscopic internal stresses). In X-ray diffraction internal stresses of the first kind give rise to a line shift or, equivalently, to a unique lattice parameter change over large areas of the surface, whereas internal stresses of the second kind give rise to a line broadening (and no line shift) due to positive and negative lattice parameter changes and their mean being unchanged.

The first year's effort in this task was concentrated exclusively on harmonic generation using acoustic bulk waves. The work was done in two phases:

A. Assembly and checkout of the equipment to detect harmonic generation due to finite amplitude waves. Since dislocations do not contribute to harmonic generation in fused silica, this material was used to check the equipment and compare the results with those expected from other work and from theoretical predictions.

B. Selected experiments on harmonic generation due to the internal stress field of dislocations (or other defects) in ductile materials to investigate the effects of internal stresses of second kind on ultrasonic harmonic generation.

The results may be summarized as follows:

(1) At present, the equipment operates very well for bulk wave experiments and a paper describing some interesting relationships between the second and higher harmonics was submitted for publication.

(2) Internal stresses of the second kind can be detected, although not all of the causes are understood at the present time.



Experiments and Discussion

Phase A was completed in March, 1975, and is described in a paper², "Higher Harmonics of Finite Amplitude Ultrasonic Waves in Solids," submitted to J. Acoust. Soc. Am. (see attachment). The equipment consists of a fused quartz transducer to excite sinusoidal finite amplitude acoustic waves and a capacity microphone and heterodyne receiver to detect the harmonics. The characteristics of this microphone are that the output voltage is directly proportional to the displacement of the specimen surface, independent of frequency (10-250 MHz). The heterodyne receiver serves as a frequency spectrum analyzer. The dynamic range of the equipment is in excess of 60 dB. For more details the reader is referred to Reference 2.

During the checkout period experiments on the harmonic generation in fused silica was extensively studied. At room temperature fused silica is a very brittle material so that dislocation contributions to harmonic generation are virtually suppressed. This makes fused silica an ideal material to study the lattice contributions to harmonic generation. Such measurements thus allow calculations of third order elastic constants which can be checked against results from other authors using different techniques. We succeeded in showing that:

(1) Third order elastic constants obtained by second harmonic generation are in good agreement with the ones obtained by other authors, thus establishing that the equipment works satisfactorily.

(2) The dependence of harmonic generation on specimen length and fundamental amplitude is as predicted theoretically.

(3) Fourth and (higher) order elastic constants are unimportant for the interpretation of harmonic generation in brittle materials. With respect to the second harmonic, the first and second point can be summarized as

$$U_{2l} = U_1^2 \omega^2 x [f(C_{ij}, C_{ijk})] e^{2i(\omega t - kx)} \quad (1)$$

in which the indices 2 and l are used to indicate that eqn. (1) describes the lattice contribution to the second harmonic, U_1 is the amplitude of the first harmonic, ω the circular frequency of the first harmonic, x the specimen length, and C_{ij} and C_{ijk} the second and third order elastic constants. The third point above is important in cases where contributions other than originating from the lattice contribute to third (or higher) harmonic generation. Knowledge of C_{ij} and C_{ijk} alone is then sufficient to calculate the signal background due to the lattice contributions and separate it from contributions due to lattice defects. Again, the interested reader is referred to Reference 2 for more details.

In Phase B the effects of compressive loads of aluminum, below and exceeding the yield stress, as well as annealing and fatigue effects on

second harmonic generation were studied. Some of these effects had been studied previously by Elbaum et al.³ and attributed to dislocation motion during application of the cyclic stress field. Such dislocation motion yields a second harmonic contribution

$$U_{2d} = U_1^2 \omega^2 x[f(\ell, \Lambda)] e^{2i(\omega t - kx)} \quad (2)$$

due to the nonlinearity of stress and strain as the dislocation vibrates. In Eqn. (2) ℓ and Λ describe the dislocation loop length and density, respectively. The index d indicates the dislocation contribution and the other terms are as explained with respect to Eqn. (1). ℓ and Λ are important parameters determining the state of internal stresses of the "second kind." Such stresses extend over microscopic distances (μm) and yield line broadening in X-ray Bragg reflection. They are responsible for work hardening. In many cases these stresses τ_1 are related to the dislocation density by

$$\tau_1 \propto \sqrt{\Lambda} \quad (3)$$

Internal stresses of the "first kind" are, in contrast, extended over macroscopic distances (mm) and give rise to a line shift in the Bragg reflection (change in lattice parameter). A typical example of such stresses occurs during three-point bending of a material during which the elastic limit is not exceeded. In the following the experiments are described in terms of effects of first and second kind internal stresses on harmonic generation of acoustic bulk waves.

Internal Stresses of the First Kind

Al 2219 in the solid solution treated condition (T3) was exposed to homogeneous external stresses not exceeding the yield stress (maximum stress applied $\approx 1/3$ yield stress). During application of those stresses the second harmonic amplitude was monitored. As shown in Fig. 1 the amplitude of the second harmonic U_2 (at constant U_1) is independent of the external stresses as expected from Eqns. (1) and (2).

Internal Stresses of the Second Kind

(a) Compressive stresses exceeding the yield stress and room temperature recovering experiments. Second and third harmonic generation was monitored in an as-grown aluminum single crystal and after application of 5 and 10 times the yield stress σ_y of the material ($\sigma_y \approx 1 \text{ MNm}^{-2}$). The results are shown on the left-hand side of Fig. 2. U_2 is unusually high in the as-grown condition. This is expected since the dislocation contribution to second harmonic generation is high due to a long dislocation loop length and low dislocation density. As the crystal is deformed this dislocation contribution diminishes (internal stresses of the second kind increase)

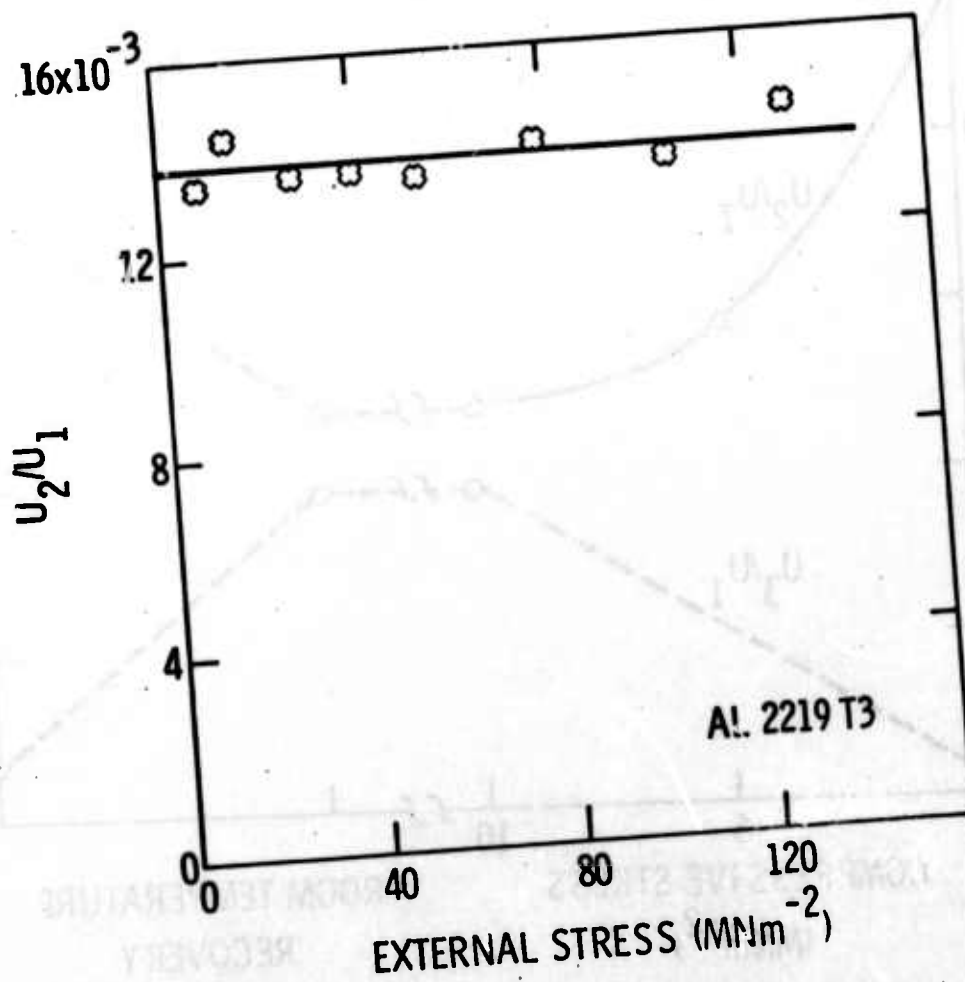


FIG. 1

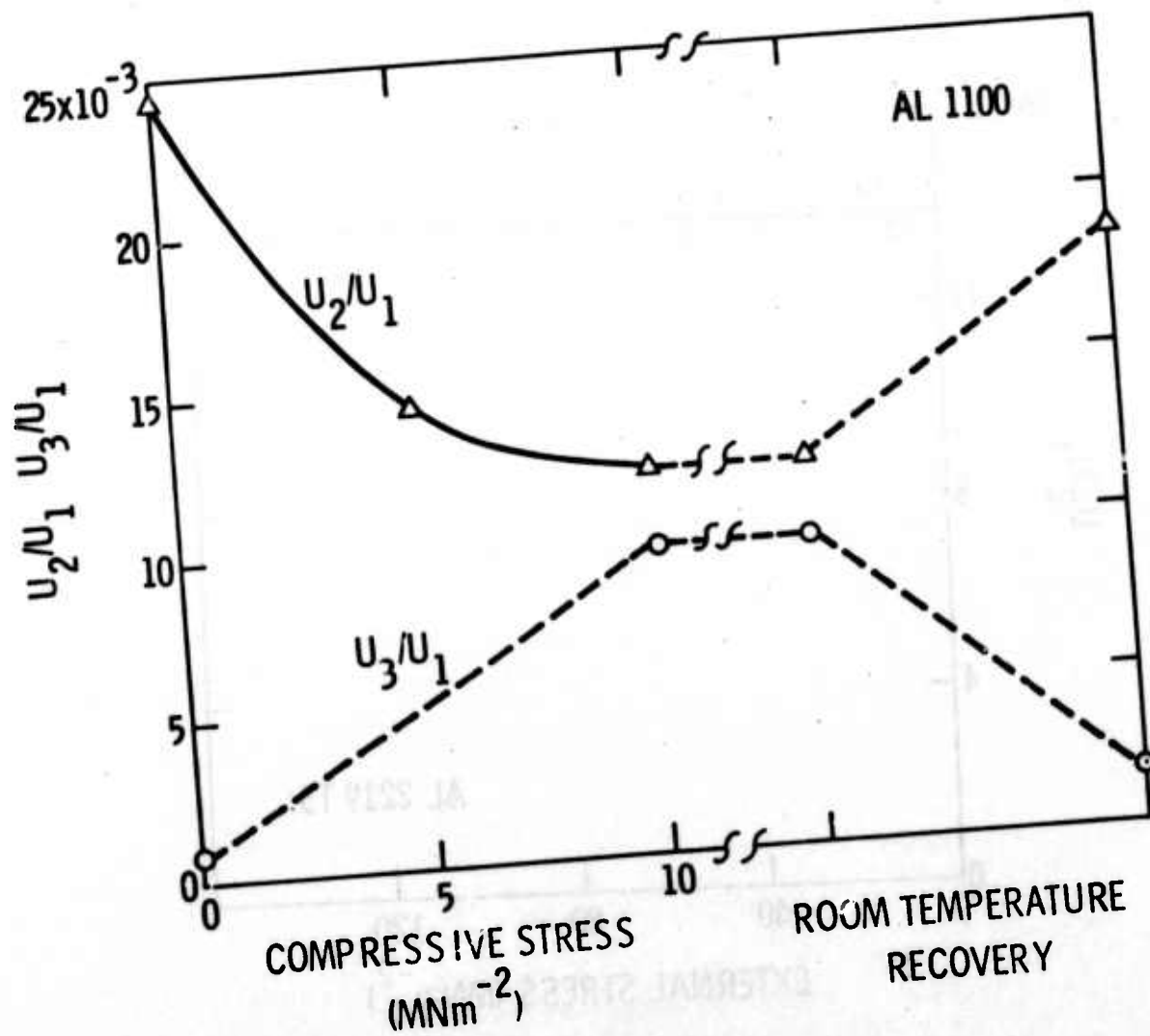


FIG. 2

and the second harmonic approaches a value expected from the lattice contribution U_{2l} (Eqn. (1)). As observed by Elbaum et al.¹,

$$U_2(\text{total}) = U_{2l} + U_{2d} \quad (4)$$

from which the internal stress could be calculated if the exact relations in Eqns. (1)-(3) were known.

During long-time room temperature anneal (see right-hand side of Fig. 2) the second harmonic increases again. For a deformed Al single crystal this result is not surprising since the stacking fault energy is so high that dislocation cross-slip and dislocation annihilation can easily occur, reducing the internal stress of the second kind.

(b) Fatigue softening experiments. After application of a compressive stress ($\approx 15 \sigma_y$) U_2 as well as the Knoop hardness were determined. Thereafter the specimen was fatigued in compression-compression at $R = \frac{\sigma_{\min}}{\sigma_{\max}} = 0.1$ with $\sigma_{\max} = 5 \sigma_y$. After several fatigue periods, both U_2 and Knoop hardness were measured again. As shown in Fig. 3, U_2 increases and the Knoop hardness decreases as a function of fatigue. Again this result is expected qualitatively since it is clear from the hardness measurements that fatigue softening occurs leading to an increasing U_2 . Microscopically this effect is caused by a typical fatigue induced dislocation cell structure with long dislocation loops oscillating back and forth in areas of relatively low dislocation density. These long loops lead to extrusion-intrusions at the specimen's surface and eventually to microcracks (see Grosskreutz,³ e.g.).

(c) Other structural changes affecting second harmonic generation. The aluminum alloy Al 2219 was exposed to the solid solution treatment (T3) and to an aging treatment at 190°C for various amounts of time. Knoop hardness and U_2 are shown in Fig. 4. The increase of the Knoop hardness in these experiments is due to the formation of precipitate particles. The concomitant increase of the second harmonic, however, cannot be explained at the present time. As evidenced by transmission electron microscopy (Dr. N. E. Paton, Science Center) interface dislocations have been formed during precipitation. These interface dislocations may be responsible for the increase in U_2 during aging.

References

1. A. Hikata and C. Elbaum, Phys. Rev. 144, 469 (1966).
2. R. B. Thompson, O. Buck and D. O. Thompson, "Higher Harmonics of Finite Amplitude Ultrasonic Waves in Solids," submitted to Journal of Acous. Soc. of America (SC-PP-75-87).
3. J. C. Grosskreutz, Phys. Stat. Sol. (b) 47, 11 and 359 (1971).

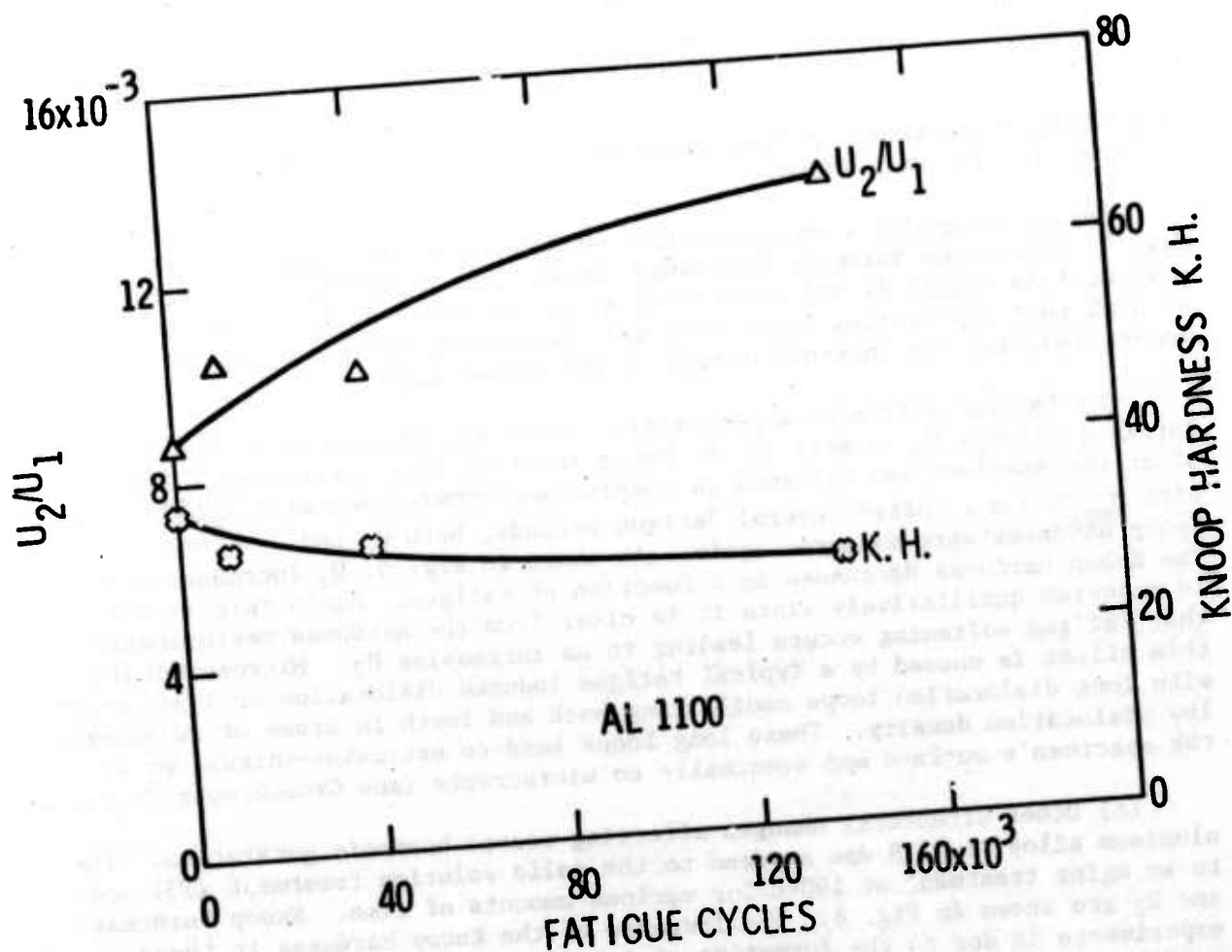


FIG. 3

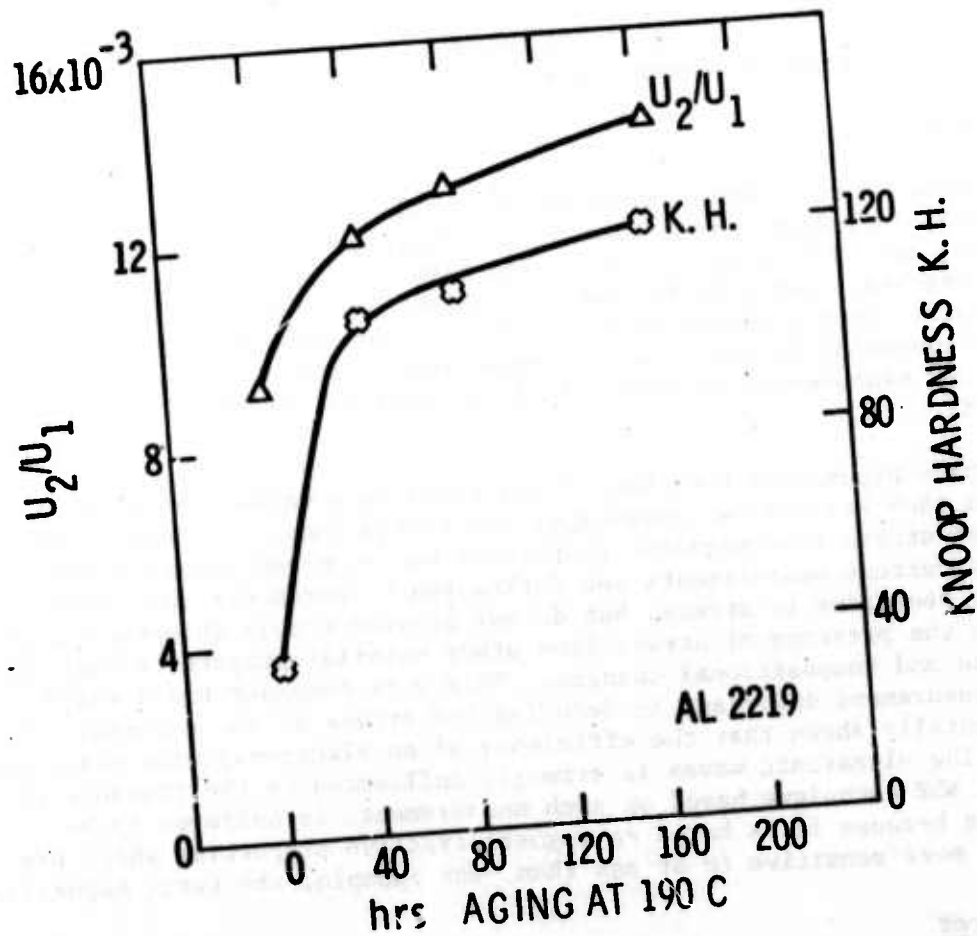


FIG. 4

PROJECT III, UNIT I, TASK 2

RESIDUAL STRESS DETECTION BY MEASUREMENT OF
EFFICIENCY OF ELECTROMAGNETIC GENERATION OF ULTRASOUNDR. B. Thompson
Science Center, Rockwell InternationalIntroduction

The presence of residual stresses in metals can have varied deleterious consequences, including a reduction in the resistance of a part to corrosion and fatigue, and warping of a part during machining when a heavily stressed region is removed. X-ray techniques for stress detections are available, but they suffer from a number of limitations. The apparatus is bulky and often time-consuming to use, surfaces must have a certain amount of preparation, and the measurement is made only in a layer of thickness less than a mill (25 μ m).

Alternate procedures have been found based on a variety of physical principles, and each has its own advantages and limitations. In ferrous materials deduction of stress from magnetic properties has received considerable attention. Eddy current measurements and Barkhausen measurements have each been shown to be sensitive to stress, but do not provide enough information to distinguish the presence of stress from other material properties such as cold working and compositional changes. This work demonstrates a third magnetic measurement important in deducing the stress of the material. It is experimentally shown that the efficiency of an electromagnetic transducer for generating ultrasonic waves is strongly influenced by the presence of stress. An NDE technique based on such measurements is believed to be advantageous because it is based on magnetostrictive properties which are shown to be more sensitive to stress than, for example, the total magnetization.

The Transducer

Figure 1 shows the experimental situation under consideration. The electromagnetic transducer consists of a serpentine coil of wire carrying current at the ultrasonic frequency ω , and a magnet producing a static field H_0 . When the transducer is placed on a metal, ultrasonic waves are radiated along the surface, with greatest efficiency occurring when the surface wavelength is equal to the period of the coil. If the waves are detected by a receiving transducer (of any type) and the static field is varied, the signal changes are shown in the bottom of the figure. In a non-ferrous metal, the signal strength increases linearly with the static magnetic field (dotted curve). The generation of ultrasound occurs as a result of the reaction of the induced eddy currents and the static magnetic field, i.e., the Lorentz force on the eddy currents. In ferrous metals, this same process is observed at high fields for which the material is magnetically saturated. At lower fields, however, there is a considerable

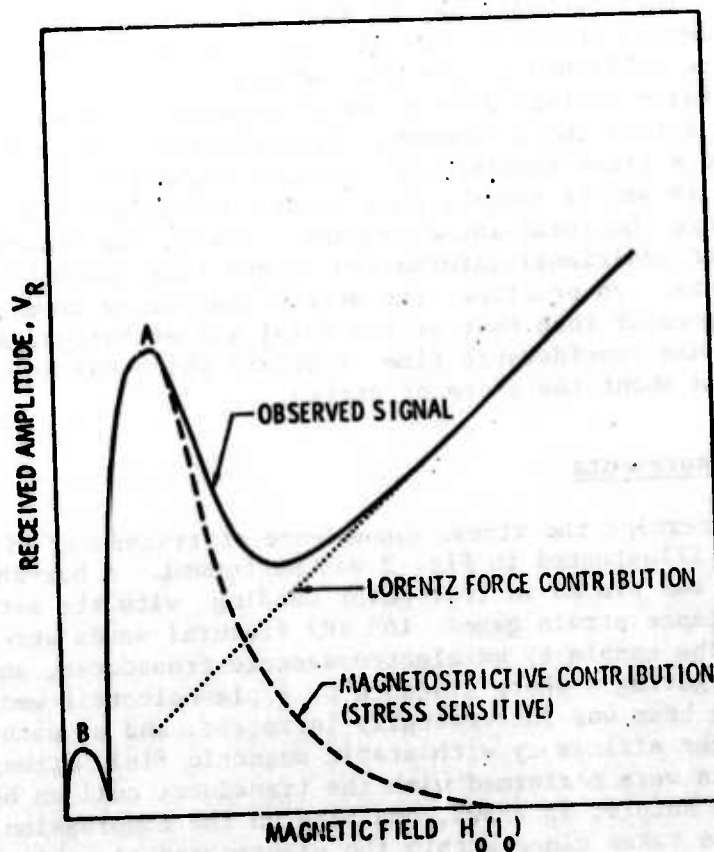
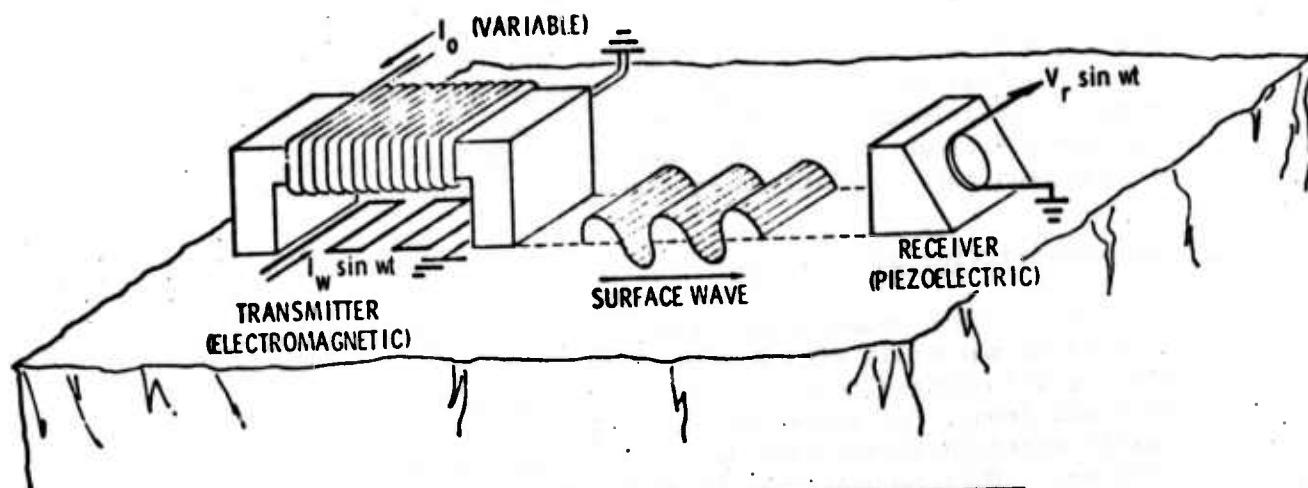


Fig. 1 Experimental measurement of transducer efficiency as a function of magnetic field. Typical result for iron shown schematically at bottom.



deviation from linearity. In iron and low carbon steel, 2 distinct peaks occur. It has previously been established¹ that the mechanism for this enhanced efficiency is magnetostriction, and in particular that the transduction efficiency is proportional to the differential magnetostriction at the bias point determined by the static field.

Magnetostriction and Stress

Others have demonstrated that the magnetostriction, or change in length of ferrous materials with applied field, is very sensitive to stress. This is illustrated in Fig. 2 by the static data of Kuruzar and Cullity² on Armco iron. The magnetostriction is changed markedly, and in an easily distinguishable fashion, by the application of tensile or compressive stresses. This response may be qualitatively understood in terms of magnetic domain theory as was discussed in the verbal review of this work and will be published in the proceedings.³ The key concept is that applied stresses favor certain directions of magnetization within the material, and hence alters the microscopic distribution of magnetic moments which constitute a given macroscopic state of magnetization. Magnetostriction, or change in sample length, only occurs during certain of the processes which change the total magnetization. Hence, its measurement provides significant additional information beyond that available in other magnetic measurements. In practice, the stress dependence of magnetostriction is somewhat greater than that of the total magnetization, and in ferrous materials has considerable fine structure which can be used to gain detailed information about the state of stress.

Stress Measurements

To determine the stress dependence of transducer efficiency, the experiment illustrated in Fig. 3 was performed. A bar-shaped sample of 1018 steel was placed in four-point bending, with the extension monitored by a resistance strain gage. 165 kHz flexural waves were excited at the center of the sample by an electromagnetic transducer, and were detected after propagating a short distance by a piezoelectric wedge pickup. The bend of the beam was incrementally increased, and at each step the variation of transducer efficiency with static magnetic field strength was measured. Measurements were performed with the transducer coil on both the tension side of the sample, as shown, and also on the compression side. The generation process takes place within the electromagnetic skin depth, a few mills in this experiment. Hence, one transducer position determined the response to a tensile strain as indicated on the strain gage, while the second position determined the response to an equal magnitude compressive strain. The bending was primarily elastic, with maximum deformation calculated to produce the yield stress at the sample surface. Some yielding did occur, however, as a permanent deformation of the sample was observed upon completion. The measured strain after release of load was 6.5×10^{-4} as compared to the total strain of 3×10^{-3} applied.

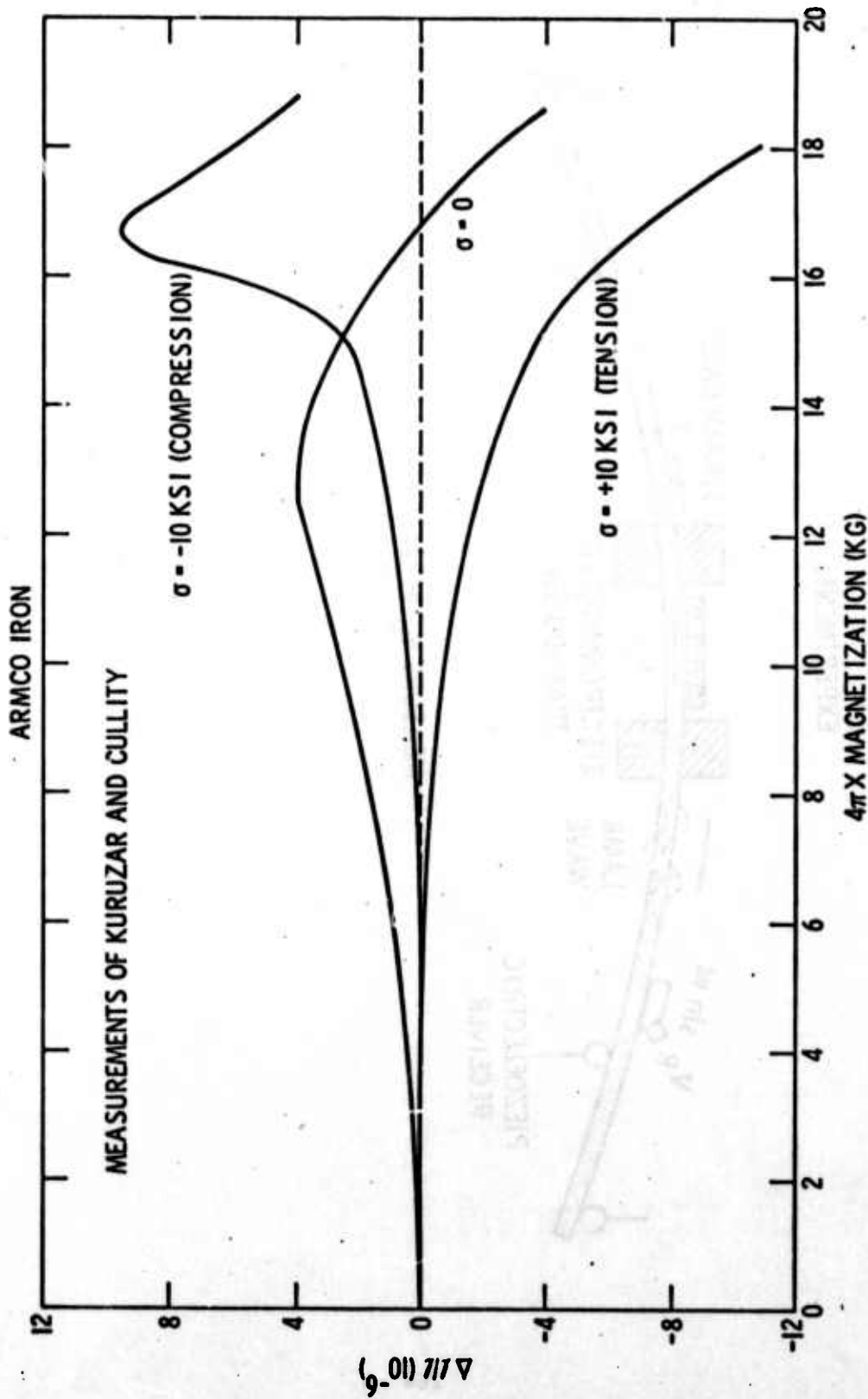
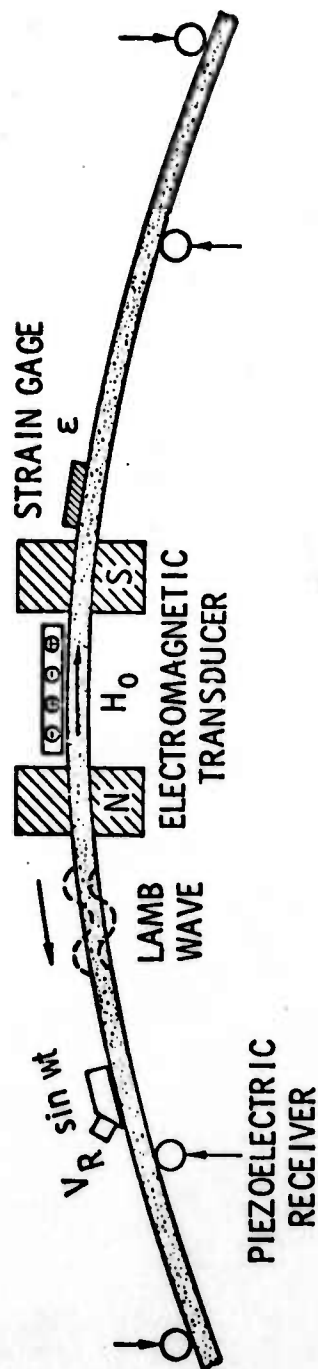


Fig. 2 Static magnetostriction of iron (Ref. 2)

EXPERIMENT:



MEASURE $V_R(H_0, \epsilon)$

Fig. 3 Apparatus for measuring stress dependence of transducer efficiency

Figure 4 shows the signals obtained for no applied stress, and for calculated surface stresses of 60 ksi compression and tension. Only at fields of a few hundred Oersteds and lower was there a large variation of transducer efficiency with stress. Referring to Fig. 1, this is the region below peak A and including peak B. Peak B is clearly seen for the case of zero stress in Fig. 4. However, the tensile load causes this peak to vanish and moved the side of peak A to lower fields. Conversely, the compressive load causes peak B to split into a doublet and moves the side of peak A to higher fields. These results, which are proportional to the differential magnetostriction, are qualitatively consistent with the static data in Fig. 2.

The data illustrated the large sensitivity of transducer efficiency to residual stress. It is clear that considerable additional work is needed before the information contained in the fine structure can be fully interpreted. At the present time, a number of features have been identified which show promise as stress indicators. Figure 5 shows one which is simply defined and could be measured automatically. Here the magnetic field has first been increased to saturate the sample magnetically and then decreased past peak A until the signal dropped to 1/3 of its maximum value. The electromagnet voltage (roughly proportional to applied field) at this point is plotted versus calculated stress in the lower half of the figure. It is seen that the indicator is quite sensitive to stress, particularly under compression. The effect saturates, but only at very large stresses.

It will also be noted that the data obtained in tension (side A) is slightly offset from that in compression (side B), suggesting the presence of a residual stress. This would not be surprising since the sample was prepared by a 1700°F anneal followed by cold drawing to the final bar shape. Subsequent X-ray analysis⁴ showed side A to have a compressive stress of 3 ksi and side B to have a compressive stress of 16 ksi, consistent with the offset.

Comparison To Other Techniques

It is important to compare this measurement to other magnetic techniques. As noted previously, the approach differs from eddy current and other techniques sensitive to total magnetization because magnetostriction is not sensitive to magnetization changes caused by 180° domain wall motion. Our measurement only senses the reversible changes in magnetization produced by 90° domain wall motion and by magnetization rotation within a domain. It is also quite distinct from the Barkhausen effect⁵, which senses the irreversible changes in magnetization, mostly 180° wall motion, which occur during the magnetization process. Further studies are needed to determine the influence of texture, composition, etc. on the measurement and to see in what manner the information obtained can be optimally used, either alone or in conjunction with that provided by these other techniques.

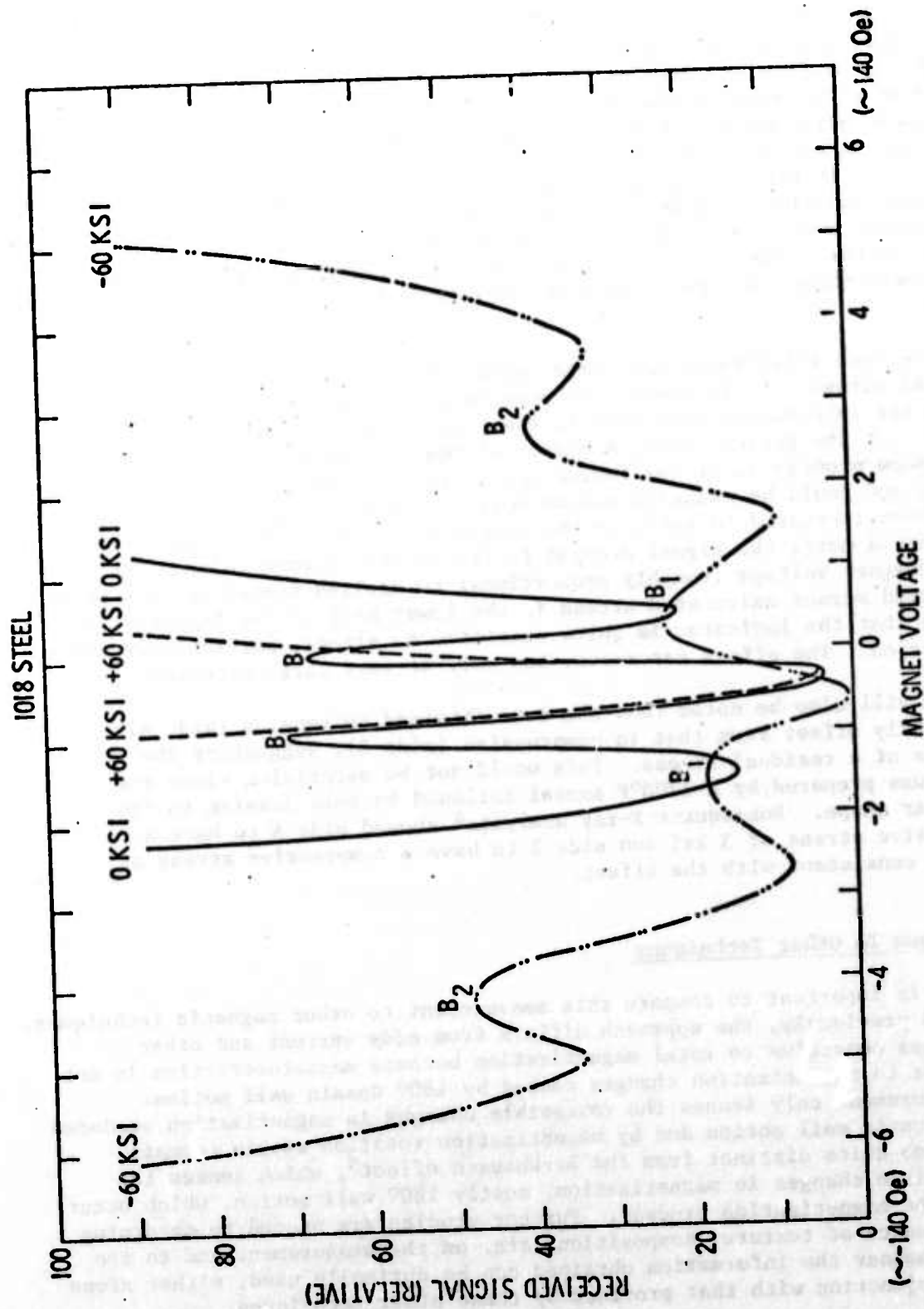


Fig. 4 Field dependence of efficiency for 1018 steel at different stress levels.

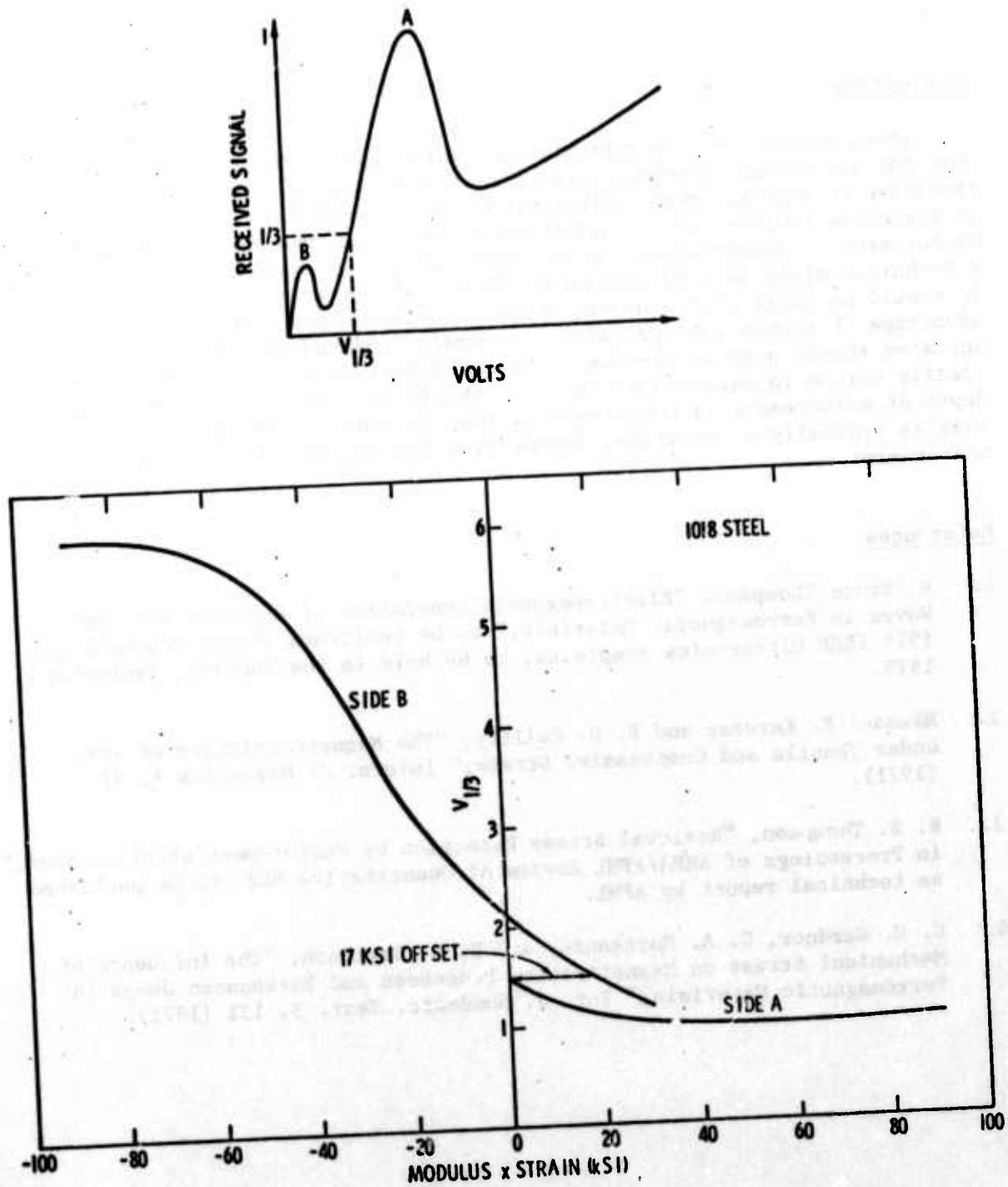


Fig. 5 Correlation of simply measured parameter with stress.



Conclusions

These exploratory experiments have established, for the first time, that the efficiency of electromagnetic transduction of ultrasound is quite sensitive to stress. Much additional study is needed and it would certainly be hazardous to proclaim a new NDE technique based upon this limited set of measurements. Nevertheless, it is important to ask what characteristics such a technique might have if continued studies are equally promising. First, it should be noted that a device would be quite simple and would have the advantage of noncontact operation. Secondly, painted or moderately rough surfaces should pose no problem. The technique would thus appear to be ideally suited to maintenance use. It should be finally noted that the depth of measurement is comparable to that in eddy current measurements. This is typically a few mills, deeper than X-rays, but certainly not a bulk measurement.

References

1. R. Bruce Thompson, "Electromagnetic Generation of Rayleigh and Lamb Waves in Ferromagnetic Materials," to be published in the Proceedings, 1975 IEEE Ultrasonics Symposium, to be held in Los Angeles, September, 1975.
2. Michael E. Kuruzar and B. D. Cullity, "The Magnetostriction of Iron under Tensile and Compressive Stress," Intern. J. Magnetism 1, 323 (1971).
3. R. B. Thompson, "Residual Stress Detection by Measurement of Ultrasound," in Proceedings of ARPA/AFML Review of Quantitative NDE, to be published as technical report by AFML.
4. C. G. Gardner, G. A. Matzkanin, and D. L. Davidson, "The Influence of Mechanical Stress on Magnetization Processes and Barkhausen Jumps in Ferromagnetic Materials," Int. J. Nondestr. Test. 3, 131 (1971).



Science Center
Rockwell International

PROJECT III, UNIT II, TASK 1

SOURCES OF ACOUSTIC EMISSION IN ALUMINUM ALLOYS

L. J. Graham and W. L. Morris
Science Center, Rockwell International

Introduction

The relatively recent technology of acoustic emission (AE) monitoring of growing flaws in structures would be a much more valuable NDE tool if more were known about the sources of AE. It is well known that AE signals are generated by the sudden release of elastic stored energy over a localized region in a material. This sudden release of energy can be associated with crack growth, plastic deformation, phase transformations, and twinning. These processes do not always produce detectable acoustic emissions, however, and a greater understanding of the micromechanical processes that occur is required to increase the reliability of the AE method for monitoring flaw growth. Two goals of studies of the basic processes of AE generation would be for extrapolation of present knowledge of AE behavior of materials to new conditions, and for predicting flaw criticality. Past studies aimed at attaining these goals have been in the areas of understanding the basic AE generation processes and in correlating engineering and fracture mechanics parameters to AE parameters. Some notable examples have been studies of AE generation in metal¹ and ionic² single crystals, phase transformations in steels³ and in intermetallic compounds⁴, the identification of slow crack growth processes in steel through AE amplitude distributions^{5,6}, and in ceramics by frequency analysis of AE⁷, and studies relating the AE generation rate to stress intensity factors and crack growth rates in both metals⁸ and ceramics⁹. In the present study we have attempted to determine the effects of microstructure on the micromechanical processes of AE generation, and to identify characteristic features of the AE which are related to these effects. The sources of AE during tensile tests of laboratory specimens and the effect of the microstructure on these sources were determined for six commercial aluminum alloys. Also, some preliminary work on two steel alloys was performed.

Experimental Method

In order to survey a wide variety of parameters on the AE behavior of several metals, a simple, inexpensive specimen geometry was chosen. This geometry is shown in Fig. 1. The specimen blanks were machined out of rolled plate material so that the tensile axis of the specimens could be aligned along each of the three principal orientations of the rolled plate as shown at the right of Fig. 1. Two exceptions to this were that the 2048 aluminum alloy was an experimental cast and forged ingot and the 1100 aluminum alloy was a 1/8" thick sheet. The aluminum alloys used in this study are shown in Table I along with their nominal chemical compositions. In addition to these six

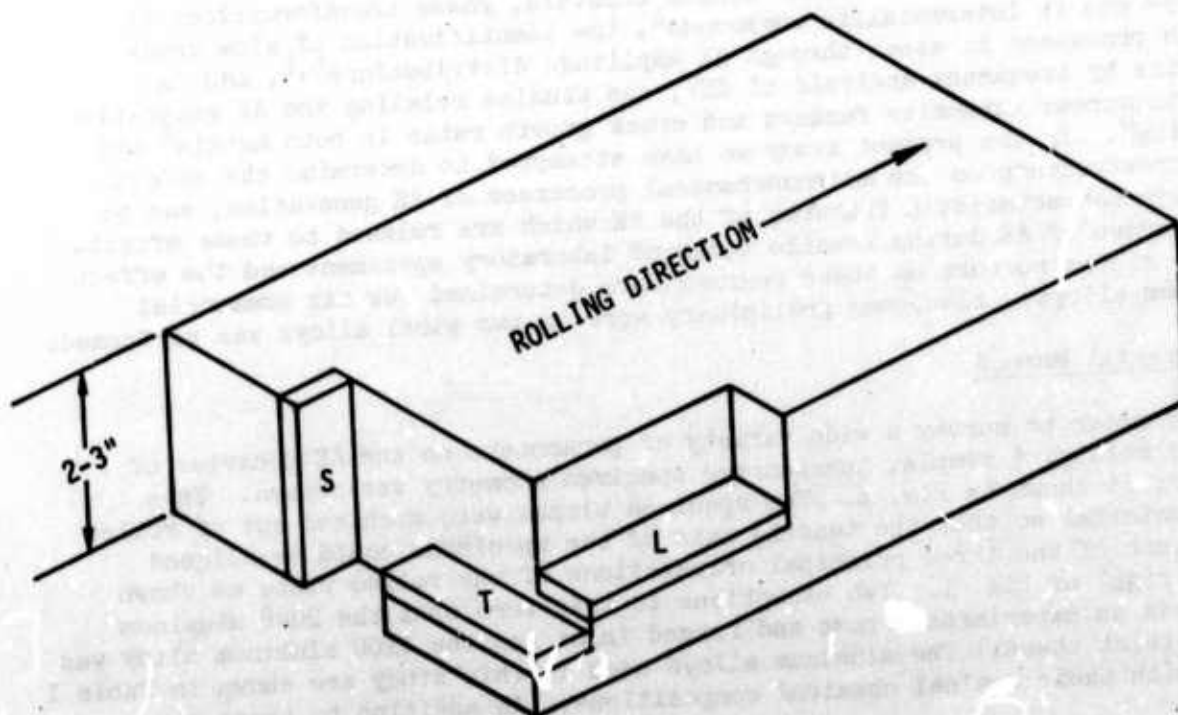
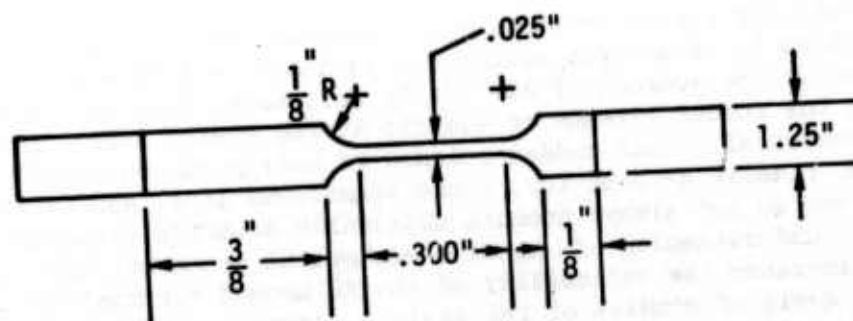
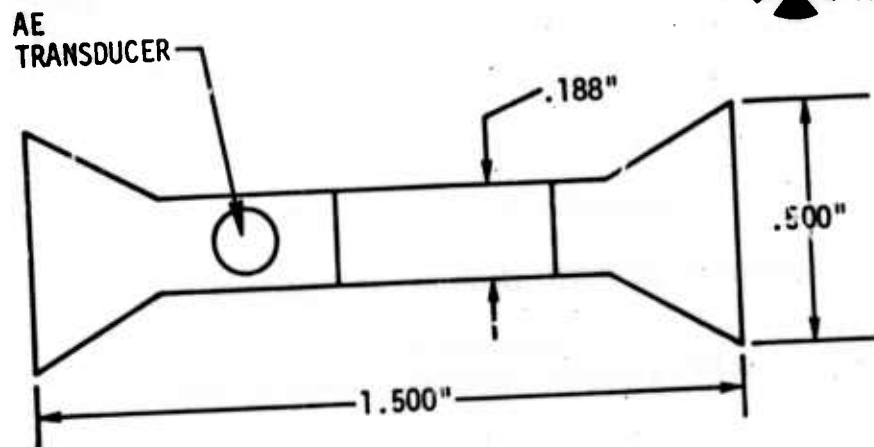


Fig. 1. Tensile specimen configuration which was used throughout the study and the orientation of their tensile axes in the rolled plate material.

Table I. The aluminum alloys of this study arranged in order of decreasing acoustic emission activity indicating the appearance of the intermetallic particles and the size range of the majority that were fractured.

Alloy	Typical Size of Fractured Particles μm	Particle Appearance	Si	Fe	Cu	Mg	Mn	Zn	Cr	Ti	Other
2024	10-20	Many in stringers - 100-500 μm long, many smaller, a few larger, all fractured.	.5	.5	3.8-4.9	1.2-1.8	.3-.9	.25	.1	-	.15
2219	5-10	Many dispersed, many smaller, a few larger, all fractured.			.63		.3			.06	.19
7075	2-5	Many dispersed. Many very small < 2 μm	.5	.7	1.2-2.0	2.1-2.9	.3	5.1-6.1	.18-.4	.2	.15
2048	10-20	Lower density compared to 2024	-	-	4.4	1.5	.6	-	-	-	-
6061	2-5	At grain boundaries. Many very small < 2 μm .	.4-.8	.7	.15-.4	.8-1.2	.15	.25	.15-.35	.15	.15
1100	2-5	Most very small. < 2 μm Only rare particle fracture and mostly the largest.	~ 1.0		.2		.05	.1			.15

*Metals Handbook, 8th Ed., ASM, 1961, p. 917.

aluminum alloys, some work was also done on A533-Grade B-Class 2 steel and HY-80 steel. All the tensile specimens were of the same geometry so that comparison of the AE behavior could be made directly between specimens under different conditions. The experimental variables used to change the microstructure and fracture behavior of the materials are shown in Table II, along with the AE parameters which were measured. Also indicated are parameters which are planned for use in a continuation of this study.

The AE monitoring system which was used has been described in detail elsewhere¹⁰. The bandwidth selected for this study was from 50 kHz to 3 MHz. The low frequency limit was determined for rejection of the Instron tensile machine noise and the high frequency limit was determined by the bandwidth of the modified video tape recorder which was used to record all of the analog AE signals. A special trigger level circuit was used to maintain a constant trigger level of $50 \pm .05$ mV for all tests. Acoustic emission event counting was done rather than the usual ring-down counting since a correlation between the number of events and features on the fracture surface of the specimen was desired. During the tensile tests strip chart recordings were made of the cumulative event count, the event count rate, the AE rms voltage level (Hewlett-Packard Model 3403A rms voltmeter), and the load on the specimens. The AE signals recorded on the broadband video tape recorder were later played back for observation of the appearance of the bursts, their duration, relative amplitudes, rise times, time of occurrence, and general appearance. Also frequency analyses of individual AE bursts were obtained using a Hewlett-Packard Model 8552A/8553B swept frequency spectrum analyzer. Several hundred AE bursts were analyzed for each specimen at different times in the loading history to get an indication of changes in the processes involved in the AE generation.

Both optical and scanning electron microscope observations were made of the fracture surface and of the lateral surfaces in the gage length of the specimens. These observations were used to identify the effects of the test parameters on the deformation and fracture behavior of the specimens for correlation with changes in the AE behavior, so that the sources of AE could be identified.

Experimental Results and Discussion

Tensile specimens were tested in batches of 10-20 specimens at a time. The load behavior, acoustic emission behavior, and appearance of the lateral and fracture surfaces of the specimens were determined, and then all of this data digested. Certain inferences could then be made about the effect of the test parameters on the fracture behavior and the effect of the fracture behavior on the AE's which were produced. To test the validity of these inferences, test parameters were changed and a new batch of specimens tested including some specimens which were tested under the same conditions as the previous tests as control specimens. In this way our knowledge of the sources of AE and the effect of changing the microstructure on these sources was established.



SC595.10AR

Conclusions of this study. The conclusions of this study will be stated now and then a discussion of the experimental results will be made showing how the various experimental parameters and microstructural conditions of the material affected these basic conclusions. The first conclusion is that the AE behavior of the various materials under the various conditions was markedly different. A second conclusion was that the AE had four basically different frequency spectral types and this information could be used to help identify the sources of the AE. The third conclusion deals with the identification of the sources of AE. The primary source in all of the aluminum alloys tested was the brittle fracture of 2-20 μ m second phase intermetallic particles. A secondary source under some test conditions was the brittle fracture of small regions of matrix material. These two sources were responsible for 99% of the AE in most of the materials. Other sources which were identified occurred more rarely, but were important in that they could be distinguished by a different frequency spectrum of the AE they produced which indicated a different microstructural or crack growth condition. Specific examples of these sources are grain boundary separation, delamination along grain boundaries, and matrix cleavage. Another source of AE produced what is termed "continuous emission" which was usually of a low amplitude. It is believed that this source of AE was due to either gross plastic deformation of the matrix or of the brittle fracture of sub-micron size intermetallic particles caused by the plastic deformation. These three conclusions of this study (the variability of the AE behavior of various materials, the classification of the frequency spectra of the AE, and the identification of the sources of the AE) will now be discussed in terms of the experimental observations.

Overall AE behavior. The tensile test results of Fig. 2 are typical for most of the aluminum alloy specimens tested, and show the effect of specimen orientation on both the loading behavior and on the AE behavior. (For purposes of identification the specimen numbers include the letters L, T, and S indicating orientation as shown in Fig. 1; specimen listing is in Table III.) For each of the specimens of Fig. 2 there are shown two curves for the AE event rate, \dot{N}_E . The curve at the left goes with the scale shown on the ordinate and gives more of the details of \dot{N}_E below the yield point. For the other curve, the numbers on the ordinate must be multiplied by a factor of 10. This curve shows the features of \dot{N}_E throughout the loading history. The main feature of these data is that for the longitudinal (L) and the long transverse (T) specimen, \dot{N}_E goes through a maximum shortly past the yield point while for the short transverse (S) specimen, \dot{N}_E continually increases right to fracture. It should be noted that for specimen 2S4 shown in Fig. 2, \dot{N}_E increased to a value which exceeded the capabilities of the counter system. This was the only specimen tested for which this happened. In contrast, the two steels had a very different AE behavior as illustrated by the data of Figure 3, which are typical for both the A533 and the HY-80 materials. Not shown in Figs. 2 and 3 are curves for the rms voltage level of the AE signals. With the proper scaling these usually fell right on top of the \dot{N}_E curves. However, under some conditions the rms voltage curve was skewed to either early or late in the tensile test relative to the \dot{N}_E curve. This means that the AE amplitude distribution changed during the test, which might also

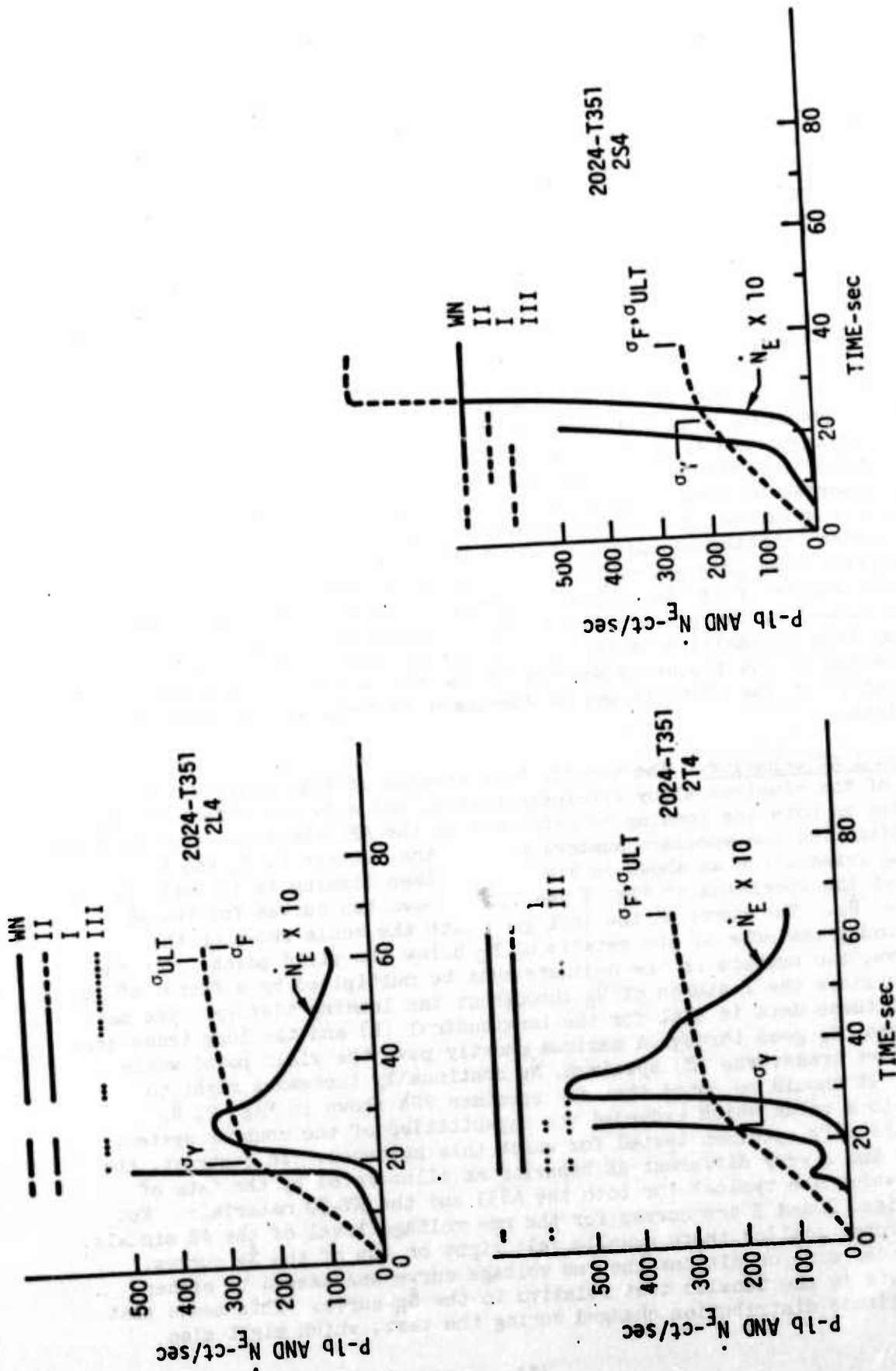


Fig. 2. Tensile test results for the 2024-T351 specimens of the L, T, and S orientations as an illustration of the acoustic emission behavior of many of the aluminum specimens.

Table II. Parameters of this study on acoustic emission source identification and parameters planned for use in a continuation of this study.

Experimental Variables

Alloy content	
Impurity content	
Heat treatment	
Surface condition	
Specimen orientation	
Specimen origin	
Strain rate	

Specimen geometry	} Future
Grain size	
Temperature	

Observations

Event count	} vs. time
Event count rate	
rms voltage	
Load	
Signal appearance	
Frequency analysis	
Fractography - SEM and optical	

Amplitude distribution	} Future
Signal phase	

Table III. Mechanical and acoustic emission event count (N_E) data for all the tensile specimens tested.

Specimen Number	Cond.	Special X-Head Cond. in/min	σ_Y ksi	σ_{ULT} ksi	ϵ_P %	N_E	N_E/ϵ_P
<u>2219</u>							
1L4	T851	.05	45.8	62.3	9.6	32292	3370
1L8	T851	.05	45.9	60.3	9.2	21380	2330
1L1	T851	EP-SS	46.0	61.7	9.2	-	-
1L5	T851	SS	49.8	65.2	9.1	22360	2460
1L6	T6	.05	43.9	59.8	13.1	(60000)	(4500)
1L2	T6	EP	34.5	51.5	10.6	55300	5220
1L3	ST	.05	17.3	44.2	26.3	78138	2970
1L7	ST	EP	16.3	43.1	25.0	(70000)	(3000)
1T4	T851	.05	45.2	62.6	6.0	68365	11400
1T2	T851	.005	48.2	63.2	8.1	81600	10100
1T1	T851	SS	47.8	64.7	8.8	34510	3920
1T5	T851	EP-SS	48.2	64.0	7.9	24000	3040
1S4	T851	.05	45.2	60.9	4.5	69601	15500
1S6	T851	.05	48.2	61.7	4.2	61570	14650
1S1	T851	.005	48.8	60.3	3.2	75698	23600
1S10	T851	90°	48.7	58.5	2.5	41500	16600
1S5	T851	EP	48.6	60.9	3.3	13660	4140
1S7	T851	EP	47.7	53.0	1.1	11600	10500
1S9	T851	EP-90°	47.3	51.8	1.3	10520	8100
1S8	T6	.05	44.4	57.2	4.6	(40000)	(9000)
1S2	T6	EP	30.2	48.2	6.3	6250	990
1S3	ST	.05	17.5	43.2	18.4	56354	3060
<u>2024</u>							
2L4	T351	.05	53.2	71.0	8.9	72466	8150
2L5	T351	EP	55.6	71.9	11.5	39700	3450
2L1	T351	SS	49.1	64.0	16.7	36470	2190
2L9	T351	SS	50.1	65.0	16.4	(30000)	(2000)
2L8	T351	EP-SS	52.3	68.4	20.5	33270	1620
2L7	T6	.05	53.4	65.1	6.2	(70000)	(10000)
2L2	T6	EP	41.0	51.0	7.8	7040	900
2L3	ST	.05	16.0	42.7	17.8	75839	4260
2L6	ST	EP	22.1	50.0	18.2	(40000)	(2000)
2T4	T351	.05	48.2	67.9	9.8	111574	11400
2T3	T351	.05	48.4	66.0	11.1	124967	11300
2T6	T351	.05	48.3	65.1	10.1	(110000)	(10000)
2T5	T351	.01	51.5	67.7	8.9	94050	10600
2T2	T351	.005	50.6	68.6	12.4	125488	10100
2T1	T351	SS	50.6	66.2	12.9	50773	3940
2T8	T351	EP-SS	48.8	66.9	13.6	48210	3540

NOTES:

1. Specimen surface in fine ground condition unless specified otherwise.
2. EP (MP) - Electropolished (mechanically polished) surface in gauge length.
3. SS - Specimen cut from position adjacent to the surface of the rolled plate.
4. 90° - Rolling direction aligned 90° to the plane of the specimen.
5. The letters L, T, and S in the specimen number refer to the tensile axis being along the plate longitudinal, long transverse, and short transverse directions.

Table III. (continued)

Table III. (continued)								
Specimen Number	Cond.	Special Cond.	X-Head in/min	σ_Y ksi	σ_{ULT} ksi	ϵ_P %	N_E	N_E/ϵ_P
<u>2024</u>								
2S4	T351		.05	46.1	58.3	3.4	104116	30600
2S9	T351		.01	46.7	59.0	3.3	54400	16500
2S8	T351		.005	45.6	57.0	2.5	53000	21200
2S7	T351	EP	.005	44.4	56.9	6.8	58400	8600
2S1	T351	MP	.05	42.7	55.8	4.1	~67000	16000
2S5	T6		.05	53.6	59.3	1.8	(70000)	(40000)
2S2	T6	EP	.05	42.8	50.5	3.8	12750	3360
2S3	ST		.05	15.5	41.7	10.2	46632	4570
2S6	ST	EP	.05	23.3	44.8	9.1	-	-
<u>2048</u>								
5L5	(T6)	EP	.05	59.5	64.8	5.9	11620	1970
5L4	(T6)	EP	.05	61.2	65.8	5.2	11580	2230
5T5	(T6)		.05	61.4	66.5	3.8	11300	2970
5T4	(T6)	EP	.05	61.8	66.7	4.1	14200	3470
5S5	(T6)		.05	57.8	64.2	4.8	11100	2320
5S4	(T6)	EP	.05	58.5	65.0	3.9	18500	4750
<u>7075</u>								
7L6	T6		.05	75.8	88.0	12.8	23380	1830
7L7	T6		.05	76.4	87.4	9.4	(20000)	(2100)
7L5	T6	EP	.05	68.7	79.4	13.3	(16000)	(1200)
7S6	T6		.05	70.5	79.0	1.9	15250	8030
7S5	T6	EP	.05	70.8	78.9	2.2	(12000)	(5500)
<u>1100</u>								
8L1	H14	EP	.05	15.0	16.0	16.5	298	18
8L2	0	EP	.05	~1.0	11.7	50.0	21716	410
8T1	H14	EP	.05	15.8	16.6	11.7	130	11
8T2	0	EP	.05	~1.0	10.6	50.3	9400	190
<u>6061</u>								
9L2	T6		.05	40.6	43.8	11.1	570	51
9L3	T6		.05	39.2	42.9	14.0	(6000)	(400)
9L1	T6	EP	.05	41.2	44.4	15.5	(5000)	(300)
9S2	T6		.05	40.3	44.6	6.7	8430	1260
9S1	T6	EP	.05	38.2	41.2	5.7	(6000)	(1000)
<u>A533 Steel</u>								
3L4	Gr.B-C1.2		.05	79.8	101.5	21.0	1139	54
3T4	Gr.B-C1.2		.05	78.9	99.2	22.5	3990	177
3S4	Gr.B-C1.2		.05	72.2	87.6	7.0	11934	1710
<u>HY-80 Steel</u>								
4L4	AR		.05	82.0	103.1	21.1	504	24
4T4	AR		.05	84.5	105.9	22.8	1820	80
4S4	AR		.05	84.7	105.5	20.8	3450	166

indicate a change in the dominant AE generation mechanisms. More work is needed to clarify this point.

Frequency spectra of AE. Above each of the curves in Figs. 2 and 3, the relative numbers and times of occurrence of AE having four distinct frequency spectral types are indicated by the relative densities of the lines drawn there. In Fig. 4 are shown frequency spectra of single AE bursts illustrating these four spectral types; (a) white noise (WN), (b) high frequency (Type II), (c) low frequency (Type I), and (d) peaked (Type III). It can be seen in reference to Figs. 2 and 3 that most of the AE bursts had a spectrum which was either very nearly white noise or was shifted to higher frequency than WN as illustrated by the Type II frequency spectrum. There was some tendency for AE's having these two types of spectra to occur at specific times during a given tensile test, but some specimens were predominantly either Type II or WN emitters. In all instances large numbers of brittle fractured intermetallic particles were observed on the main fracture surface. However, there was a large variability in the amount of brittle matrix fracture with the various test conditions and no correlation could be detected between the occurrence of these two AE sources and the two principal spectral types. Mathematical models of the sources of AE which predict the occurrence of both WN and Type II spectra^{11,12} suggest that a common feature of these sources is that the stress release occurs very rapidly (comparable to the reciprocal of the highest frequency observed) over a localized region. Both the primary and secondary sources of the AE which we believe to be operative (the brittle fracture of intermetallic particles and of small regions of matrix material observed in these specimen) can be described by such a model. An iterative feedback process between the experimental results and the mathematical modeling is in progress and may soon provide a better description for the subtle source differences that produce WN as opposed to Type II spectra.

A small percentage, perhaps 1%, of all the AE bursts analyzed did not fall into either one of the two spectral classes described above. These are illustrated in Fig. 4 by the Type I low frequency spectrum and the Type III peaked spectrum. In addition to these there were a few (less than 0.1%) which could not be classified into any of the four types shown on Fig. 4. Although there were relatively few of the Type I and Type III AE bursts, their occurrence is of importance since they tended to occur only at specific times during a test or only under certain test parameter conditions. An example is for A533 steel where, for the specimens having S-orientation (specimen 3S4 in Fig. 3), the majority of the AE bursts which occurred during the final stages of crack growth had the Type I frequency spectrum. For A533 specimens in the other two orientations this was not the case. A striking difference in the appearance of the fracture surface, observed using Scanning Electron Microscopy (SEM), was the occurrence of large regions of low energy fracture on the fracture surface of specimen 3S4 as illustrated in Fig. 5c. The precise nature of these areas is not currently known. Another example of the occurrence of the Type I AE bursts was for 2048 Al specimen 5T5. A feature of the fracture surface which was observed for this specimen was the delamination of the layered alloy structure along grain boundaries

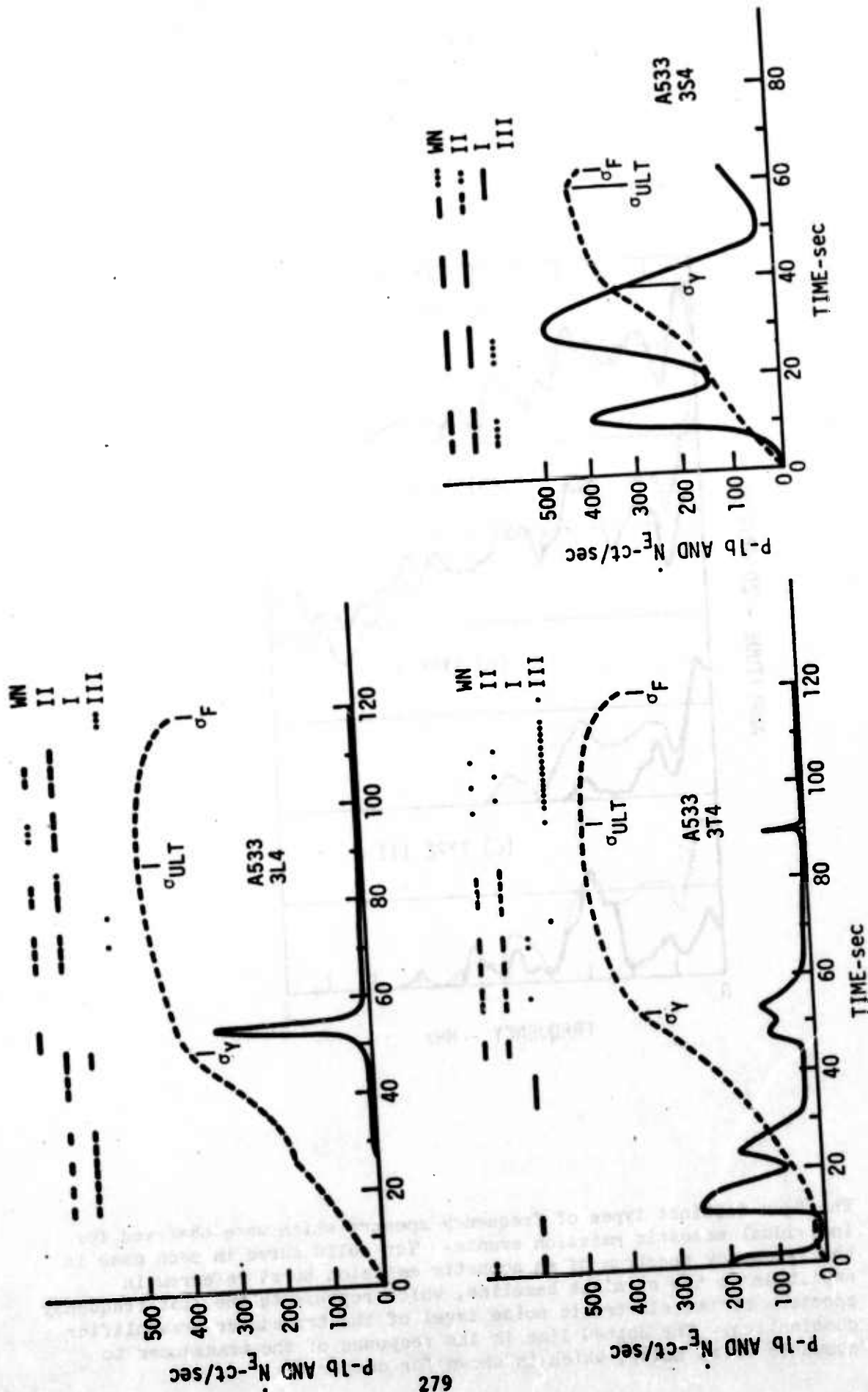


Fig. 3. Tensile test results for the A533-B steel specimens illustrating the difference between the acoustic emission behavior of the two steel alloys tested and the aluminum alloys.

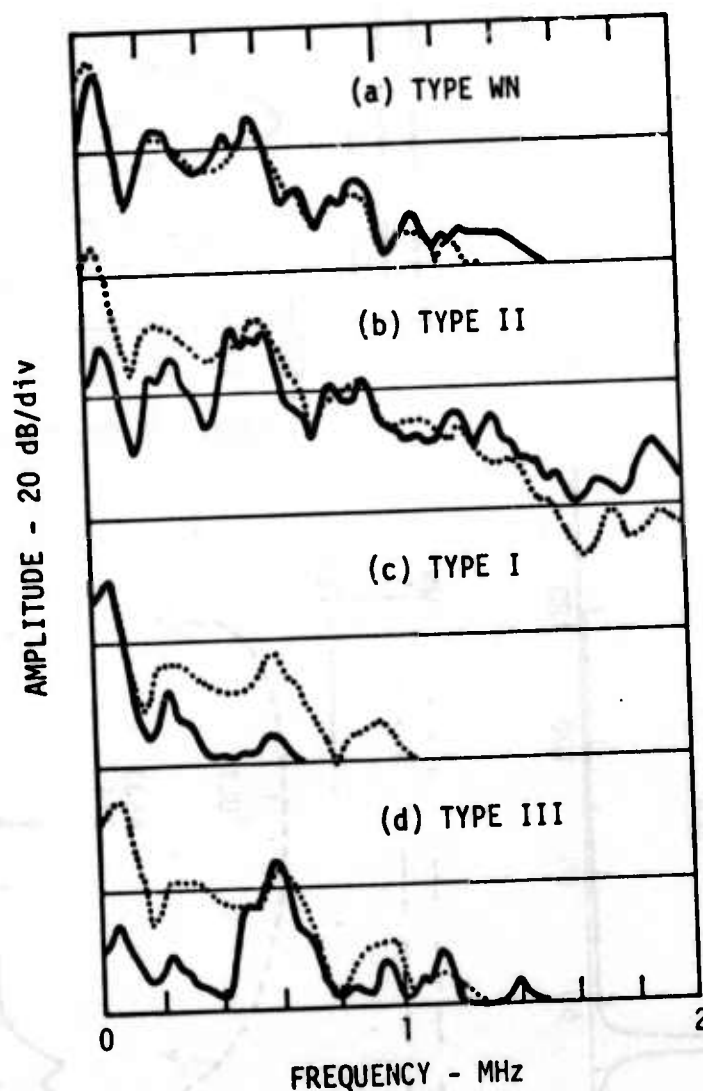
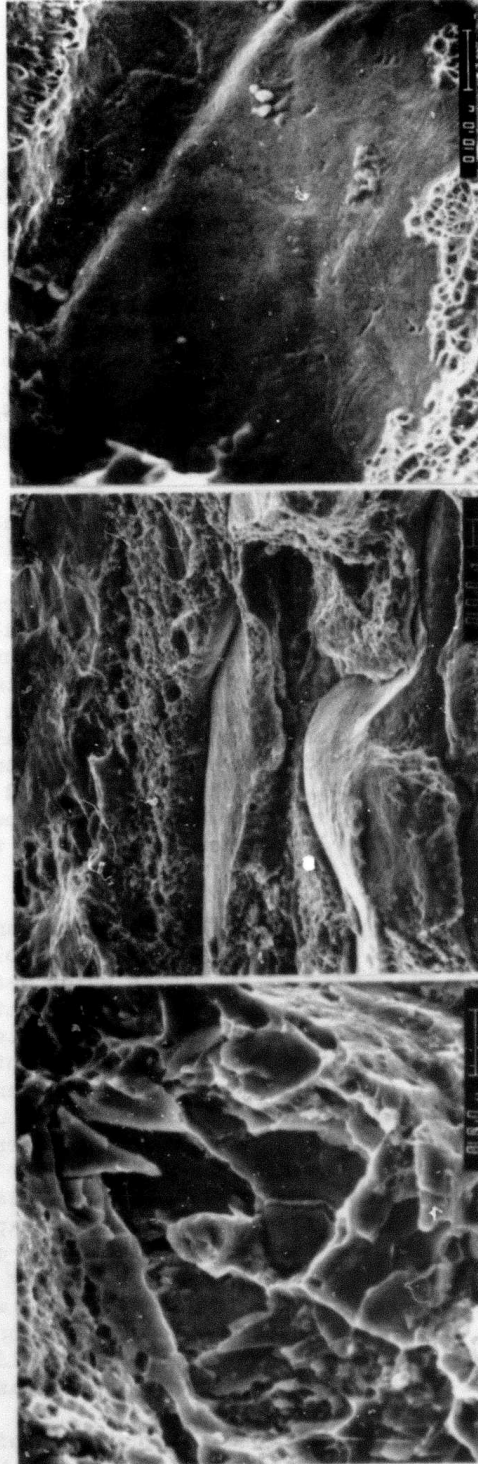


Fig. 4. The four distinct types of frequency spectra which were observed for individual acoustic emission events. The solid curve in each case is the frequency spectrum of an acoustic emission burst referred in amplitude to the straight baseline, which represents the flat frequency spectrum of the electronic noise level of the transducer-preamplifier combination. The dotted line is the response of the transducer to acoustic white noise, which is shown for comparison.

A533-B STEEL #3S4

2048 A1 #5T5

2024 A1 #2S2



LARGE REGIONS OF
BRITTLE FRACTURE

(a)

DELAMINATION

(b)

LARGE REGIONS OF
LOW ENERGY FRACTURE

(c)

Fig. 5. Regions of exceptional appearance on the fracture surfaces of specimens in which acoustic emissions having the Type I and Type III frequency spectra were observed.

which occurred when the tensile axis was in the long transverse direction. Figure 5b is a micrograph showing the delamination. Quite a few of the Type I AE bursts were generated during the test of this specimen, whereas there were none observed for the other two orientations of this material for which no delamination occurred. A common feature of the sources of AE which are believed to result in the Type I frequency spectrum in the 2048 Al and in the A533 steel was that large regions fractured in a low energy but not entirely brittle fashion which can be imagined to have occurred over a period of several microseconds. Referring again to the mathematical models which have been developed, a source which undergoes a stress release with a duration of several microseconds would result in the frequency spectrum which we have designated as Type I.

Acoustic emissions having the Type III frequency spectrum occurred more rarely and at more random intervals during specimen testing than did the Type I AE bursts. However, in 5 of the specimens tested (1S5, 1S2, 2L2, 2S2, 9L2), the Type III burst predominated. Three of these (1S2, 2L2, 2S2) were in a heat treat condition which was different from all other specimens, as will be discussed later. The appearance of the fracture surfaces of these three specimens was unique in that there were large regions of brittle fracture involving both intermetallic particles and small regions of matrix as shown in Fig. 5a. It is, therefore, tempting to correlate the Type III AE with the occurrence of brittle fracture of large regions of material. However, two additional specimens, 1S5 and 9L2, which had a predominance of the Type III AE showed only a small amount of this type of fracture on the main fracture surface. This leaves some question as to the source of the Type III AE bursts.

Effect of experimental parameters. The mechanical and AE data for all the specimens tested are shown in Table III. The last column of this table shows the ratio of the total number of AE events which were counted to the total percentage plastic strain in the specimen. This ratio is only a convenient way of normalizing the AE data to some parameter of the widely varying mechanical properties of the specimens. It is not our intent to imply that it has any basic physical significance. The entries in the last two columns which are in parentheses are data which were obtained during testing of a single batch of specimens. The event counter which had been used for all of the other specimens was not available for use for this batch and another one was substituted. The result was that a larger number of events were counted for each of the specimens than was expected. Corrections to these data were made using the results of a number of control specimens which had experimental parameters identical to previously tested specimens, and by observation of the AE signals on the oscilloscope when played back from the magnetic tape recording. As a result comparisons between the data which are in parentheses can be considered completely valid, while comparisons with the rest of the data may include an uncertainty of as much as 50%.

Table IV is a summary of the effect of orientation of the tensile axis on emission behavior including some comments on the general AE and fracture behavior of

Table IV. Effect of orientation on N_E/ϵ_P for all the materials tested in the as received condition.

	L	T	S	COMMENTS:
2024 T351	8000	11000	23000	L - Many broken inclusions on fracture surface - ductile matrix fracture. S - More crack growth on parallel planes from crack initiation sites on the lateral surfaces; more brittle fracture of matrix; T-intermediate between appearance of L and S specimens. 90° - (Specimens 1S10 and 1S9) large peak in \dot{N}_E at $\sim \sigma_y/2$.
2219 T851	2800	11000	18000	
7075 T6	2000	-	8000	Insufficient number of broken inclusions on main fracture surface to account for N_E . Sufficient broken inclusions on lateral surfaces - generally ductile fracture.
2048 (T6)	2000	3000	3000	Nearly isotropic fracture and AE behavior - very little brittle fracture of matrix. Delamination in T-orientation. Low inclusion content and fewer broken compared to 2219 & 2024.
6061 T6	400	-	1300	Limited numbers of broken inclusions - increased brittle fracture of matrix in S-orientation contributed to high AE for S.
1100 H14	18	11	-	Very few broken inclusions - very ductile fracture.
A533-B	54	177	1710	Very ductile fracture - few regions of brittle grain cleavage - quite a few large regions of low energy fracture (at grain boundaries?) in S-orientation.
HY-80	24	80	166	Very ductile fracture - few regions of brittle matrix fracture.

the various materials. There is an excellent qualitative correlations between the number of AE events (normalized to the total plastic strain) and the occurrence of brittle particle or matrix fracture. In reference to the data of Table I, it is seen that the larger intermetallic particles in the aluminum alloys are found to be much more prone to brittle fracture. So, for instance, for Al 6061 which contains only small intermetallics, burst emission was low and visible fracture of intermetallics was minimal. The appearance of the AE signals for this material compared to that for Al 7075, an average emitter, at the maximum AE event rate are shown in Fig. 6. The appearance of the fracture surfaces of Al 2024 (a high AE material) specimens having the three orientations are illustrated in Fig. 7. Brittle particle fracture is seen in all three cases, and, particularly for the S-orientation, large areas of the main fracture surface involve low energy matrix fracture.

In testing of solution treated 2024 and 2219 aluminum, load drops were observed during loading in the plastic strain region. The load drops have been associated with flurries of AE activity as illustrated by the oscilloscope trace of Fig. 8c. Similar, but lower amplitude AE activity was observed near failure for Al 1100. The fracture of Al 1100 is, of course, very ductile (Fig. 8a) and the solution treated 2000 series also results in more ductile fracture. It is presently not clear if gross plastic deformation or the fracture of sub-micron size intermetallic particles associated with gross plastic deformation participates in such flurry emission. Conflicting evidence supporting the possibility of both sources has been obtained by others^{13,14}.

Following solution treatment, some of the 2024 and 2219 specimens were further heat treated to the T6 condition resulting in more brittle matrix fracture which was particularly obvious in the L-orientation specimens. These specimens also produced more AE events. One batch of specimens which was presumably heat treated in this way (1L2, 1S2, 2L2, 2S2) had a much lower yield point and ultimate strength than normal. Three of these specimens were the ones discussed previously which produced relatively few AE which were predominantly Type III in their frequency spectra.

For aluminum specimens cut from near the surface of the plate stock (the top 1/8 inch), the total number of AE generated during a test was reduced by about a factor of two, and their generation was delayed until well past the yield point. This may be due to pre-test fracture of some of the intermetallics.

The electropolishing of selected specimens over their gage length was found to reduce the number of crack initiation sites as illustrated by Fig. 9. Specimens tested with their surfaces in the fine ground (unpolished) condition had more cracks initiated at the intermetallic particles at the surface of the specimens. By halting a tensile test when the load was about three-quarters of the load required for yielding, it was established that surface cracks initiated below this load level and were the primary cause of the AE events which occurred below the yield point. In the electropolished condition

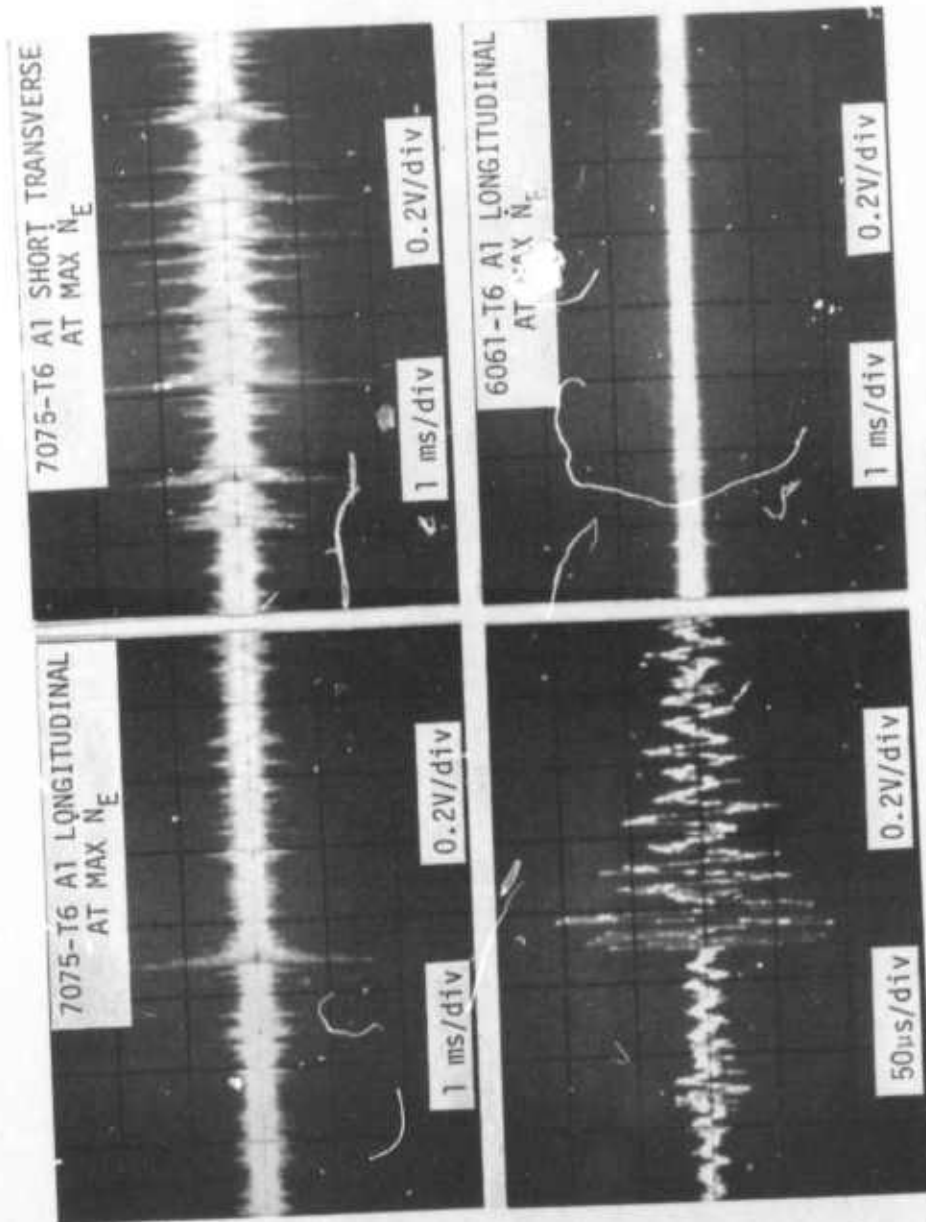


Fig. 6. The appearance of the burst type acoustic emission signals at the maximum event rate in three specimens pulled in tension at a cross-head speed of 0.05 in/min.

2024-T351 ALUMINUM

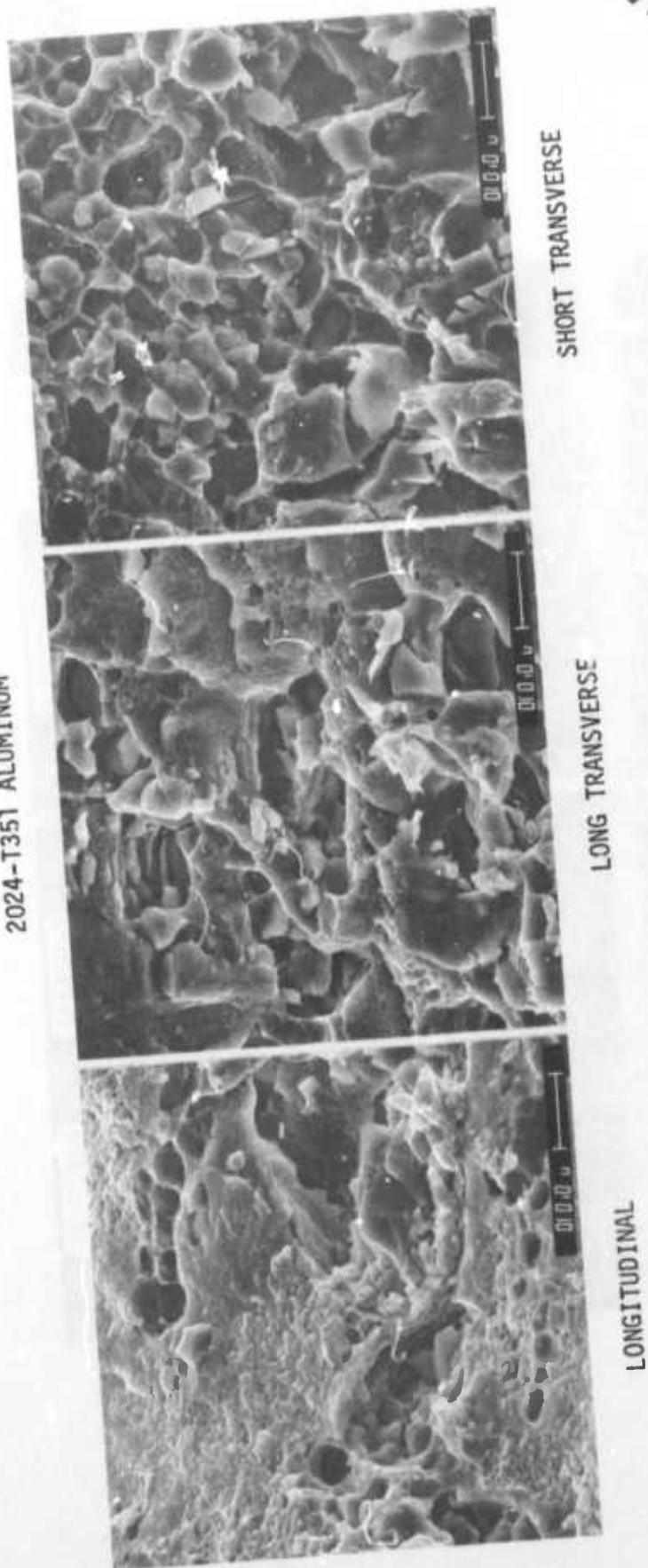


Fig. 7. The effect of specimen orientation on the fracture behavior which was typical of most of the aluminum alloys.

2024 SOLUTION TREAT ALUMINUM

1100-H14 ALUMINUM

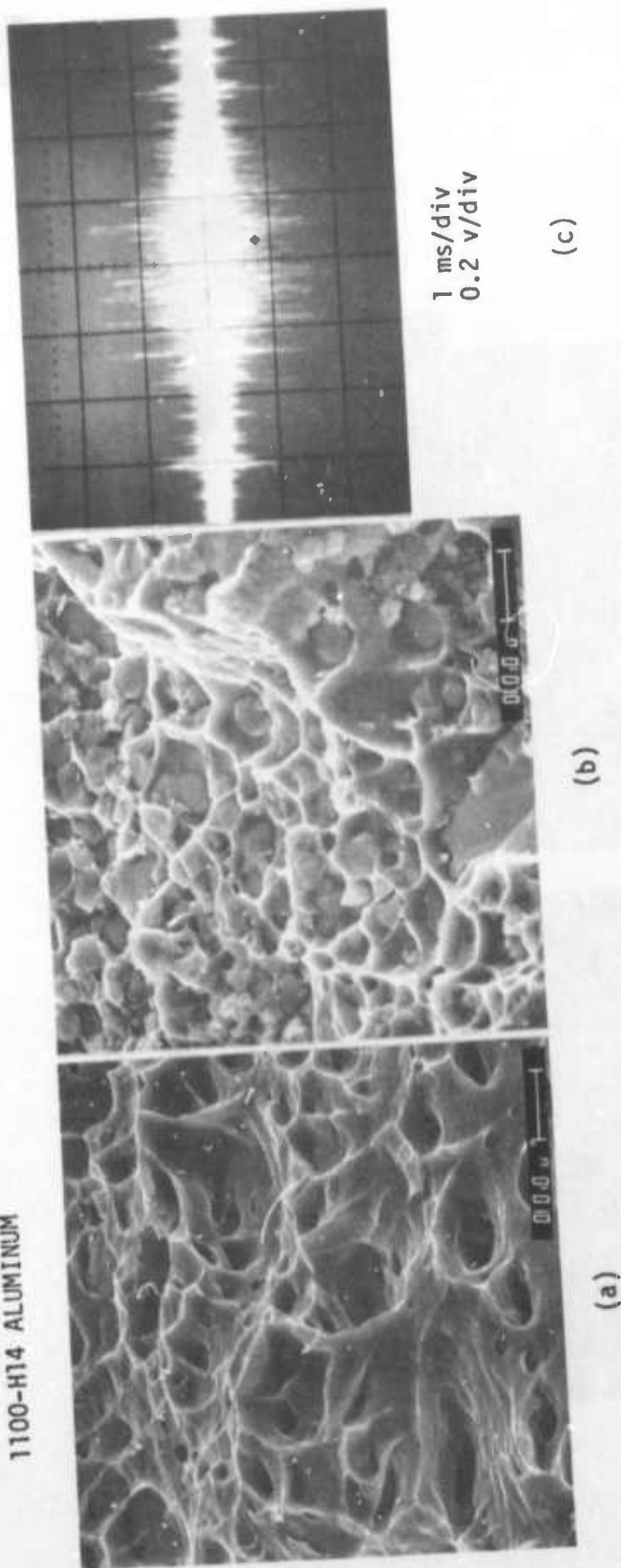
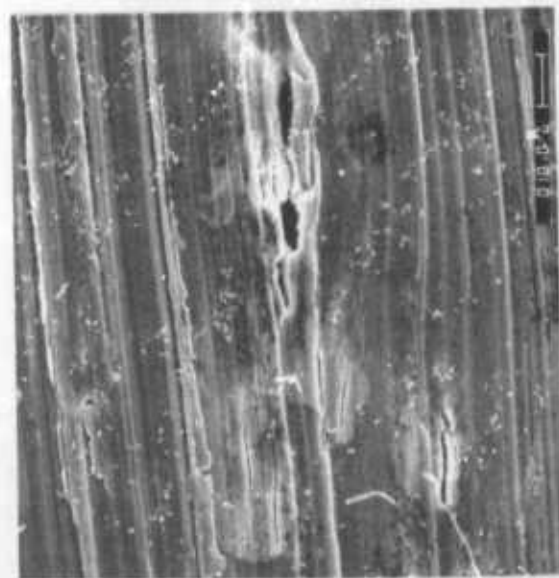
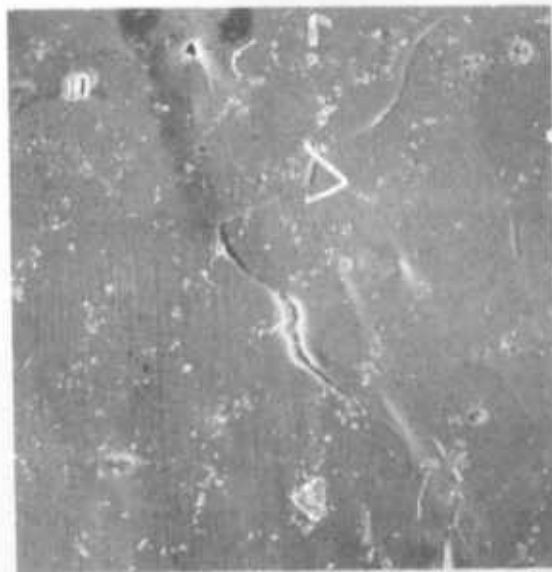


Fig. 8. A comparison of the ductile fracture of 2024 aluminum tested in the solution treated condition with that of 1100-H14 aluminum. Flurries of continuous acoustic emission occurred simultaneously with load drops during the tensile tests of the 2000 series alloys.

2219-T851 ALUMINUM



FINE GROUND



ELECTROPOLISHED

Fig. 9. The effect of electropolishing in reducing the number of crack initiation sites at intermetallic particles on the surface. The electropolished micrograph is for a location much closer to the main fracture surface which is the only region of significant lateral surface cracking for the specimen shown.



Science Center
Frockwell International



a fewer number of the particles at the surface were fractured and a smaller proportion of these fractures propagated into the matrix material. The net effect was a reduction by about a factor of two in the number of AE events generated in most electropolished aluminum specimens. An opposite effect was observed to occur for the 2048 aluminum, however. In this material electropolishing resulted in the reduction of below yield crack initiation, but produced large areas of brittle matrix cleavage in zones near the surfaces of the specimens later in the loading history. This increased the total number of AE observed, many of which had the low frequency Type I spectrum.

The effect of mechanically polishing the surfaces of one Al 2024 specimen with 0.5 μm aluminum oxide powder delayed the occurrence of AE until well past the yield point, but otherwise had no effect on the fracture behavior or the number of AE's generated.

The strain rate of the tensile test had no effect on either the fracture behavior or the AE behavior of the 2024 and 2219 aluminum specimens. This can be seen particularly for the T-orientation specimens in Table III. The AE data for the S-orientation specimens was less reproducible apparently because of the greater tendency for specimens of this orientation to randomly develop significant crack growth along several parallel fracture planes. However, even for S specimens it can be seen that there is no systematic variation in the AE behavior with changing strain rate.

Summary

In terms of the immediate aims and ultimate goals of this AE study, we have identified the sources of AE in the aluminum alloys studied as a function of the various experimental parameters and have qualitatively characterized the quite different AE behavior of the two steel materials. We have identified characteristic features in the AE frequency spectra which, in some cases, were uniquely associated with the source of the AE. Comparison of these frequency spectra with mathematical models indicates that the white noise or high frequency Type II AE are generated by a very rapid stress release over a localized region of material while the AE having the low frequency Type I spectrum are created by a much slower stress release mechanism acting over a larger region of material. A source of the Type III AE has not been positively identified. However, the occurrence of this unusual frequency spectral type provides another possibility for the identification of an AE source by identification of a characteristic feature of the AE signal itself.

In terms of the ultimate goal of extrapolating AE data from one material or one set of test conditions to another, it seems that an understanding of the direct effects of the various parameters of the test and the indirect effects of the microstructure on the fracture behavior and associated AE need to be better understood before reliable extrapolations can be made.

In terms of the goal of determining flaw criticality from characteristics of the AE signal two points might be inferred from this study. In some of the specimens tested the transitions from slow stable crack growth to unstable rapid crack growth was accompanied by the occurrence of Type I AE and the appearance of larger regions of low energy fracture. This observation has a direct bearing on defining flaw criticality in these specimens. The transfer of this type of information to other geometries, such as for flaw growth in a structure, has not been shown as yet, but the possibility is an exciting one. A second possibility for determining flaw criticality is related to the observation of a skewness between the rms voltage amplitude of the AE signals and the event rate curves, particularly near the end of some of the tensile tests. This suggests the need for a careful determination of amplitude distributions in future studies in order to relate changes in the amplitude distribution of the AE with changes in test parameter and, more specifically, with the onset of unstable crack growth.

References

1. R. M. Fisher and J. S. Lally, *Canad. J. Phys.*, 45, 1147-1159 (1967).
2. Darrell R. James and Steve H. Carpenter, *J. Appl. Phys.*, 42, 4685-4695 (1971).
3. G. R. Speich and A. J. Schwoeble, *ASTM STP 571*, 1975, pp. 40-58.
4. A. G. Beattie, *Proc. IEEE Symposium*, Boston, Oct. 4-7, 1972, pp. 13-17.
5. J. C. Radon and A. A. Pollock, *Engr. Fract. Mech.*, 4, 295-310 (1972).
6. Yosio Nakamura, C. L. Veach, and B. O. McCauley, *ASTM STP 505*, 1972, pp. 164-186.
7. L. J. Graham and G. A. Alers, "Characteristics of Acoustic Emission Signals from Ceramics," Final Report, Naval Air Systems Command Contract No. N00019-73-C-0174, AD778015, Feb. 1974.
8. C. E. Hartbower, W. W. Gerberich, and P. P. Crimmins, *Weld. J. Research Suppl.* 47, 1s-18s (1968).
9. A. G. Evans and M. Linzer, *J. Amer. Ceram. Soc.*, 56, 575-81 (1973).
10. L. J. Graham and G. A. Alers, *ASTM STP 571*, 1975, pp. 11-39.
11. W. J. Pardee, in these proceedings.
12. K. Malen and L. Bolin, *Phys. Stat. Sol.* 61b, 637 (1974).
13. M. A. Hamstad, private communication.
14. S. H. Carpenter, private communication.